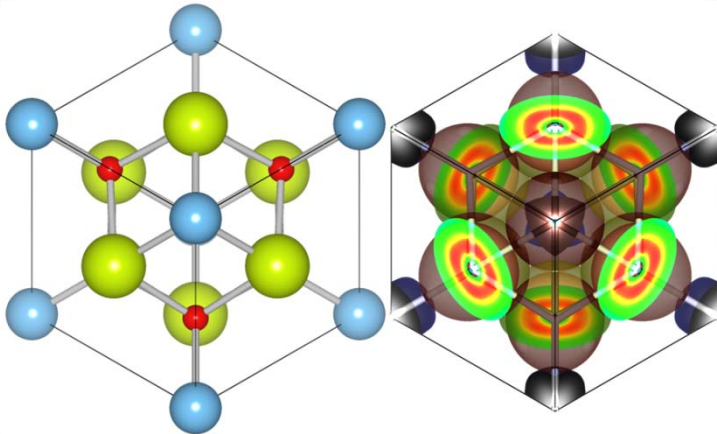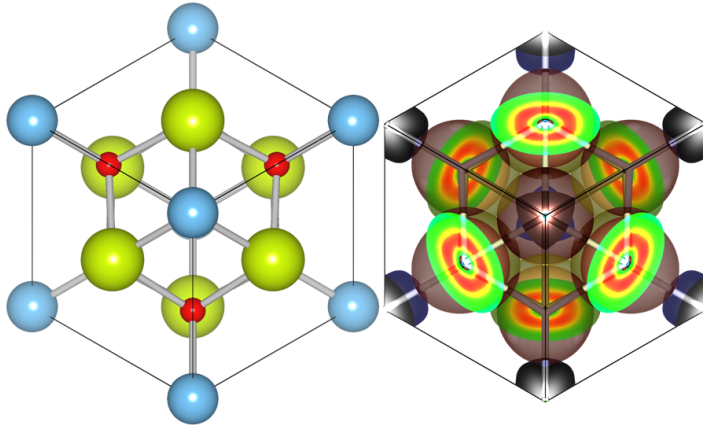# Investigation of tunable buffer layers for coated superconductors:
from solid state physics to quantum chemistry

Danny Eric Paul Vanpoucke

Investigation of tunable buffer layers for coated superconductors:

from solid state physics to quantum chemistry

Danny Eric Paul Vanpoucke

Composition of the reading and examination commission

Prof. Dr. A. Adriaens   Ghent University (Chairwoman)
Prof. Dr. I. Van Driessche   Ghent University (Promoter)
Prof. Dr. P. Bultinck   Ghent University (Promoter)
Prof. Dr. S. Cottenier   Ghent University (reading commission)
Prof. Dr. F. Peeters   University of Antwerp (reading commission)
Prof. Dr. Á. Martín Pendás   Universidad de Oviedo (reading commission)
Prof. Dr. Ir. V. Van Speybroeck   Ghent University
Dr. P. Lommens   Ghent University
Prof. Dr. A. Cedillo   Universidad Autónoma Metropolitana,
     and Ghent University

Investigation of tunable buffer layers for coated superconductors:
from solid state physics to quantum chemistry
by Dr. Danny E. P. Vanpoucke,

Investigation of tunable buffer layers for coated superconductors:

from solid state physics to quantum chemistry

Dissertation submitted in fulfillment of the requirements for the degree
of Doctor of Science : Chemistry
by

DANNY ERIC PAUL VANPOUCKE

Department of Inorganic and Physical Chemistry
Faculty of Sciences

The anthropologists got it wrong when they named our species Homo sapiens ('wise man'). In any case it's an arrogant and bigheaded thing to say, wisdom being one of our least evident features. In reality, we are Pan narrans, the storytelling chimpanzee.
Terry Pratchett, The Science of Discworld II: The Globe

CONTENTS

I INTRODUCTION

II   CERIA DOPING

III   ATOMS IN MOLECULES

IV   CONCLUSIONS

V   APPENDICES

Beknopte samenvatting

Deze dissertatie kadert in het onderzoek naar de optimalisatie van CeO_2 bufferlagen in gecoate supergeleiders. Hogetemperatuursupergeleiders zijn keramische materialen, hetgeen ervoor zorgt dat deze van nature uit broos zijn. Om toch gebruik te kunnen maken van de supergeleidende eigenschappen van deze materialen in draden, kunnen deze materialen (veelal $YBa_2Cu_3O_{7-\delta}$) als een dunne film op een metalen (Ni+5%W) draad worden afgezet. Om te voorkomen dat de metaalatomen van deze draad hierbij in de supergeleidende laag diffunderen, en zo de supergeleidende eigenschappen vernietigen, wordt gebruik gemaakt van één of meerdere bufferlagen. Een bijkomende eigenschap van deze bufferlagen is dat ze het verschil in roosterconstante tussen de nikkeldraad en de supergeleidende laag overbruggen, wat de interne spanningen tussen de twee vermindert. Ook dienen deze bufferlagen ervoor te zorgen dat de textuur van de nikkeldraad goed wordt overgedragen op de dunne film, zodat de $YBa_2Cu_3O_{7-\delta}$-microkristallen waaruit deze bestaat perfect uitgelijnd zijn. Dit laatste aspect is uiterst belangrijk gezien bij niet-uitgelijnde kristallen de supergeleidende stroom een sterke weerstand ondervindt aan de korrelgrenzen tussen verschillende microkristallen.

De meest gebruikte combinaties van bufferlagen in dit systeem eindigen vaak met een $La_2Zr_2O_7$-laag met hierbovenop nog een CeO_2-laag. Bij het groeien van deze laatste is er echter een belangrijke beperking: als deze laatste laag te dik wordt, beginnen er zich breuken te vormen. Dit gebeurt reeds bij laagdiktes van amper 50 nm. Vanuit economisch standpunt is het echter interessant om zo weinig mogelijk lagen te moeten groeien, wat inhoudt dat de individuele lagen zo dik mogelijk dienen te zijn.

De oorzaak van de breukvorming in de CeO_2-laag is niet helemaal duidelijk, maar wordt verondersteld het gevolg te zijn van het onderlinge verschil in ofwel de roosterconstanten van CeO_2 en $La_2Zr_2O_7$, ofwel hun thermische expansiecoëfficiënten. Een eenvoudige manier om deze eigenschappen aan te passen in de CeO_2-laag is door deze te doperen met andere elementen.

In deze dissertatie worden, met behulp van quantummechanische berekeningen, de invloeden van verschillende doperingselementen op de eigenschappen van CeO_2 onderzocht. In eerste instantie worden de elementen van groep IV onderzocht, gezien deze net zoals cerium een valentie van +4 hebben en er dus geen nood is aan het toevoegen van ladingscompenserende zuurstofvacatures. Uit dit onderzoek blijkt dat de elementen in groep IVa en groep IVb duidelijk verschillen qua gedrag als doperingselement. Indien de vormingsenergie van een zuurstofvacature in CeO_2 als referentie wordt gebruikt voor de stabiliteit, dan vertonen alle elementen van groep IVa een defectvormingsenergie die erop wijst dat het inbouwen van dit doperingselement niet

stabiel is, terwijl dit wel het geval is voor de elementen behorende tot groep IVb. Er wordt ook aangetoond dat de stabiliteit sterk wordt beïnvloed door de elektronenconfiguratie van het doperingselement. Bij dit laatste wordt duidelijk dat ook elektronen die niet tot de valentie-elektronen behoren een niet te onderschatten rol spelen voor de stabiliteit. Verder tonen we aan dat bij de groep IV elementen, de compressiemodulus en de thermische expansiecoëfficiënt een invers verband vertonen: een relatieve verhoging van de ene gaat hand in hand met de relatieve verlaging van de andere. Met betrekking tot de CeO_2-bufferlagen is dit slecht nieuws gezien zowel de compressiemodulus als de thermische expansiecoëfficiënt van $La_2Zr_2O_7$ lager zijn dan die van CeO_2, wat een perfecte onderlinge afstemming van beide onmogelijk maakt.

Ook met betrekking tot de compressiemodulus onderscheiden de groep IVa en IVb elementen zich van elkaar. Waar de IVa elementen zorgen voor een verlaging van de compressiemodulus, veroorzaken de IVb elementen een lichte verhoging. Anderzijds is de verlaging van de compressiemodulus bij de IVa elementen (het niet stabiel zijn van deze dopanten even buiten beschouwing latend) onvoldoende om deze van $La_2Zr_2O_7$ te bereiken met een redelijke concentratie aan dopanten. Als gevolg hiervan kunnen de groep IV elementen als geheel buiten beschouwing worden gelaten indien men enkel interesse heeft in het afstemmen van de compressiemodulus van CeO_2 op deze van $La_2Zr_2O_7$.

Wordt er echter naar de roosterconstante gekeken, dan is de situatie rooskleuriger, gezien alle groep IV elementen (lood uitgezonderd) voor een samentrekking van het rooster zorgen waarbij de $La_2Zr_2O_7$ roosterconstante perfect wordt bereikt voor alle doperingselementen bij een concentratie lager dan 10%.

Indien er afstand wordt genomen van de groep IV elementen en er wordt gebruik gemaakt van dopeerelementen met een valentie die mogelijk verschilt van vier, dan weet men vanuit experimenten dat er zich ladingscompenserende zuurstofvacatures zullen vormen. Bij het bestuderen van dergelijke elementen is er initieel onderzocht wat de invloed is indien er geen vacatures aanwezig zijn. Dit is te vergelijken met experimenten waarbij dergelijke systemen onder zuurstofrijke atmosfeer voorkomen. Voor deze doperingselementen vinden we dat de meesten kleiner zijn in de simulaties dan zou verwacht worden uit de werkelijke inbedding in CeO_2. Dit wijst erop dat een verschil in valentie ook daadwerkelijk een verschil in het aantal aangegane bindingen met de omringende zuurstof atomen tot gevolg heeft, of toch minstens een verzwakking hiervan. Van de onderzochte elementen vertonen enkel vanadium en niobium een atoomstraal in overeenkomst met valentie +4.

In de afwezigheid van ladingscompenserende zuurstofvacatures tonen deze doperingselementen dezelfde algemene trends als er gevonden zijn voor de groep IV elementen: de defectvormingsenergie is weinig afhankelijk van de concentratie; en de compressiemodulus en de thermische expansiecoëfficiënt vertonen tegengestelde aanpassingen van de respectievelijke eigenschap in CeO_2. Een interessante opmerking is hier dat er geen duidelijk verband bestaat tussen de stabiliteit van het doperingselement in CeO_2 enerzijds en de covalente straal of atomaire kristalstraal van het doperingselement anderzijds. Dit toont aan dat dergelijke stabiliteitsrelaties met een zekere omzichtigheid dienen gehanteerd te worden.

Het toevoegen van zuurstofvacatures in CeO_2 toont aan dat deze een significante invloed hebben op de compressiemodulus. Naast het verlagen van de compressiemodulus zorgen de vacatures ook voor het uitzetten van het rooster. Dit laatste valt te begrijpen indien men in aanmerking neemt dat een cerium ion uitzet bij de overgang van $Ce^{4+} \longrightarrow Ce^{3+}$. Het combineren van doperingselementen met zuurstofvacatures zorgt enerzijds voor een stabilisatie van het systeem en anderzijds voor een relatieve uitzetting van het rooster in vergelijking met het systeem zonder deze vacatures. Als gevolg hiervan voorspellen we dat er iets hogere concentraties van de doperingselementen zullen nodig zijn voor perfecte afstemming van roosterconstanten dan wat is bepaald op basis van systemen zonder vacatures. Anderzijds wordt de compressiemodulus zodanig beïnvloed dat bij een vergelijkbare concentratie voor bepaalde doperingselementen eveneens een afstemming van de compressiemodulus met deze van $La_2Zr_2O_7$ mogelijk wordt. Verder tonen de berekeningen met zuurstofvacatures ook aan dat de vacaturepositie een sterke invloed heeft op de stabiliteit ervan.

In het geval van $La_2Ce_2O_7$ blijken deze vacatures zelfs een drijvende kracht voor ordening te zijn. Bij dit laatste materiaal bestaat er immers enige onenigheid over de exacte grondtoestandskristalstructuur. Van de twee voorgestelde structuren wordt de defecte-fluorietstructuur gekenmerkt door wanorde, zowel in de kationverdeling als in de verdeling van de zuurstofvacatures. De pyrochloorstructuur wordt dan weer gekenmerkt door sterke ordening, met elke zuurstofvacature omringd door vier cerium atomen. Indien in dit systeem geen zuurstofvacatures aanwezig zouden zijn ($La_2Ce_2O_8$), dan blijkt uit onze berekeningen dat de wanordelijke structuur lichtjes stabieler is. Wanneer echter de juiste hoeveelheid zuurstofvacatures aanwezig is, slaat het stabiliteitsvoordeel over naar de pyrochloorstructuur. Meer nog, op basis van de berekende X-stralendiffractiespectrum voor de pyrochloorstructuur is duidelijk waarom deze vaak niet wordt herkend in experimenten: de meest prominente van de prototypische pyrochloorreflecties zijn extreem klein – kleiner dan zou verwacht worden op basis van bijvoorbeeld het $La_2Zr_2O_7$-spectrum.

In het tweede deel van de dissertatie kijken we naar de aard van atomen in een vaste stof. Sinds jaar en dag worstelen chemici met de vraag of een atoom, eens opgenomen in een molecule, zijn identiteit behoudt of opgaat in het geheel en hierbij alle individualiteit verliest. Op basis van eeuwenlange praktische ervaring is men ervan overtuigd dat een atoom iets van zijn identiteit bewaart in een molecule. Als gevolg hiervan zoekt men naar manieren om een molecule op te delen in "atomen" zodat de eigenschappen van de molecule kunnen gevonden worden als een eenvoudige som van de eigenschappen van de atomen.

In deze dissertatie implementeren we een dergelijk ontbindingsschema, meer specifiek het Hirshfeld-I schema, voor periodieke systemen en vaste stoffen. Door direct gebruik te maken van elektronendichtheden is de implementatie onafhankelijk van de manier waarop deze laatste is gegenereerd. In onze voorbeeldsystemen maken we gebruik van pseudovalentiedichtheden. Gezien de bekomen resultaten, voor een grote groep moleculen, een goede overeenkomst vertonen met "*all electron*"-berekeningen, toont dit enerzijds aan dat kernelektronen volledig aan het betreffende atoom dienen toegewezen te worden, en anderzijds dat de vorm van de valentie-elektronendichtheid

in het gebied zeer dicht bij de kern weinig van belang is. Met behulp van deze methode is het mogelijk om de ladingsverschuivingen in een vaste stof te gaan kwantificeren. In geval van groep IV dopering toont dit aan dat de ladingsverschuivingen hoofdzakelijk plaatsvinden tussen het doperingselement en de omliggende zuurstofatomen.

We eindigen deze dissertatie met een bundeling van algemene conclusies en een specifieke focus op de gevolgen hiervan voor het doperen van CeO_2 met betrekking tot het gebruik als bufferlaag voor gecoate supergeleiders. We werpen ook een korte blik op wat nog allemaal nodig en mogelijk is. In dit werk worden indicaties van verschillende trends gepresenteerd; echter de achterliggende oorzaken zijn vaak nog onduidelijk en kunnen dienen als bron van inspiratie voor nieuw werk. Om de gepresenteerde trends ten volle te kunnen onderzoeken en onderbouwen is verder gecombineerd experimenteel-theoretisch werk een absolute must.

OUTLINE

As with all modern research, this work started as a project focussed on a problem observed in a small aspect within the context of a solution for a 'highly socially relevant' problem. The relevant problem under consideration here is nothing less than energy consumption, and the solution is the use of superconducting materials. The small aspect referred to is the growth/production of coated superconducting wires, and the problem can be stated as 'the too small critical thickness of the CeO_2 buffer layer'. To show how this is all linked, **Chapter 1** starts from the global energy problem and moves via a short history of superconductivity down to the development of coated superconductors, and into the problems related to the critical thickness of the buffer layer. This critical thickness of the CeO_2 buffer layer is a central aspect in the growth of efficient buffer layers. First of all, the buffer layer needs to serve as an efficient chemical barrier, preventing metal substrate atoms to reach the superconducting thin film, which requires a minimal thickness of the buffer layer. Secondly, lattice matching with both the (metallic) substrate and the superconducting thin film is required to transfer the patterning of the former to the latter. However, beyond a certain critical thickness the CeO_2 buffer layer starts to shows micro-cracks, which are detrimental for good lattice matching and pattern transfer from the textured substrate to the superconducting thin film.

This is not the only application of CeO_2 (or ceria-based materials in general). As will be shown in **Chapter 2**, CeO_2 is a widely used material for other applications besides superconductors as well. Its use in many, quite different applications, going from polish over (component in) automotive catalysts to buffer layers for coated superconductors, makes that (improved) fundamental knowledge of its properties and how these can be modified is not only useful for future applications using coated superconductors, but also for everyday applications such as car catalysts and airplane engines. Because different applications require the modification of different properties in different ways, the focus will not be to optimize properties for one specific application. Instead, general trends in the properties of doped CeO_2 are studied and linked to atomic properties.

Since this dissertation is a theoretical work considering the *ab initio* study of the influence of dopants on the physical and mechanical properties of CeO_2, a short overview of the theoretical methods used, is given in **Chapter 3**. Also basic properties of CeO_2 and Ce_2O_3 will be presented within the theoretical framework, as an introduction to the material.

Because different dopants influence the properties of CeO_2 in different ways, either directly or indirectly, I will gradually increase the complexity of the problem. In **Chapter 4**, group IV elements are used as the first dopants to investigate, because Ce is tetravalent in CeO_2. Next, aliovalent dopants are introduced in **Chapter 5**,

initially without the presence of oxygen vacancies, and later including charge compensating oxygen vacancies. This way, different contributions to the modification of the CeO_2 properties due to atomic species, valency and presence of oxygen vacancies will be isolated.

For theoretical work like this, the exact atomic scale geometry is of great importance. In the case of $La_2Ce_2O_7$, which can be considered an extreme case of La-doped CeO_2, this structure is still the topic of much discussion, although the material was first produced in 1939 by Zintl and Croatto. In **Chapter 6**, several different configurations for $La_2Ce_2O_7$ are investigated and a ground state crystal geometry is presented.

When using aliovalent dopants, the different valence of these dopants results in a different charge distribution around the dopant sites. In addition, many elements are multivalent. A way to have a more quantitative estimate of the charge transfer induced by dopants is through the introduction of the chemical concept of *'atoms in a molecule'* into solids. This can be considered a first step in the direction of answering the experimental question of which charge an atom has in a given compound. Being able to calculate atomic charges using the Hirshfeld-I approach in solids also introduces a quantitative way of investigating charge transfer. In **Chapter 7**, modern atomic models are presented and the question of the existence of atoms in molecules is discussed in light of quantum mechanical theory. A way of implementing the Hirshfeld-I approach for solids is then presented in **Chapter 8**, while calculated atomic charges for CeO_2 and CeO_2 doped with group IV elements are presented in **Chapter 3** and **Chapter 4**, respectively.

In **Chapter 9**, some specific conclusions, focussed on the application of CeO_2 as a buffer layer in coated superconductor architectures are presented. In addition, pointers are given toward further investigations within the theoretical framework, both for the research on ceria-based materials, and the development of atoms-in-a-molecule partitioning schemes for solids. As part of the former, the work on the crystal structure of $La_2Ce_2O_7$ is revisited, and the recent experimental work in response to our work is discussed briefly. Based on this outlook, we reach the general conclusion that the future of materials science lies in a close(r) collaboration between experimental and theoretical investigators.

Part I

Introduction

CHAPTER

1

Superconductors: from 4 to 140 K

*Chemistry itself knows altogether too well that—given the real fear
that the scarcity of global resources and energy might threaten the
unity of mankind—chemistry is in a position to make a contribution
towards securing a true peace on earth.*

–Kenichi Fukui (1918 – 1998)

1.1 Introduction

A typical aspect of an economically and/or technologically advancing society is its exponentially growing energy consumption.[1, 2] Over the last centuries this has been a clear global trend. Only in the last few decades the finite size of global resources has become a cause of increasing concern, with the concept of peak-oil being probably the most (in)famous manifestation hereof. As a result, alternative energy sources are sought for and devices with ever higher energy-efficiency are developed.[3] In our energy demanding society, the discovery of superconductivity offers new and interesting opportunities to increase the energy-efficiency of many devices and applications.[4, 5] However, there are some significant problems that need to be overcome before applications based on superconductivity can become commonplace in everyday households.

Since the first discovery of superconductivity, much progress has been made and industrial-scale applications are becoming more frequent. Superconducting electromagnets are already mainstream in the medical industry where they are used in Nuclear Magnetic Resonance scanners (NMRs), better known as Magnetic Resonance Imaging scanners (MRIs).[6] Another well known example of superconductivity in 'real life' is the Magnetic Levitation train (MAGLEV), based on the Meissner effect. Here, superconductors are used to levitate a train above a magnetic rail, and allow it to move nearly frictionless at speeds up to 581 km/h. To date only three commercial MAGLEVs are in use for public transport: Linimo (Japan), Shanghai Maglev Train (China), and Daejeon (South Korea). Another impressive application using superconducting magnets, albeit a bit less accessible to the general public, is the Large Hadron Collider (LHC). This synchrotron near Geneva has a circumference of 27 km and uses over 1600 NbTi superconducting magnets, which are cooled to 1.9 K with 96 tonnes of liquid Helium, making this the largest cryogenic apparatus on earth. When running at full power the dipole magnets will need to produce magnetic fields of 8.3 Tesla, allowing the protons to reach energies up to 7 TeV.[1]

---

[1]Currently the machine operates only up to 4 TeV, but is expected to start running at full potential end 2014.

Another application of great academic interest is the Josephson junction. The observed Josephson effect is a tunneling effect between two superconducting layers which are separated by a thin insulating layer.[7] Such a junction could be used as a transistor, but would use a thousand times less energy than a standard semiconductor transistor.[2] Another more successful application is the superconducting quantum interference device (SQUID), which can be used to measure microscopic magnetic field. This sensitivity makes it ideal for magnetoencephalography, to study the neural activity in the brain. In addition, SQUIDs are used as high precision movement sensors, such as those needed to detect gravitational waves, and a SQUID sensor was also used in each of the gyroscopes of Gravity Probe B studying the limits of the general theory of relativity via the predicted geodetic effect[3] and frame-dragging effect of the earth's gravitational field.[13]

Moreover, there are a large number of superconductivity based applications at different stages of development. The fact that superconducting wires do not experience resistance and are able to carry very high currents, makes coils of superconducting wires excellent candidates to be used as energy storage devices. This can either be to temporarily store overproduction at low-peak moments in what is called superconducting magnetic energy storage (SMES), or as a fault current limiter in a power transmission network. Furthermore, superconducting coils would also allow for the construction of smaller and more efficient generators since the wires can carry a higher current.[12, 14]

1.2 A short history of superconductivity

It was in 1908, just over a century ago, that Heike Kamerlingh Onnes succeeded for the first time in liquifying helium.[15] This was crucial for the discovery of superconductivity, since it allowed him and his co-workers—(PhD student) Gilles Holst and (Dr.) Cornelis Dorsman—to study the conductivity of mercury at cryogenic temperatures. In 1911, they observed the sudden disappearance of the resistivity of mercury at 4.2 K, which they first assumed to be due to a short circuit in their setup. After repeating the measurement several times, it was clear that it was no short circuit but rather a new conducting state: '*superconductivity*'.[4][16, 17] This

---

[2]As a result, IBM invested heavily in the development of a computer using such junctions. The project, however, was terminated in 1983 for two reasons. Firstly, because the at that point available lead based Josephson circuits were not much faster than the available semiconductor circuits (Although later niobium based Josephson chips have been shown ten times faster than comparable GaAs semiconductor chips.[8, 9]). And secondly, because of the difficulty of making high-speed cache memory. The latter was in part due to unstable behavior of the critical current of the junctions. For the lead-alloy junctions, it was observed to increase during storage at room temperature, resulting in the eventual breakdown of the junction.[8–12] Room temperature superconductors would alleviate many of the difficulties in this project; for example the requirement of (constant) cryogenic cooling would no longer be present, removing the problems with the critical current due to low-temperature-room-temperature-cycles.

[3]Also known as "de Sitter precession", referring to the precession of a vector resulting from the curvature of space-time.

[4]Onnes initially named the phenomenon **supra**-conductivity and not superconductivity since conductivity indicates the specific value of the conductance of the material.[16]
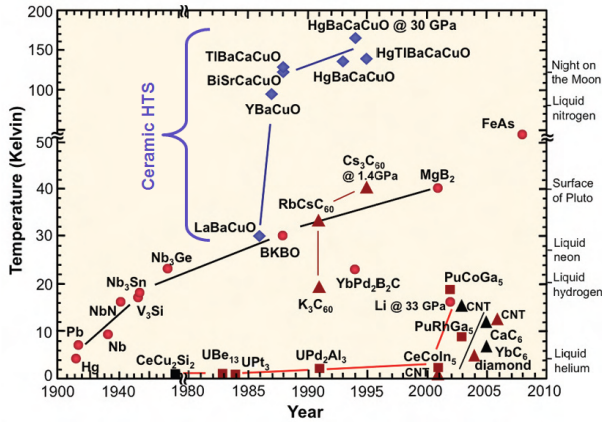
Figure 1.1: *Different classes of superconductors and the evolution of critical temperature* $\mathbf{T}_c$ *development over the last century. Adapted from Reference [5].*

new state is not unique for mercury, and it was soon observed for other pure metals (such as Sn: 3.7 K and Pb: 7.2 K [18]). The importance of this discovery is best presented by the fact that already in 1913 Onnes was awarded the Nobel Prize in Physics for this pioneering work.[19]

This work also presents the first serious problem which hampers the widespread (industrial) application of superconductivity in pure metals: the extremely low temperature required to reach the superconducting state (*cf.* Fig. 1.1). Regardless of this technical difficulty, both theoretical and experimental work continued over the following decades. In 1933, *the Meissner effect* was first observed by Meissner and Ochsenfeld.[20] They showed that a superconductor when transitioning into the superconducting state expels an external magnetic field, allowing for magnetic levitation.[5]

By 1957, Bardeen, Cooper, and Schrieffer (BCS) had developed a successful theory behind the phenomenon of superconductivity in pure metals and simple alloys.[21, 22] In what is now known as BCS theory, electrons near the Fermi surface form Cooper-pairs at low temperature. The macroscopic effect of superconductivity is a result of the condensation of these Cooper-pairs.[6] The Nobel Prize in Physics for Bardeen, Cooper, and Schrieffer in 1972 underlines the importance of their work.[7][19]

---

[5]Combined with flux pinning, this is why superconducting (toy) trains float over their magnetic rail and keep following it even if the path is curved.

[6]Since a pair of electrons can be considered as a boson, this condensation can be related to Bose-Einstein condensation. Both phenomena can be explained by means of Bogoliubov transformations.

[7]Despite the fact that BCS theory was universally accepted by 1969, there remained one strong voice of descent. Bernd Teo Matthias, a well-respected experimentalist at the Westinghouse lab, remained unconvinced that BCS theory could be true. Matthias had predicted several new superconducting materials based on empirical rules he had deduced from the many superconducting materials he had investigated. Since he found no guidance in this effort in the BCS theory, he

Despite this theoretical progress, BCS theory is insufficient to fully describe superconductivity at higher temperatures in more complicated materials. A fully satisfying (simple) theory describing high temperature superconductivity remains elusive.[24]

As mentioned above, the extremely low temperature at which superconductivity is observed is a serious problem for practical application. As a result, much of the experimental work focussed and still focusses on the optimization of existing materials and the development[8] of new superconducting materials that show superconducting behavior at higher temperatures. A first true breakthrough in this regard can be considered the discovery of superconducting ceramics by Bednorz and Müller in 1986.[25] Although the material had a critical temperature of only 30 K, this was 6.7 K above the previous high temperature record for Nb_3Ge.[12] More importantly, the discovery also showed that ceramics could present superconductivity, giving a new boost to the field. This discovery resulted already the following year in a Nobel Prize in Physics for Bednorz and Müller.[19] In the years following, many new superconducting ceramic materials were discovered, of which $YBa_2Cu_3O_{7-\delta}$ (discovered by Maw-Kuen Wu and collaborators in 1987 [12, 26]) is still one of the most successful. Becoming superconducting at a temperature of 92 K, well above the temperature of liquid nitrogen, this material presented cheap(er) access to superconductivity, due to the much lower price of liquid nitrogen compared to that of liquid helium.[9] Since then, many more ceramic materials with superconducting properties have been discovered with critical temperatures as high as 138 K (or $-140°C$) for $Hg_{0.8}Tl_{0.2}Ba_2Ca_2Cu_3O_{8+\delta}$.[27] Recently, another new class of superconductors was discovered: iron pnictides (or ferropnictides).[28–30] Although the critical temperatures for these new materials are currently still lower than those of the ceramics (only up to 56 K), superconductivity at liquid nitrogen temperatures might be possible in the future, making them a second class of commercially interesting materials, next to the high temperature ceramic superconductors.[31]

1.2.1   Critical fields and currents

Soon after the discovery of superconductivity, Onnes mentioned at a conference that it would be possible to build a strong electromagnet using superconducting wires.[12] Referring to the work of Jean Perrin, who had calculated that it should be possible to generate a field of 10 Tesla using a coil of conducting wire, Onnes noted that where Joule-heating would require cryostatic cooling for a normal conducting wire, making it extremely expensive, this would not be the case for a superconducting wire. Though it would still require cryostatic cooling, the coolant would not boil away as quickly since no Joule-heating would be present. After obtaining the neces-

---

was convinced it could not be correct. Although Matthias voiced this argument in papers and at conferences, he never obtained any followers in the physics community. With his passing in 1980 this last voice of descent also went silent.[12, 23]

[8]The lack of a good and in depth understanding of the physics underlying the phenomenon of high temperature superconductivity makes most discoveries of *new* suitable materials look accidental rather than intentional.

[9]In addition, $YBa_2Cu_3O_{7-\delta}$ also remains superconducting at high external magnetic field, due to a low irreversibility line.
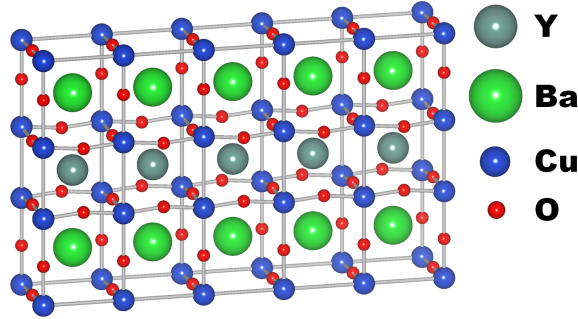
Figure 1.2: *Ball-and-stick representation of the crystal structure of $YBa_2Cu_3O_7$. Two types of copper-oxide planes are present: the CuO-planes (top and bottom) and the CuO_2-planes (middle, surrounding the Y atoms). Experiments suggest that it are the latter copper-oxide planes which are responsible for the superconductivity, while the former serve as charge reservoirs. The structure is obtained from Reference [32] and generated using VESTA.[33]*

sary funding for this project, it soon became clear that it would not be as simple as this. Onnes observed that in a strong magnetic field (such as generated in an electromagnet coil) the superconductivity disappeared above some critical field strength (in the order of a few Tesla). He also noted that there was a limit to the current that could pass through a superconducting wire, introducing a third limiting parameter. The theoretical understanding of these two additional limiting factors would have to wait until the explanation of the Meissner effect by the London brothers.

If one were to consider a superconductor to be a perfect conductor then it would be expected that the application of an external magnetic field would induce a current in the superconductor which would in turn generate a magnetic field which would cancel the external field in the bulk of the material. However, in 1933 Meissner observed that for a solid superconductor, the external magnetic field is actively expelled from the material during the transition into the superconducting phase, resulting in the superconductor to start floating.[10] It were the brothers Fritz and Heinz London who were able to explain this effect. From their work it became clear that in a small region near the surface of a superconductor a screening current was present which was responsible for this effect. The thickness of the region in which these screening currents run is called the "*London penetration depth*" (λ_L), and is typically of the order of 50–500 nm. If, however, an external magnetic field exceeds a critical value H_c, the magnetic field lines will overcome the effect of the screening current and penetrate into the bulk of the superconductor, destroying the superconductivity. This also poses an upper limit to the maximum current that can run inside a superconducting wire, due to the induced magnetic field. This is called the "*critical current*

---

[10]In contrast, if one would use a hollow cylinder, as was done by Willem Tyun, a student of Onnes, there would be no levitation effect.[12]

density" ($\mathbf{J}_c$).

1.3 Ceramics: from flower pots to superconductors

With the discovery of the high temperature superconductors (HTS), the problem of the extremely low temperature of metal superconductors is already partially alleviated.[11] However, these ceramic HTS come with a new set of problems.

A major industrial application in the field of superconductivity is the production of superconducting wires (which in turn can be used for energy transport, or as coils to produce superconducting magnets). For the production of HTS wires and in the development of devices using superconducting components, the HTS $YBa_2Cu_3O_{7-\delta}$ (YBCO) remains one of the most important materials (the crystal structure of $YBa_2Cu_3O_7$ is shown in Fig. 1.2.).[34–36] Because it is a ceramic, it is, just like ceramic roof tiles and flower pots, brittle by nature.[12] In addition, since the superconducting current is known to run mainly along the CuO_2 planes, a wire ideally should consist of a single crystal of YBCO. Because such a single crystal would not be flexible, even if it was possible to grow one the size of an industrial scale wire, a different approach is required: *'coated (super)conductors'*.

In such an architecture, shown in Fig. 1.3, a thin film of YBCO is deposited on a metal substrate combining the superconducting properties of YBCO with the (industrially required) mechanical flexibility of the metal substrate. To retain optimum superconducting properties in the thin film, the YBCO grains should be aligned both biaxially in the *ab*-plane as well as along the *c*-axis, with YBCO grain boundaries showing angles no larger than $5 - 6°$.[38, 39] To obtain such a grain growth, the YBCO film is grown epitaxially on a textured Ni+5%W substrate. Furthermore, one or more buffer layers are introduced to prevent the diffusion of substrate metal atoms into the superconducting layer, destroying the superconductivity of the YBCO thin film. In addition, the buffer layers are also used to overcome the difference in lattice parameters between the YBCO thin film and the metal substrate, and transfer the patterning of the latter to the former.

Several different layered architectures exist in literature, in which $SrTiO_3$ and CeO_2-based buffer layers are two common examples.[40, 41] In experiments, it is shown that lattice matching of the buffer layers to the YBCO layer reduces the interfacial strain.[42] This promotes the preservation of the metal substrate texture, which in turn forces the alignment of the YBCO grains, resulting in high quality superconducting properties for the coated superconductors.

---

[11]Though the search for room temperature superconductors continues.

[12]A material is referred to as brittle if it breaks without (plastic) deformation when subjected to stress. In such a material, cracks propagate without the introduction of dislocations, as is the case for a ductile material.[37] In the latter, the dislocations provide a means to absorb some of the experienced stress. In case of an YBCO single crystal, the complex crystal structure (*cf.* Fig. 1.2) makes the formation of a dislocation very unfavorable, since this would lead to a mismatch of the crystal planes (*e.g.* CuO_2 planes being connected to BaO planes). In addition, grain boundaries in polycrystalline ceramic materials provide the sites for crack formation and propagation without the formation of dislocations.
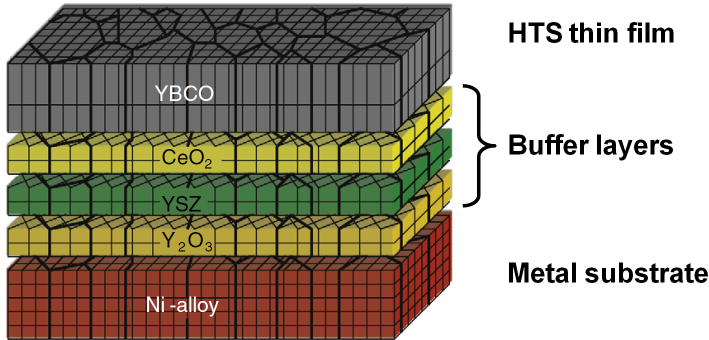
Figure 1.3: *Example of an architecture for a coated (super)conductor. Adapted from Reference [39]. YSZ refers to Y stabilized zirconia.*

In addition to these difficulties inherent to the materials themselves, economic factors demand the entire architecture to contain as few layers as possible. As a result, one aims to reduce the number of buffer layers. In case of CeO_2 buffer layers, this introduces a new problem: CeO_2 buffer layers start to show micro-cracks for thin films of more than 80 nm.[42–45] These cracks are detrimental for the growth of high quality YBCO films. Some authors have suggested that these micro-cracks are caused by interfacial strain due to lattice mismatching, and/or a mismatch between the thermal expansion coefficients of the different layers.[42, 45] Doping of the CeO_2 buffer layers is suggested to reduce this strain.[13][45, 46] However, there is no clear understanding which dopants influence the physical properties of CeO_2 in a beneficial way.[14] This makes an in depth theoretical study of the influence of dopants on CeO_2 properties of great interest.

This work originated from the above perspective, and in the following chapters the physical properties of CeO_2 and doped CeO_2 will be investigated in such a way as to provide a link between the modification of the studied physical property (lattice parameter, bulk modulus, density of states,*etc.*) and the dopant element's properties (atomic radius, electronic structure, valence,*etc.*).

---

[13]In addition, Ce tends to form a barium-cerate layer at the interface between the CeO_2 buffer layer and the YBCO thin film. Also for this aspect, the use of dopants is expected to be beneficial through stabilizing the CeO_2 lattice and preventing the formation of the barium-cerate interface layer.

[14]At this point, it is important to note that this remark is rooted in the theoretical perspective of *ab-initio* calculations. Experimental concepts such as "improved roughness", "denser films" or "better texturing" are not considered theoretically accessible (and thus useful) properties, which can be related to atomic properties and thereby allow for practical prediction.

②

Ceria as multi-purpose material

We think that ceria is an intriguing material. It holds a lot of potential for many applications, but it is also a fairly complicated material.

– Mogens Mogensen, Nigel M. Sammes, Geoff A. Tompsett
Solid State Ionics 129, p91 (2000)

Over the last decade, the amount of literature on cerium oxide and ceria-based materials has increased dramatically as can be seen in Fig. 2.1. A simple investigation on 'Web of Knowledge' results in more than 12.000 peer reviewed papers which have **ceria** as topic, and nearly 10.000 papers that contain either the term **ceria**, **cerium oxide** or **CeO$_2$** in their title. The larger fraction of this work is experimental, with a major focus on catalysis. Of the five most cited articles, three focus on catalysis and two on solid oxide fuel cells, showing the large industrial interest in these materials.[47–51]

In this chapter a short review of the large body of literature which is available on cerium oxide and ceria-based materials is presented. Due to the extent of this literature such a review cannot be complete, but it should provide sufficient starting points for more specific literature studies.

2.1 The Ce f-electron

In the periodic table of elements, Ce is the first element containing an f electron. It is this $4f$ electron which is involved in many of the unique properties of Ce. In pure form at different temperatures and pressures Ce can be an antiferromagnet or a superconductor. It also presents a solid-solid critical point and Kondo scattering. These phenomena are made possible by the special nature of the Ce $4f$ electron, namely the fact that the energy of the lowest $4f$ level is nearly the same as that of the valence $5d$ and $6s$ levels. As a result, only little energy is required to change the electronic structure of the system.[52] In CeO$_2$, this makes the transition from Ce^{4+} to Ce^{3+} and back easily accessible through reduction and oxidation of the system.

As will be seen in **Sec.** 2.3, the ability of the Ce $4f$ electron to behave either as core electron or as valence electron constitutes a serious challenge in its theoretical description. As a consequence, also the theoretical description of reduced ceria faces this challenge.
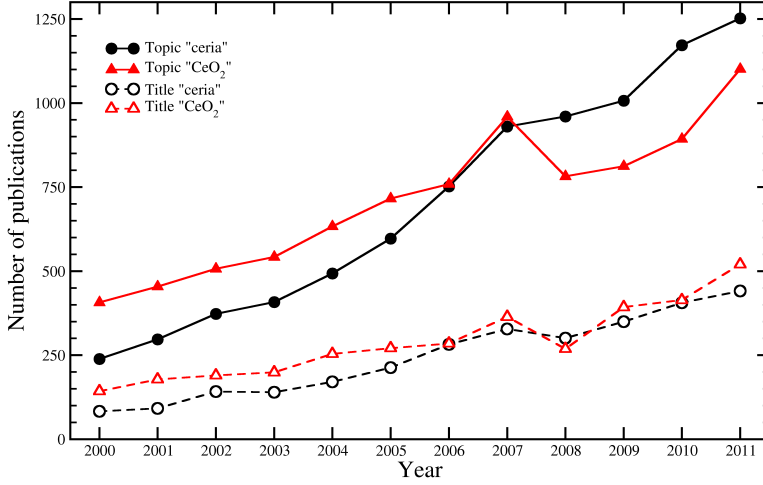
Figure 2.1: *Number of publications found in the Web of Knowledge database containing either the word 'ceria' (circles) or 'CeO$_2$' (triangles) in their topic (solid lines) or title (dashed lines). The data were retrieved on August 3rd 2012. It is interesting to note that apparently after 2007 the popularity of the topic terms CeO$_2$ and ceria reversed order, though they appear to remain equally popular as publication titles.*

2.2 Ceria in experiment

Stoichiometric cerium oxide has a fluorite crystal structure (space group Fm$\bar{3}$m) over a wide temperature range. Even with significant oxygen-reduction this fluorite crystal structure is maintained. The reduction of CeO$_2$ to CeO$_{2-x}$ introduces two types of defects. First of all, there is the formation of oxygen vacancies. When such a vacancy is formed this can be considered to result in two electrons remaining in the system, giving rise to two Ce^{3+} ions. These Ce^{3+} ions are then considered negatively charged compared to the normal lattice Ce^{4+}, and form the second type of defects. In the Kröger–Vink-notation, the reduction process in CeO$_2$ can be written as:[53]

$$O_O + 2\,Ce_{Ce} = \frac{1}{2}O_2(\text{gas}) + V_O^{\bullet\bullet} + 2\,Ce'_{Ce}, \qquad (2.1)$$
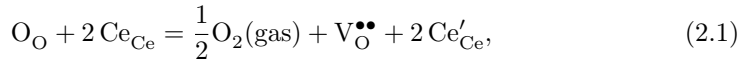
where V$_O^{\bullet\bullet}$ indicates the formation of an oxygen vacancy with double positive charge and $2\,Ce'_{Ce}$ refers to the substitution of two of the lattice Ce^{4+} ions with a 'negatively charged' Ce^{3+} ion.

It is the combination of this facile Ce$^{4+} \longleftrightarrow$ Ce^{3+} redox conversion and the fact that ceria can tolerate large reduction at high temperatures without phase transition which lies at the basis of the broad use of ceria in heterogeneous catalysis.[47]

H													IV$_a$					He
Li	Be												B	C	N	O	F	Ne
Na	Mg		IV$_b$										Al	Si	P	S	Cl	Ar
K	Ca	Sc	Ti	V	Cr	Mn	Fe	Co	Ni	Cu	Zn	Ga	Ge	As	Se	Br	Kr
Rb	Sr	Y	Zr	Nb	Mo	Tc	Ru	Rh	Pd	Ag	Cd	In	Sn	Sb	Te	I	Xe
Cs	Ba	*	Hf	Ta	W	Re	Os	Ir	Pt	Au	Hg	Tl	Pb	Bi	Po	At	Rn
Fr	Ra	**	Rf	Db	Sg	Bh	Hs	Mt	Ds	Rg	Cn	Uut	Uuq	Uup	Uuh	Uus	Uuo

*	La	Ce	Pr	Nd	Pm	Sm	Eu	Gd	Tb	Dy	Ho	Er	Tm	Yb	Lu
**	Ac	Th	Pa	U	Np	Pu	Am	Cm	Bk	Cf	Es	Fm	Md	No	Lr

Figure 2.2: *Periodic table indicating (green background) the elements found to be used in the experimental literature as dopants for CeO$_2$, during our study of doped CeO$_2$. The columns of the group IVa and IVb elements are marked, and the dopant elements studied in this work are shown in blue.*

As a result, it is a major component in automotive exhaust catalysts, promoting the water-gas shift reaction in three-way catalysts (TWC), where it stores oxygen under oxygen rich conditions while releasing it under oxygen poor conditions.[54, 55] Furthermore, ceria has been used as support for Cu, Pd, Au, Ag and other catalysts.[46, 56]

In addition to its oxygen storage capacity (OSC), the mobility of the vacancies/oxygen ions is such that ceria and ceria-based materials have been of interest as solid oxide-ion electrolytes in ionic conductors and fuel cells. In recent years, the thermal stability of ceria-based materials has resulted in interest from the field of thermal barrier coatings (TBC).[57–59] The low thermal conductivity and high thermal expansion coefficient (TEC) of CeO$_2$ make it a well-suited material both as a TBC itself or to dope known TBCs.[59, 60]

As presented in **Sec.** 1.3, CeO$_2$ is also used as buffer layer in architectures for coated superconductors on Rolling Assisted Biaxially Textured Substrates (RABiTS). In combination with YBCO as the superconducting material, CeO$_2$ is ideally suited due to the very small lattice mismatch between the two materials.[61]

2.2.1 Doped CeO$_2$

In all these applications, researchers are constantly striving to improve the properties of CeO$_2$ to obtain even better performance. Next to modifying the environment parameters of the production process (deposition temperature, calcination time, atmosphere,...), the most common way to 'change' CeO$_2$ is through doping with other elements.[44, 47] Figure 2.2 shows the dopant elements commonly used in experimen-

tal (and theoretical) literature. From the literature, it is clear that different elements have different influences on different properties of CeO_2. In these studies, the dopant concentrations strongly depend on the application and vary from $< 1\%$ all the way up to 50% (or more) for mixed oxides.[1]

A.   Preparation of ceria

(Doped-)CeO_2 (thin) films and crystals can be deposited, synthesized or grown in many different ways. There are the standard physical and chemical methods: physical evaporation,[62] chemical vapor deposition,[63] spin coating,[64] molecular beam epitaxy,[65] sputtering, e-beam evaporation,[43, 66] sol-gel deposition,[45, 61, 67] metal-organic deposition,[68] and chemical solution deposition.[41, 45] But also electrodeposition[69] and combustion synthesis[70, 71] have been used; for example by Bera *et al.*[70] in their investigation of $Ce_{1-x}Cu_xO_{2-\delta}$ and by Li *et al.*[71] for their study of Mg co-doped $Gd_{0.1}Ce_{0.9}O_{1.95}$. Among these techniques, the physical vacuum deposition techniques are best suited for growing very thick or very thin (nearly) monocrystalline films, providing the perfect reference systems for theoretical atomistic simulations. On the other hand, the chemical solution deposition techniques (such as for example the sol-gel method combined with dip-coating or inkjet-printing) are better suited for industrial upscaling, though providing lower quality films. Furthermore, Rossignol *et al.*[72] found that the preparation method has a strong effect on the structure, texture and surface properties of Zr doped CeO_2, but also the oxygen storage capacity and thermal stability are influenced. This is an important aspect to keep in mind when experimental and theoretical results are being compared, since one may well be comparing quite different systems.

B.   Crystal structure

X-ray and Raman studies by McBride *et al.*[73] show that rare earth doping, at least in the low doping regime, leads to solids solutions that retain the CeO_2 fluorite crystal structure.[2] They also observe that the lattice expansion is roughly proportional to the dopant concentration, and that the slope of the lattice expansion is approximately proportional to the ionic radius. From the offset of the Pr and Tb ionic radii with regard to this linear relation, they deduce that both Pr and Tb probably reside in a mixed valence state.[3] Work by Rossignol and collaborators shows that CeO_2 with either Zr or Pr doping (up to tens of %) retains the fluorite

---

[1]The large concentration range found in the literature comes with a variety of names. Some authors use the term 'doping' to refer to the entire range, while other authors use it only in reference to very small concentrations ($\ll 1\%$) and use the term 'mixed oxide' (since the system can be considered a combination of oxides: CeO_2 and MO_x, with M the 'dopant' element) or solid solution for higher concentrations. In this dissertation, I will use the term 'doping' in the very broad meaning covering the entire concentration range. This to simplify everything a bit, and to prevent semantic discussion.

[2]The term 'solid solution' is used to refer to a solid state mixture of two or more compounds which are considered to behave rather as one would expect of a 'liquid' solution; *i.e.*, the solutes mingle with the solvent while the latter retains its original crystal structure. Since this is generally the case for CeO_2, this terminology is also often encountered in literature on CeO_2 doping.

[3]A mix of the 3+ and 4+ state.

structure.[72, 74] They also show that Pr doping stabilizes the thermally induced lattice expansion with regard to an H_2 atmosphere.

Doping with Cu was studied by several authors.[55, 70, 75] Bera *et al.*[70] observed that the Cu dopants cluster and migrate to the surface of the CeO_2 grains, in agreement with the low dopant concentration electron spin resonance experiments of de Biasi and Grillo.[75]

For Gd dopants, on the other hand, de Biasi and Grillo have shown through similar electron spin resonance experiments on CeO_2 doped with Gd (0.01–1.00%) that no clustering takes place at low concentrations.[76] As a result, these authors suggest that the electron spin resonance linewidth data can be used to estimate the Gd dopant concentrations for such low concentration systems.

C. Mobility and oxygen vacancies

An important consequence of the introduction of aliovalent dopants in the CeO_2 crystal structure is the formation of charge compensating oxygen vacancies.[73] This can result in an increase of the OSC, which is considered beneficial for example in ionic conductors, where the motion of the dopant-introduced oxygen vacancies can be the main contributor to the conduction. Tuller and Nowick investigated the effect of divalent Ca and trivalent Y dopants, and noted that for high concentrations of oxygen vacancies ($> 4\%$) defect interactions become important and can give rise to ordering effects which trap the vacancies.[77] In **Chapter** 6 of this dissertation, the interaction between oxygen vacancies and the lattice Ce and La ions will be shown to be a driving force for the pyrochlore ground state crystal structure of 50 % La doped CeO_2 (*i.e.* $La_2Ce_2O_7$).

On the other hand, de Leitenburg *et al.*[78] attributed the reducibility and increased OSC of Zr doped CeO_2 to the defective fluorite structure resulting from the introduction of the smaller Zr^{4+} ions.

D. Codoping of ceria

In addition to the work on CeO_2 with a single dopant species, also much work is performed on the codoping of CeO_2.[71, 79–81] The use of multiple different dopant species can have several reasons. In the case of the work by Fagg *et al.*,[79] Pr doped CeO_2 is codoped with Zr to improve the behavior of the TEC of Pr doped CeO_2. As a result of this codoping, less oxygen vacancies are formed at elevated temperatures, while a larger fraction of the Pr ions is in the 3+ oxidation state. This indicates that the oxygen vacancies might be pinned down to form defect complexes with the Pr dopant ions.

In their report on the catalytic properties of CeO_2 and La doped CeO_2, Miki *et al.*[82] show a significant improvement of the OSC when La doping is combined with the presence of Pt or Rh on the surface of the oxide. Although no explicit codoping is present, one might expect similar behavior for truly codoped $Ce_{1-x}La_xO_2$. In this system, segregation of the codopant to the system surface may even be a preferred property.

Li *et al.*[80] use Nd codoping to increase the grain conductivity of Gd and Sm doped CeO_2 grains for their application in solid oxide fuel cells. In the context of

ionic conductivity, the use of codoping is quite common, since it is widely accepted that optimum ionic conductivity in an oxide material is related to the dopant radius. In the case of CeO_2, it is found that this optimum radius is close to the ionic radius of Gd. Furthermore, it is assumed that in the case of codoping the (weighted[4]) average of the ionic radii of the dopants can be used to obtain the optimum dopant ionic radius.[80, 81]

2.2.2 CeO_2 buffer layers for coated superconductors

In buffer layer architectures for coated superconductors, the role of the buffer layer is threefold:

1. Prevent (or slow down) oxidation of the metal substrate.

2. Reduce the lattice mismatch between the metal substrate and the YBCO superconductor (and in extension also reduce the thermal expansion mismatch).

3. Act as a buffer to prevent the diffusion of metal atoms into the superconductor, which would possibly destroy the superconductivity.

In the case of a CeO_2 buffer layer, there is the earlier mentioned problem of crack formation. Paranthaman *et al.*[43] have found that for biaxially textured CeO_2 buffer layers on a Ni substrate, the layer thickness is crucial for crack formation. For 100 nm thick buffer layers they observed cracks, while none were observed for 50 nm thick layers. In contrast, Oh *et al.*[42] observed that on a Ni substrate only CeO_2 thin films with a thickness less than 20 nm were crack free. Based on their comparison to CeO_2 thin films on Pt substrates (showing much lower crack formation), they conclude that rather lattice mismatch and not the difference in the TEC is the plausible cause of crack formation. In light of the use of CeO_2 as a buffer layer in coated superconductors, an important observation by these authors is that both Ni and Pt atoms diffuse easily 10 nm deep into the CeO_2 thin film, showing that (much) thicker films are needed (*cf.* point 3).

In 2004, Penneman *et al.* showed that 25 nm thick CeO_2 films could be obtained through dip-coating, providing an alternative for vacuum deposition techniques. In addition, it is clear from their work that a high temperature thermal treatment is necessary to obtain highly crystalline films. Takahashi *et al.*[68], on the other hand, used metal-organic deposition (MOD) to deposit YBCO coated superconductors with Gd doped CeO_2 buffer layers. They found that the use of Gd as a dopant prevented the formation of a $BaCeO_3$ layer at the interface between the YBCO and CeO_2 layers, which is detrimental for the superconductivity of the coated superconductor. For Gd-rich $Ce_{1-x}Gd_xO_{2-x/2}$ buffer layers, they observed no crack formation; however, when the Gd content rose above 45 %, needle-shaped structures started to form. Furthermore, beyond this concentration also no further linear expansion of the CeO_2 lattice parameter was observed. This might indicate that these structures consisted of pure (excess) Gd_2O_3. Another important problem that Takahashi *et al.* encountered

---

[4]In the case of different concentrations.

was that substrate Ni atoms were able to diffuse through the $Ce_{1-x}Gd_xO_{2-x/2}$ buffer layer, reducing its suitability for coated superconductors. By making use of a double buffer layer architecture, where the Gd doped CeO_2 is grown on a $La_2Zr_2O_7$ buffer layer, Knoth *et al.*[41] did not encounter this problem. At a dopant concentration of 30 %, they observe neither cracks nor needle-shaped crystals on their doped CeO_2 buffer layer, making it well-suited for subsequent YBCO deposition.

Also other dopant elements appear to have a beneficial effect in reducing the tendency of crack formation in CeO_2 thin films. Van de Velde *et al.*[45] showed that doping with either 5 % Gd or Yb or with 10 % Co or Bi significantly improves the properties of the obtained thin films, and prevents the formation of cracks up to film thicknesses of at least 80 nm. Here, further investigation of other dopants may lead to the ability to grow even thicker crack free layers, allowing for the reduction of the number of buffer layers in coated superconducting architectures. As such, the theoretical work presented in this dissertation aims at increasing the understanding of the influence of dopants on the properties of CeO_2 and to give clues at which dopants may improve the current experimental findings.

2.3 Ceria in theory

Although the theoretical body of work on ceria is much smaller than the experimental one, it still remains quite extensive. Interest in cerium oxide and ceria-based materials from the theoretical perspective can be split roughly in two categories:

1. Experimentally Oriented

2. Fundamentally Theoretical

The first category primarily focusses on experiments, and tries to explain and predict the experimental results. Such studies quite often focus on ionic conductivity and dopant-induced lattice expansion trends. Also studies of catalytic processes at surfaces and the influence of nobel metals like Au on these processes are part of this category. As such, this part of the theoretical literature is quite closely related to the experimental work described in **Sec.** 2.2. The work presented in **Chapters** 4, 5, and 6 of this dissertation also belongs to this category.

With regard to the study of series of dopants in CeO_2, both experimental and theoretical work focusses nearly exclusively on the lanthanide series (*cf.* Fig. 2.2). The fact that no other series are studied, even in the theoretical literature, can be considered as quite strange, since such studies would provide many new insights in the way dopants modify the properties of CeO_2.[5] Because the lanthanide series has already been studied exhaustively, it will not be studied in this dissertation, and we will initially focus on the group IV series in **Chapter** 4 instead.

The second category stems mainly from the last decade, and is related to the theoretical description of the f electron of Ce (*cf.* **Sec.** 2.1). Conventional density

---

[5]Only one group was found to have performed a study of tetravalent dopants, and this work was focussed on ionic mobility and oxygen vacancy formation.[83, 84]

functional theory (DFT) schemes are known to fail to capture the localization be-
havior of this f electron correctly. It was only in recent years that new methods were
developed or became available to the solid state community to tackle the different
ceria systems successfully.

2.3.1 Experimentally oriented theoretical work

In early work, Catlow and collaborators investigated the relation between the ionic
conductivity and dopant ion radius.[85, 86] In their static lattice simulations, they
observed, in agreement with experiment, a maximum in the conductivity with regard
to the dopant concentration for several different doped CeO_2 systems. They state
that this behavior must be caused by the interaction between the dopants and the
vacancies. In their model, this maximum coincides with the situation where, for a
random distribution of dopants, an '*appreciable number*' of oxygen sites is surrounded
by two or more dopants. These would then serve to pin the oxygen vacancies, limiting
mobility and ionic conduction. When linking this to the ionic radii of the dopants
they conclude that for dopants with radii smaller than the Ce ionic radius, inward
relaxation of the dopants toward the vacancy stabilizes the system, while for dopants
with a larger ionic radius it is the formation of the vacancy that releases some of the
system strain, stabilizing the system. However, in both cases a clear clustering of the
vacancies with the dopants is predicted.

Later, Kim proposed a set of empirical equations to calculate the lattice parameter
in doped fluorite structure oxides:[87]

$$d = 5.413 + \sum_k (0.0220\Delta r_k + 0.000015\Delta z_k)m_k \qquad (2.2)$$

where d is the lattice parameter (in Å) of the doped system, Δr_k and Δz_k are the
differences in ionic radius and valence between the kth dopant species and Ce, and
m_k the mole percent of the kth dopant species. This equation was the result of a
regression analysis on data obtained from literature, which explains why the constant
slightly differs from the experimental lattice constant of CeO_2. Just like Catlow, this
author concludes that maximum conductivity is obtained when the ionic radius of
the (average) dopant minimizes the change of the CeO_2 lattice parameter. At this
point it is interesting to note that this author assumes that the introduction of oxy-
gen vacancies automatically leads to a lattice contraction. In this dissertation, we
will see this is not always the case.

More recent work, based on state of the art *ab initio* calculations, by Andersson
et al. find similar behavior.[88] In their study of CeO_2 doping with lanthanide series
elements, they find a minimum in the vacancy activation energy for dopants with
atomic number 62 (Sm). As in previous work, they conclude that smaller dopants
prefer positions next to oxygen vacancies, while large dopants prefer oxygen vacancies
in next nearest neighbor positions. Similar results are also found in the atomistic
calculation of Wei *et al.*[89]

With the introduction of the Hubbard U Coulomb correction to the density func-
tional theory (DFT+U) framework for ceria (*cf.* **Sec.** 2.3.2) in 2005, a new and

improved framework became available for studying the structure and properties of ceria. The relative stability of the different CeO_2 surface terminations was one of the first topics to be examined by Jiang *et al.*[90] They obtained a slightly different relative ordering compared to previous work based on interatomic potentials, though they all agree that the [111] surface is the most stable for a wide range of oxygen partial pressures. An interesting result, with regard to the application of CeO_2 in coated superconductor architectures, is the observation that the CeO_2[100] surface termination appears to be one of the least stable surface configurations studied by Jiang *et al.*[90]

The formation of oxygen vacancies, due to its importance in applications of catalysts and ionic conductors, has also received a significant amount of attention in the theoretical literature.[89, 91–95] Yang *et al.* have shown the oxygen vacancy formation energy to be greatly reduced in Pd doped CeO_2 due to the Pd induced gap states, while for Zr doped CeO_2 surfaces, the surface geometry appears to play a crucial role.[91, 92] The presence of the Pd gap state is also in agreement with the calculated Bader charges of Mayernick and Janik for the formation of oxygen vacancies in Pd substituted CeO_2 surfaces, which show that all the excess charge moves to the Pd atom and none to the Ce atoms.[93]

From the atomistic calculations of Ye *et al.*,[95] we learn that oxygen vacancies tend to form curved chains in bulk rare-earth doped ceria. Furthermore, we learn that the formation of nanosized domains, in which the dopant segregates to form ordered structures with the oxygen vacancies, block oxygen migration and thus reduce the ionic conductivity. On the other hand, oxygen vacancies on ceria surfaces are predicted to form linear chains. For single vacancies, both the surface and subsurface vacancies are equally stable, while for a trimer a triangular configuration of surface vacancies is most stable.[96, 97] Upon removal of a surface oxygen ion, the remaining two electrons localize on two Ce ions, with higher coordinated Ce^{3+} ions being less stable than lower coordinated Ce^{3+} ions.

2.3.2 Fundamental theoretical work

Examining the cubic oxide CeO_2 and hexagonal sesquioxide Ce_2O_3, it is clear that in the former case the Ce ions are formally tetravalent, while they are trivalent in the latter. These different valences have been related to the occupation of the Ce $4f$ orbital in CeO_2 and Ce_2O_3. As a result, some authors have constructed models in which the $4f$ orbital is included or excluded from the Hamiltonian, referred to as the *Valence-band model* (VBM) and the *Core-state model* (CSM).[98] By investigating both CeO_2 and Ce_2O_3 with both models, and comparing the results for the lattice parameter and bulk modulus with those of experiment, they find (as expected) that the VBM gives the best results for CeO_2 while the CSM is preferred for Ce_2O_3. Although such models contribute greatly to our understanding of the ceria systems, they have one major shortcoming: they lack predictive power for any new ceria-based material. For this, one needs a single model which can handle both systems adequately.

A.   Density functional theory + Hubbard U (DFT+U)

In reduced ceria, Ce_2O_3 and CeO_{2-x}, the Ce $4f$ band splits upon occupation due to the electronic correlation resulting from the strong localization of the $4f$ states. As a consequence, a fully occupied gap-state is detected 1.2–1.5 eV above the valence band.[62, 65] The difficulty to provide a good description for the Ce $4f$ electron with standard energy band methods may be caused by the on-site electron repulsion: "*Hubbard U*".[99–101] This repulsion may be large compared to the bandwidth of the f-band. By introducing an additional Hubbard U term for the Ce $4f$ state, it is possible to consistently describe reduced ceria and the non-reduced CeO_2.[102]

Within standard implementations of the DFT+U framework there is, however, the problem that many calculated properties of the system depend linearly on the size of the Hubbard U value.[90] Fabris *et al.* have shown that this is due to the projector functions used to define the Hubbard U functional, and that if one uses Wannier-Boys functions no such behavior is observed while retaining the expected influence on the electronic structure.[102–104]

However, since this is not the case if one uses a plane waves approach (which is natural for periodic systems), a DFT+U study scanning a range of U values is required. In 2007 several such studies were performed, all aimed at finding an optimal U value which consistently describes the different ceria compounds.[101, 105, 106] The suggested U values vary slightly between authors with U= 5–6 eV for LDA functionals, and U= 4–5 eV for GGA functionals. Though the precise optimum value of U may be debated, there seems to be a general agreement that the U value for a GGA functional should be lower than that for an LDA functional.[101, 105, 107]

B.   Hybrid functionals

An alternative approach to investigate the different ceria(-based) materials in a consistent *ab initio* way is through the use of hybrid functionals. Such functionals are widely used in chemistry and differ from the standard LDA and GGA approaches used in solid state physics in the fact that a portion of exact Hartree–Fock (HF) type exchange is introduced into the exchange correlation functional. Although hybrid functionals are known to provide a better description of a quantum mechanical system than standard LDA and GGA functionals, their application in solids and periodic systems has only recently become more or less feasible. The calculation of exact exchange lattice sums are computationally extremely demanding, and even with modern computational resources and hybrid functionals specifically designed for periodic systems, only very small systems can reasonably be studied.

In 2006, Hay *et al.*[108] presented a hybrid functional study of CeO_2 and Ce_2O_3 using a Gaussian basis set and the hybrid functional proposed by Heyd, Scuseria and Ernzerhof (HSE).[109] This functional allows the electrons to localize as much as is required based on the properties of the system and the variational principle alone. They find good values for the lattice parameters of both systems, and the correct anti-ferromagnetic ground state for Ce_2O_3.

In another hybrid functional study, Da Silva *et al.*[110] compare the hybrid HSE and PBE0 functionals to DFT+U calculations. They show that all approaches are able to find the anti-ferromagnetic ground state of Ce_2O_3, but they also note that the

precise volume and shape of the unit cell used has a large influence on the preferred ground state's stability.

Recently, two studies employed the B3LYP functional, the workhorse of quantum chemistry, to investigate the behavior of this functional and the properties of ceria.[111–113] Interestingly, both conclude that the structural properties obtained with B3LYP are not as good as those obtained with the simple LDA(+U) functional. The study by Kullgren *et al.* also shows that compared to a plane wave basis sets, Gaussian basis sets clearly fail to calculate a high quality density of states, and very small core basis sets are required. Kullgren *et al.* come to the final conclusion:

> Qualitatively both hybrid functionals PBE0 and B3LYP give a description of CeO_2 and Ce_2O_3, which is consistent with experiment, at least if we assume the largest plausible levels of experimental uncertainty. However, while both are reasonably good, neither is as good as the LDA+U or PBE+U with their material specific adjustable U parameters.
>
> – Taken from Reference [111].

The general conclusion is that at least equal quality (and in some cases even better quality) results are obtained within the LDA(+U) or GGA(+U) framework as with computationally expensive hybrid functionals, which is one of the reasons why the latter will not be used in this dissertation.

CHAPTER

③

Computational background

> *The fundamental laws necessary for the mathematical treatment of a large part of physics and the whole of chemistry are thus completely known, and the difficulty lies only in the fact that application of these laws leads to equations that are too complex to be solved.*
>
> –Paul Dirac (1902 – 1984)

In this dissertation, the properties of ceria-based materials are investigated using quantum mechanical simulations. These calculations are performed using the Vienna Ab-initio Simulation Package (VASP), which solves the Hohenberg–Kohn–Sham equations numerically to obtain the total energy of the system. In the following sections, some of the key concepts used by VASP (and other solid state physics or quantum chemical codes) will be introduced. It is not the intention to present a detailed study of these topics, so for more in depth information the reader is referred to the cited literature or standard textbooks on these topics.

3.1 The electronic structure of solids

3.1.1 Starting from a single particle

In quantum mechanics (QM)[1], a system is fully described by its Schrödinger equation, which for a single particle of mass m is given by:[114]

$$\hat{H}\Psi = E\Psi \tag{3.1}$$

with E the total energy, Ψ the wavefunction of the system and the Hamiltonian given by:

$$\hat{H} = \hat{T} + \hat{V} = \frac{-\hbar^2}{2m}\nabla^2 + V_{ext}(\mathbf{r}) \tag{3.2}$$

where the first term represents the kinetic energy and the second the contribution due to the external potential.[2] In the case of a solid or a molecule, or even a single atom, a system will consist of multiple particles. If one were to assume that these particles are non-interacting, the Schrödinger equation of such a system would be

---

[1] Or quantum physics or quantum chemistry. It is interesting to note that the same quantum theory employed by different people (chemists and physicists) is referred to with a different name. Although it is true that both groups have (slightly) different interests, the basic theory and approaches are the same.

[2] In this work vectors are indicated in bold.

a simple sum of the single particle Schrödinger equations over all particles. The interaction of the particles, however, results in an additional set of terms describing the interaction of each pair of particles. The system Hamiltonian then becomes:

$$\hat{H} = \sum_i \left((\hat{T}_i + \hat{V}_i) + \frac{1}{2} \sum_{j \neq i} \hat{V}_{i,j} \right). \tag{3.3}$$

The factor $\frac{1}{2}$ is intended to prevent double counting of the pairwise interactions. For the practical applications we are interested in, there are two types of particles to be considered: electrons and nuclei. Because nuclei are $10^3 - 10^6$ times heavier than electrons, there will exist two different timescales on which events take place in the system. For the fast moving electrons, the nuclei will appear nearly static, while for the nuclei the electrons present themselves as a constant potential energy surface to move on.[3] The existence of these two timescales is often used to justify the Born–Oppenheimer approximation. In the Born–Oppenheimer or adiabatic approximation, the wavefunction of the system is split into a nuclear and an electronic part.[115] As a result, the system Schrödinger equation is rewritten as a set of coupled single particle Schrödinger equations. This set of equations is then solved in two steps, first the electronic Schrödinger equations are solved for a system with fixed nuclei and neglecting the nuclear kinetic energy. The resulting electronic wavefunction is then used to provide the electronic potential experienced by the nuclei in the nuclear Schrödinger equations. Solving this set of equations then results in the total energy of the system including both electronic and nuclear contributions.

A further approximation that is often introduced is the following: because one may assume that the quantum effects on the nuclear motion are negligible, it is possible to replace the set of computationally expensive nuclear Schrödinger equations by a set of much simpler classical Newtonian equations of motion. As a result, only the electronic part of the system is described through QM, giving rise to a purely electron based Hamiltonian of the form:

$$\hat{H} = \sum_i \left(\frac{-\hbar^2}{2m_e} \nabla_{\mathbf{r}_i}^2 + \hat{V}_{ext}(\mathbf{r}_i) + \frac{1}{2} \sum_{j \neq i} \frac{e^2}{4\pi\varepsilon_0 \|\mathbf{r}_i - \mathbf{r}_j\|} \right), \tag{3.4}$$

where the first term gives the kinetic energy of the system as the sum of electron kinetic energies, the second term describes the Coulomb interaction between the electrons and the set of (static) nuclei, and the third term gives the electron–electron Coulomb interactions. Again, the factor $\frac{1}{2}$ is to prevent double counting.

---

[3]Although the latter is used to indicate the motion of the nuclei on the (Coulombic) potential due to the electrons, the potential energy surface is actually due to the interaction between the nuclei and electrons.

3.1.2   To approximate many particle systems: the Hartree–Fock approximation.

In QM, there is no analytic solution for the general two-body problem,[4] although for a few simple many-body systems analytic solutions exist.[5] In contrast, numerically exact solutions can be obtained for all small systems. For larger systems, a straightforward separation of the many-body wavefunction is required to make the problem computationally tractable. This, however, has the consequence that important (and complex) electron interactions are neglected. Already in 1928, Hartree proposed to approximate the N-body wavefunction as a product of N single particle wavefunctions:

$$\Psi(\mathbf{r}_1, \ldots, \mathbf{r}_N) = \psi_1(\mathbf{r}_1) \cdot \psi_2(\mathbf{r}_2) \cdots \psi_N(\mathbf{r}_N) \tag{3.5}$$

where the single particle wavefunctions satisfy the one electron Schrödinger equation:

$$\left[\frac{-\hbar^2}{2m_e} \nabla_{\mathbf{r}}^2 + V_{ext}(\mathbf{r}) + V^{H,i}(\mathbf{r}) \right] \psi_i(\mathbf{r}) = \varepsilon_i \psi_i(\mathbf{r}) \tag{3.6}$$

with $V^{H,i}$ the Hartree potential experienced by the ith electron due to the other $N-1$ electrons:

$$V^{H,i}(\mathbf{r}) = \frac{e^2}{4\pi\varepsilon_0} \int \frac{\rho^i(\mathbf{r}')}{\|\mathbf{r}' - \mathbf{r}\|} \mathrm{d}^3\mathbf{r}' \tag{3.7}$$

with

$$\rho^i(\mathbf{r}') = \sum_{\substack{j=1 \\ j \neq i}}^{N} \|\psi_j(\mathbf{r}')\|^2. \tag{3.8}$$

As can be seen from Eq. (3.6) to (3.8), the Hartree approximation replaces the N^2 electron–electron interactions of Eq. (3.4) by N interactions between each electron and the average potential due to the other $N-1$ electrons, which is why this is called a "mean field" approximation. Because the electrons interact through the Hartree potential $V^{H,i}$, it is possible to solve these equations through an iterative scheme. In practice, this is done by making an initial guess for the electron density ρ^i, which allows for the Hartree potential $V^{H,i}$ to be calculated and the one-electron wavefunction to be determined from Eq. (3.6). From these one-electron wavefunctions the electron densities for the next iteration can be obtained. The iterative scheme continues until the results are converged (*i.e.* the electron density does not change anymore) and self consistency is reached. This procedure is known as the self consistent field procedure (SCF) and also applies to higher levels of theory such as Hartree–Fock (HF) and density functional theory (DFT).

An important contribution which is missing in the Hartree approximation, as was shown by Fock, is the exchange contribution. Because electrons are fermions,

---

[4]This is still possible in classical Newtonian mechanics, for which a general analytic solution to the three-body problem does not exist.

[5]For example, the hydrogen atom.

the many-body wavefunction of a many-electron system needs to be anti-symmetric, which means that the exchange of two electrons results in a sign-change. This is not the case for the many-body wavefunction given by Eq. (3.5). However, such a wavefunction can be constructed as a linear combination of $N!$ Hartree type many-body wavefunctions. The simplest way to represent such a linear combination is as a determinant of an $N \times N$ matrix and is called the Slater determinant.[116] The many-body wavefunction of an N-electron system is then approximated as:

$$\Psi(\mathbf{r}_1, \ldots, \mathbf{r}_N) = \frac{1}{\sqrt{N!}} \det\left[\psi_1(\mathbf{r}_1) \cdots \psi_N(\mathbf{r}_N)\right]. \tag{3.9}$$

Taking the missing exchange contribution into account, the single electron Schrödinger equation is written as

$$\left[\frac{-\hbar^2}{2m_e}\nabla_{\mathbf{r}}^2 + V_{ext}(\mathbf{r}) + V^{H,i}(\mathbf{r})\right]\psi_i(\mathbf{r}) + V^{x,i}(\mathbf{r}, \psi_i(\mathbf{r})) = \varepsilon_i \psi_i(\mathbf{r}) \tag{3.10}$$

with the Hartree potential $V^{H,i}$ given in Eq. (3.7) and the exchange potential given as

$$V^{x,i}(\mathbf{r}, \psi_i(\mathbf{r})) = \frac{-e^2}{4\pi\varepsilon_0} \sum_{\substack{j=1 \\ j\neq i}}^{N} \int \frac{\psi_j^*(\mathbf{r}')\psi_i(\mathbf{r}')}{\|\mathbf{r} - \mathbf{r}'\|} \mathrm{d}^3\mathbf{r}' \psi_i^*(\mathbf{r})\psi_j(\mathbf{r}) \tag{3.11}$$

within the HF approximation.

In addition to the exchange term included by Fock, electrons also feel the change of the Coulomb potential of one another. As a result, the movement of one electron will result in a change of the Coulomb potential for all other electrons in the system. This means that the motion of the electrons will be correlated. Such a correlation is not included in the HF approximation, but it is present in higher levels of theory.

3.1.3 From indiscernible electrons to densities: Density Functional Theory

The mean field concept, which is at the heart of the HF approximation, also points to another possible level of abstraction. Since electrons are indistinguishable, and we are mainly interested in their total behavior, one might imagine replacing the electrons by their density distribution. As such, the electrons lose their identity as particle and a more probabilistically inclined view emerges. Such an approach is followed in DFT. In this approach, the electron density is the central variable.[6] Consequently, the computational cost does no longer scale with the number of particles, but instead it scales with the grid size of the electron density. This allows for the investigation of systems which are at least one order of magnitude larger than is usually possible with HF.

---

[6]More recently, the development of *conceptual density functional theory* emerged in the field of quantum chemistry as a route to provide stronger theoretical foundations to standard (empirical) chemical concepts.[117]

It were Hogenberg and Kohn (HK), who in 1964 first formulated a DFT based on two theorems:[118]

Theorem 1 For a many-electron system in an external potential V_{ext}, this external potential, and consequently the total energy, is uniquely determined as a functional of the electron density $\rho(\mathbf{r})$.

Theorem 2 The exact ground state energy of a system in an external potential V_{ext} is the variational global minimum of a universal energy functional $E[\rho(\mathbf{r})]$. The density which minimizes this functional is the exact ground state density.

In their work, Hohenberg and Kohn showed that, using the electron density as a basic variable, the total energy of an electron gas is a unique functional of this density, which includes both exchange **and** correlation contributions. However, the proof of the existence of such an energy functional is of little practical use since its exact form is not known. This was later partially resolved by Kohn and Sham who proposed the existence of a non-interacting system described by the total energy functional

$$E_{KS}[\rho(\mathbf{r})] = T[\rho(\mathbf{r})] + V_{ext}[\mathbf{r}] + E^H[\rho(\mathbf{r})] + E^{xc}[\rho(\mathbf{r})] \tag{3.12}$$

in which the first term represents the (non-interacting) kinetic energy contribution, the second term represents the contribution due to the external potential,[7] the third term is due to the electron–electron Coulomb interaction (also known as the Hartree term) and the fourth term contains both the exchange and correlation contribution.[8] Exact analytical forms are known only for the first three terms. In the fourth term, it is the correlation contribution which lacks a general analytic form. As a result, this last term needs to be approximated. The resulting set of equations is known as the Hohenberg–Kohn–Sham (HKS) equations:

$$\left\{ \frac{-\hbar^2}{2m_e}\nabla^2 + V_{ext}(\mathbf{r}) + \frac{e^2}{4\pi\varepsilon_0}\int\frac{\rho(\mathbf{r}')}{\|\mathbf{r}-\mathbf{r}'\|}\mathrm{d}^3\mathbf{r}' + E^{xc}\big[\rho(\mathbf{r})\big]\right\}\psi_i(\mathbf{r}) = \varepsilon_i\psi_i(\mathbf{r}) \tag{3.13}$$

with $E^{xc}[\rho(\mathbf{r})] = \frac{\delta\{\rho(\mathbf{r})\varepsilon_{xc}[\rho(\mathbf{r})]\}}{\delta\rho(\mathbf{r})}$. At this point, an expression is required for E^{xc}. In solid state calculations, one of the most simple approximations is the local density approximation (functional) (LDA) in which E^{xc} is based on results obtained for the homogeneous electron gas. E^{xc} consists of two parts, the exchange and the correlation part, $E^{xc} = E^x + E^c$. For the homogeneous, electron gas the exact expression is known for the exchange part:[119, 120]

$$E^x[\rho(\mathrm{r})] = -\frac{3}{4}\sqrt[3]{\frac{3}{\pi}}\int\rho(\mathbf{r})^{4/3}\mathrm{d}^3\mathbf{r}. \tag{3.14}$$

However, for the correlation part no analytic expression is known. Instead a parameterized expression is used, originally presented by Perdew and Zunger, which fitted

---

[7]For solids and molecules, we will assume that only the contributions due to the nuclei are included.

[8]In practice, this fourth term also includes a correction introduced by the assumption that the analytical form used for the kinetic energy term is exact.

the results obtained in high quality Monte Carlo calculations on the homogeneous electron gas performed by Ceperley and Alder (CA).[121, 122] Since this example of an exchange correlation functional is only a function of the density, it can be considered a zeroth order approximation, and a first order approximation would then include also the gradient of the density. This is the idea behind generalised gradient approximation (functional) (GGA) for which the exchange correlation functional has the general form:

$$E_{GGA}^{xc}[\rho(\mathbf{r})] = \int f(\rho(\mathbf{r}), \nabla(\rho(\mathbf{r})))\rho(\mathbf{r})\mathrm{d}^3\mathbf{r}. \tag{3.15}$$

Unlike LDA, there are many different kinds of GGA of which the formulation by Perdew, Burke and Ernzerhof (functional) (PBE) has become fashionable in recent years in the solid state community.[123]

Another approach which has become available to the solid state community only recently is the use of hybrid functionals. Such functionals, which consist of a linear combination of LDA and/or GGA functionals with the exchange part of the HF approximation, are commonly used by the chemistry community. Their introduction for solids is mainly hampered by the large increase in computational cost required by the non-local HF part. Of the hybrid functionals known by the chemistry community, the B3LYP functional is probably the most widely used and is given by:[113]

$$E_{B3LYP}^{xc} = E_{LDA}^{xc} + a_0(E_{HF}^x - E_{LDA}^x) + a_x(E_{GGA}^x - E_{LDA}^x) + a_c(E_{GGA}^c - E_{LDA}^c) \tag{3.16}$$

with $a_0 = 0.20$, $a_x = 0.72$ and $a_c = 0.81$—three empirical parameters. Specifically for solids, Heyd, Scuseria, and Ernzerhof (functional) (HSE) developed a hybrid functional in which the exchange correlation functional is split in a long-and short-range part to improve the computational efficiency:[109]

$$E_{HSE}^{xc} = aE_{HF,s}^x + (1-a)E_{PBE,s}^x(\omega) + E_{PBE,l}^x(\omega) + E_{PBE}^c \tag{3.17}$$

with mixing parameter $a = 0.25$, s and l indicating short-and long-range, respectively, and an adjustable parameter ω controlling short-/long-range behavior of the interaction. For all hybrid functionals, the parameters controlling the mixing of the different contributions are generally obtained through fitting to an example set (of molecules).[9]

DFT as presented here is a strictly ground state formalism, which means that the energy of excited states is too low and as a result band gaps tend to be underestimated. However, the work done over the last decades has shown that DFT correctly describes the ground state properties of most systems using the functionals presented here.

---

[9]This is an interesting aspect to keep in mind with regard to the discussion about the tunable U parameter in the DFT+U approach. At the VASP workshop in 2012, Cesare Franchini for example, presented the results for tuning the mixing parameter a of the HSE functional when working with solids. In the work of Alkaukas et al.,[124] this optimized value is shown to present good correlation with the inverse of the dielectric constant.

3.1.4 Periodic boundary conditions and plane waves

Whereas a molecule contains only a (small) finite number of atoms, a macroscopic solid contains a number of atoms of the order of Avogadro's number N_A; *i.e.* infinite from the practical computational point of view.[125] In case of a crystalline material, however, this infinite number of atoms is organized in 'small' units (called unit cells) which are infinitely repeated in all directions. This allows the computational reduction of a solid to a manageable small system. Taking the periodic boundary conditions (PBC) into account, it is possible to simulate the behavior of an infinitely sized solid using only a single unit cell.

Due to the periodic placement of the atoms, the external potential V_{ext} of the previous section is also periodic,[10] and the electrons moving in this potential can be described using a "*Bloch wave*". Such a Bloch wave consists of two parts: a periodic function $u(\mathbf{r})$ with the same periodicity as the crystal, and a plane wave:[126]

$$\psi_{n\mathbf{k}}(\mathbf{r}) = u_{n\mathbf{k}}(\mathbf{r})e^{i\mathbf{k}\cdot\mathbf{r}} \tag{3.18}$$

with $\mathbf{k}$ a wave vector and n the band index. From the periodicity relation

$$u_{n\mathbf{k}}(\mathbf{r} + \mathbf{R}) = u_{n\mathbf{k}}(\mathbf{r}) \tag{3.19}$$

for any lattice vector $\mathbf{R}$, the Bloch theorem follows easily:

$$\psi_{n\mathbf{k}}(\mathbf{r} + \mathbf{R}) = \psi_{n\mathbf{k}}(\mathbf{r})e^{i\mathbf{k}\cdot\mathbf{R}}. \tag{3.20}$$

In addition, because of the periodicity of $u_{n\mathbf{k}}$, this function can also be decomposed in a Fourier series of plane waves. Consequently, the entire Bloch wave can also be decomposed in a Fourier series of plane waves. This shows that plane waves are ideally suited to represent periodic systems, and makes it natural to use them to construct the basis set for solving the HKS equations. From the numerical point of view, there is the additional advantage that they allow fast passing between real and reciprocal space using fast Fourier transforms (FFT), and Hellmann–Feynman forces on the ions do not need to be corrected, whereas the use of localized atomic orbitals require Pulay corrections.[127–129] The use of plane waves as a basis set also allows for straightforward and consistent improvement of the basis set convergence, in contrast to, for example, the use of Gaussian basis sets. The main drawback, however, is the relatively slow convergence which originates from the fast oscillations of the tightly bound atomic core orbitals.

3.1.5 Density of states

In a system at zero temperature containing N electrons, these electrons will occupy the N lowest one-electron states. In a solid, these states can be very close in energy giving rise to bands of states instead of clearly distinguishable levels.[11] The number

---

[10]We assume no additional external non-uniform potentials to be present.
[11]Ignoring degenerate states for the moment.

of states per energy interval $[\varepsilon, \varepsilon + \mathrm{d}\varepsilon]$ is called the "*density of states*" (DOS) and can be constructed as:[126]

$$g_n(\varepsilon)\mathrm{d}\varepsilon = \frac{2}{V} \times N_{n,k} \tag{3.21}$$

where V is the volume of the unit cell, n indicates the band index (introduced in **Sec.** 3.1.4), and $N_{n,k}$ is the number of allowed wave vectors $\mathbf{k}$ in the nth band which lies in the energy interval $[\varepsilon, \varepsilon + \mathrm{d}\varepsilon]$, which is the volume of a $k-$space unit cell divided by the volume per allowed wave vector. As a result we can write Eq. (3.21) as:

$$g_n(\varepsilon)\mathrm{d}\varepsilon = \int \frac{\mathrm{d}\mathbf{k}}{4\pi^3} \times \left\{ \begin{array}{ll} 1 & \varepsilon \leq \varepsilon_n(\mathbf{k}) \leq \varepsilon + \mathrm{d}\varepsilon \\ 0 & \text{elsewhere.} \end{array} \right. \tag{3.22}$$

For an infinitesimal $\mathrm{d}\varepsilon$, this can also be written as a surface integral. Within the unit cell, for a surface $S_n(\varepsilon)$, defined in k-space as the surface $\varepsilon_n(\mathbf{k}) = \varepsilon$, one then obtains:

$$g_n(\varepsilon)\mathrm{d}\varepsilon = \int_{S_n(\varepsilon)} \frac{\mathrm{d}S}{4\pi^3} \delta k(\mathbf{k}) \tag{3.23}$$

with $\delta k(\mathbf{k})$ the perpendicular distance between the surfaces $S_n(\varepsilon)$ and $S_n(\varepsilon + \mathrm{d}\varepsilon)$. Since the surfaces $S_n(\varepsilon)$ are energy iso-surfaces, the gradient $\nabla \varepsilon_n(\mathbf{k})$ is normal to these surfaces, and for a distance $\delta k(\mathbf{k})$ along this normal, the change in energy $\mathrm{d}\varepsilon$ is given as:

$$\varepsilon + \mathrm{d}\varepsilon = \varepsilon + |\nabla \varepsilon_n(\mathbf{k})|\delta k(\mathbf{k}), \tag{3.24}$$

such that $\delta k(\mathbf{k})$ is found to be:

$$\delta k(\mathbf{k}) = \frac{\mathrm{d}\varepsilon}{|\nabla \varepsilon_n(\mathbf{k})|}. \tag{3.25}$$

As a result the DOS is given by:

$$g_n(\varepsilon)\mathrm{d}\varepsilon = \int_{S_n(\varepsilon)} \frac{\mathrm{d}S}{4\pi^3} \frac{1}{|\nabla \varepsilon_n(\mathbf{k})|}, \tag{3.26}$$

showing the explicit relation with the band structure in $k-$space.

This 'total' DOS can be decomposed in both s, p, d or f and site projected contributions. The components in such a decomposition are referred to as the local density of states (LDOS) and allow for specific features in the total DOS to be qualitatively identified with specific atoms or orbitals in the system.

Within the context of population analysis, the decomposition of the DOS with regard to the atomic sites is in essence a Mulliken-type population analysis (*cf.* **Chapter** 7). However, its practical implementation as is available in the used VASP program requires one to provide a so-called Wigner Seitz radius. This radius determines the spheres around the atoms within which the decomposition and projection is performed. Because there is no unambiguous way to define these radii, the absolute values of the populations obtained through integration of the LDOS are meaningless; non-overlapping spheres lead to unaccounted densities; overlapping spheres, on the other hand, lead to a double counting of certain regions while other regions may still be unaccounted for. As a result, one cannot use such an implementation to study charge transfer on a quantitative level.

3.1.6 Pseudo-potentials: removing the heart of the problem

As was noted in a previous section, the fast oscillations of atomic core orbitals is detrimental to the use of plane wave basis sets. However, from chemistry it is known that chemical interactions, such as bond formation, mainly involve valence electrons and occurs 'far' away from the core. In solid state physics, on the other hand, most of the properties of interest are related to the electronic states near the Fermi level, which are also dominated by valence electrons. So, from both we learn that low lying core states and core orbitals are generally not relevant for the properties of interest, and may as such be ignored or replaced. The introduction of pseudo-potentials (PP) does just this. The basic idea behind PP stems from the work of Fermi, and consists of replacing the strong interaction potential due to the tightly bound core electrons, by a much weaker interacting effective potential.[130] However, this PP should have the exact same scattering properties as the original potential in the core region, while on the other hand being so smooth that the 'pseudo'-wavefunction shows no nodes in the core region (*cf.* Fig. 3.1).

Since PP are not unique and their construction can be modified to meet specific computational, physical or chemical needs, several different types and classes of PP have been developed over the years.[131–135] The construction of a PP starts from defining a list of desired properties. An example of such a list for an *ab initio* PP is given by Hamann, Schlüter and Chiang:[131]

1. Real and pseudo valence eigenvalues agree for a chosen "prototype" atomic configuration.

2. Real and pseudo atomic wave functions agree beyond a chosen "core radius" r_c.

3. The integrals from 0 to r of the real and pseudo charge densities agree for $r > r_c$ for each valence state (norm conservation).

4. The logarithmic derivatives of the real and pseudo wave function and their *first energy derivative* agree for $r > r_c$.

–Taken from Reference [131]

Of the different types of PP, the norm-conserving pseudo-potentials (NCPP) are one of the more simple examples. These PP give the correct charge distribution between the core and interstitial region, since the pseudo-wavefunctions are normalized. In addition, the pseudo-wavefunctions are chosen as solutions of the PP scheme such that they reproduce the all-electron (AE) valence electron properties, making them more accurate. An often used recipe for constructing such a NCPP is provided by Troullier and Martins.[135] Ultra-soft pseudo-potentials (USPP) are slightly more complex. In this case, the requirement of orthogonality of the pseudo-wavefunctions is released in favor of more smooth PP, which results in fewer plane waves being required, in turn reducing the total computational cost.[134, 136] With the introduction of the projector augmented waves (PAW) approach, the computational cost was further decreased while accuracy and complexity further increased.[137, 138] Furthermore, the
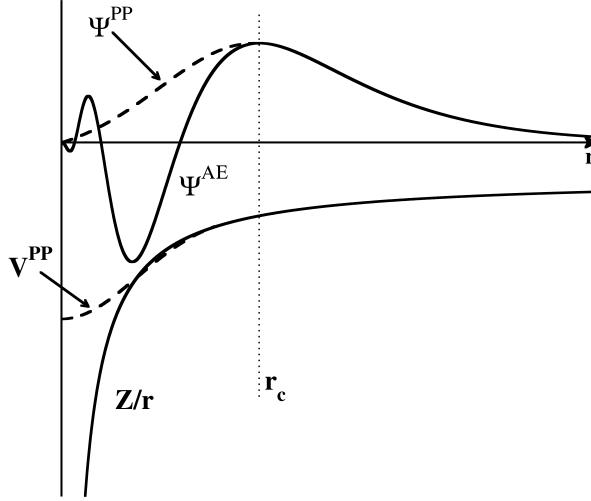
Figure 3.1: *Pseudo-potentials are constructed in such a way that the pseudo-wavefunctions contain no nodes in a core region, while being the exact wave-function outside the core region.*

PAW approach is considered to be an AE formalism. It is this last approach which is employed by the VASP program. In **Chapter 8**, we will focus on some of the consequences of the PAW approach for the implemented atoms-in-molecules method.

3.2 Ceria in Density Functional Theory

In this dissertation, the influence of doping on the properties of CeO_2 is studied. So, it is important to first have a close look at the base material itself. Cerium oxide presents itself most commonly in two different stoichiometries: CeO_2 and Ce_2O_3. In this section, I will present the results of basic DFT calculations for CeO_2 and Ce_2O_3, and compare them to results found in the literature.

3.2.1 Crystal structure

For the two most stable stoichiometries, the structure of cerium oxide is well-known: CeO_2 has a cubic fluorite structure (space group $Fm\bar{3}m$, or Pearson symbol cF12) shown in Fig. 3.2a and Ce_2O_3 has a hexagonal sesquioxide A-type structure (space group $P\bar{3}m1$, or Pearson symbol hP5) shown in Fig. 3.2c.

The CeO_2 fluorite structure can be considered to consist of a face-centered cubic (fcc) Ce-lattice with an imbedded simple cubic O-lattice. In this structure, all Ce atoms have coordination 8, while the O atoms are 4-coordinated, located at the center of a tetrahedron of nearest neighbor Ce atoms. While in CeO_2 all O atoms are
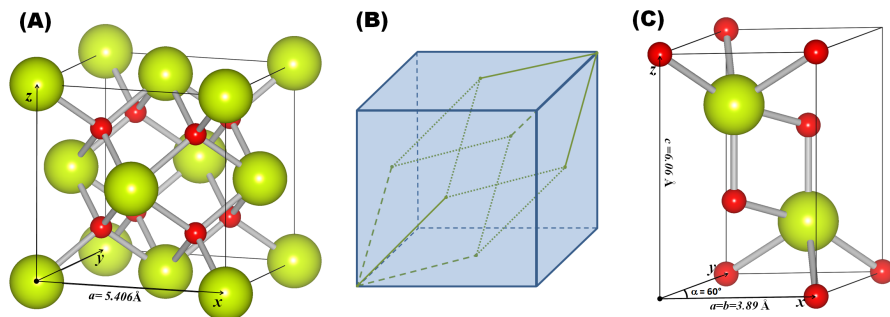
Figure 3.2: *Ball-and-stick representations of the cubic fluorite (A) and hexagonal (C) crystal structures for CeO_2 and Ce_2O_3, respectively. Big yellow/small red spheres indicate the positions of the Ce/O atoms. (B) The shape and position of the unit cell for CeO_2 with the cubic super cell as shown in (A); solid and dashed lines give the edges of the unit cell located in the visible and invisible faces of the cube; dotted lines indicate edges of the unit cell located inside the cube.*

equivalent (also all Ce atoms are equivalent), there are two inequivalent O sites in Ce_2O_3, as can be seen in Fig. 3.2c.

The cubic cell shown in Fig. 3.2a is not the unit cell for CeO_2, but since this representation gives a clearer picture of the fluorite structure it is often presented instead of the actual unit cell. CeO_2 has a unit cell with fcc lattice vectors. Figure 3.2b shows the unit cell (green) in relation to the presented cubic cell (blue). In following chapters, we will often make use of super cells based on periodic copies of both the cubic representation and the primitive unit cell representation. For this, we will use the following convention: first, one letter indicating which of the two cells is started from (c for the cubic cell, and p for the primitive unit cell), and then three integer values indicating the number of copies along each of the lattice vectors (222 would indicate a doubling in each of the three directions).

Tables 3.1 and 3.2 show the optimized geometries of CeO_2 and Ce_2O_3. Comparison to the experimental values and the values found in theoretical literature shows good agreement. For the CeO_2 lattice constant, the usual underestimation of LDA and overestimation of GGA (PBE) is observed, while for Ce_2O_3 both LDA and PBE values of the lattice and internal parameters underestimate the experimental values, with PBE giving the best results. The quality of the PBE results for the Ce_2O_3 structure are comparable to those of hybrid calculations, as can be seen in Table 3.2.

In addition, we have calculated the bulk modulus for both systems, by fitting the total energy of a set of fixed volume calculations to the Birch-Murnaghan third-order isothermal equation of state (*cf.* **Appendix** A.1).[143, 144] Here, the LDA values for CeO_2 show very good agreement with experimental values, while the PBE

Table 3.1: *Bulk properties of fluorite type CeO_2. Lattice parameter a_0 and bulk modulus B_0 in comparison to experimental values and theoretical values found in the literature.*

	$a_0(\text{Å})$	$B_0(\text{Mbar})$
LDA[a]	5.363	2.017
PBE[a]	5.462	1.717
Expt.[b]	5.406/5.411	2.04/2.36
LDA[c]	5.36/5.39	1.93/2.15
PBE[c]	5.38/5.52	1.70/2.02
HSE[c]	5.40/5.41	2.06
PBE0[c]	5.39/5.42	
B3LYP[c]	5.43/5.50	1.99/2.11

[a] Present work.
[b] References [98, 105–108, 111, 112, 139–142] and references therein.
[c] Theoretical literature: References [98, 105–108, 111, 112, 142] and references therein.

Table 3.2: *Bulk properties of hexagonal Ce_2O_3 in a ferromagnetic spin state. a_0 and c_0 are the lattice constants. u_{Ce} and u_O are the internal parameters. Also the bulk modulus B_0 is given. Experimental and other theoretical values found in the literature are included for comparison.*

	$a_0(\text{Å})$	$c_0(\text{Å})$	u_{Ce}	u_O	$B_0(\text{Mbar})$
LDA[a]	3.767	5.868	0.2427	0.6415	1.384
PBE[a]	3.836	6.047	0.2454	0.6434	1.153
Expt.[b]	3.888/3.891	6.059/6.063	0.245/0.251	0.647/0.648	
LDA[c]	3.77/3.89	5.86/5.88	0.2429	0.6413	1.24/1.66
PBE[c]	3.83/3.88	5.98/6.08	0.2459	0.6420/0.6435	1.13
HSE[c]	3.86/3.87	6.07	0.2459	0.6459	
PBE0[c]	3.87	6.06	0.2460	0.6459	
B3LYP[c]	3.90	6.19/6.21	0.247	0.646	

[a] Present work.
[b] References [106–108, 111] and references therein.
[c] Theoretical literature: References [98, 105–108, 111] and references therein.

value shows a significant underestimation (which is also observed in the theoretical literature). For Ce_2O_3, no experimental data is available; however, our calculated values seem to be in the range of the values present in the theoretical literature.

Table 3.3: *The heat of formation ΔH_f per formula unit for CeO_2 and Ce_2O_3 in comparison to experimental values and theoretical values found in the literature. ΔH_f was calculated with regard to bulk α-Ce and gas phase O_2, the reduction energy E_{red} for $2\,CeO_2 \longrightarrow Ce_2O_3 + \frac{1}{2}\,O_2$.*

	ΔH_f(eV)		E_{red}(eV)
	CeO_2	Ce_2O_3	
LDA[a]	-11.483	-18.057	4.909
PBE[a]	-10.417	-16.573	4.261
Expt.[b]	$-10.44/-11.30$	$-17.70/-18.58$	$3.57/4.03$
LDA[b]	-11.49	-18.07	4.92
PBE[b]	$-10.24/-10.35$	$-16.30/-16.47$	$4.18/4.24$
HSE[b]	-11.00	-18.85	3.16
PBE0[b]	-11.15	-19.18	3.14

[a] Present work.
[b] References [106, 142] and references therein.

3.2.2 Thermodynamic properties

The heat of formation for CeO_2 and Ce_2O_3 can, at zero temperature and pressure, be calculated as:

$$CeO_2: \qquad \Delta H_f \;=\; E_{CeO_2} - E_{Ce} - E_{O_2} \qquad (3.27)$$

$$Ce_2O_3: \qquad \Delta H_f \;=\; E_{Ce_2O_3} - 2E_{Ce} - \frac{3}{2}E_{O_2} \qquad (3.28)$$

with E_{CeO_2} and $E_{Ce_2O_3}$ the total energy of bulk CeO_2 and Ce_2O_3, respectively. E_{Ce} is the total bulk energy per atom for pure α-cerium, and E_{O_2} is the total energy of an O_2 molecule. The choice of using α-cerium as a reference rather than γ-cerium—such as for example done by Loschen *et al.*—is based on the fact that our *ab initio* calculations are performed at zero temperature and pressure, for which α-cerium is the experimentally observed ground state.[52, 107] The fact that at room temperature () and standard pressure both the double hexagonal β and fcc γ phases of cerium exist, shows that extrapolation to RT will not be straightforward. The total energy of the O_2 molecule was obtained by placing a single O_2 molecule in a large asymmetric periodic box of $14 \times 15 \times 16$ Å^3. The size of the box was sufficient to reduce the contribution to the total energy of the interaction between periodic copies below 1 meV, while the asymmetry reduced the symmetry of the periodic system. Only the k-point at Γ was used to prevent artifacts due to the periodic boundary conditions.

In addition to the heat of formation, also the energy of reduction is calculated as:

$$E_{red} = E_{Ce_2O_3} + \frac{1}{2}E_{O_2} - 2E_{CeO_2}. \qquad (3.29)$$

The calculated values are shown in Table 3.3. The heat of formation calculated within the LDA framework shows good agreement with the experimental values,
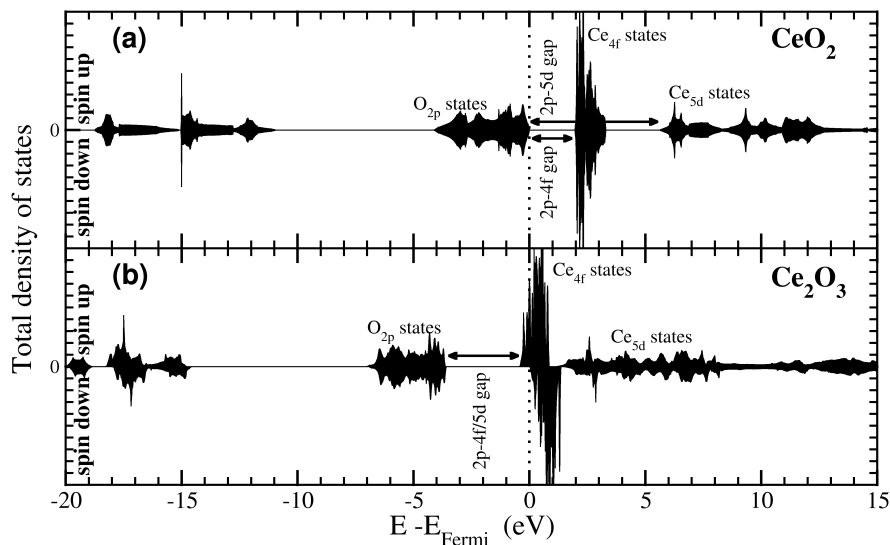
Figure 3.3: *Total density of states for CeO$_2$(a) and ferromagnetic Ce$_2$O$_3$(b) within the LDA framework.*

while the PBE values show a clear underestimation. Both LDA and PBE seem to overestimate the reduction energy. In contrast, reduction energies obtained with hybrid functionals are shown to be greatly underestimated.[106, 142]

At this point, It is important to note that the comparison of reduction energies and heats of formation is a problematic issue for ceria. First of all, there is a large spread in the experimentally presented values (up to 1 eV) making it hard to make a definitive statement on the quality of the results of different functionals. Secondly, as was already mentioned, there exist several different phases for pure cerium, and the choice of which to use will influence the obtained values. Finally, there is the known problem of the underestimation of the O$_2$ binding energy. Wang *et al.* found that GGA functionals tend to underestimate the reaction energies in metal oxides by roughly 1.36 eV/O$_2$.[145] Some authors therefore opt to add a 'correction term' (*i.e.* shift the calculated energies by a constant). Although for PBE this results in an improvement of the heat of formation for both CeO$_2$ and Ce$_2$O$_3$, at the same time it results in a significant deterioration of the previously reasonable reduction energy.

In conclusion, the predictive quality of a functional needs to be based on other properties in the case of ceria.

3.2.3 Electronic structure

The spin-projected DOS of CeO$_2$ and Ce$_2$O$_3$ are shown in Fig. 3.3. It is clear from this image that similar features are present for both systems. Near the Fermi level there exists a sizable band gap, with a highly localized band of Ce 4f states. In

Table 3.4: *Sizes of different band gaps (eV) in CeO_2 and Ce_2O_3 within the LDA and PBE framework in comparison to the experimental values. For CeO_2 also the width of the empty $4f$ band (Δ_{4f}), located in the band gap, is given.*

	LDA	PBE	Expt.[a]
		CeO_2	
O_{2p}-Ce_{4f}	1.98	1.90	3
O_{2p}-Ce_{5d}	5.66	5.70	6
Δ_{4f}	1.30	1.19	1.2
		Ce_2O_3	
O_{2p}-$Ce_{4f/5d}$	3.16	3.15	2.4

[a] Taken from References [107, 146, 147], and references therein.

the case of CeO_2, this band is unoccupied, making CeO_2 a wide-band-gap insulator with a fundamental band gap of about 6 eV.[148] In the case of Ce_2O_3, the $4f$ band is partially occupied. In experiment, the occupied part of the $4f$ band gives rise to an anti-ferromagnetic (AF) Mott-Hubbard insulating ground state for Ce_2O_3.[147] In contrast, Fig. 3.3b shows a metallic ground state. This is a known failure of the DFT approach for this material, and we will get back to this in the following section.[106, 107, 142]

Table 3.4 shows the calculated sizes of the band gaps indicated in Fig. 3.3 in comparison to their experimental values. For CeO_2, both band gaps are slightly underestimated, which is in line with the expectancy for a DFT calculated band gap (*cf.* **Sec.** 3.1.3). The width of the unoccupied $4f$ band, however, shows good agreement with the experimental value.

In contrast, the band gap in Ce_2O_3 appears overestimated, but in reality the DOS near the Fermi level is wrong. When CeO_2 is reduced to Ce_2O_3, the formal valence of the Ce atoms goes from +4 to +3. As a result, each Ce atom will also accommodate a single $4f$ electron. (The part of the $4f$ band below the Fermi level in the spin-polarized total DOS, presented in Fig. 3.3, integrates exactly to 2 electrons. In addition, the ferromagnetic (FM) nature of the system results in occupation of only one spin component for the $4f$ band.) The occupied $4f$ states are expected to split off from the unoccupied states of the $4f$ band forming a gap state. From experiments, the location of this occupied gap state is known to be located 1.2–1.5 eV above the valence band and about 2.4 eV below the conduction band.[149] The conduction band is expected to consists of the Ce $4f$ and $5d$ bands. To obtain the correct electronic behavior, one can make use of either hybrid functionals or the DFT+U framework with the inclusion of a Hubbard U term.[98, 101, 102, 105–108, 111, 112, 142]

In conclusion, plain DFT is sufficient to obtain general structural properties for both CeO_2 and Ce_2O_3. Also the electronic structure of CeO_2 is correctly described; however, the electronic structure for reduced systems requires a more advanced approach.
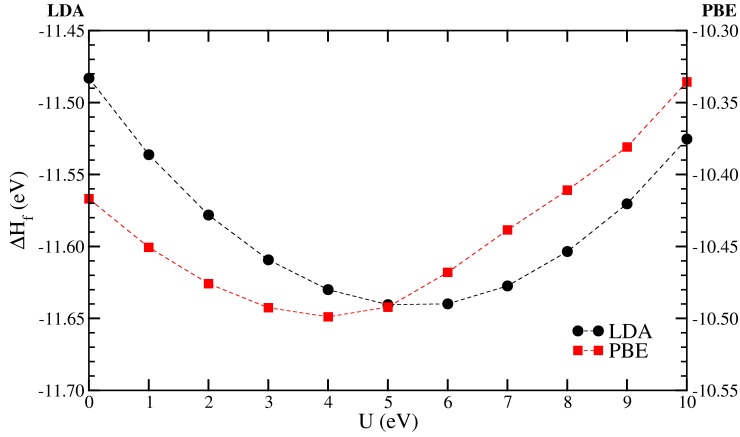
Figure 3.4: *Calculated heat of formation ΔH_f of CeO$_2$ as function of the Hubbard U parameter. The left and right energy scales are for the LDA and PBE curves, respectively.*

3.3 DFT+U approach for CeO$_2$

An intuitive solution to correct the strong correlation of the Ce $4f$ electron is to modify the intra-atomic Coulomb interaction through the introduction of a Hubbard U term. This can be interpreted as the introduction of a penalty function which inhibits non-integer occupation numbers of the on-site density matrix. Fabris *et al.* have shown that this approach can be used to successfully describe the electronic structure of the Ce$_2$O$_3$ system.[102–104] However, the DFT+U approach has one major drawback: there is no unique value for the Hubbard U parameter. Moreover, many system parameters are linearly dependent on the value of the U parameter. As a result, different groups have tried to obtain the "optimum" value of U for the CeO$_2$ and Ce$_2$O$_3$ systems.[101, 105, 107] In the following sections, we will follow in their footsteps, and present the influence of the Hubbard U term on several properties of CeO$_2$.

A. Heat of formation

The inclusion of the on-site Coulomb correction, in the form of a Hubbard U term, results in a change of most properties of the system. The total energy increases almost linearly with the size of the Hubbard U term. The increase in the total energy, however, depends on the system studied.[12] As a result, the heat of formation for CeO$_2$, presented in Fig. 3.4, shows a minimum around U= 5 and U= 4 eV for LDA and PBE, respectively. Interestingly, these are also the two values most often presented as the 'optimum' value for U in literature.

---

[12]Within DFT+U, the total energy also depends on the specific choice of the projector function used to define the the Hubbard U functional.[102–104]
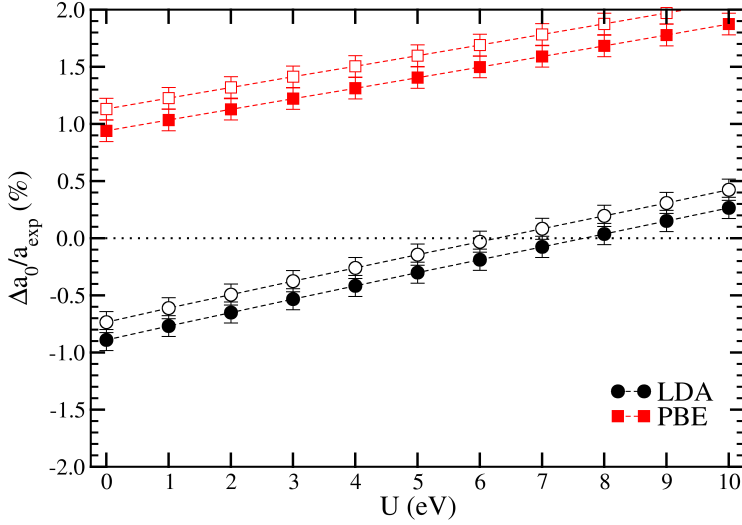
Figure 3.5: *Difference between the calculated lattice parameter a_0 and the experimental lattice parameter $a_{exp}(= 5.411 \text{ Å})$ for CeO$_2$ as function of the Hubbard U parameter. Filled/open symbols indicate the 0K/RT calculated value of the lattice parameter is used. The error bars show the effect of a variation of ± 0.005 Å on the experimental lattice parameter.*

B. Crystal structure

Figure 3.5 shows that with in creasing U, the lattice parameter increases linearly. As a result, the overshoot obtained with the PBE functional becomes worse, while the underestimation obtained from the LDA functional shows a correction toward the experimental value. A perfect reproduction of the experimental lattice parameter is found around U= 6–8 eV for LDA, with the precise value depending on the reference experimental value. In Fig. 3.5, the experimental value is taken to be $a_0 = 5.411$ Å. The error bars are obtained by varying this experimental lattice parameter by ± 0.005 Å. This shows that agreement with experiment can already be found for lower values of U. It is however also important to bear in mind that the experimental lattice parameter is obtained at RT, while the calculated one is at 0 K. For a true comparison of the two, either the theoretical value should be extrapolated to RT or the experimental value should be extrapolated to 0 K. If, for simplicity, we assume the linear thermal expansion coefficient to be independent of the Hubbard U term, then the difference between the calculated and experimental the lattice parameter is given by the open symbol curves in Fig. 3.5. Both for LDA and PBE, the resulting curves show higher values for the lattice parameter, deteriorating the agreement of the PBE values with experiment, while improving those for LDA calculations. In the case of LDA, perfect agreement with the experimental value is now found in the range of U= 5–6 eV, comparable to the position of the minimum in the heat of formation.

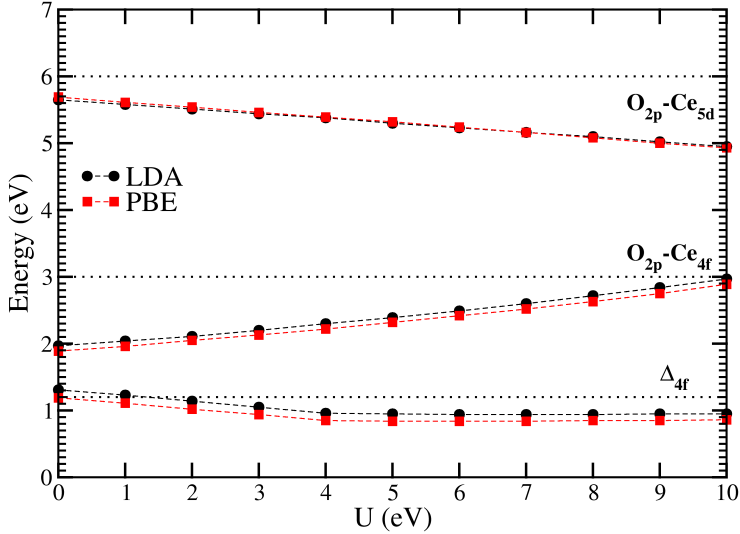**Figure 3.6:** *Size of the O_{2p}–Ce_{4f} and O_{2p}–Ce_{5d} band gaps, and the width of the unoccupied Ce 4f band Δ_{4f} in CeO$_2$. Experimental values are indicated with dotted lines.*

C. Density of states

Also the DOS of CeO$_2$ is modified due to the introduced on-site Coulomb correction. Figure 3.6 shows the evolution of the two band gaps with respect to the Hubbard U term. The O_{2p}–Ce_{5d} band gap clearly decreases, while the unoccupied Ce 4f band moves toward the conduction band. The width of this band, however, changes very little. Experimental values are indicated in the figure as dotted lines. From this, it appears that increasing the Hubbard U term improves the O_{2p}–Ce_{4f} band gap while worsening the O_{2p}–Ce_{5d} calculated band gap. However, it is important to take into account that there are large uncertainties on the experimental values, due to both experimental resolution and the features used to define the gap width. Experimentally, the O_{2p}–Ce_{5d} band gap is suggested to have a width between 5.4 and 8.4 eV, based on X-ray data.[101, 146, 149]. Similarly, a width between 2.6 and 5.8 eV is suggested for the O_{2p}–Ce_{4f} band gap. In these cases, the lower values refer to the edge-to-edge distances, while the higher values point to the distance between peak maxima. Since our calculated values refer to edge-to-edge distances, agreement with the experimental lower boundaries should be sought. This results in good agreement for the O_{2p}–Ce_{4f} band gap at U=$\sim$ 7 eV and for the O_{2p}–Ce_{5d} band gap at U=$\sim$ 4 eV, making U= 5–6 eV a good compromise for both band gaps.

D. Atomic charges

The change in the geometry and the electron distribution is also expected to slightly affect the atomic charges. Using the Hirshfeld-I partitioning scheme (*cf.* **Chapters 7**
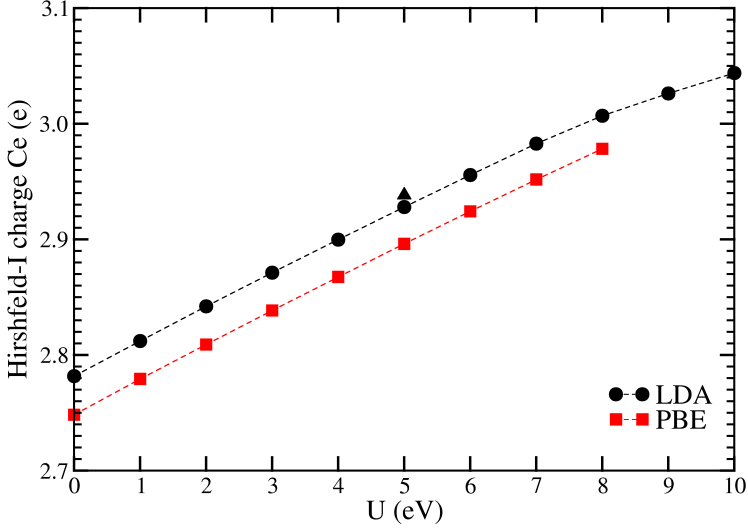
Figure 3.7: *Calculated Hirshfeld-I charges for Ce in CeO₂. Atomic reference densities used for Ce are at U= 0 eV. The triangle indicates the Hirshfeld-I charge for Ce in LDA+U calculations, using atomic reference densities for Ce with U= 5 eV.*

and **8**), we have also calculated the atomic charge[13] on the Ce and O atoms using the CeO₂ electron densities obtained for varying U. As can be seen in Fig. 3.7, the charge on the Ce atom increases roughly linearly with the value of U, at a rate of ∼ 0.026 e/eV. In these calculations, however, the reference atomic densities for Ce are not corrected with a Hubbard U term. The effect of including this correction for the U= 5 eV case for LDA is shown as a solid black triangle in Fig. 3.7. It shows that although there is an effect (an increase of the Ce atomic charge by 0.01e), it remains fairly limited. The oxygen charges on the other hand decrease at half the rate of the increase of the Ce charge, to preserve the charge neutrality of the system.

In conclusion, based on the dependence of the CeO₂ properties on the effective Hubbard U parameter, and the comparison to experimental values for these properties, a more or less general purpose optimum value for the Hubbard U term is U= 5 eV. This is in agreement with the values suggested in several other such studies in the literature.[101, 107, 111, 142]

---

[13]Note that this is will not provide the formal valence of the atoms, although it is shown in **Chapter 8** that non-equivalent atoms can be distinguished as having clearly different charges.

Part II

CeO$_2$ doping

CHAPTER

④

Group IV doping of CeO$_2$: On the tuning of buffer layers and the impact of valence electron character.

From time immemorial, man has desired to comprehend the complexity of nature in terms of as few elementary concepts as possible.
–Abdus Salam (1926 - 1996)

The appearance of microcracks in CeO$_2$ buffer layers, as used in buffer layer architectures for coated superconductors, indicates the presence of stress between this buffer layer and the substrate. This stress can originate from the differences in thermal expansion or differences in lattice parameters between the CeO$_2$ buffer layer and the substrate. In this chapter, the influence of group IV dopants on the lattice parameter and bulk modulus of fluorite CeO$_2$ is studied within the DFT framework. Vegard's law behavior is found for the lattice parameter in systems without oxygen vacancies, and the Shannon crystal radii for the doping elements are retrieved from the lattice expansions. We show that the lattice parameter of the doped CeO$_2$ can be matched to that of the La$_2$Zr$_2$O$_7$ coated NiW substrate substrate for dopant concentrations of about 5%, and that bulk modulus matching is either not possible or would require extreme doping concentrations. Concentration dependent formation energies are calculated for Ce$_{1-x}$M$_x$O$_2$ (M= C, Si, Ge, Sn, Pb, Ti, Zr, Hf) with $0 \leq x \leq 0.25$ and a roughly decreasing trend with ionic radius is observed. The influence of the valence and near valence electronic configuration is discussed, indicating the importance of filled d and f shells near the Fermi level. The influence on the bulk modulus and thermal expansion coefficients is presented. We are able to show that an inverse relation exists between these two properties.

4.1   Introduction

Over the last two decades, interest in ceria based materials has grown dramatically. The facile Ce^{4+} $\longleftrightarrow$ Ce^{3+} redox conversion in combination with the fact that CeO$_2$ retains its fluorite crystal structure even at significant reduction levels makes this an ideal material to control the oxygen atmosphere in three-way catalysts.[47, 50, 54, 55] Furthermore, the introduction of dopants like Zr has been shown to increase the oxygen storage capacity, increasing the range of practical applicability.[78] The remarkable redox properties of CeO$_2$ make ceria based materials also of interest in several

other industrially important applications, such as: catalytic support, thermal barrier coatings, ionic conductors and fuel cells.[46, 56, 67, 80, 150]

More recently, cerium oxide (CeO$_2$) has been used as thin film buffer layer in YBCO coated superconductors (CSC) [41–43, 45, 61, 68]. In an YBCO–CSC architecture, an YBCO thin film is grown on a metallic substrate. To prevent the metal atoms of diffusing into the YBCO, one or more buffer layers are required. In addition, these buffer layers also prevent the oxidation of the metallic substrate during YBCO deposition. Due to its structural compatibility with YBCO, CeO$_2$ is preferred as the top layer in such a multilayer architecture. However, the layer thickness of the CeO$_2$ buffer layer is limited by the formation of cracks during deposition [42, 43]. This phenomenon has been linked to internal stress due to lattice mismatch or different thermal expansion coefficients (TECs) of the substrate and the CeO$_2$ buffer layer [42, 45]. A simple way to reduce the mismatch and stress is through doping [41, 45, 68].

For this and all other applications there is a constant search for ways to improve the properties of ceria based materials ever further beyond the values already inherently present. And for all these applications, one of the most common ways to improve CeO$_2$ is through the introduction of dopants, with regimes ranging from light doping ($< 1\%$) to mixed oxides containing 50% dopants or more.[44, 47] Different applications also require different properties to be optimized, and sometimes an improved property for one application means a worsening for another: *e.g.* for ionic conductors one wishes to maximize the ionic conductivity, while for a buffer layer one often wishes to minimize this property. Such opposing and varying requirements make a more general theoretical study of the influence of dopants on the properties of CeO$_2$ of general interest.

Investigation of the experimental literature shows that lanthanide elements are the most often studied dopants, in addition to standard catalyst *d*-block metals (Au, Pd, Cu, ...).[44, 47, 50, 56, 70, 72, 73, 75, 79, 80, 151–159] Since all these elements are aliovalent dopants, charge compensating vacancies are introduced, contributing to the observed modification of the CeO$_2$ properties. However, to have a clear understanding of the influence dopants have on the properties of CeO$_2$ it is important to first understand the influence of clean dopants without charge compensating vacancies. Due to the tetravalent nature of Ce in CeO$_2$ this makes group IV elements ideally suited for such investigations.

To this date only few authors have investigated group IVa dopants in ceria based materials, although for example silica is a widely used catalyst support.[160, 161] This limited experimental work originates from the difficulty of forming solid solutions with CeO$_2$ in a controlled way. A few groups have attempted to prepare mixed CeO$_2$-SiO$_2$ and CeO$_2$-SnO$_2$ materials, presenting improved redox properties compared to pure and Zr doped CeO$_2$.[160, 162–164] Andersson *et al.* have studied the redox properties of tetravalent dopants at low dopant concentrations of 3% and correlated the reducibility of the doped system with the ionic radius of the introduced dopant.[83, 84]

In this chapter, we study the influence of doping on lattice mismatch and stress using *ab initio* atomistic calculations. Stress due to volumetric changes, which are
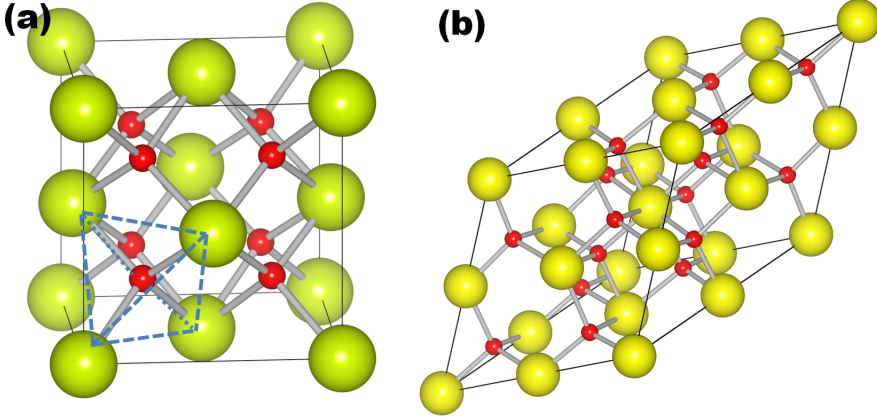
Figure 4.1: *Ball-and-stick model presenting the CeO$_2$ cubic fluorite structure supercells (a) c111 and (b) p222 (cf. text). The big yellow and small red spheres indicate the positions of the Ce and O atoms, respectively. The tetrahedral surrounding of a single O atom is indicated by the tetrahedron for the c111 supercell.*

present during the heating and cooling cycles of the production process, are investigated through the bulk modulus (BM) of the doped systems. Because the CeO$_2$ buffer layer is often grown on a La$_2$Zr$_2$O$_7$ (LZO) buffer layer in multilayer architectures, a match with the LZO BM will reduce the inter-layer stress. The change in the CeO$_2$ lattice parameter is derived directly from the calculated atomic structure, and a match with the LZO lattice parameter is searched for to reduce inter-layer stress due to lattice mismatch.

In **Sec.** 4.2 the details of the different methods are presented. In **Sec.** 4.3.1 the Vegard's law is analytically derived for fluorite type doped CeO$_2$, allowing for atomic radii to be deduced and presented in **Sec.** 4.3.2. We will show there is a clear difference in energetics between group IVa and IVb elements, and link this to the different nature of the valence electrons (**Sec.** 4.3.3–4.3.4). An inverse relation between the bulk modulus and the thermal expansion coefficients will be presented (**Sec.** 4.3.5) and the change in the charge distribution around the dopants will be discussed (**Sec.** 4.3.6).

4.2 Theoretical method

We perform *ab-initio* DFT calculations within the PAW method as implemented in the VASP program using the LDA functional as parameterized by Ceperley and Alder and the GGA functional as constructed by Perdew, Burke and Ernzerhof (PBE)

.[122, 123, 137, 138, 165, 166] Since our focus goes mainly to the mechanical and structural properties of the system this should be sufficient. To be able to assess the influence of the strong on-site Coulomb repulsion among the Ce $4f$ electrons on the electronic properties such as formation energies and the DOS, calculations are also performed within the DFT+U level framework. For this the DFT+U scheme as formulated by Duradev et al.[167] is applied. There have been several DFT+U studies which focused on finding an optimum value for the Hubbard U parameter for ceria.[101, 105, 107, 110] In these studies a value for U of 5–6 and 4–5 eV is suggested for LDA and GGA, respectively. For this reason we have chosen to use U= 5 eV for both LDA+U and PBE+U calculations. The plane wave kinetic energy cutoff is set to 500 eV.

Symmetric supercells, containing a single substituent per supercell are used to simulate homogeneous distributions of the substituents.[1] For all systems the fluorite symmetry (space group $Fm\bar{3}m$) is maintained allowing for easier comparison of the observed trends to the dopant atomic properties. The supercells used are the fluorite cubic $1 \times 1 \times 1$ cell with 12 atoms (c111) (*cf.* Fig. 4.1a), the primitive $2 \times 2 \times 2$ cell with 24 atoms (p222) (*cf.* Fig. 4.1b), the primitive $3 \times 3 \times 3$ cell with 81 atoms (p333) and the cubic $2 \times 2 \times 2$ cell with 96 atoms (c222). Replacing a single Ce atom with a group IV element in these specific supercells results in metal concentrations of $25, 12.5, 3.7037$, and 3.125 %, respectively.

Monkhorst-Pack special k-point grids are used to sample the Brillouin zone.[168] For the two smaller cells we use an $8 \times 8 \times 8$ k-point grid while for the two large supercells a $4 \times 4 \times 4$ k-point grid is used.

To optimize the structures, a conjugate gradient method is used. During relaxation both atom positions and cell-geometry are allowed to change simultaneously. The convergence criterion is set to the difference in energy between subsequent steps becoming smaller than 1.0×10^{-6} eV.

The TEC are calculated as the numerical derivative of V(T) data. These V(T) data in turn are obtained through minimization of the thermal non-equilibrium Gibbs function, which is calculated using the quasi-harmonic Debye approximation, and is implemented as a module in our HIVE code.[169–172] The BM is calculated by fitting $E(V)$ data from fixed volume calculations to the third order isothermal Birch-Murnaghan equation of state.[143, 144]

To calculate the atomic charges of the doped systems, we used the iterative Hirshfeld-I approach.[173, 174] Our implementation makes use of the grid stored (pseudo-) electron density distributions which are standardly obtained from VASP (*cf.* **Chapter** 8). The atom centered spherical integrations are done using Lebedev-Laikov grids of 1202 grid points per shell, and a logarithmic radial grid.[175, 176] The iterative scheme is considered converged when the largest difference in charge of an atom in the system is less than 1.0×10^{-5} electron in two consecutive iterations.

---

[1]In this and the following chapter all substituents are "neutral" (atoms), charged defects (ions) are beyond the scope of this work.

4.3   Results and Discussion

4.3.1   Analytic derivation of Vegard's Law

In metallurgy, Vegard's empirical law states that lattice parameters of alloys can be found as a linear interpolation of the lattice parameters of the compound metals.[177] In this section, we show how a Vegard's law for lattice parameters can be retrieved by assuming the lattice parameter of a material to be directly related to the atomic radii of the compound elements via the geometry of the atomic bonds in the system.

CeO_2 is known to have a cubic fluorite structure (space group $Fm\overline{3}m$). Figure 4.1a shows the c111 supercell. Since every O atom is tetrahedrally surrounded by Ce atoms, the following relation can be derived from the Ce–O bond length:

$$R_O + R_{Ce} = a_{CeO_2} \frac{\sqrt{3}}{4}, \tag{4.1}$$

with R_O and R_{Ce} the atomic crystal radii of O and Ce respectively, and a_{CeO_2} the CeO_2 lattice parameter. For a cubic system, this allows us to calculate the atomic crystal radius R_M of a Ce substituent M via:

$$R_M = \left(\frac{\sqrt{3}}{4} a_{M_x Ce_{1-x} O_2} - R_O - (1 - n_x) R_{Ce} \right) / n_x \tag{4.2}$$

with $a_{M_x Ce_{1-x} O_2}$ the lattice parameter of the doped system and n_x the dopant concentration. The lattice parameter of the doped system can now be found by combining Eqs. (4.1) and (4.2):

$$a_{M_x Ce_{1-x} O_2} = a_{CeO_2} + \left(\frac{4}{\sqrt{3}} (R_O + R_M) - a_{CeO_2} \right) n_x. \tag{4.3}$$

This results in a clear linear relation between the lattice expansion/contraction of CeO_2 and the dopant concentration n_x which is known as Vegard's empirical law [177]. These analytical results show Vegard's law behavior should be expected when the dopants are homogeneously distributed in CeO_2 in case of tetravalent dopants, but also for non-tetravalent dopants this behavior should be expected under oxidizing conditions.

Although Eqs. (4.2) and (4.3) can be derived from one another, the latter is more interesting from the experimental point of view, since lattice parameters and concentrations are readily available while atomic radii are not. Values for the two radii R_O and R_M can be taken from tabulated values for atomic radii. This, however, can be problematic since there are several different definitions for 'atomic radius' available, giving values which can easily differ 20%.[2] In light of this problem, Eq. (4.2) becomes interesting. It could tell us which definition of atomic radius to use for the doped CeO_2 systems. This would allow one to predict the Vegard's law behavior for any doped CeO_2 system prior to its synthesis.

---

[2]*E.g.* for oxygen one finds the calculated atomic radius to be 0.48 Å while the empirical atomic radius is given to be 0.60 Å [178, 179].

Table 4.1: *Dopant radii calculated using Eq. (4.2), averaged over the four dopant concentrations (avg), and standard deviation (stdev) of this value. This is done for both LDA and PBE calculated geometries. The Shannon crystal radii for the 8-coordinated tetravalent atoms R_{sh}^8, taken from Ref. [180], are shown in comparison. a_0 and b are the intercept and slope of the Vegard's law linear fit to the calculated geometries for doped CeO₂ systems. The lattice parameter calculated for pure CeO₂ and La₂Zr₂O₇ (LZO) are given as reference.*

| | R_M (Å) | | | | R_{sh}^8 | Vegard's Law | | | |
| | LDA | | PBE | | | LDA | | PBE | |
	avg	stdev	avg	stdev	(Å)	a_0(Å)	b	a_0(Å)	b
CeO₂ LZO	1.0819[a]	0.0001	1.1257[a]	0.0004	1.11	5.3623[b] 10.6923[c]		5.4629[b] 10.8906[c]	
C	0.9243	0.0137	1.0096	0.0130	—	5.3656	−0.4161	5.4657	−0.3077
Si	0.7951	0.0052	0.8321	0.0044	—	5.3626	−0.6688	5.4643	−0.6936
Ge	0.8786	0.0031	0.9270	0.0034	—	5.3618	−0.4640	5.4631	−0.4578
Sn	0.9764	0.0020	1.0199	0.0049	0.95	5.3618	−0.2383	5.4629	−0.2400
Pb	1.0686	0.0034	1.1293	0.0042	1.08	5.3612	−0.0174	5.4633	0.0050
Ti	0.8421	0.0043	0.8862	0.0050	0.88	5.3629	−0.5640	5.4644	−0.5706
Zr	0.9548	0.0019	0.9791	0.0052	0.98	5.3622	−0.2938	5.4634	−0.3409
Hf	0.9205	0.0023	0.9612	0.0056	0.97	5.3622	−0.3733	5.4635	−0.3849

[a] The Ce radius is calculated using Eq. (4.1), where the 4-coordinated Shannon crystal radius for oxygen is taken as 1.24 Å [180].

[b], [c] The actual lattice parameter as calculated from the pure, relaxed geometries of CeO₂ and LZO. Note that the LZO lattice parameter is double the CeO₂ lattice parameter.
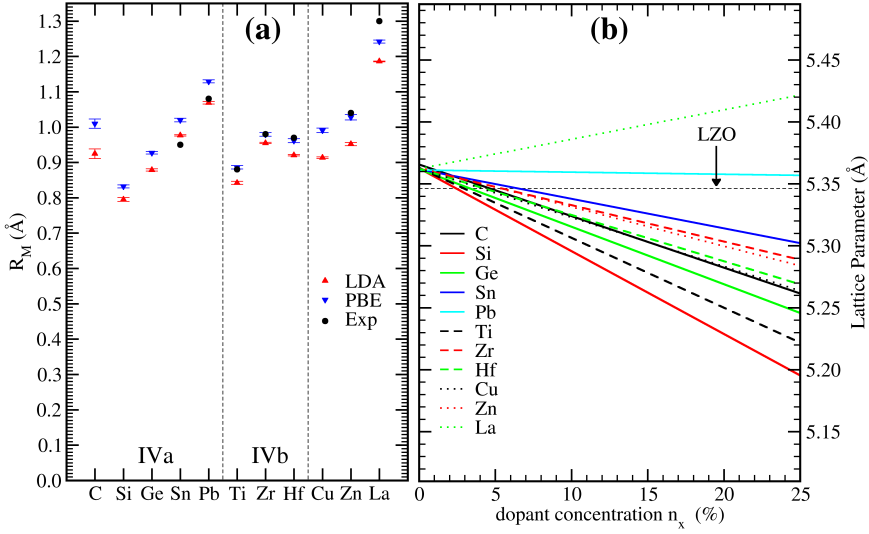
Figure 4.2: *(a) The dopant radii calculated using Eq. 4.2 for both the LDA and PBE results. The standard deviation is shown as error bars, and, where available, the experimental Shannon crystal radii R_{sh}^8 (cf. Table 4.1) are shown as reference. (b) The lattice parameter as function of the dopant concentration, calculated using Eq. 4.3. Only the LDA results are shown. The LZO half lattice parameter is shown as reference.*

4.3.2 Lattice parameter and Vegard's law

Using Eq. (4.2) we have calculated the atomic crystal radius for each of the four concentrations for each group IV element. The average values and their standard deviations are shown in Table 4.1 and Fig. 4.2a. In these calculations we have used the Shannon crystal radius for four-coordinate O^{2-}; $R_O = 1.24$ Å.[3] The radius of eight-coordinate Ce^{4+} is calculated from the non-doped CeO_2 system using Eq. (4.1) and shows very good agreement with the Shannon crystal radius for eight-coordinate Ce^{4+}[180, 181]. For the group IV elements, the LDA and PBE calculations show the same relative trends, with the PBE values always slightly larger than the LDA ones, as one would expect. Due to the underbinding nature of GGA functionals such as PBE and the overbinding nature of LDA, we expect the LDA and PBE values to be a slight under- and overestimation of the actual crystal radius, respectively. Comparison of the calculated dopant radii to the Shannon crystal radii for eight-coordinated tetravalent atoms R_{sh}^8 shows a very good correlation. This indicates that the *Shannon crystal radius* is an excellent parametrization to predict the lattice expansion of

---

[3]Note that for lower O coordination, the Shannon crystal radius is only slightly smaller (two- and three-coordinate O^{2-}; $R_O = 1.21$ and $R_O = 1.22$ Å, respectively), such that the assumption of a constant O radius is a reasonable one to make.

doped CeO$_2$.

Based on lattice parameters obtained from the *ab initio* calculations for the different dopant concentrations, a fitting of Vegard's law is done for each of the group IV elements. Table 4.1 shows the intercept a_0 and the slope b of this linear fitting. For the LDA results, the fitted curves of the lattice parameter as function of the dopant concentration n_x are shown in Fig. 4.2b. With the exception of Pb, all systems show a nearly perfect fit, with correlation coefficient (R^2) values better than 0.99 for both LDA and PBE calculations. The poor fit of Pb is related to the negligible expansion of the lattice. As a result, small deviations can transform an expansion into a contraction going from one concentration to the next. A zero expansion can thus be assumed for Pb doping. The high quality of the other linear fits, with intercepts that are within 0.01 Å of the CeO$_2$ lattice parameter, shows that the analytically obtained Vegard's law is a good model for the lattice expansion in these doped systems.

Both LDA and PBE results show the same qualitative behavior, and the optimum substitution concentrations, for lattice parameter matching with LZO, are $\sim 5\%$ for all group IV elements, with, due to its negligible contraction, the exception of Pb substitution.

4.3.3   Formation energies

The stability of the different group IV substitutions in fluorite CeO$_2$ is investigated through the comparison of the defect formation energies E$_f$, which is calculated as:

$$E_f = E_{Ce_{1-x}M_xO_2} - E_{CeO_2} + N_{df}(E_{Ce} - E_M), \qquad (4.4)$$

with $E_{Ce_{1-x}M_xO_2}$ the total energy of the doped system, E_{CeO_2} the total energy of a CeO$_2$ fluorite supercell of equal size, E_{Ce} and E_M the energy per atom of bulk α-Ce and the bulk phase of the substituent element M, respectively.[4] N_{df} is the number of substituent atoms in the system. Positive values indicate the amount of energy required to substitute a Ce atom by a group IV element atom.

Table 4.2 shows the formation energies of the different systems at different concentrations. As can be seen from this table, the formation energies vary only slightly with the substituent concentration showing that within the given ranges no solubility limits are being crossed. For supercells with a dopant concentration of 3.125% formation energies are also calculated within the DFT+U framework. For this, a static self consistent calculation is performed using the LDA/PBE optimized geometry and a Hubbard U= 5 eV for the Ce f electrons. As can be seen in Table 4.2 for all systems the formation energies become slightly larger in the DFT+U framework. This, however, does not change the relative stability of the systems, showing that the qualitative results obtained from the pure LDA/PBE calculations are maintained.

For different substituent elements the formation energies show a spread over quite a large range, with roughly 20 eV/atom required to imbed a C atom, down to the

---

[4]Pure Ce metal has several different phases depending on the external pressure and temperature. In our case we chose to use the α-phase, since the calculations are performed at zero temperature and pressure.

Table 4.2: *Formation energy* E_f *for doped* CeO_2 *at different dopant concentrations. For the DFT+U calculations a Hubbard U= 5 eV was chosen both for the LDA and PBE calculations.*

	E_f (eV)				
	25%	12.5%	3.704%	3.125%	3.125%
			LDA		LDA+U
CeO_2			-11.484[a]		–
$La_2Zr_2O_7$			-42.421[a]		–
C	20.424	20.643	20.736	20.737	21.077
Si	8.288	8.078	8.050	8.052	8.358
Ge	9.404	9.134	9.110	9.105	9.341
Sn	7.061	6.866	6.851	6.851	7.013
Pb	8.963	8.757	8.742	8.745	8.866
Ti	3.168	3.254	3.248	3.233	3.563
Zr	0.530	0.555	0.548	0.543	0.796
Hf	0.105	0.139	0.131	0.128	0.392
			PBE		PBE+U
CeO_2			-10.418[a]		–
$La_2Zr_2O_7$			-38.253[a]		–
C	19.819	20.022	20.086	20.099	20.275
Si	8.737	8.547	8.530	8.562	8.764
Ge	9.495	9.257	9.242	9.254	9.386
Sn	7.129	6.967	6.962	6.960	7.031
Pb	8.960	8.788	8.777	8.780	8.812
Ti	3.454	3.526	3.524	3.532	3.740
Zr	0.851	0.884	0.885	0.883	1.033
Hf	0.484	0.517	0.517	0.517	0.666

[a] Instead of the formation energy the heat of formation is given.

mere 0.1 eV/atom required to add a Hf atom. This shows that none of the group IV elements will increase the stability of CeO_2. However, since doping experiments are not performed at zero Kelvin and zero atmosphere, and often involve steps which will release additional energy into the system, we can assume that the doping process can profit from this, and as a result metastable doped systems become available. Because of the large range in energies shown in Table 4.2 we still need a reference energy to decide which dopants are more favorable than others. As such a reference, the formation energy for O vacancies in a CeO_2 cubic fluorite is considered. From experiment it is known that these vacancies form "spontaneously" in CeO_2.[47] This allows us to assume that substitutions requiring the same amount of energy or less should be considered more likely while those requiring more energy less likely. For the LDA and PBE functionals we calculated the O vacancy formation energy to be

Table 4.3: *Size of the $Ce_{1-x}M_xO_2$ (with $x = 0.03125$) band gaps between the O 2p and Ce 4f bands and between the O 2p and Ce 5d bands (cf. Figs. 4.3 and 4.4). The position of the gap state (gs) with regard to the valence band edge is given for the group IVa elements (s state), and the group IVb elements (d state). All values are given in eV.*

	LDA+U			PBE+U		
	2p–4f	2p–5d	gs	2p–4f	2p–5d	gs
CeO$_2$	2.45	5.35	–	2.37	5.35	–
C	2.26	5.18	−0.17	2.12	5.14	−0.21
Si	2.14	5.11	3.87	2.06	5.10	3.62
Ge	2.24	5.16	1.80	2.18	5.19	1.67
Sn	2.30	5.25	3.88	2.22	5.26	3.65
Pb	2.38	5.29	1.79	2.29	5.29	1.61
Ti	2.36	5.02	4.18	2.27	5.05	3.82
Zr	2.42	5.19	4.63	2.33	5.19	4.44
Hf	2.41	5.48	5.37	2.32	5.43	5.25

4.035 and 3.097 eV per vacancy, respectively, at a vacancy concentration of 1.5625%, in excellent agreement with values found in literature.[5][83] For higher O vacancy concentrations higher formation energies are found, up to 5.006 and 4.145 eV for LDA and PBE respectively, at 12.5%, which is within the range of experimentally derived values.[182]

Based on these reference energies the results in Table 4.2 nicely split up the group IV elements in the groups IVa, which have a higher formation energy, and IVb, which have an equal or lower energy, making the latter group better suited for substitution or oxide mixing experiments. This agrees with the observation that Zr-doped CeO$_2$ is widely used and easily produced in experiments, while it is much harder to form Si and Sn doped CeO$_2$ in a controlled way.[160, 162–164]

Both groups show a generally decreasing trend in the formation energy with increasing atomic number, which could be related to a better match in size with Ce and the resulting reduced strain on the system (*cf.* previous section). The oscillations in the trend of the formation energy for the group IVa elements is interesting, and is retained even with the introduction of the Hubbard U correction. The slight increase in the formation energy for Ge and Pb coincides with the introduction of a 'new' filled shell, the d shell in case of Ge, and the f shell in case of Pb. This shows that not only the pure valence electrons play a role in the stability of the system but also the presence of filled shells near the Fermi level.

---

[5]Comparing the 4.035 eV found for pure LDA to the 3.61 eV for LDA+U presented by Andersson *et al.*, shows that the introduction of a Hubbard U term will not have a qualitative influence on the stability difference observed for the group IVa and IVb dopants. Note however that the pure LDA value is closer to the experimental value of 4.65–5.00 eV for bulk reduction.[83, 182]
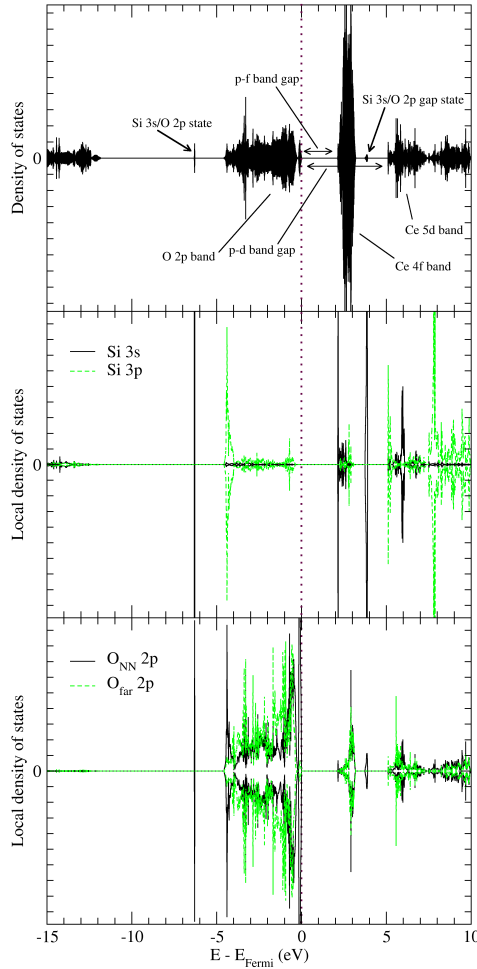
Figure 4.3: *The total* DOS *for* $Ce_{0.96875}Si_{0.03125}O_2$, *indicating important features (top). The* $3s$ *and* $3p$ *Si* local density of states, *showing the origin of the gap state and atomic state below the O* $2p$ *band (middle). The* $2p$ *O* local density of states *for the 8 nearest neighbor (NN) O atoms surrounding the Si dopant, and a O atom far away from the dopant (bottom). The upper and lower panels present the spin up and spin down channels, respectively.*
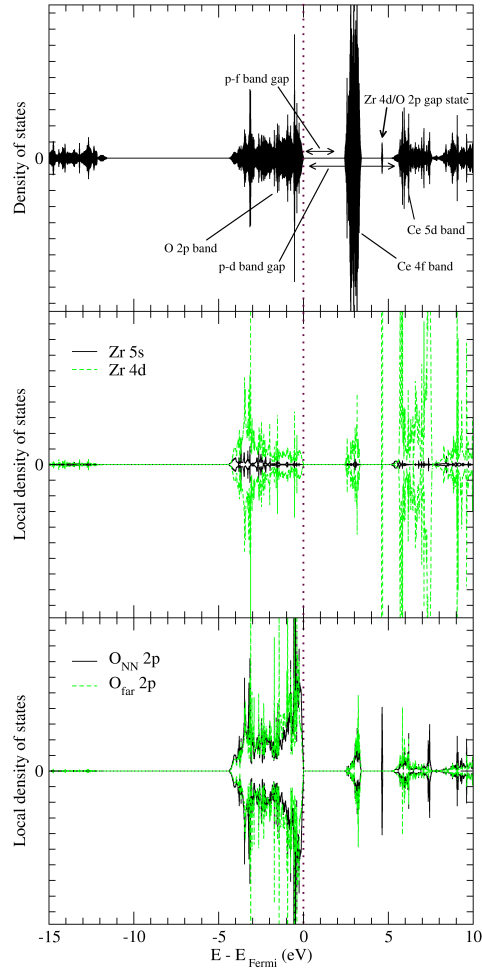
Figure 4.4: *Similar as Fig. 4.3, but this time for* $Ce_{0.96875}Zr_{0.03125}O_2$.

4.3.4 Density of states

We investigated the contribution and influence of the dopants on the DOS of $Ce_{1-x}M_xO_2$ within the DFT+U framework at low dopant concentration $x = 3.125$ %. Due to the low concentration, the general shape of the DOS is comparable to the DOS of pure CeO_2. There is a conduction band of unoccupied Ce $4f$ states in the band gap between the O $2p$ valence band and Ce $5d$ conduction band. Table 4.3 shows that the band gap between the unoccupied Ce $4f$ states and the O $2p$ valence band is always smaller than is the case for pure CeO_2. Excluding C, we find for both the group IVa and IVb dopants an increase in the gap size with the atomic number (within each group). The same behavior is also observed for the O $2p$ – Ce $5d$ band gap, and the trends are independent of the functional used. In case of the group IVa elements, there is an atomic band roughly 2 eV below the O $2p$ band (*e.g.* Fig. 4.3). From the local DOS (LDOS) it is clear that this localized state is a combination of the dopant s state and the O $2p$ state of the O ions surrounding the dopant. This is clearly shown for Si doping in Fig. 4.3, and agrees well with the work of Andersson *et al.*[83] where a symmetry broken configuration was studied. In contrast to that work we also observe such a localized combined state in the $2p$–$5d$ band gap (*cf.* Fig. 4.3).[6] Closer investigation reveals that both bands each integrate to two electrons, indicating that this is a pair of bonding and anti-bonding states. Table 4.3 shows the position of these gap states with regard to the valence band edge. This shows that only for C doping this state is occupied and is located at the edge of the valence band (hence the negative value). For the other IVa elements the band is either located above or below the unoccupied Ce $4f$ band. The relation between these gap states and the atomic state below the O $2p$ valence band becomes even more clear due to the strong correlation of their position, placing the atomic states for the Ge and Pb doped systems roughly 0.7 eV below those of the Si and Sn doped systems.

In the LDOS of the heavier group IVa elements also filled d and f states near the Fermi level are observed, in line with the behavior expected from the calculated formation energies, gap state positions and mechanical properties (*cf.* **Sec.** 4.3.5).

For the group IVb elements no atomic state below the O $2p$ valence band is present, only a gap state above the unoccupied Ce $4f$ band is observed (*e.g.* Fig. 4.4). This state moves toward the Ce $5d$ band, with increasing ionic size of the dopant (*cf.* Table 4.3). For Ti and Zr dopants the band integrates to 6 and 4 electrons, respectively. For the Hf dopant the band already slightly overlaps with the Ce $5d$ band allowing us only to estimate a value in the same range as found for Ti and Zr. Just as for the IVa elements, this localized state is a combination with O $2p$ states of the O ions surrounding the dopant, as is shown for Zr in Fig. 4.4.

In addition, also a superficial investigation of the DOS and LDOS of the systems

---

[6]To investigate this discrepancy the LDOS for a symmetry broken configuration $(Ce_{0.96875}Si_{0.03125}O_2)$ was calculated. With the exception of the Ce $4f$ gap state, due to the presence of an oxygen vacancy in the structure of Andersson *et al.*, we obtained qualitatively the same LDOS as was reported by these authors.[83] This indicates that our observed s–p gap state originates from the different chemical environment for the Si dopant. However, it remains unclear to us if this state simply vanished upon symmetry breaking, or merely merged with the Ce $5d$ band.

Table 4.4: *Calculated* BM B_0 *for* CeO_2 *at a dopant concentration of* 25%, *for* LDA *and* PBE *calculations. The linear* TEC α *at the same dopant concentration and a temperature of* 500 *K. The full* TEC *curves are shown in Fig.* 4.5.

	B_0 (Mbar)		α (10^{-6}K^{-1})	
	LDA	PBE	LDA	PBE
CeO_2	2.017	1.715	11.218	12.955
$La_2Zr_2O_7$	1.774	1.542	11.313	12.551
C	1.528	1.235	16.287	20.379
Si	2.057	1.738	12.335	14.994
Ge	1.909	1.573	14.390	18.454
Sn	2.004	1.692	12.157	14.357
Pb	1.845	1.516	14.006	17.715
Ti	2.145	1.825	11.195	12.971
Zr	2.153	1.878	10.960	12.212
Hf	2.194	1.881	10.652	12.146

with high dopant concentrations was performed. This was done within the DFT framework. Also here it is found that the introduction of dopant elements with filled d and f shells gives rise to states just below the Fermi-level. In contrast to the low concentration results, the $2p$-$4f$ band gap, between the O $2p$ and Ce $4f$ states is much reduced for the group IVa dopants (except C). This is mainly due to the presence of s conduction states of these elements, and we expect this to be extensions of the gap states observed for low concentrations. Furthermore, the position of the maximum of these s bands in the band gap appears correlated with the calculated formation energies. Comparison to the behavior of the DOS and LDOS of the group IVb doped systems, shows that the $2p$-$4f$ band gap is retained in the latter. Also the unoccupied Ce $4f$ band contains a significant contribution of the d-state of the group IVb elements. The more closely related LDOS of the group IVb dopants to the Ce LDOS, may be an important factor in the clearly better stability of these elements. In addition, the correlation between the closure of the $2p$-$4f$ band gap with s states and the system formation energy appear to indicate either that this band gap is somehow crucial for the stability of the system, or that the presence of s states near the Fermi-level is detrimental for its stability (as is also found for the low concentration calculations).

4.3.5 Thermal expansion coefficients and bulk moduli

Figure 4.5 shows the linear (α) and volumetric (β) TEC for each of the group IV elements. To reduce the computational cost, substituent concentrations of 25% are used. Again the group IVa and group IVb elements can be clearly distinguished.
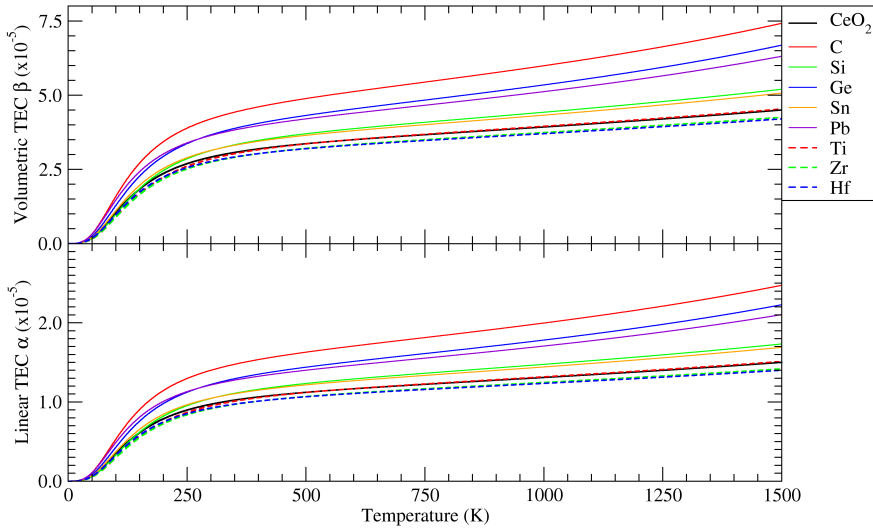
Figure 4.5: *Volumetric (top) and linear (bottom) TECs for LDA calculations. Dopant concentrations of 25% are used.*

Where the former result in a significant increase of the TEC, the latter result in a status quo or a very small decrease of the CeO_2 TEC.

Since both the TEC and the BM give a measure of how easily a material deforms under external conditions, we compare the calculated linear TEC at 500 K and the calculated BM of the doped CeO_2 in Table 4.4. As a general trend, doping of CeO_2 using group IV elements only has a small influence on the system BM (C being an exception). Note that for the BM presented here a dopant concentration of 25% is used, much more than the concentrations used in most doping experiments, so even smaller changes in the BM would be present in these experiments. Also note that for the group IVa elements, the same modulated behavior is encountered as is for the formation energies. This again shows the importance of the presence of filled shells near the Fermi-level. For the group IVa elements presented here, either the introduction of a filled d or f shell near the Fermi-level or the gap states in the O $2p$ – Ce $4f$ band gap reduces the resistance to compression (*i.e.* BM).

Comparison of the BM and TEC in Table 4.4 shows that for the group IVb elements opposite trends are present. Careful investigation of the BM and TEC of the group IVa elements shows a similar behavior. A reasonable increase in one is linked to a reasonable decrease in the other. Upon closer investigation one notices that this behavior seems not exact, since the relative positions of Si and Sn appear reversed, as do those of Ge and Pb. Examining the TEC curves presented in Fig. 4.5 shows that around 250 K the order of the Si and Sn curves switches (the same for Ge and Pb), restoring the opposite behavior of the TEC and BM for the group IVa elements at lower temperatures. Because the BM is calculated at zero temperature we can

Table 4.5: *Calculated Hirshfeld-I atomic charges for Ce$_{1-x}$M$_x$O$_2$ with x = 3.125% using LDA charge density distributions. All values are in e. The first column gives the atomic charge of the dopant M. With regard to the dopant atom the shell of nearest and next nearest neighboring atoms (NN and NNN) consist entirely of O and Ce, respectively. The atomic charges of these atoms are compared to the charges of O and Ce atoms at a longer distance (indicated as 'far').*

	M	O		Ce	
		NN	far	NNN	far
CeO$_2$	−	−1.408		2.806	
C	0.941	−1.171	−1.406	2.792	2.809
Si	2.297	−1.295	−1.411	2.787	2.813
Ge	2.327	−1.313	−1.410	2.793	2.811
Sn	2.638	−1.369	−1.409	2.803	2.809
Pb	2.489	−1.359	−1.408	2.803	2.808
Ti	2.653	−1.367	−1.410	2.801	2.811
Zr	2.974	−1.421	−1.409	2.809	2.809
Hf	3.029	−1.416	−1.394	2.803	2.801

assume the trend of the opposite behavior to be a general one. This is also in perfect agreement with expectancy, since the BM is a measure of the resistance of a material against uniform compression/expansion, it stands to reason that a large BM will lead to a small TEC. In addition, it is, on the one hand, well known that both the BM and cohesive energy correlate to the melting temperature, implying that the BM and cohesive energy correlate with each other as well.[183] On the other hand, the linear TEC α and the cohesive energy show an inverse correlation,[184] implying the above observed inverse correlation between the BM and linear TEC α.

If we assume the BM to behave linearly with regard to the dopant concentration (*cf.* **Chapter** 5), then it is possible to estimate the optimum dopant concentration which would result in a perfect matching of the BM of the doped CeO$_2$ and LZO. For the elements of group IVb, table 4.4 shows a BM which is larger than that of CeO$_2$. This makes BM matching with La$_2$Zr$_2$O$_7$, which has a smaller BM, impossible. In addition, the BM seems to increase very slightly with increasing atomic number. The group IVa elements show a more complex behavior. With the exception of Si, all group IVa elements lower the BM of CeO$_2$. However, the effect is generally too small to allow for a BM matching at reasonable dopant concentrations. In case of the IVa elements, the BM is lowered with the introduction of every newly filled shell (d for Ge and Sn, and f for Pb), while it increases with increasing atomic radii. Combining the results of the groups IVa and IVb shows that not only the valency electrons but also electrons in filled shells near the Fermi level play a crucial role for the BM.

4.3.6   Atomic charges and charge transfer

The introduction of dopants in CeO_2 will not only influence the electronic structure at the level of bands and the density of states, but also at the level of the local charge density distribution. To investigate this effect we calculate the atomic charges in the doped systems using the Hirshfeld-I method (*cf.* **Chapter** 8).[173, 174] Table 4.5 shows the calculated charges on the dopant elements. The charge of the O and Ce atoms in pure CeO_2 is shown as reference.

For all dopants a small increase of the dopant charge with the dopant concentration is observed. Increasing the dopant concentration from 3.125% to 25% the atomic charges of the dopants show an increase of no more than $0.05e$, which is a first indication that the influence of the dopants on the electron density distribution is quite localized. Of all atoms, mainly the atomic charge of the nearest neighbor O atoms is influenced. The atoms furthest removed from the dopant in the c222 supercell show atomic charges which differ only slightly from those in pure CeO_2. The atomic charges of the next nearest neighboring Ce atoms already shows very little influence due to the presence of the dopant.

Although all dopants are tetravalent the atomic charges vary significantly. The difference in atomic charge of the dopants and Ce is almost entirely compensated by the change in atomic charge on the nearest neighbor O atoms, showing that even the nearby O-Ce bonds should be barely affected by these dopants. For all group IV elements the amount of non-compensated charge is less than $0.05e$ per O atom in the nearest neighbor shell.

Of all dopants, the results for C stick out, and may be an indication of the much weaker bonds of the C atom with the surrounding O atoms than the other dopants, which would be in agreement with the fact that the small C atom prefers short bonds[7]. Note that even in this case the effects remain localized to the C dopant and the surrounding O atoms in the nearest neighbor shell.

Based on this and the results shown in Table 4.5 it is clear that group IV dopants will not give rise to any serious charge transfer toward or away from the dopant beyond the nearest neighbor shell.

4.4   Conclusion

Using *ab initio* DFT calculations we have investigated the influence of tetravalent doping on the properties of fluorite CeO_2. Based on the calculated defect formation energies we conclude that Ce-substitution with group IVa elements is rather unlikely, while group IVb should be good substituents, and thus ideal for tuning the CeO_2 fluorite lattice. This qualitative result is shown to be independent of the used functional and Coulomb correction.

Investigation of the DOS and LDOS for both high and low dopant concentrations shows that the presence of states in the O $2p$–Ce $4f$ band gap are detrimental for

---

[7]The small size of C (Shannon crystal radius of 0.29(0.3)Åfor four (six) coordinated C) might make it very suited as an interstitial dopant, which is an interesting scenario for a study focussing on C doping of CeO_2.

the system. Low dopant concentration calculations show that group IVa dopants introduce localized gap states due to the overlap of their valence s states with the O $2p$ states of the surrounding O atoms. These gap states are connected to occupied atomic states below the O $2p$ band. In case of the IVb elements the gap state is always located above the unoccupied Ce $4f$ band resulting in a much reduced influence on the CeO_2 properties.

Comparison of the BM and the TEC shows that an inverse relation between these properties exists. Also here, group IVa and IVb elements differentiate, with group IVb elements resulting only in a slight increase of the BM, while a decrease in the BM is observed for group IVa dopants.

The influence of group IV dopants on the charge distribution of the systems are very limited, and it is shown that no serious charge transfer is taking place beyond the shell of nearest neighbor atoms around the dopant, though significant changes may be observed there.

Throughout all the results presented, the impact of the filled d and f shells located near the Fermi level is observed. As a result, going through the series of IVa elements shows oscillations in the general trends which coincide with the introduction of a new shell. This shows that to have a general understanding of the influence dopants have on a material, not only the purely valence electrons play a role, but also filled shells can promote significant modifications of the expected results.

With regard to lattice and bulk modulus matching of doped CeO_2 to $La_2Zr_2O_7$ it is shown that optimum dopant concentrations for lattice matching appears to be about 5%. For the group IVb dopants it is shown that the bulk modulus slightly increases, while group IVa dopants lead to a decrease. This decrease, however, is insufficient to obtain bulk modulus matching at concentrations comparable to those found for lattice parameter matching with $La_2Zr_2O_7$.

⑤

Aliovalent Doping of CeO$_2$: DFT-study of Valence and Vacancy Effects.

Simplicity is a great virtue but it requires hard work to achieve it and education to appreciate it. And to make matters worse: complexity sells better.

–Edsger Wybe Dijkstra (1930 - 2002)

The modification of the properties of CeO$_2$ through aliovalent doping are investigated within the *ab initio* density functional theory framework. Lattice parameters, dopant atomic radii, bulk moduli and thermal expansion coefficients of fluorite type Ce$_{1-x}$M$_x$O$_{2-y}$ (with M= Mg, V, Co, Cu, Zn, Nb, Ba, La, Sm, Gd, Yb, and Bi) are presented for dopant concentrations in the range $0.00 \leq x \leq 0.25$. The stability of the dopants is compared and discussed, and the influence of oxygen vacancies is investigated. It is shown that oxygen vacancies tend to increase the lattice parameter, but strongly decrease the bulk modulus. Defect formation energies are correlated with calculated crystal radii and covalent radii of the dopants, but are shown to present no simple trend. The previously observed inverse relation between the thermal expansion coefficient and the bulk modulus is shown to persist independent of the inclusion of charge compensating vacancies.

5.1 Introduction

Cerium oxide based materials have been receiving increasing attention during the last decades. Since 2007 about 1000 peer reviewed journal articles a year have appeared containing ceria as a topic. The interest in these materials is due to their versatile nature in industrial applications, which generally originate from the remarkable oxidation and reduction properties of CeO$_2$. The major fraction of the investigations of ceria based materials are linked to solid oxide fuel cells and catalysis.[47–51, 54, 56, 77, 91, 93, 112, 185] In case of the latter, these materials play both the role of catalyst support and catalyst. In addition to being used in automotive three-way catalysts (TWC) and in water-gas-shift reactions, ceria based materials are also used as oxygen sensors, thermal barrier coatings and much more.[48, 50, 57, 58, 73] Recently, CeO$_2$ and doped CeO$_2$ have been used as buffer layers for thin film YBa$_2$Cu$_3$O$_{7-\delta}$ coated superconductors.[41–43, 45, 61, 67, 68]

In experiments, ceria based materials have been doped with many different types of elements.[44, 47] These experiments also show different dopant elements to have

different effects on different properties. Furthermore, based on the application of interest, dopant concentrations can vary from $< 1\%$ up to mixed oxides where dopant concentrations of 50% and more are used. In addition, also the preparation methods vary greatly (*e.g.* combustion synthesis, chemical and physical vapor deposition, sol-gel deposition *etc.*), influencing the investigated properties.[72, 186] In contrast to all this variation, ceria based materials generally tend to have the same structure (more specifically fluorite), adding to their usefulness for general applications.

Although the body of theoretical work on ceria is smaller than the amount of experimental work published, it remains quite impressive. Much of this work focusses on a single aspect of a single application, often investigating the effect of a single dopant element.[88, 91–93, 185, 187, 188] Investigations of series of dopant elements are much less frequent, and with only few exceptions almost exclusively focus on the lanthanide series.[88, 89, 95, 189] This is mainly due to the fact that this series (or elements from it) is also the most often investigated in experiments. Recently, also the series of tetravalent/group IV elements have been investigated by means of *ab initio* calculations. Where Andersson *et al.* focused on the ionic conductivity properties of oxygen vacancies for tetravalent dopants in CeO_2, present authors investigated the stability and influence of group IV dopants on mechanical and structural properties of CeO_2 (*cf.* **Chapter** 4).[83, 84, 190, 191]

With the large variety of applications comes a large variation of the required properties. Where, for example, a good solid oxide fuel cell should present high ionic conductivity, a good buffer layer should minimize it. Alternately, lattice matching through doping of a buffer layer requires a homogenous distribution of the dopants in the bulk of the material, while doping of a catalyst often benefits from dopants residing at the surface.

Because of this, we will refrain from focussing on one specific application in this work, and present general trends instead. This chapter expands on the previous chapter through the study of aliovalent dopants, and the introduction of charge compensating vacancies.[1] For practical reasons we have limited our work to a subset of the aliovalent dopants investigated in experimental work: Mg, V, Co, Cu, Zn, Nb, Ba, La, Sm, Gd, Yb, and Bi.[41, 44–47, 55, 56, 66, 67, 70, 71, 73, 75, 76, 80, 81, 152, 154, 155, 157–159, 192–200]

In this chapter, we show that the inverse relation between the bulk modulus (BM) and thermal expansion coefficient (TEC) persists for aliovalent dopants with and without charge compensating vacancies. Furthermore, dopant radii are calculated

---

[1] It is at this point important to note that all the systems under study in this work are charge neutral from the electronic point of view, *i.e.* there are as many positive as negative charges in each cell. As such the term "charge compensating vacancy" and reference to it by the use of terms like "charge compensation" may be considered confusing. The terminology, however, originates in the study of ionic conductivity. There, the substitution of one cation by another will, when using the Kröger-Vink notation, always indicate the change in valence at the substitution site as a charge on the substituent element. For example, if MgO is dissolved in CeO_2, tetravalent Ce is substituted by divalent Mg, wich in Kröger-Vink notation can be written as:[53]
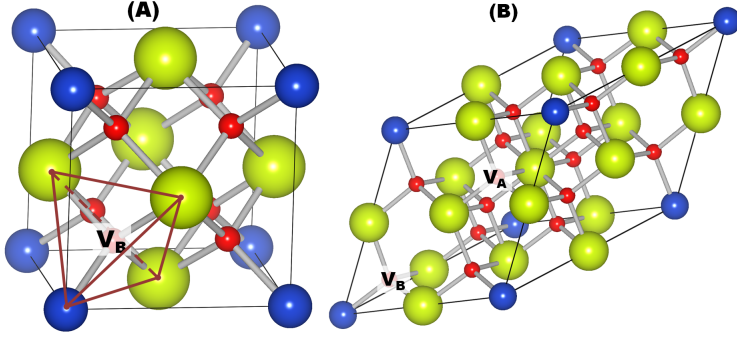
$$MgO \xrightarrow{\;CeO_2\;} Mg''_{Ce} + O^\times_O + V^{\bullet\bullet}_O.$$
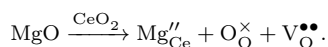
Figure 5.1: *Ball-and-stick representations of doped CeO$_2$ c111 (a) and p222 (b) supercells. Yellow (red) spheres indicate the positions of the Ce (O) atoms, while the dopant position is given by the blue sphere. Vacancy positions are indicated (V$_A$ and V$_B$), as is the surrounding tetrahedron (red lines).*

to be in good agreement with Shannon crystal radii. It is also shown that the introduction of charge compensating vacancies has a beneficial influence on the defect formation energy, albeit insufficient to stabilize unstable dopants such as Zn, Cu or Co. The introduction of charge compensating vacancies is shown to have a significant influence on the BM and TEC, in addition to compensating dopant induced lattice contraction and increasing lattice expansion. In **Sec.** 5.2 the used theoretical methods and system geometries are presented. The results for aliovalent dopants without charge compensating vacancies are presented and discussed in **Sec.** 5.3 and the modifications due to the introduction of vacancies are presented and discussed in **Sec.** 5.4. Finally, a summary and conclusions are presented in **Sec.** 5.5.

5.2 Computational setup

We perform *ab-initio* DFT calculations within the PAW method as implemented in the Vienna *ab-initio* Package (VASP) program using the LDA functional as parameterized by Ceperley and Alder and the GGA functional as constructed by Perdew, Burke and Ernzerhof (PBE) .[122, 123, 137, 138, 165, 166] [2] From previous work it is clear that the obtained results give the same qualitative picture as results obtained

---

The right hand side shows how one CeO$_2$ unit is replaced by a MgO unit: The Mg at a Ce site, in which case the valence of the site changes from +4 to +2, indicated as a double negative charge at the site; the O atom at an O site, with no valence change; and a vacancy (V) at an oxygen site, changing the site valence from −2 to 0, indicated as a double positive charge. If within such a description the vacancy is omitted, the sum of the site charges will be non-zero. For this reason the vacancy is referred to as a "charge compensating vacancy". One may remark that one is actually balancing valencies and not charges, and as such "valence compensating vacancy" would be a better suited term. However, charge compensating vacancy is the terminology used in (experimental) literature, so we will also use it to keep this link, and to avoid confusion on this account.

[2]LDA values for Sm, Gd, and Yb are missing since no LDA PAW potentials are available in the used distribution of the VASP program.
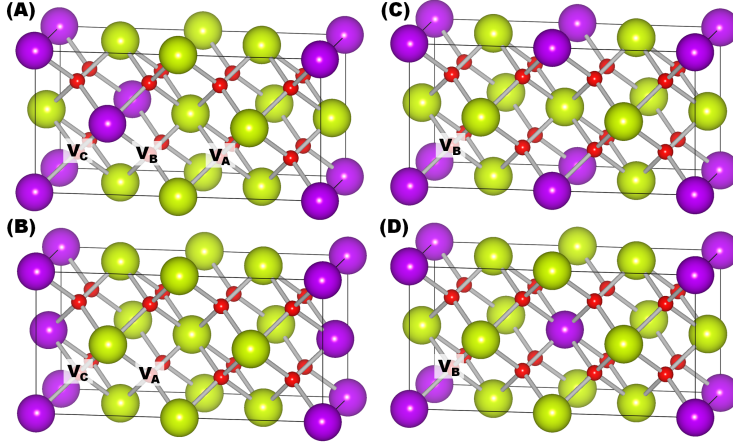
Figure 5.2: *Ball-and-stick representations of different $Ce_{0.75}Gd_{0.25}O_{1.875}$ configurations in a double c111 supercell. Yellow, red, and purple spheres indicate the positions of the Ce, O, and Gd atoms. Vacancy positions are indicated (V_A, V_B, and V_C).*

within the DFT+U framework.[150, 191] The plane wave kinetic energy cutoff is set to 500 eV.

To optimize the structures a conjugate gradient method is used. During relaxation both atom positions and cell-geometry are allowed to change simultaneously. The convergence criterion is set to the difference in energy between subsequent steps becoming smaller than 1.0×10^{-6} eV.

The TECs are calculated as the numerical derivative of V(T) data. This V(T) data in turn is obtained through minimization of the thermal non-equilibrium Gibbs function, which is calculated using the quasi-harmonic Debye approximation, and is implemented as a module in our HIVE code (*cf.* **Appendix** A.2).[169–172] The BM is calculated by fitting $E(V)$ data from fixed volume calculations to the third order isothermal Birch-Murnaghan equation of state (*cf.* **Appendix** A.1).[143, 144]

A. Non-vacancy systems:

Symmetric supercells, containing a single dopant per supercell are used to simulate homogeneous distributions of the dopants without charge compensating vacancies.[1] For all these systems, relaxations started from the fluorite geometry (space group $Fm\bar{3}m$), while maintaining the crystal symmetry. The supercells used are the fluorite cubic $1 \times 1 \times 1$ cell with 12 atoms (c111), the primitive $2 \times 2 \times 2$ cell with 24 atoms (p222), the primitive $3 \times 3 \times 3$ cell with 81 atoms (p333) and the cubic $2 \times 2 \times 2$ cell with 96 atoms (c222). The c111 and p222 supercells are presented in Fig. 5.1. Replacing a single Ce atom with a dopant element or a vacancy results in dopant concentrations of $25, 12.5, 3.7037$, and 3.125 %, respectively.[3]

---

[3]In case of oxygen vacancies the concentration is halved.

Monkhorst-Pack special k-point grids are used to sample the Brillouin zone.[168] For the two smaller cells we use an $8 \times 8 \times 8$ k-point grid while for the two large supercells a $4 \times 4 \times 4$ k-point grid is used.

B.   Systems containing compensating O vacancies:

For doped systems containing a single oxygen vacancy, only the c111 and p222 supercells are used, giving rise to dopant concentrations of 25 and 12.5%, respectively, and oxygen vacancy concentrations of 12.5 and 6.25%, respectively. The c111 and p222 configurations without vacancies are shown in Fig. 5.1. Every oxygen atom is positioned at the center of a cation-tetrahedron, as is shown in Fig. 4.1a of the previous chapter. As a result every vacancy site can have up to four dopant atoms as nearest neighbor. For calculations containing two dopants and one vacancy a double c111 supercell is used. Four inequivalent dopant distributions (A, B, C, and D) are used, shown in Fig. 5.2. For the investigation of the influence of oxygen vacancies, we assume a homogeneous distribution of the vacancies,[4] just as we did for the dopants. Effects due to clustering are beyond the scope of this work, and as such will not be treated.

In this work vacancy sites with 0 neighboring dopants are indicated as V_A, if 1 dopant is present in the surrounding tetrahedron it is referred to as V_B, and if 2 dopants are present as V_C (*cf.* Figs. 5.1 and 5.2). Since only single oxygen vacancies are present, all Ce atoms in each of the systems will either be 7-or 8-coordinate.

Similar as for the supercells without vacancies, Monkhorst-Pack special $k-$point grids of $8 \times 8 \times 8$ grid points are used for the c111 and p222 cells.[168] For the double c111 supercells a $4 \times 8 \times 8$ grid is used instead.

5.3   Aliovalent dopants without compensating oxygen vacancies

The use of aliovalent dopants in CeO_2 introduces two (related) complications from the theoretical point of view. Firstly, aliovalent dopants give rise to charge compensating vacancies, which increases the number of possible configurations per dopant concentration significantly if the ground state configuration is not known. Secondly, since many elements can have multiple valencies this introduces additional uncertainties with regard to the number of required compensating vacancies and thus the ground state crystal structure.

For these reasons, we start by investigating non-compensated dopants in fluorite $Ce_{1-x}M_xO_2$ with M=Mg, V, Co, Cu, Zn, Nb, Ba, La, and Bi. This has the advantage that only effects directly due to the aliovalent dopants are observed. In **Sec.** 5.4 compensating vacancies are added, allowing to discriminate the contributions to the

---

[4]For low oxygen vacancy concentrations, we assume that results for random distributions of vacancies can be approximated as linear combinations of configurations as the ones studied in this work. However, to retain a clear image of the specific influences different configurations have, we will only investigate these homogeneous distributions of vacancies.

modification of system properties induced by the vacancies. In addition, the non-compensated situation can be physically interpreted as doped systems under highly oxidizing atmosphere, which may be of interest for catalytic processes in for example automotive TWC.[47, 48, 54, 201, 202]

5.3.1 Dopant radii and Vegard's law

In **Chapter** 4, on group IV dopants in CeO_2, we have shown that for cubic systems without oxygen vacancies the radius of the dopant element can be calculated as:[190]

$$R_M = \left(\frac{\sqrt{3}}{4} a_{Ce_{1-x}M_xO_2} - R_O - (1 - n_x)R_{Ce} \right)/n_x, \tag{5.1}$$

with n_x the dopant concentration, $a_{Ce_{1-x}M_xO_2}$ the lattice parameter of the doped system, and R_O and R_{Ce} the radii of O and Ce, respectively. From this the empirical Vegard law was derived.[177, 190] In doping experiments, lattice parameters are often linearly fitted with regard to the dopant concentration. Deviation with respect to this Vegard law behavior is interpreted as being due to the presence of secondary phases, phase transitions or saturation, depending on the observed deviation.[67, 194, 195, 197, 203, 204]

Table 5.1 shows the calculated dopant radii and coefficients of Vegard's Law. The intercept a and slope b of the latter are found from rewriting Eq. (5.1) as

$$a_{Ce_{1-x}M_xO_2} = a_{CeO_2} + \left(\frac{4}{\sqrt{3}}(R_O + R_M) - a_{CeO_2} \right) n_x, \tag{5.2}$$

as was shown in the previous chapter. The standard deviations on the calculated dopant radii of ≤ 0.01Å show consistent values are found for the systems of different concentrations. The calculated lattice parameter for $Ce_{0.75}Sm_{0.25}O_2$ seems to be in good agreement with the experimental lattice parameter of 5.4314Å for $Ce_{0.8}Sm_{0.2}O_{2-\delta}$ by Yao *et al.*[200] and $\sim$ 5.435 for $Ce_{0.85}Sm_{0.15}O_{1.925}$ by Xu *et al.*[199], knowing that PBE generally overestimates lattice parameters by roughly a few percent. Also the very small variation of the experimental lattice parameter with the Sm concentration is in agreement with the calculated slope of the Vegard law, if one takes into account that the different synthesis methods have an influence on the obtained lattice parameters. Yao *et al.* also calculated the Vegard law slope for Co doped $Ce_{0.8}Sm_{0.2}O_{2-\delta}$ and find a lattice contraction, in qualitative agreement with our theoretical results.[200] The smaller experimental lattice contraction is mainly due to the presence of oxygen vacancies, which, as will be shown later for other aliovalent dopants, gives rise to a lattice expansion compared to a system without oxygen vacancies, and thus compensates the lattice contraction due to the Co dopants to some extend, lowering the strength of the lattice contraction.

In Fig. 5.3 the calculated atomic radii are compared to the Shannon crystal radii for 6-,7-, and 8-coordinated configurations.[180, 181] For the tetravalent V and Nb, both LDA and PBE results are in good agreement with the 8-coordinate Shannon crystal radius, while for the trivalent Yb, Gd, Sm, and La the 7-coordinate values give

Table 5.1: *Dopant radii calculated using Eq. (5.1), averaged over the four dopant concentrations (avg), and standard deviation (stdev) of this value. This is done for both LDA and PBE calculated geometries. a and b are the intercept and slope of Vegard's law linear fit (cf. text) to the calculated geometries for doped CeO_2 systems. Lattice parameters at zero Kelvin a_0 and room temperature (RT) a_{RT} (300 K) are given for $Ce_{0.75}M_{0.25}O_2$. The CeO_2 values are given as reference.[2]*

| | R_M (Å) | | | | Vegard's Law | | | | LDA | | PBE | |
| | LDA | | PBE | | LDA | | PBE | | | | | |
	avg	stdev	avg	stdev	a(Å)	b	a(Å)	b	a_0 (Å)	a_{RT} (Å)	a_0 (Å)	a_{RT} (Å)
CeO_2	1.0819^a	0.0001	1.1257^a	0.0004					5.362	5.388	5.463	5.492
Mg	0.958	0.008	1.022	0.011	5.364	−0.315	5.465	−0.273	5.285	5.316	5.396	5.432
V	0.823	0.005	0.870	0.005	5.363	−0.613	5.464	−0.610	5.209	5.235	5.312	5.341
Co	0.883	0.005	0.949	0.007	5.363	−0.478	5.464	−0.427	5.243	5.273	5.357	5.392
Cu	0.913	0.002	0.991	0.006	5.362	−0.395	5.463	−0.307	5.264	5.299	5.387	5.428
Zn	0.952	0.005	1.028	0.008	5.363	−0.317	5.464	−0.239	5.283	5.315	5.404	5.440
Nb	0.926	0.005	0.961	0.005	5.363	−0.375	5.464	−0.395	5.269	5.292	5.365	5.392
Ba	1.332	0.003	1.403	0.001	5.363	0.566	5.464	0.635	5.504	5.533	5.622	5.656
La	1.186	0.001	1.242	0.004	5.362	0.237	5.464	0.260	5.422	5.448	5.529	5.559
Sm	–	–	1.169	0.004	–	–	5.464	0.095	–	–	5.487	5.517
Gd	–	–	1.139	0.005	–	–	5.464	0.015	–	–	5.468	5.498
Yb	–	–	1.104	0.008	–	–	5.464	−0.056	–	–	5.449	5.482
Bi	1.107	0.003	1.165	0.009	5.363	0.044	5.465	0.060	5.373	5.400	5.480	5.511

[a] The Ce radius is calculated using Eq. (5.1), where the 4-coordinated Shannon crystal radius for oxygen is taken as 1.24 Å [180].

the best agreement, despite the fact that all dopants are placed in the 8-coordinate environment of CeO_2.[5] Furthermore, the radii for divalent Mg and Zn show good agreement with the 8-coordinate radii, while monovalent Cu and trivalent Bi present 6-coordinate radii. The deduced 6-coordination for Cu shows nice agreement with the coordination number 5–6 obtained by Wang *et al.* from X-ray adsorption fine structure (XAFS) measurements.[154] It differs, however, from the 4-coordination found in calculations by Lu *et al.*[188] where a broken symmetry structure for the Ce doped CeO_2 was used. The resulting tetragonal structure for such a broken symmetry system is 0.667% larger in volume than the cubic fluorite structure used in this work, making the calculated atomic radius for Cu slightly larger than the one presented. The value for divalent Co in turn indicates toward 7-fold coordination. Note that the Shannon crystal radii for Co^{3+} and Co^{4+} would be too small, showing the divalent nature inferred from the calculated radius supports the experimental suggestion of divalent Co dopants.[155, 157, 159, 197][6]

The results for Ba are a bit peculiar, since the calculated radius is significantly lower than either 6-, 7-, or 8-coordinate Shannon crystal radii for divalent Ba. Assuming the general trends seen in the Shannon crystal radii for other elements are also valid for Ba (i.e. increasing valence results in decreasing radius under constant coordination) this would lead to the conclusion that Ba behaves as having a valence higher than 2 when used as a dopant for CeO_2, which is puzzling.

In conclusion, in contrast to previous work on group IV elements, aliovalent dopants tend not to present full 8-coordination, but rather act as if they are only 7- or 6-coordinated.[190]

On the other hand, as might be expected, perfect Vegard law behavior is observed for all the systems under investigation. Combined with the calculated atomic radii, this provides a way to experimentally estimate the valence of dopant elements based on the obtained lattice parameter under oxidizing atmosphere. This is done by calculating the atomic crystal radius of the dopant based on the measured lattice

---

[5]In *ab-initio* calculations as presented in this work, the valence of the atoms is not strictly defined, and our reference to any type of valence should not be taken as an absolute truth, but rather an educated guess. All elements used as dopants in this work have either a single (most common) valence which is different from +4 (e.g. Zn) or are multivalent with most common valencies different from +4 (e.g. Yb or V). Since Shannon crystal radii are given both for different coordinations and different valences (though some combinations which might be of interest for this work are missing) we have attempted to derive the valence of the dopants in the presented systems, based on the magnetization of the ground state system, under the assumption of integer values for this magnetization. In most cases these results pointed at the most common valence, and in some cases degeneracies were present, with Co being the most extreme case. In cases where the valence was uncertain, Shannon crystal radii in the ball-park of our calculated atomic radii were used as indicator for the dopant valence. As a result, the stated valences should only be considered as a guess, although they might point out underlying physical relations with the atomic valence.

[6]Of all systems investigated, Co doping is the most problematic one due to the near degeneracy of different magnetic configurations (magnetization varying from 1 to 5 μ_B show differences in total energy of ~ 0.20 and ~ 0.08 eV for 3% doped systems). Interestingly enough, experiments seem to encounter similar variation in the observed magnetic moment, with values varying with the Co concentration, substrate, and deposition method. Where Tiwari *et al.* present $6\mu_B$ at 3% Co doping, Vodungbo *et al.* measure about $1.5\mu_B$ at 4.5%, while Fernandez *et al.* and Song *et al.* measure about $5\mu_B$ at concentrations of 5 and 3%, respectively.[155, 157, 158, 196]
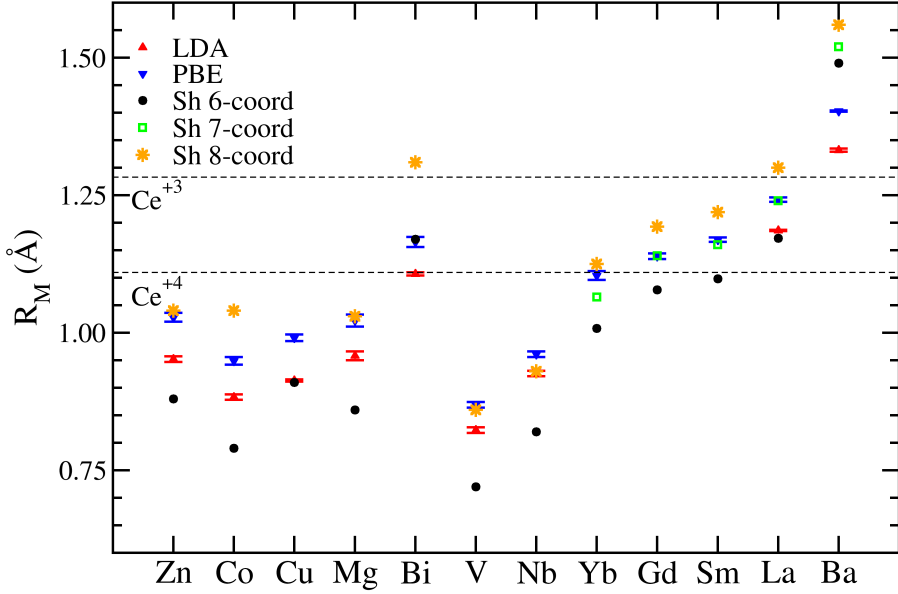
Figure 5.3: *Comparison of calculated dopant radii in $Ce_{1\text{-}x}M_xO_2$ to the Shannon crystal radius for $M=Mg^{2+}$, V^{4+}, Co^{2+}, Cu^{1+}, Zn^{2+}, Nb^{4+}, Ba^{2+}, La^{3+}, Sm^{3+}, Gd^{3+}, Yb^{3+}, and Bi^{3+} with coordination numbers 6, 7, and 8 (where available).[180, 181] The standard deviation is shown as error bars. The dopant elements are sorted according their Covalent radius, with Zn the smallest and Ba the largest element.[205] The Shannon crystal radii for 8-coordinate Ce^{3+} and Ce^{4+} are indicated with dashed lines.*

parameter, and then comparing this radius to the tabulated values by Shannon, to deduce the dopant valence.

5.3.2 Formation energies

The stability of the different doped systems is investigated through the comparison of the defect formation energy E_f defined as:

$$E_f = E_{Ce_{1-x}M_xO_2} - E_{CeO_2} + N_{df}(E_{Ce} - E_M), \qquad (5.3)$$

with $E_{Ce_{1-x}M_xO_2}$ the total energy of the doped system, E_{CeO_2} the total energy of a CeO_2 supercell of equal size, N_{df} the number of dopant atoms, and E_{Ce} and E_M the bulk energy per atom of α-Ce and the bulk phase of the dopant M. Positive values indicate the amount of energy required to substitute a single Ce atom by a dopant.

Defect formation energies given in Table 5.2 show the same qualitative behavior for the LDA and PBE calculations. Furthermore, as was observed for group IV dopants, formation energies show only limited dependence on the dopant concentration indi-

Table 5.2: *Defet formation energy* E_f *for doped* CeO_2 *at different dopant concentrations.*[2]

	E_f (eV)			
	25%	12.5%	3.704%	3.125%
	LDA			
CeO_2	-11.484^a			
$La_2Zr_2O_7$	-42.421^a			
Mg	8.221	8.409	8.470	8.475
V	6.243	6.313	6.338	6.322
Co	12.353	12.425	12.479	12.473
Cu	13.517	13.464	13.463	13.458
Zn	11.465	11.651	11.696	11.707
Nb	3.738	3.445	3.400	3.415
Ba	7.621	7.777	7.933	7.956
La	2.403	2.389	2.418	2.422
Bi	7.902	8.069	8.114	8.095
	PBE			
CeO_2	-10.418^a			
$La_2Zr_2O_7$	-38.253^a			
Mg	8.036	8.223	8.275	8.284
V	6.256	6.320	6.348	6.361
Co	11.750	11.780	11.800	11.801
Cu	12.922	12.878	12.878	12.879
Zn	11.057	11.249	11.282	11.300
Nb	4.059	3.746	3.726	3.761
Ba	7.518	7.681	7.850	7.882
La	2.438	2.429	2.464	2.469
Sm	-2.181	-2.218	-2.228	-2.236
Gd	2.396	2.445	2.449	2.448
Yb	4.438	4.495	4.508	4.500
Bi	7.912	8.069	8.111	8.093

^{a} Instead of the defect formation energy the heat of formation is given.

cating no solubility limits are being crossed within the investigated range.[191] The results in Table 5.2 also show that only Sm doping is stable in an absolute sense with regard to segregation into CeO_2 and bulk Sm.[7] Of all the other compounds only meta-stability should be expected. All the dopants presented in this work have been used in experiments, and of several a $Ce_{1-x}M_xO_{2-y}$ phase is experimentally observed.[41, 44–47, 55, 56, 66, 67, 70, 71, 73, 75, 76, 80, 81, 152, 154, 155, 157–

---

[7]The DFT+U study of Sm doped CeO_2 by Ismail *et al.* may be an indication that this also holds for PBE+U calculations, though they only included the Coulomb correction for Ce.[206]

159, 192–200] However, these experimental compounds contain charge compensating oxygen vacancies, which are not included in the systems presented in this section. In **Sec.** 5.4 we will show that the inclusion of such vacancies has only limited influence on the formation energies, allowing the presented defect formation energies to be used as initial indicators of the system stability.

Since the formation energies presented here are spread over quite a wide range it is obvious that not all dopants will form a compound system as easily. In consequence, a reference is needed to indicate which are more likely to form a doped bulk phase and which dopants are more likely to segregate (to the surface in case of for example catalyst nanocrystals). It is well-known for CeO_2 to spontaneously form oxygen vacancies, so the oxygen vacancy formation energy of pure CeO_2 is used as a reference for the likelihood of forming a $Ce_{1-x}M_xO_2$ bulk-phase.[44, 47] Table 5.4 shows the calculated oxygen vacancy formation energy for $CeO_{1.96875}$ to be 4.035 and 3.097 eV for LDA and PBE, respectively, going up to 5.006 and 4.145 eV in $CeO_{1.75}$. From this we conclude that the lanthanides presented in this work and Nb are likely to form fluorite based bulk-phases of $Ce_{1-x}M_xO_2$, while the other dopants are expected to segregate either to internal domains or the surface of the grains. However, combining this knowledge, with the results of the calculated dopant radii, could also indicate another option is available in the latter case. For dopants with a high defect formation energy a crystal radius indicative of a preference for lower coordination may indicate that local reconstructions around the dopant are present. Such reconstructions would lead to a better suited chemical environment, with better matched coordination, and should give rise to lower defect formation energies.

Of all dopants presented in this work, Cu shows the highest formation energy, making it the most likely candidate for phase segregation and/or reconstruction. The existence of such reconstruction is shown in the work of Wang *et al.*[154] and Lu *et al.*[188] where a symmetry breaking reconstruction for the Cu dopant was found and investigated. But even when this reconstructed structure is taken into account, Cu doped CeO_2 remains one of the most unstable systems. The tetragonal reconstruction is only 1.223 eV more stable than the cubic fluorite structure, resulting in a defect formation energy of about 11.7 eV in PBE calculations. In the literature several experimental groups have investigated CuO doped/modified CeO_2 showing a general trend of phase segregation for medium to high Cu content.[46, 55, 70, 75, 152, 154, 164, 192] Kundakovic and Flytzani-Stephanopoulos investigated the reduction characteristics of CuO dispersed on $Ce_{1-x}La_xO_2$ catalyst supports.[46, 152] They found that for low Cu content, copper is present as small clusters or even isolated ions. For higher concentrations, also CuO particles are observed.[152] Similar observations are made by Lin *et al.* and also de Biassi and Grillo present evidence of Cu clustering.[75, 164] In addition, Kundakovic and Flytzani-Stephanopoulos also present the observation of bulk doped $Ce_{0.99}Cu_{0.01}O_{2-y}$ for calcining temperatures below 500°C, and state that for higher calcining temperatures the Cu ions segregate to the surface to form clusters. This supports the instability of Cu doped CeO_2 predicted by our calculated formation energies.

In contrast, Bera *et al.* do not observe any CuO related lines in their X-ray diffraction (XRD) spectra for $3-5\%$ Cu doping, nor do they observe CuO particles

in their transmission electron microscope (TEM) measurements. As a result they conclude Cu ions to be present in the CeO_2 crystal matrix. However, they also note that there are 4 to 6 times as many Cu ions located on the surface of the CeO_2 particles.[70] Combined with the results for low calcining temperatures of Kundakovic and Flytzani-Stephanopoulos this would appear to indicate that a significant kinetic barrier is present for the Cu ions, limiting clustering and segregation to the surface.

In contrast, Co bulk-doping, which is shown in Table 5.2 to be almost as unfavorable as Cu doping, is widely used in experimental studies in the context of dilute semiconductors. In many of these experiments, samples which are often thin films, are prepared via pulsed laser deposition.[155, 157, 158] Observation of $Ce_{1-x}Co_xO_{2-y}$ in these samples may be an indication that quite high kinetic barriers are present, effectively pinning the Co ions in place despite the unfavorable energetics. Alternatively, Co may segregate into very small Co/CoO clusters, which could at higher Co concentrations give rise to the Co_3O_4 impurities observed by Sacanell et al.[198] This would also be in line with the calculated preference of oxygen vacancies near Co ions.[207] Yao *et al.* investigated the codoping of CeO_2 with Co and Sm.[200] They observe no evident secondary CoO and Co_3O_4 phases. In combination with the observation of a Vegard law behavior as function of the Co content, they conclude the Co ions to be incorporated into the ceria lattice to form a solid solution. This seems to indicate that the codoping with Sm in this case stabilizes the Co dopants somewhat. In addition, Yao *et al.* also observe the grain boundary conductivity to show a maximum at 5% of Co doping.[200] This they link to the segregation of Co to the grain boundary, showing that the Sm dopants can only stabilize a limited amount of Co.

Another interesting dopant to have a closer look at is Ba. Of the dopants investigated, it shows the largest decrease in defect formation energy for increasing concentration. Combined with the relatively large defect formation energy this could be an indication that the $BaCeO_3$ interface observed between superconducting $YBa_2Cu_3O_{7-\delta}$ thin films and CeO_2 buffer layers is rather due to Ce moving into BaO layers than Ba moving into the CeO_2 buffer layer.[68, 208] However, before any conclusive statement can be made further theoretical work will be needed.

In Fig. 5.4 the obtained defect formation energies are correlated with the calculated atomic crystal radius R_M (Fig. 5.4(a)) and the covalent radius (Fig. 5.4(b)).[205] Figure 5.4(a) shows the most stable dopants to have a crystal radius between that of 8−coordinate Ce^{4+} and Ce^{3+}, while Fig. 5.4(b) shows high stability for elements with a covalent radius close to that of Ce. In both cases, the Nb dopant appears as an exception, showing a reasonably beneficial defect formation energy, while presenting a significantly lower atomic radius than the other more stable dopants. The Nb covalent radius, however, is nicely in the range of those of the group IVb elements (Ti: 1.60Å, Zr and Hf: 1.75Å) which were shown to provide stable dopants.[191, 205] The same is true for the calculated atomic radii R_M.[190] The main difference between Nb and the other elements presented here is the fact that it acts as a tetravalent dopant in a $Ce_{1-x}Nb_xO_2$ system. This shows that the relation between dopant stability and radius is more complex, and that the valence (in the compound) plays an important role. As such, higher valence results in smaller radii for stable dopants. In addition,

Table 5.3: *Calculated* BM B_0 *for* CeO_2 *at a dopant concentration of* 25%, *for* LDA *and* PBE *calculations. The linear* TEC α *at the same dopant concentration and a temperature of* 500 K.[2]

	B_0 (Mbar)		α (10^{-6} K^{-1})	
	LDA	PBE	LDA	PBE
CeO$_2$	2.017	1.715	11.218	12.955
Mg	1.644	1.389	14.693	16.867
V	2.132	1.796	11.510	13.601
Co	1.867	1.542	13.779	16.567
Cu	1.704	1.374	16.186	19.902
Zn	1.712	1.410	14.968	17.656
Nb	2.187	1.871	10.621	12.226
Ba	1.580	1.321	13.544	15.608
La	1.835	1.556	11.809	13.618
Sm	–	1.595	–	13.678
Gd	–	1.588	–	13.744
Yb	–	1.534	–	15.229
Bi	1.874	1.575	12.631	14.836

it is also apparent from these figures that the order of the atomic radii differs significantly depending of the definition used. Consequently, simple stability rules based on ratios of atomic radii, for example used in the study of the fluorite-pyrochlore transitions, should be considered as ill-defined.[189, 209]

Based on the results presented in this work, it is also possible to make some predictions about other dopant elements. Let us assume that the trend observed for the defect formation energies of group IVa and IVb dopants also hold for other groups.[191] Then, from the defect formation energies for Mg and Ba, we can conclude that all elements of the group IIa will segregate when used as a dopant in CeO$_2$. From the values calculated for V and Nb on the other hand, the value for Ta is expected to be below the oxygen vacancy formation energy, indicating Ta to be a good dopant candidate for presenting a meta-stable bulk phase.

5.3.3 Bulk modulus and Thermal expansion coefficients

The modification of the elastic properties of CeO$_2$ due to aliovalent doping is investigated through the BM and linear TEC α. To reduce the computational cost, only BM and TEC are calculated for dopant concentrations of 25%. Table 5.3 shows these BM and the linear TEC at 500 K. The BM and TEC for pure CeO$_2$ are given as reference. These show the LDA based value for the TEC to be in excellent agreement with the experimental value ($(11.0 \pm 0.5) \times 10^{-6}$ K^{-1} at RT, and $(11.5 \pm 0.5) \times 10^{-6}$ K^{-1} at 500 °C), while the PBE value is clearly an over-estimation.[44] With regard to the BM it is again the LDA value which shows best agreement with experiment
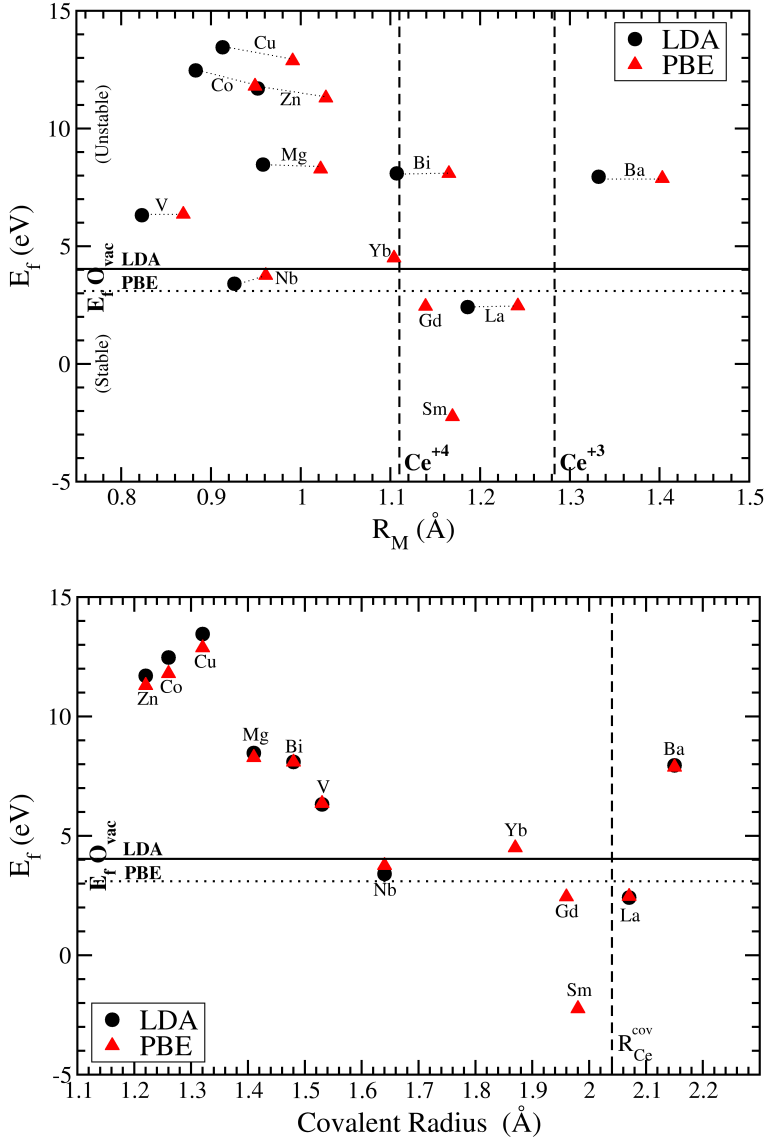
Figure 5.4: *The calculated formation energy E_f, for $Ce_{1-x}M_xO_2$ with $x = 0.03125$, as function of the calculated atomic radius R_M (top) and the covalent radius (bottom).[205] Top: Vertical dashed lines indicate the Shannon crystal radii for $8-$coordinate Ce^{3+} and Ce^{4+}.[180, 181] Bottom: Vertical dashed line indicates the covalent radius for Ce R_{Ce}^{cov}.[205] Top+Bottom: The O vacancy formation energy at a vacancy concentration of 1.5% is indicated with a solid (LDA) or dotted (PBE) line.*
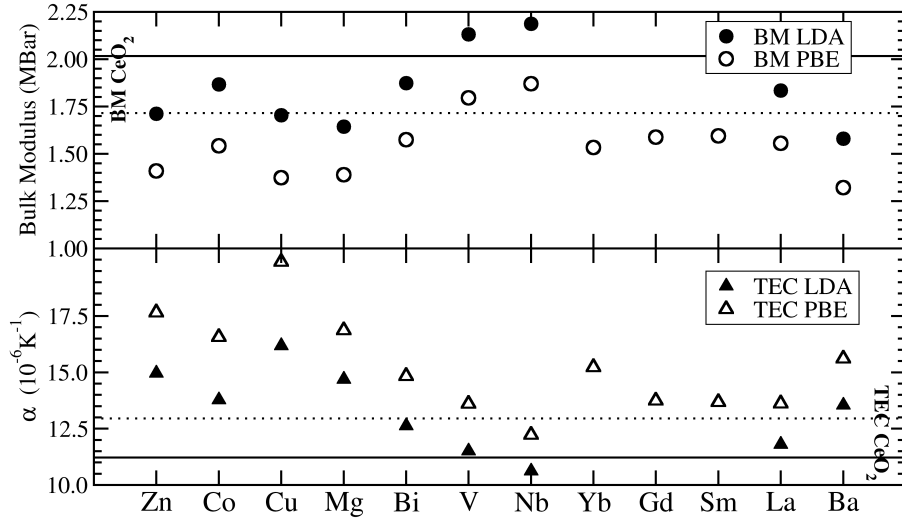
Figure 5.5: *Calculate* BM *and linear* TEC α *at 500 K for* $Ce_{0.75}M_{0.25}O_2$. *Calculated values (*LDA*: solid line,* PBE*: dotted line) for pure* CeO_2 *are given for reference. The elements are sorted with regard to increasing Covalent radius.*[205]

where values in the range of 2.04–2.36MBar are measured.[139–141] The PBE value shows a significant underestimation, in line with the overestimation of the TEC. Of all dopants investigated here, only V and Nb give rise to an increase in the BM, all other dopants reduce the BM in varying degrees. Comparing the BM for (the tetravalent) V and Nb dopants to those found for group IVb dopants shows them to present similar values.[190, 191] For Cu the BM was also calculated for $Ce_{0.875}Cu_{0.125}O_2$, and found to be 1.867 and 1.553 Mbar for LDA and PBE, respectively. This is within 0.01 Mbar of the average of the BM for pure CeO_2 and $Ce_{0.75}Cu_{0.25}O_2$, showing that a linear relation between the BM and dopant concentration is a reasonable assumption to make for $Ce_{1-x}M_xO_2$.

With the exception of Nb, all investigated dopants result in an increase of the TEC. Sorting the values shown in Table 5.3 shows a correlation with the valence of the dopant, where low dopant valence leads to a large increase in the TEC and high valence leads to a small increase and even decrease of the TEC.

Comparison of the BM and the TEC in Fig. 5.5 shows clearly the opposite trends of the BM and TEC, as was also observed for group IV elements, again showing the expected inverse correlation between the BM and the TEC.[184, 191] Only Vanadium shows a slightly different behavior with both the TEC and BM being larger than the CeO_2 values. Close investigation of the Vanadium TEC in Fig. 5.6a shows that the Vanadium curve crosses the TEC curve for pure CeO_2 at around 250 K, so below this temperature the inverse behavior of the TEC and BM is restored.

Figure 5.6a also shows the TEC for two different Cu dopant concentrations.

In the range of roughly RT up to at least 1000 K a nearly linear influence of the dopant concentration on the TEC change is observed, indicating that for aliovalent dopants in highly oxidizing atmosphere the TEC may also be linearly interpolated. This linear behavior supports the inherent assumption underlying the experimental practice of codoping in several ceria based applications.[79, 81]

Figure 5.6b shows the TEC of the lanthanides La, Sm, and Gd to coincide nicely, while the Yb curve shows much higher values. This difference in behavior is most likely linked to the filled $4f$ shell of Yb (which is only partially filled for Sm and Gd). Further investigation of lanthanide dopants is required to have the full picture of the mechanism at work. Similar as was found for group IV dopants, this behavior indicates the importance of filled shells near the Fermi-level.

With regard to the comparison of calculated to experimentally obtained lattice parameters for CeO_2, several authors have noted that one should be very careful, since the former are generally calculated at zero Kelvin, while the later are measured at RT. These authors suggest to linearly extrapolate the calculated lattice parameter making use of the '*linear TEC*'. In this setup the coefficient is assumed to be a constant, and often taken from experiment. As is shown in Fig. 5.6, the linear TEC shows quite a non-linear behavior at low temperature.[8] Taking this behavior into account one can obtain a more accurate value of the lattice parameter at RT. Zero Kelvin and RT values of the lattice parameter of doped CeO_2 are shown in Table 5.1. The thermal contribution to the lattice parameter at RT is fairly limited and is of the order of 0.02–0.04 Å, for dopant concentrations of 25%. Since this can be comparable to the lattice parameter change due to the introduction of a dopant, this can result in different doped systems to have the same lattice parameter at elevated temperatures (e.g. Sm and Bi doped (25%) CeO_2 at about 1065 K, and pure and Yb doped (25%) CeO_2 at about 1024 K). As a result, co-doped systems or interfaces between layers of differently doped CeO_2 may experience reduced strain at elevated temperatures. The opposite is to be expected as well, and increased segregation or interface strain at elevated temperatures could be a consequence. This latter aspect is of importance when perfect interfaces are required, and should be considered when crack formation in thin films is an issue.[42, 43, 45, 68]

5.4 Inclusion of Vacancies

Since the configuration of dopants and oxygen vacancies for the systems studied is essentially unknown, different configurations need to be investigated. However, since it is neither our goal nor our intent to find the exact ground state configuration of these systems, but rather to investigate the influence introduced vacancies have, we will restrict ourselves to a subset of dopants and a small set of configurations for the different dopants. The subset of dopants consists of Cu^{1+}, Zn^{2+}, and Gd^{3+}. In addition, vacancies in pure CeO_2 are added as reference.

---

[8]Note that the 'linear' in linear TEC refers to thermal expansion in one dimension, and does not indicate any linearity with regard to this coefficient. Adding to the confusion however is the fact that for a large experimental temperature range the coefficient changes roughly linearly, as is shown in Fig. 5.6.
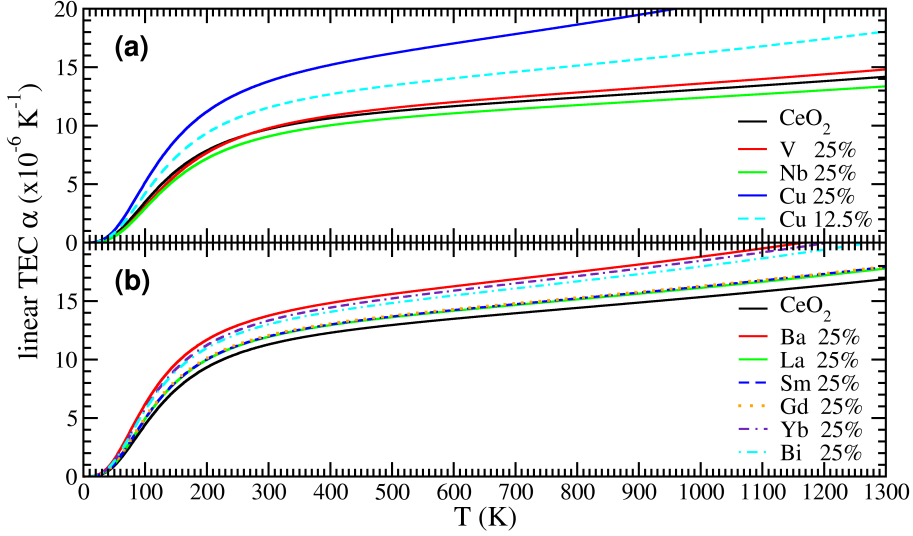
Figure 5.6: *Calculated linear* TEC *α for different dopants based on* LDA *(a) and* PBE *(b) total energies and volumes. The calculated* TEC *of CeO$_2$ (black solid curve) is given as reference.*

The different vacancy geometries are described in **Sec.** 5.2 and the notation NV is used to indicate the 'No Vacancy' reference systems, i.e. Ce$_{1-x}$M$_x$O$_2$ with M=Cu, Zn, or Gd. All systems presented, contain 1 oxygen vacancy per dopant atom, resulting in charge under-compensation (Cu), compensation (Zn), and over-compensation (Gd).[1] For these systems a vacancy formation energy E$_{vac}$ is calculated as:

$$E_{vac} = E_{Ce_{1-x}M_xO_{2-y}} + \frac{N_{vac}}{2}E_{O_2} - E_{Ce_{1-x}M_xO_2}, \tag{5.4}$$

with N_{vac} the number of oxygen vacancies[9], E_{O_2} the total energy of an oxygen molecule, and $E_{Ce_{1-x}M_xO_{2-y}}$ and $E_{Ce_{1-x}M_xO_2}$ the total energies of the system with and without vacancies, respectively.

5.4.1 Oxygen and cerium vacancies in CeO$_2$.

Before investigating the combined influence of dopants and vacancies, the influence of oxygen and cerium vacancies on pure CeO$_2$ is quickly revisited. Table 5.4 shows the vacancy formation energy of both Ce and O vacancies. From this it is clear that Ce vacancies are highly unfavorable, in agreement with experimental observations.[44, 47] In addition the relatively small change of the lattice parameter appears to be strongly functional dependent.

---

[9]In this, N_{vac} is related to y via the relation $N_{vac} = yN_{uc}$ with N_{uc} the number of unit cells required to build the supercell of the doped system.
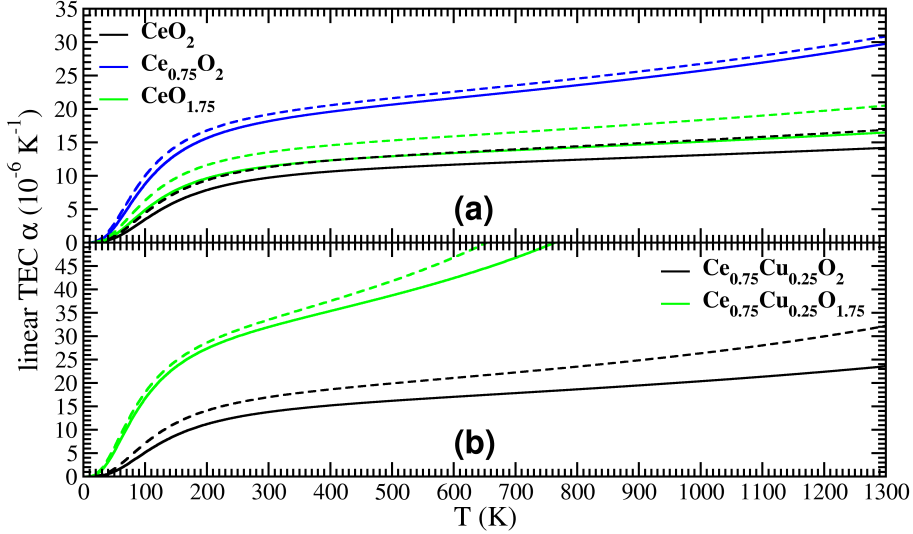
Figure 5.7: *Calculated linear TEC α for different systems containing vacancies. (a) Comparison of the influence of oxygen and cerium vacancies, (b) Cu doping with and without oxygen vacancies. LDA results are shown as solid lines and PBE as dashed lines.*

The vacancy formation energy of the oxygen vacancies on the other hand shows a significant concentration dependence (in contrast to the dopant calculations of the previous section). In addition, the calculated lattice expansion is clearly non-linear, with a similar trend for LDA and PBE calculations. The expansion of the lattice parameter due to the presence of oxygen vacancies is experimentally known, and theoretically understood as a consequence of the transition from Ce^{4+} to Ce^{3+} of two Ce atoms neighboring the oxygen vacancy. Since the atomic crystal radius of Ce^{3+} is significantly larger than Ce^{4+} (1.283Å instead of 1.11Å) the lattice will expand.[44, 47] The non-linearity shown here, indicates that for aliovalent dopants charge compensating vacancies may give rise to non-Vegard law behavior, due to $Ce^{4+} \longrightarrow Ce^{3+}$ transitions.

Interesting to note is the large impact of the vacancies on the BM and TEC of CeO_2. Figure 5.7a shows a dramatic increase in the linear TEC due to the presence of vacancies. It is clear that the inverse relation between the BM and the TEC is retained for vacancies.

Table 5.4: *Properties of vacancies in non-doped CeO_2: vacancy formation energy E_{vac}, lattice expansion Δa_0, bulk modulus B_0 and linear thermal expansion coefficient α. Vacancy concentrations are indicated and the linear thermal expansion coefficient value α is given for a temperature of 500 K.*

		E_{vac} (eV)				Δa_0 (%)				B_0 (MBar)	α (10^{-6} K^{-1})
Vac. conc. (%)		12.5%	6.25%	1.852%	1.563%	12.5%	6.25%	1.852%	1.563%	12.5%	12.5%
O Vac.	LDA	5.006	4.440	4.054	4.035	0.775	0.510	0.176	0.141	1.568	12.912
	PBE	4.145	3.476	3.075	3.097	0.908	0.606	0.193	0.165	1.320	15.287
Vac. conc. (%)		25%	12.5%	3.704%	3.125%	25%	12.5%	3.704%	3.125%	25%	25%
Ce Vac.	LDA	17.549	17.779	17.857	17.829	−0.270	−0.032	−0.016	−0.028	1.023	20.650
	PBE	16.255	16.543	16.611	16.592	0.560	0.266	0.063	0.061	0.858	21.609

Table 5.5: *Calculated vacancy formation energies (E_{vac}), bulk modulus (B_0), and change in volume (ΔV) and lattice expansion (Δa_0) for Cu, Zn, and Gd doped CeO_2 including a single vacancy per supercell. ΔV and Δa_0 are taken with regard to pure CeO_2. All calculations are performed using* PBE *functionals. Vacancy concentrations are 12.5 (c111) and 6.25 % (p222). The different configurations are shown in Fig.* 5.1. NV *indicates the reference systems without vacancies.*

	E_{vac} (eV)			B_0 (Mbar)			ΔV (%)			Δa_0 (%)		
	Cu	Zn	Gd	Cu	Zn	Gd	Cu	Zn	Gd	Cu	Zn	Gd
c111 NV	12.922^a	11.057^a	2.396^a	1.37	1.41	1.59	−4.124	−3.189	0.274	−1.394	−1.074	0.091
c111 V$_B$	−0.800	−0.882	1.929	0.87	0.38	0.86	−0.568	−1.529	1.563	−0.190	−0.512	0.518
p222 NV	12.878^a	11.249^a	2.445^a	1.55	–	–	−2.145	−1.529	0.158	−0.733	−0.526	0.039
p222 V$_A$	−0.048	−0.604	1.395	1.01	1.03	1.00	0.619	0.552	1.371	0.193	0.170	0.442
p222 V$_B$	−0.422	−1.200	1.364	1.04	1.09	1.31	−1.173	−1.416	1.116	−0.406	−0.488	0.357

[a] For the systems without vacancies, the formation energy E_f is repeated. Note that the formation energy of a doped system with oxygen vacancies $E_{f,vac} = E_f + E_{vac}$.

5.4.2 Aliovalent dopants Cu, Zn and Gd combined with a single oxygen vacancy.

A. Vacancy formation energy.

If one assumes the valences of Cu, Zn and Gd as dopants for CeO_2 to be +1, +2, and +3, respectively, then the introduction of a single oxygen vacancy for every dopant ion will result in under-compensation in case of Cu, nominal charge compensation for Zn, and over-compensation in case of Gd.[5] Table 5.5 shows the vacancy formation energies for these three dopants. For all systems, the absolute value of E_{vac} is of the order of 1 eV. Because the formation energy of a doped system including oxygen vacancies can be written as $E_{f,vac} = E_f + E_{vac}$, where E_f is the formation energy of the NV system, the introduction of an oxygen vacancy in a Cu or Zn doped system will result in an improved stability. However, since $E_{f,vac}$ is positive this means that the formation of oxygen vacancies will not prevent phase segregation and promote the formation of bulk doped CeO_2. This would require E_{vac} to be more negative than E_f is positive.

In contrast, the Gd doped system appears to destabilize due to the introduced oxygen vacancy. This destabilization is merely a consequence of the fact that the vacancy concentration is higher than the nominal concentration required for charge compensation. Table 5.6 shows the vacancy formation energies for different configurations containing two Gd dopant ions and a single vacancy leading to exact charge compensation. In this situation, the vacancies also have a stabilizing effect on the Gd doped system. Note that the effect of different configurations without vacancies is quite small, all have defect formation energies within a range of 50 meV. The oxygen vacancy formation energies on the other hand are spread over a wider range, and show a correlation with chemical environment defined as the surrounding cation tetrahedron (*cf.* Fig. 5.1a). The oxygen vacancy appears to prefer multiple dopant cations in the tetrahedral surrounding in case of Gd doping. Based on the A and B configurations, there appears to be an improvement of the vacancy formation energy of 150 meV per Gd cation included in the tetrahedron. This shows good agreement with the association energy of 0.13 eV for the Gd-oxygen vacancy complex.[49] Furthermore, this is in line with earlier atomistic calculations of Catlow and collaborators, and supports the predicted instability of a pyrochlore phase for $Ce_2Gd_2O_7$ by Minervini and collaborators.[85, 86, 189] For La, which is also a trivalent dopant for CeO_2, an opposite trend was noted for the 50% doped system.[150]

Also for Cu and Zn dopants a beneficial behavior is observed when dopant cations are present in the tetrahedron surrounding the vacancy, although in these cases the effect is more pronounced. In addition, comparison of the vacancy formation energies at different dopant concentrations shows that also the dopant concentration (annex vacancy concentration) has a strong influence on E_{vac}. For Cu doping an increase with the concentration is shown, while a decrease for both Zn and Gd is seen. The origin of this different behavior may be either due to the dopant species or because the Cu system contains a too low vacancy concentration per dopant. In the latter case, increasing the Cu concentration also increases the system vacancy concentration. As a result, single oxygen vacancies may be able to interact with different Cu

Table 5.6: *Oxygen vacancy formation energies for different $Ce_{0.75}Gd_{0.25}O_{1.875}$ configurations. NV indicates configurations without oxygen vacancies. The different configurations are shown in Fig. 5.2. The number of Gd ions in the tetrahedron surrounding the vacancy is given.*

		E_{vac} (eV)			$\Delta V(\%)$
	NV^a	V_A	V_B	V_C	V_B
# Gd	na	0	1	2	1
A	2.380	−0.137	−0.273	−0.440	0.943
B	2.365	−0.037	–	−0.310	–
C	2.398	–	−0.392	–	0.871
D	2.402	–	−0.402	–	0.866

^{a} For the systems without vacancies, the formation energy E_f is presented. Note that the formation energy of a doped system with oxygen vacancies $E_{f,vac} = E_f + E_{vac}$.

ions, presenting a higher apparent oxygen vacancy concentration for the Cu ions. This reduces the effective vacancy deficiency increasing E_{vac}. The same interaction between the vacancies and the dopant elements would, in the case of Zn, result in an apparent over-compensation, or, in the case of Gd, even further increase the already present over-compensation.

B. Crystal structure.

Where the introduction of a homogeneous distribution of dopants mainly results in an isotropic lattice expansion, the addition of charge compensating oxygen vacancies also results in an increase of the angles between the lattice vectors. Although these changes tend to be quite small ($< 5°$ in $Ce_{0.75}Cu_{0.25}O_{1.75}$, and $< 0.5°$ in $Ce_{0.75}Gd_{0.25}O_{1.75}$), they are often anisotropic. As a result we define the change in the lattice parameter for doped systems containing oxygen vacancies as:

$$\Delta a_0 = \frac{(\sqrt[3]{V} - a_{CeO_2})}{a_{CeO_2}} \cdot 100\% \tag{5.5}$$

with a_{CeO_2} the lattice parameter of pure CeO_2 and V the volume per formula unit of the doped system. Table 5.5 shows both the change in the volume and lattice parameter for the Cu, Zn, and Gd doped systems. In each case, the oxygen vacancies result in an expansion of the volume (lattice parameter) compared to the system without vacancies, either compensating the lattice compression (Cu and Zn) or further increasing the lattice expansion.

In experiments, Bera *et al.* observe only a very small lattice contraction of -0.01% for a system with 5% Cu doping.[70] This is much less than we present here, but can easily be understood. Firstly, the Cu doped systems presented here, contain much higher Cu concentrations (25 and 12.5%) than the system of Bera *et al.*, and sec-

ondly, the oxygen vacancy concentration in the system of Bera *et al.* contains a much higher relative oxygen vacancy concentration than in the presented systems. As a result, the lattice contraction theoretically presented in Table 5.5 would be even further compensated if a higher vacancy concentration was used, indicating that values of the order presented by Bera *et al.* are reasonable (though small expansions should also be considered possible).

Comparison of ΔV for $Ce_{0.75}Gd_{0.25}O_{1.75}$ in Table 5.5 (+1.563%) to the values for $Ce_{0.75}Gd_{0.25}O_{1.875}$ in Table 5.6 (+0.9%) shows a clear dependence on the vacancy concentration. As a result, doped CeO_2 compounds should be expected to show breathing behavior under varying oxidizing atmosphere, such as for example car exhaust catalysts.

As would be expected from the vacancy induced $Ce^{4+} \longrightarrow Ce^{3+}$ transition, Table 5.5 also shows the volume (lattice parameter) to increase with the number of Ce atoms in the tetrahedral surrounding. This is also in line with earlier results obtained for $Ce_{0.5}La_{0.5}O_{1.75}$.[150]

C. Bulk modulus.

In the **Sec.** 5.4.1 it was shown that the introduction of vacancies has a strong influence on the CeO_2 BM. Unlike the volume and lattice parameter change, dopants and the oxygen vacancies have a compound effect on the BM (and TEC), as is seen in Table 5.5. It is also interesting to note that the chemical environment of the vacancy has only limited influence on the BM (compare the V_A and V_B values of the p222 supercell), when no charge over-compensation is present. Figure 5.7b shows that the decrease of the BM goes hand in hand with the increase of the TEC as was observed for systems without vacancies, showing this behavior to be a universal trend.

5.5 Conclusion

In summary, we have studied fluorite CeO_2 doped with several aliovalent dopants using *ab-initio* DFT calculations. Dopant concentrations in the range of $0 \leq x \leq 25$ % are investigated, and for Cu, Zn, and Gd dopants also the influence of additional oxygen vacancies is studied.

We have shown that for fluorite CeO_2 doped with an aliovalent dopant the lattice expansion shows Vegard law behavior under oxidizing atmosphere. In addition, the Shannon crystal radius of the dopant element can be simply calculated from the lattice parameter, indicating lowered coordination for (most) aliovalent dopants. The introduction of charge compensating oxygen vacancies results in an increase of the lattice parameter, which (partially) compensates the lattice contraction observed for small dopants.

As was previously found for group IV dopants, aliovalent dopants also show an inverse relation between the change in bulk modulus and thermal expansion coefficient. Different dopants give rise to different changes in the bulk moduli and thermal expansion coefficients, however, the introduction of oxygen vacancies has a much larger effect, and decreases the bulk modulus significantly.

Defect formation energies are calculated and compared to the oxygen vacancy formation energy to indicate the preference for bulk doping over segregation of the dopant. For the systems investigated we conclude that bulk (substitutional) doping is very unfavorable for Cu, Co, and Zn, while La, Gd, and Sm present themselves as very favorable bulk dopants. No clear correlation between the defect formation energy and either the covalent or calculated crystal radius appears to exist.

Vacancy formation energies are calculated for different configurations containing 25 and 12.5% Cu, Zn or Gd. For systems where the oxygen vacancies over compensate the charge deficiency due to the aliovalent dopant, the oxygen vacancies are found to be unstable, while being stable otherwise. Although oxygen vacancies are found to stabilize the systems, their contribution remains too small to make bulk doping favorable for Cu, Co and Zn.

CHAPTER

⑥

DFT study of $La_2Ce_2O_7$: disordered fluorite vs pyrochlore structure

There is one thing even more vital to science than intelligent methods; and that is, the sincere desire to find out the truth, whatever it may be.

–Charles Sanders Peirce (1839 - 1914)

The crystal structure of Lanthanum Cerium Oxide ($La_2Ce_2O_7$) is investigated using *ab initio* DFT calculations. The relative stability of fluorite- and pyrochlore-like structures is studied through comparison of their formation energies. These formation energies show the pyrochlore structure to be favored over the fluorite structure, apparently contradicting the conclusions based on experimental neutron and XRD. By calculating and comparing XRD spectra for a set of differently ordered and random structures, we show that the pyrochlore structure is consistent with diffraction experiments. For these reasons, we suggest the pyrochlore structure as the ground state crystal structure for $La_2Ce_2O_7$.

6.1   Introduction

Since the pioneering work of Zintl and Croatto,[210] $La_2Ce_2O_7$ has been studied for over half a century. During this time, $La_2Ce_2O_7$ and more generally the $La_xCe_{1-x}O_{2-x/2}$ compounds have been studied in the context of three-way automotive catalysts,[201, 202, 211, 212] as an ionic conductor in solid oxide fuel cells,[77, 151, 195] and as oxygen sensor. In recent years, it has also become of interest as a new material for thermal barrier coatings.[57–59] It might also be considered as a new buffer layer in combination with perovskite superconductors for the use in coated conductors on Rolling Assisted Biaxially Textured substrates (RABiTS).[67, 186, 213, 214]

Although this compound has been known for a long time, its crystal structure remains a point of discussion. The two competing models for the crystal structure are the disordered fluorite and the pyrochlore structures.

Many ternary oxides with the formula $A_2B_2O_7$, with +III ions A and +IV ions B, adopt a pyrochlore structure, making the latter a good candidate for the $La_2Ce_2O_7$ structure. Conversely, in many cases where a pyrochlore crystal structure is observed, the A and B ions are indeed lanthanides and/or transition metals. A pyrochlore structure (space group $Fd\bar{3}m$) can be obtained from a fluorite structure

(space group $Fm\bar{3}m$) with one eighth of the oxygen ions missing ($Fd\bar{3}m$ Wickoff $8a$ site, when placing the origin at a B cation). Each oxygen vacancy is surrounded by four B^{IV} ions ($16c$ sites), while six oxygen ions ($48f$ sites) are each surrounded by two A^{III} and two B^{IV} ions, and the seventh oxygen ion ($8b$ site) is surrounded by four A^{III} ions ($16d$ sites). The pyrochlore structure has a clear short-range order. It turns out to be stable only in a certain range of ionic radius ratios of the two cations. Outside this range, a disordered fluorite structure becomes more stable.[193]

This *disordered* fluorite structure for $La_2Ce_2O_7$ is obtained by random replacement of half the Ce cations in the CeO_2 cubic fluorite lattice by La cations. In addition, one eighth of the O anions are removed, also through random selection. This structure has the required stoichiometry and the crystal structure is a cubic fluorite with each cation site occupied by 0.5 Ce and 0.5 La atoms on average, and each anion site on average occupied by 0.875 O atoms. As a result, no short-range order is present in a disordered fluorite structure, in contrast to the pyrochlore structure.

The border between the stability regions of the disordered fluorite and the pyrochlore structures has been defined empirically to reflect the experimental data as well as possible.[189] With the ionic radius ratio for $La_2Ce_2O_7$ located very close to this border, $La_2Ce_2O_7$ itself becomes interesting for investigating the order-disorder transition in pyrochlores. Minervini *et al.* show in their theoretical study of disorder in pyrochlore oxides that $La_2Ce_2O_7$ lies at the boundary of stability for pyrochlore formation. They claim that in this boundary region $La_2Ce_2O_7$ remains a disordered fluorite structure, though the pyrochlore structure appears stable with regard to cation and anion disorder.[189]

Furthermore, there is a list of experiments which are in favor of the disordered fluorite structure. In their early neutron diffraction experiments, Brisse and Knop claim $La_2Ce_2O_7$ to have a disordered fluorite structure rather than a pyrochlore one.[193] But also more recent XRD experiments point towards a disordered fluorite structure, due to the lack of pyrochlore-specific peaks in the spectrum.[153, 209] It was also shown that this structure remains stable, even at very high temperatures.[57, 59]

In contrast, recent studies of $La_xCe_{1-x}O_{2-x/2}$ show a different behavior. XRD experiments by Bae *et al.*[195] show that the CeO_2 fluorite structure is maintained for La concentrations up to $x = 0.40$ (for $La_2Ce_2O_7$ $x = 0.50$), and only at higher La concentrations the pyrochloric ordering of the cations (La^{III} and Ce^{IV}) appears. These authors also observe that the lattice parameter does not expand in a linear fashion as was reported earlier by Chambonnet *et al.*[215], and assume this reduced expansion is due to the clustering of O-vacancies. Other authors find multiple non-linear regions in the expansion of the lattice parameter. Ryan *et al.*[194] link this behavior to the presence of two phases with different La concentration. Of these, the phase with the high La density shows a discontinuity in the lattice parameter just around 38% La, and a constant lattice parameter above 40% La. Though they do report observing local ordering in the system, unlike Bae *et al.*[195], they refrain from linking the second phase to a pyrochlore phase. In contrast, O'Neill and Morris find only a single phase in their investigation of $La_xCe_{1-x}O_{2-x/2}$.[216] However, they only go up to a La concentration of 10%, where Ryan *et al.*[194] observed the appearance of the second phase at a La concentration of $\sim 20\%$, indicating that below this
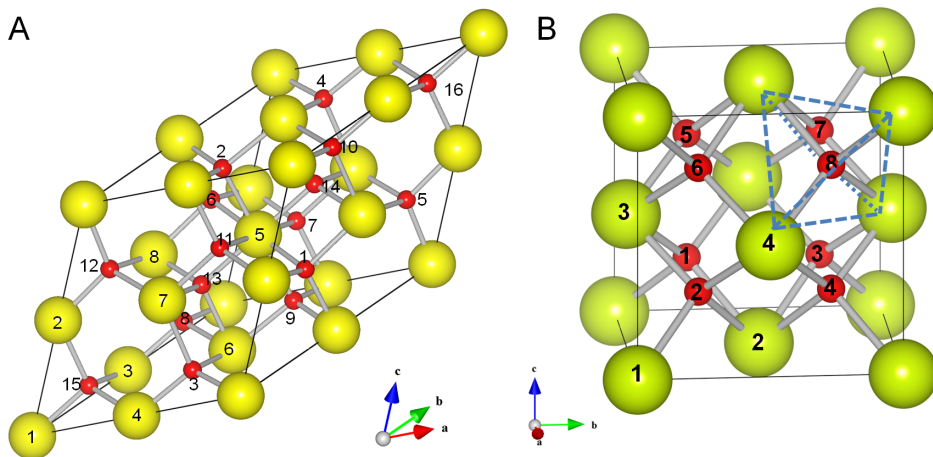
Figure 6.1: *Ball-and-stick representations of (A) the fcc primitive $2 \times 2 \times 2$ (p222) and (B) the cubic (c111) CeO_2 fluorite super cells. All the inequivalent Ce (big yellow spheres) and O (small red spheres) atom positions are indicated. The dashed tetrahedron on the cubic cell indicates the surrounding tetrahedron around the oxygen atom 8.*

La concentration, the second phase was either not present or not distinguishable.

As a result of this complex behavior, no definitive crystal structure has been established for $La_2Ce_2O_7$, and there exists only a single entry in the ICSD database, referring back to the work of Zintl and Croatto.[210, 217, 218] Experiments are interpreted in favor of the disordered fluorite as well as the pyrochlore structure, and some authors even refer to $La_2Ce_2O_7$ both as a pyrochlore and a fluorite structure in the same work.[219]

In this chapter we present an *ab initio* DFT study of the $La_2Ce_2O_7$ crystal structure. Based on the order–disorder contrast of the experimentally proposed pyrochlore and disordered fluorite structures, we focus on the effect of order in possible $La_2Ce_2O_7$ structures. By calculating and comparing the formation energies and XRD spectra for a set of different ordered and random structures, we show the pyrochlore structure to be favored over the disordered fluorite structure.

6.2 Theoretical method

Starting from the CeO_2-fluorite structure, the $La_2Ce_2O_7$ structure is obtained by replacing half of the Ce^{IV} ions by La^{III} (*i.e.* $CeO_2 \rightarrow La_2Ce_2O_8$), and, due to charge compensation, removing one eight of the O ions (*i.e.* $La_2Ce_2O_8 \rightarrow La_2Ce_2O_7$). This can be achieved in a large number of ways, resulting in both ordered structures and disordered structures. Because an exhaustive study is impossible within the DFT

Table 6.1: *O-vacancy and La positions for the different structures investigated. The tetrahedral surrounding of the O-vacancy is indicated as $xCeyLa$ with x and y the number of Ce and La atoms in the tetrahedron surrounding the vacancy. The notation NV indicates no vacancies are present in the system. The indexes are shown in Fig. 6.1A and B. The LZO and L111 structures are generated using the (fluorite) p222 unit cell (cf. Fig. 6.1A).*

	La positions	O-vacancies	space group
c111 $L1_0$ NV	1, 2	−	P4/mmm
c111 $L1_0$ 2Ce2La	1, 2	2	Cmm2
LZO NV	5, 6, 7, 8	−	Fd$\bar{3}$m
LZO 2Ce2La	5, 6, 7, 8	1, 6	C2/m
LZO 4Ce	5, 6, 7, 8	15, 16	Fd$\bar{3}$m
LZO 4La	5, 6, 7, 8	13, 14	Fd$\bar{3}$m
L111 NV	1, 6, 7, 8	−	R$\bar{3}$m
L111 3Ce1La	1, 6, 7, 8	15, 16	R$\bar{3}$m
L111 1Ce3La	1, 6, 7, 8	13, 14	R$\bar{3}$m

framework, and because the most prominent difference between the disordered fluorite and pyrochlore structures is their amount of short range order, our study can be confined to some highly ordered structures and a "random structure". This allows us to investigate the influence of cation-ordering on the stability of the system. Moreover, the chemical environment of the vacancies can be studied in this way.

The three ordered cation distributions we use are: the $La_2Zr_2O_7$ pyrochlore structure (LZO), the cubic CuAu $L1_0$ structure (c111 $L1_0$), with alternating La and Ce layers along the [001] orientation, and the L111 structure, with alternating Ce and La layers along the [111] orientation. Both the LZO and L111 structures can be constructed using the fluorite p222 primitive fcc supercell, shown in Fig. 6.1A, the $L1_0$ structure can be constructed using the cubic fluorite supercell, shown in Fig. 6.1B. For each of these structures a set of O-vacancies is chosen in such a way that all vacancies in a single system have the same chemical environment. Table 6.1 gives the positions of the La cations and O-vacancies in the unit cells used for these structures, and shown in Fig. 6.1A and B, and the resulting cation distributions are shown in Fig. 6.2A, B, and C. The tetrahedral surrounding (*cf.* Fig. 6.1B) of the vacancies is indicated as $xCeyLa$, with x and y integers giving the number of Ce and La cations in the tetrahedron. Cells without O-vacancies are indicated with NV.

All p222 cells, except the NV structures, contain two vacancies. To improve the comparability of the different structures, the two O-vacancies are always placed symmetrically around a single cation. This way we can assume the contribution to the formation energy due to the O-vacancy interaction energy to be the same for all p222 systems. As a consequence of this setup, all four cations surrounding the O-vacancy in the p222 cells are 6-coordinated. Note that we use the term coordination only to indicate the number of anions present surrounding the cation, not the number of
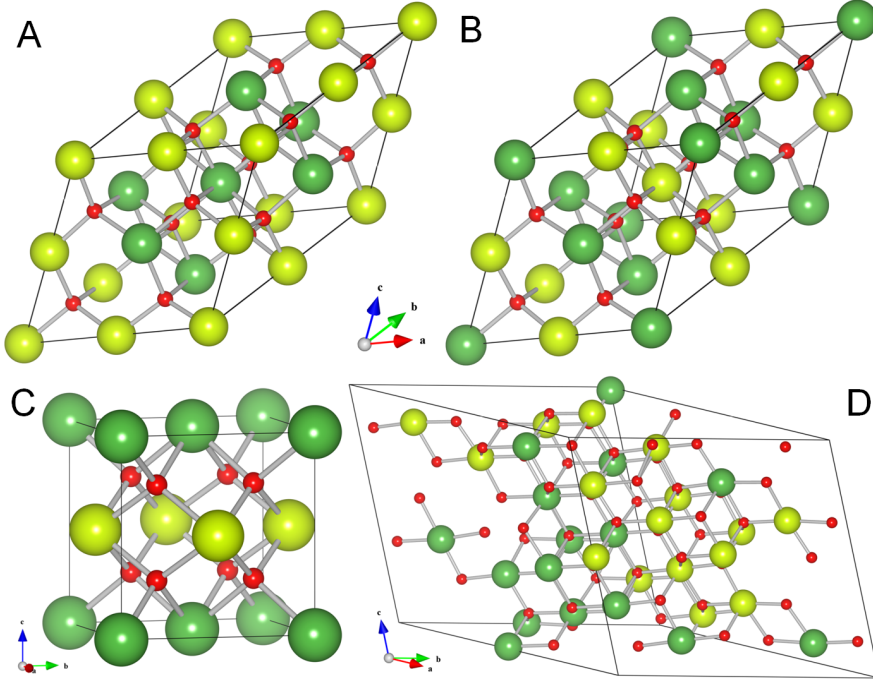
Figure 6.2: *Ball-and-stick representations of the different cation distributions, as constructed from Table 6.1 and Fig. 6.1 or taken from literature: (A) the LZO, (B) the L111, (C) the c111 $L1_0$ and, (D) the SQS distribution.[220] Red, green and yellow spheres show the O, La and Ce positions, respectively.*

anions the cation has an actual bond with.

There are several methods in literature to obtain physical properties of disordered or random structures. The most intuitive perhaps is the use of averaged potentials in the Virtual Crystal Approximation, where instead of using a specific potential for each ionic species one uses a potential representing the average atomic species present.[221] Another approach is the use of Monte-Carlo methods, and a statistical analysis of the results obtained. However, this method requires one to do thousands (or even more) of calculations, which is not feasible due to the size of our unit cell and the cost of DFT calculations. A third possible approach is the use of cluster expansions, where the configurational dependence of the physical property of interest is described as a sum over bonds or clusters. However, the configurational dependence of any variable can be described exactly by a cluster expansion only if all terms are retained, which is not the case in any practical implementation. Furthermore, predictions of the cluster expansion can depend sensitively on the choices made by the user with regard to for example input structures.[222, 223] We will make use of what is called a Special Quasi-random Structure (SQS). [224–226] This is a super cell

chosen in such a way that the correlation functions of the system resemble those of a truly random system as closely as possible. Although the super cell is a few times larger than a unit cell, and has no symmetry, the fact that we only need to do calculations with a single structure makes this technique orders of magnitude cheaper than a Monte-Carlo method. Neither is it necessary to use statistical methods to obtain system properties.

The main problem with using SQS is the fact that they need to be constructed first. For the pyrochlore(fluorite) system an SQS containing 88(96) atoms was previously given by Jiang *et al.*[220]. We use this SQS to investigate the physical properties of a disordered fluorite structure. A ball and stick representation is shown in Fig. 6.2D. Because all possible tetrahedral surroundings for the vacancies are present in this system, no tetrahedral surrounding is indicated.

The electronic structure calculations are performed within the DFT framework using the projector augmented wave (PAW) approach for the core-valence interaction and the Perdew-Burke-Ernzerhof (PBE) approximation for the exchange-correlation functional as implemented in the VASP code.[123, 137, 138, 165, 166] The kinetic energy cutoff is set at 500 eV and special k-point sets of $8 \times 8 \times 8$, $4 \times 4 \times 4$, and $4 \times 4 \times 4$ k-points are used for static self-consistent calculations in the c111, p222 and the SQS cells respectively. For the SQS cells a smaller $2 \times 2 \times 2$ k-point set is used during relaxation. To optimize the geometry a conjugate gradient algorithm is applied. Both ion positions and cell parameters are optimized simultaneously.

Because the $4f$ electron of Ce is known to be badly described in DFT at the PBE-level, we also performed calculations including on-site Coulomb corrections (PBE+U).[98, 227] The inclusion of on-site Coulomb corrections has been shown to provide a consistent treatment of Ce ions in ceria.[102, 105, 107, 110, 228] The choice of U for the Ce $4f$ electrons is found to be optimal in the range of 2–8 eV, depending on which property is under specific investigation.[101, 105, 107] For reduced ceria, and a consistent description of pure CeO$_2$ and Ce$_2$O$_3$, both Nolan *et al.*[228] and Andersson *et al.*[105] suggest for GGA+U a U$_{Ce}$ = 5.0 eV. Because La$_2$Ce$_2$O$_7$ contains a large amount of O vacancies, we will follow this suggestion.

In theoretical studies of La doping of ceria surfaces, it was also shown by Yeriskin and Nolan that an on-site Coulomb correction is required to correctly describe the localized hole on the O $2p$ state.[229] This localized hole results from the introduced La^{III} ion at a Ce^{IV} site. Since the La$_2$Ce$_2$O$_7$ structure can be interpreted as an extreme case of La doping we use the same U$_O$ = 7.0 eV on the O $2p$ states.

The XRD spectra are generated for the relaxed structures using the visualizer tool of the ICSD database.[217, 218]

6.3 Results and Discussion

6.3.1 Energetics

The energetics of the system are studied through comparison of the heat of formation ΔH_f and the vacancy formation energies E$_{vac,f}$ of the different configurations.

Table 6.2: *The heat of formation ΔH_f and vacancy formation energy $E_{vac,f}$ as calculated using Eqs. (6.1) and (6.2). The inter-vacancy distance $d_{vac-vac}$ is calculated as the distance between the centers of mass of the cation tetrahedra surrounding the O-vacancies. Due to the random nature of the SQS system no inter-vacancy distance is given. The notation NV is used to identify systems without vacancies. For the PBE+U calculations we use $U_O = 7.0$ eV on the O $2p$ states and $U_{Ce} = 5.0$ eV on the Ce $4f$ states for all calculations involved.*

	PBE			PBE+U		
	ΔH_f (eV)	$E_{vac,f}$ (eV)	$d_{vac-vac}$ (Å)	ΔH_f (eV)	$E_{vac,f}$ (eV)	$d_{vac-vac}$ (Å)
c111 L1$_0$ NV	1.177	—	—	1.280	—	—
c111 L1$_0$ 2Ce2La	0.758	-0.419	5.576	0.800	-0.480	5.570
LZO NV	1.167	—	—	1.364	—	—
LZO 2Ce2La	0.939	-0.229	4.829	1.105	-0.259	4.818
LZO 4Ce	-0.016	-1.183	4.861	0.220	-1.143	4.862
LZO 4La	1.668	0.501	4.812	1.620	0.256	4.803
L111 NV	1.169	—	—	1.564	—	—
L111 3Ce1La	0.452	-0.717	4.782	0.668	-0.896	4.787
L111 1Ce3La	1.352	0.183	4.843	1.420	-0.144	4.843
SQS NV	1.160	—	—	0.699	—	—
SQS	0.527	-0.633	n/a	0.607	-0.91	n/a

The heat of formation is calculated using:

$$\Delta H_f = \left(E_{tot} - N_{Ce}E_{CeO_2} - \frac{1}{2}N_{La}E_{La_2O_3} - \frac{1}{2}N_{O_{add}}E_{O_2}\right)/N_f, \qquad (6.1)$$

with E_{tot} the total ground state energy of the relaxed system, N_{Ce} and N_{La} the number of Ce and La atoms present in the system, E_{CeO_2} and $E_{La_2O_3}$ the bulk energy of CeO_2 and La_2O_3, $N_{O_{add}}$ the number of additional O atoms not accounted for by the CeO_2 and La_2O_3 formula units, and E_{O_2} the ground state energy calculated for a free oxygen molecule. The factor N_f is the number of formula units, which we define as the size of a supercell containing a single O-vacancy. The equivalent supercell is used for the systems without vacancies.

The O-vacancy formation energy $E_{vac,f}$ is calculated using:

$$E_{vac,f} = \left(E_{vac} + \frac{1}{2}N_{vac}E_{O_2} - E_{novac}\right)/N_{vac}, \qquad (6.2)$$

with E_{vac} and E_{novac} the ground state energies obtained for the systems with and without vacancies, respectively, and N_{vac} the total number of vacancies present in the system with O-vacancies. Negative values indicate a stabilization of the system. The resulting energies are shown in Table 6.2.

The calculated heats of formation and O-vacancy formation energies presented in

Table 6.2 show some clear trends with regard to the stability of $La_2Ce_2O_7$. If no O-vacancies are involved (*i.e.* $La_2Ce_2O_8$) PBE calculations show all possible cation distributions to be roughly degenerate. Including on site Coulomb corrections for Ce and O lifts this degeneracy and shows the disordered fluorite structure to be the most stable. However, $La_2Ce_2O_7$ contains 12.5% O-vacancies compared to the CeO_2 fluorite structure to provide the necessary charge compensation for the introduction of trivalent La in a tetravalent Ce position in the CeO_2 lattice. In contrast to the previous, the introduction of O-vacancies shows no qualitative difference between the PBE and PBE+U results. In both cases the introduction of O-vacancies is beneficial for the heat of formation. The sole exceptions are the systems with three or four La cations in the tetrahedral surrounding of the O-vacancy: L111 1Ce3La (PBE only) and LZO 4La (PBE and PBE+U).

Of all configurations studied, the LZO 4Ce system (*i.e.* the actual pyrochlore structure) has the most favored heat of formation and O-vacancy formation energy. It has a heat of formation that is roughly 0.5 eV/formula unit better than the SQS system, representing the disordered fluorite structure. Closer examination of $E_{vac,f}$ with regard to the tetrahedral surrounding of the O-vacancy shows the following order of increasing stability:

$$4La < 1Ce3La < 2Ce2La < 3Ce1La < 4Ce.$$

This shows there is a clear correlation between the number of Ce ions in the surrounding tetrahedron and $E_{vac,f}$. This result is independent of the introduced Coulomb correction, and results for both PBE and PBE+U functionals in an improvement of $E_{vac,f}$ with ~ 1.5 eV, going from the least to the most stable configuration. This also means that ordered structures containing Ce tetrahedra show large stability when the O-vacancies are enclosed in these Ce tetrahedra. On the other hand, structures with no Ce in the tetrahedron surrounding the O-vacancy show poor stability (Compare the LZO 4Ce and LZO 4La structures in Table 6.2. In both cases the cations have a pyrochlore geometry). Due to this stability trend for O-vacancy positions, it is clear why the disordered fluorite structure (*i.e.* SQS) is less favorable than ordered structures. Because of the random nature of the disordered fluorite structure, fewer pure Ce tetrahedra are present. In addition, because of their random distribution, the O-vacancies are also placed in less favorable surroundings than could be the case in ordered structures.

Irrespective of the correlation between $E_{vac,f}$ and the number of Ce cations in the tetrahedral O-vacancy surrounding, there still appears to be quite some variation in formation energies for the same surrounding when comparing the two 2Ce2La structures in Table 6.2. These two systems differ in two aspects: the inter-vacancy distance and the coordination of the cations in the system. This leads to the question which of both is responsible for the difference in vacancy formation energy.

We have studied two sets of additional systems, given in Table 6.3, to further investigate the influence of these aspects. The first set consists of the p222 $L1_0$ structure. This is the $L1_0$ distribution of the cations but this time constructed using a p222 unit cell (*cf.* Fig. 6.1 and Table 6.3). The O-vacancies are placed at opposing

Table 6.3: *O-vacancy and La positions for some additional structures. The 'L111 3Ce1La' structure of Table 6.1 has been repeated here as 'L111 3Ce1La A' for comparison.*

	La positions	O-vacancies	space group
p222 L1$_0$ NV	1, 2, 5, 6	–	P4/mmm
p222 L1$_0$ 2Ce2La	1, 2, 5, 6	1, 6	Imma
L111 3Ce1La A	1, 6, 7, 8	15, 16	R$\bar{3}$m
L111 3Ce1La B	1, 6, 7, 8	1, 7	Pm
L111 3Ce1La C	1, 6, 7, 8	7, 9	C2/m

Table 6.4: *The same as Table 6.2, for the additional structures. In addition, also the distribution of the Ce coordination is given. The c111 L1$_0$ 2Ce2La and L111 3Ce1La A structures are repeated from Table 6.2 for comparison.*

	Ce-Coord. (6|7|8)-fold (%)	PBE			PBE+U		
		ΔH$_f$ (eV)	E$_{vac,f}$ (eV)	d$_{vac-vac}$ (Å)	ΔH$_f$ (eV)	E$_{vac,f}$ (eV)	d$_{vac-vac}$ (Å)
p222 L1$_0$ NV	(0|0|100)	1.178	–	–	1.281	–	–
p222 L1$_0$ 2Ce2La	(50|0|50)	1.007	-0.171	4.784	1.115	-0.166	4.776
c111 L1$_0$ 2Ce2La	(0|100|0)	0.758	-0.419	5.576	0.800	-0.480	5.570
L111 3Ce1La A	(75|0|25)	0.452	-0.717	4.782	0.668	-0.896	4.787
L111 3Ce1La B	(50|50|0)	0.072	-1.097	3.960	0.198	-1.366	3.945
L111 3Ce1La C	(50|50|0)	0.123	-1.046	2.937	0.263	-1.301	2.934

sides of a single Ce cation,[1] reducing the inter-vacancy distance by about 0.8 Å compared to the c111 L1$_0$ structure. At the same time, the coordination changes from 7-fold coordination for all cations in the c111 L1$_0$ structure to 6-fold coordination for half the Ce and half the La ions and 8-fold coordination for the remaining cations in the p222 L1$_0$ structure. A second set of structures consists of L111 3Ce1La B and C (*cf.* Table 6.3), where the former L111 3Ce1La structure will be referred to as L111 3Ce1La A. Table 6.4 gives the energies, inter-vacancy distances and Ce-coordination for these systems.

Comparing L1$_0$ structures in Tables 6.2 and 6.4 shows that the heat of formation, ΔH$_f$, is exactly the same, as it should be, when no vacancies are present. However, with O-vacancies included, there is a significant difference in E$_{vac,f}$ of $0.2 - 0.3$ eV. This difference between the c111 and p222 L1$_0$ 2Ce2La systems is related to their different vacancy configurations. Comparing the three 2Ce2La systems studied, we

---

[1]The two O-vacancies, at positions 1 and 6 of the p222 cell shown in Fig. 6.1A, are located, due to periodic boundary conditions, at opposing sides of the La site 2, the Ce site 3, the La site 5, and the Ce site 8. This causes half the Ce cations of the system to have two neighboring O-vacancies, and half the Ce cations to have no neighboring O-vacancies. In contrast, every Ce cation in the c111 L1$_0$ system (*cf.* Fig. 6.1B) has exactly one neighboring O-vacancy.

Table 6.5: *Geometric data for the PBE and PBE+U results. We use the notation NV to indicate systems without vacancies. For these NV systems ΔV is calculated with regard to the volume of the equivalent CeO$_2$ fluorite cell, while for the other systems it is calculated with regard to the NV system. The lattice parameter a_0 (see text) is calculated as $a_0 = \sqrt[3]{V_f}$, and Δa$_0$ gives the change of this lattice parameter with regard to the lattice parameter of CeO$_2$ fluorite and the calculated lattice parameter of the NV system.*

	PBE				PBE+U			
	ΔV	a_0	Δa$_0$		ΔV	a_0	Δa$_0$	
			vs CeO$_2$	vs NV			vs CeO$_2$	vs NV
	(%)	(Å)	(%)	(%)	(%)	(Å)	(%)	(%)
c111 L1$_0$ NV	8.044	5.606	2.613	—	7.945	5.609	2.581	—
c111 L1$_0$ 2Ce2La	-1.260	5.582	2.180	-0.422	-1.631	5.579	2.021	-0.547
p222 L1$_0$ NV	8.080	5.606	2.624	—	7.947	5.609	2.582	—
p222 L1$_0$ 2Ce2La	-1.281	5.582	2.184	-0.429	-1.725	5.577	1.989	-0.578
LZO NV	8.328	5.611	2.702	—	8.479	5.618	2.750	—
LZO 2Ce2La	-0.668	5.598	2.473	-0.223	-1.533	5.590	2.222	-0.514
LZO 4Ce	0.108	5.613	2.739	0.036	-0.228	5.614	2.672	-0.076
LZO 4La	-2.889	5.556	1.704	-0.973	-3.793	5.547	1.434	-1.281
L111 NV	8.253	5.609	2.679	—	8.639	5.621	2.800	—
L111 3Ce1La A	-0.292	5.604	2.579	-0.097	-1.045	5.602	2.441	-0.350
L111 3Ce1La B	-0.081	5.608	2.651	-0.027	-0.889	5.605	2.495	-0.297
L111 3Ce1La C	0.299	5.615	2.781	0.099	-0.459	5.613	2.643	-0.153
L111 1Ce3La	-1.736	5.577	2.081	-0.582	-2.774	5.569	1.841	-0.933
SQS NV	8.530	5.614	2.766	—	9.173	5.630	2.969	—
SQS	-0.020	5.614	2.759	-0.007	-1.285	5.606	2.526	-0.430

find that both systems with half the Ce ions 6-fold coordinate are ~ 0.2 eV less stable than the third system (c111 L1$_0$ 2Ce2La), without 6-fold coordinate Ce.

The three L111 3Ce1La configurations can also be used to distinguish the effects of distance and coordination. Due to the three different inter-vacancy distances and the same Ce coordination for the B and C structures one can consider following scenarios: If a large O-vacancy distance is beneficial to the system then the O formation energies should be ranked A<B<C, with A the best configuration. Contrary, if the opposite is the case, namely clustering or coalescing of the vacancies is beneficial, the C case should be the best structure, giving rise to a ranking C<B<A. In both these scenarios the Ce coordination is assumed to have little or no influence. If on the other hand the inter-vacancy distance has little or no influence and the reduced number of 6-fold coordinate Ce cations causes the decreased vacancy formation energy, then the B and C case should be (nearly) degenerate and more stable than the A case. The resulting ranking should then be A>B=C.

Comparing the energies in Table 6.2 and 6.4 we see a significant improvement (~ 0.4 eV) in the heat of formation and O-vacancy formation energy for the B and C configurations compared to A. This change is comparable to the one found for the L1$_0$ 2Ce2La structures. Table 6.4 also shows the B and C configurations to be roughly degenerate. This shows that the improved energetics originate from the third scenario described above. The reduced number of 6-fold coordinate Ce ions causes a significant improvement of the formation energy $E_{vac,f}$. Upon closer examination we also notice that the B configuration is slightly more stable (~ 0.06 eV) than the C configuration, showing that also the O-vacancy distance plays a role, albeit a minor one, and, more importantly, that the vacancies repel each other.

The results of this section also give us some additional understanding on the structure of La$_x$Ce$_{1-x}$O$_{2-x/2}$. The above calculations show that for La$_2$Ce$_2$O$_7$ the Ce atoms prefer to cluster in tetrahedra around the O-vacancies, or vice versa, the O-vacancies prefer to appear inside Ce tetrahedra. If we assume that this behavior is also valid for La$_x$Ce$_{1-x}$O$_{2-x/2}$, then the transformation of CeO$_2$ to La$_2$Ce$_2$O$_7$ can be understood as follows: For low La concentrations, and thus low O-vacancy concentrations, the vacancies, imbedded in Ce tetrahedra, will be distributed homogeneously throughout the CeO$_2$ fluorite structure. With increasing La concentration the number of available Ce cations for Ce tetrahedra reduces while the number of O-vacancies increases. For a system where the cations are randomly distributed this means that at La concentrations of $> 42.8\%$ there are too few Ce-tetrahedra available to accommodate all the O-vacancies. This seems to coincide with the experimentally observed discontinuity in the lattice parameter observed by Bae *et al.*[195] As a result, the attraction between Ce cations and O-vacancies can thus be seen as the driving force for order in the La$_2$Ce$_2$O$_7$ system. Such a link between the ordering of the cation and anion sub-lattices is also found for other pyrochlores.[230] The resulting geometry at 50% Ce substituted by La, is then expected to be a highly ordered structure containing Ce tetrahedra surrounding the O-vacancies. This makes the pyrochlore geometry a very likely candidate for the La$_2$Ce$_2$O$_7$ geometry.

6.3.2 Lattice parameter

In addition to the energies, we also investigated the cell volume and lattice parameter. Table 6.5 shows the expansion and contraction of the system compared to the pure CeO_2 fluorite structure. Most configurations studied show small distortions of the lattice vectors compared to the cubic fluorite lattice. Only the LZO NV, 4Ce, and 4La configurations retained a cubic lattice.

Because the distortions of the different system lattices are all slightly different, it is impossible to extract a (consistent) lattice parameter from their basis vectors. However, since the distortions are relatively small, less than $4°$ for the lattice vector angles, and less than 3.5% for the lattice vector lengths, we instead choose to use a fictitious lattice parameter, which is determined as the edge of a cube containing a single formula unit, with the same mass density as the actual crystal.

Comparing the results in Table 6.5 shows the Coulomb corrections to have only limited influence on the geometry. Compared to the CeO_2 fluorite system, the $La_2Ce_2O_7$ systems without vacancies are roughly 8% larger in volume. The introduction of O-vacancies causes a small contraction of the lattice parameter of a few tenth of a percent compared to the NV systems. This contraction appears to be correlated to the amount of Ce atoms present in the tetrahedral vacancy surrounding; more Ce results in less contraction. This behavior can be understood as a consequence of the increase in ionic radius known for the $Ce^{IV} \rightarrow Ce^{III}$ transition.[180, 181]

It is also interesting to note that for the L111 3Ce1La cases the lattice parameter seems to increase with decreasing O-vacancy distance, in contrast to what is intuitively expected.

Looking at the three most stable configurations with regard to $E_{vac,f}$ of the previous section (LZO 4Ce, L111 3Ce1La B and C), we find that these are also the three systems having the largest lattice parameter. Their lattice parameter is 5.61 Å, which is $\sim 2.6\%$ larger than the normal CeO_2 fluorite structure. This is in good agreement with the experimentally observed value of $5.53 - 5.61$ Å for the $La_2Ce_2O_7$ lattice parameter.[57, 193, 195, 203, 204] It also shows good agreement with the experimentally observed relative expansion of $\sim 2.8\%$ by Ryan *et al.* and Bellière *et al.*[194, 204] In addition, the pyrochlore structure LZO 4Ce is the only one of these three structures which retained a perfect cubic lattice, as expected from experiment for $La_2Ce_2O_7$.[193]

6.3.3 X-Ray diffraction

An important argument in the discussion on the structure of $La_2Ce_2O_7$ is its XRD spectrum. The differences between the CeO_2 fluorite and a prototypical pyrochlore spectrum are very small and mainly related to the presence of the low intensity peaks of the pyrochlore (311), (331), and (511) reflections.[57, 195, 231] The strong similarity between the CeO_2 and pyrochlore spectra is due to the nearly equal X-ray scattering factors of La and Ce.[193] As a result very sensitive XRD experiments are required if one is to observe the low intensity peaks indicative of the pyrochlore
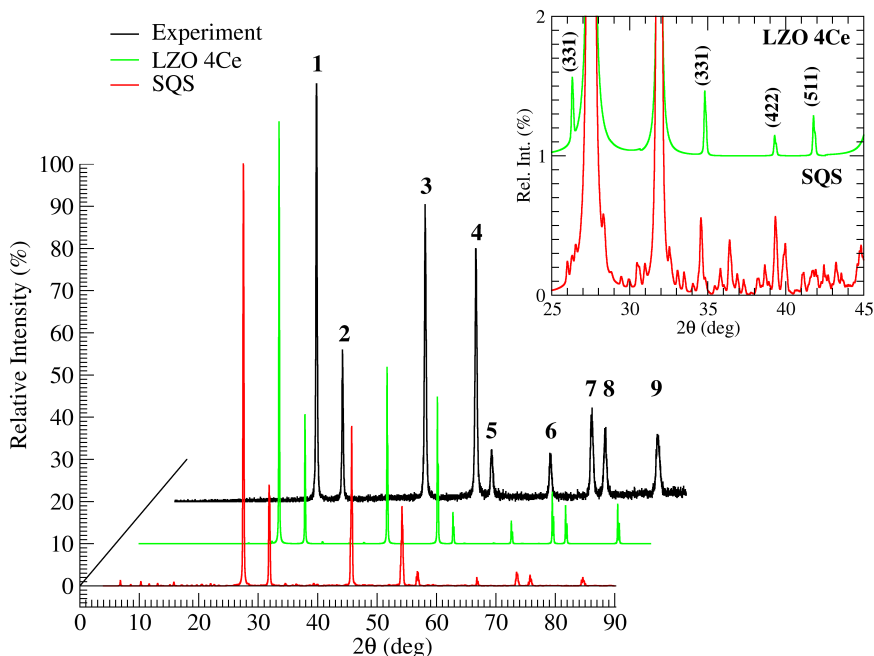
Figure 6.3: *Comparison of calculated XRD images for the disordered fluorite (SQS, red curve at the front) and pyrochlore (LZO 4Ce, green curve in the middle) geometries to the experimental La₂Ce₂O₇ spectrum (black curve at the back).[67] The relaxed PBE geometries are used to calculate the XRD spectra. The nine peaks with the highest intensity are indicated with indexes 1 through 9. All spectra are normalized with regard to the peaks with index 1. The inset shows a section of the spectra containing the pyrochlore (311), (331), and (511) peaks. The LZO 4Ce curve was shifted vertically by 1% for clarity.*

structure of $La_2Ce_2O_7$.

To address this point in the discussion, we calculated XRD spectra for all structures studied. Figure 6.3 shows calculated spectra of the SQS (disordered fluorite) and LZO 4Ce (pyrochlore) geometries in comparison to an experimental powder XRD spectrum of $La_2Ce_2O_7$.[67] The experimental spectrum shows nine clear peaks that can be identified with the fluorite peaks of CeO_2, no small secondary pyrochlore peaks are visible. This is in line with the XRD spectra of $La_2Ce_2O_7$ generally presented in literature. The two calculated spectra in Fig. 6.3 represent the spectra of the two possible structures for the $La_2Ce_2O_7$ structure. In both calculated spectra the nine experimental peaks are clearly visible and their position is still within 1° of the experimental position for the high angle peaks. Furthermore, no additional peaks with intensities > 1% are visible in the calculated spectra.

It is interesting to note that even if a pyrochlore geometry is used, the typical
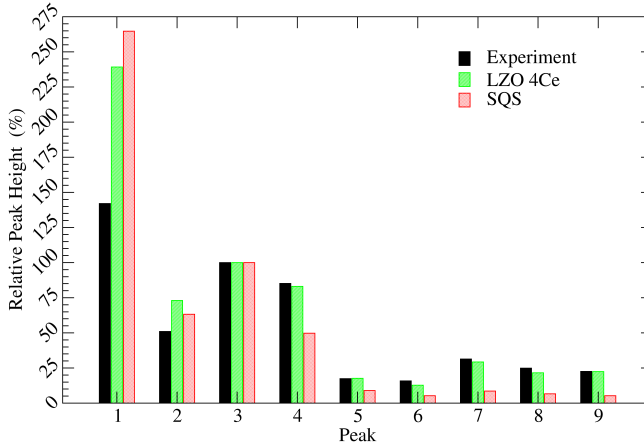
Figure 6.4: *Comparison of the nine high intensity peaks present in the spectra shown in Fig. 6.3. Scaling was done with regard to the third peak for each spectrum.*

pyrochlore peaks appear to be lacking. However, closer examination of the numerical data shows these peaks to be present, albeit at a much lower intensity than would be expected from other pyrochlore systems such as for example $La_2Zr_2O_7$. The (311), (331) and (511) peaks have an intensity of 0.5% or less (*cf.* inset Fig. 6.3). This explains why these peaks are not generally observed in experiments, but only in case of long time step scans.[195] This might lead to an erroneous assignment of the disordered fluorite structure to $La_2Ce_2O_7$. The SQS structure on the other hand presents a large number of very small secondary reflections. Though they might not be clearly distinguishable in experiments, they should introduce a noticeable additional background (*cf.* inset Fig. 6.3). This should be especially clear in experiments where increasing La concentrations in $La_xCe_{1-x}O_{2-x/2}$ are investigated. However, such experiments do not mention such behavior.[194, 195]

A thorough comparison of the nine high intensity peaks also favors the pyrochlore (LZO 4Ce) over the disordered fluorite (SQS) structure, as geometry for $La_2Ce_2O_7$. The relative peak heights of the former match the experimental peak heights much closer, as is shown in Fig. 6.4. We chose not to scale the spectra using the highest intensity peak since it appears to be overestimated for both geometries. By using a different peak as scaling reference the good correlation of the relative peak heights, with the experimental spectrum becomes much clearer.

As a final note, it is interesting to mention that the four high angle peaks, can also be used to exclude the other structures studied in this work. This is because of the broadening of those peaks due to multiple splitting. As a consequence, the
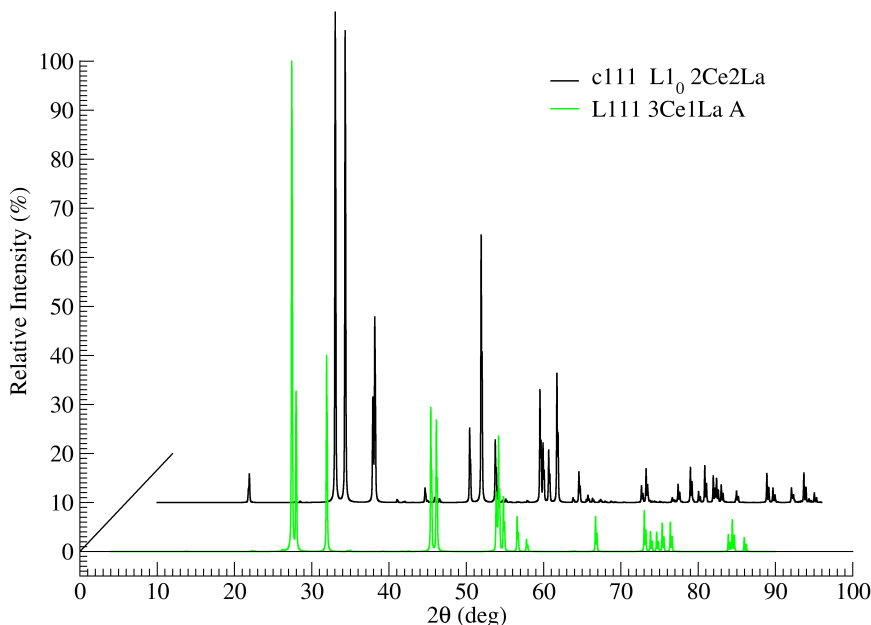
Figure 6.5: *Calculated* XRD *spectra of the* c111 L1_0 2Ce2La *and* L111 3Ce1La A *structures. Multiple peak splitting is clearly visible for the high angle peaks.*

two peaks between 70 and 80° merge into a near continuous set of reflections spread over a range of 5° in case of the L111 structures, and nearly 10° in case of the L1$_0$ structures. Two examples are given in Fig. 6.5. No simple reflections, as present in the curves of Fig. 6.3 are observed for those structures.

6.4 Conclusion

In this chapter the geometry of La$_2$Ce$_2$O$_7$ was studied using *ab initio* DFT calculations. Ordered and disordered structures were compared, modeling the pyrochlore and the disordered fluorite structures proposed for this system. Three aspects are taken into consideration: the lattice parameter, the enthalpy of formation and the XRD spectrum.

The calculated lattice parameters and relative lattice expansion of both the pyrochlore and disordered fluorite geometry are found to be in good agreement with the experimentally observed values. Of these the pyrochlore structure retained a perfect cubic lattice, while the disordered fluorite structure showed a small distortion.

Charge compensating O-vacancies are shown to play a crucial role in the stability

of La$_2$Ce$_2$O$_7$. If no O-vacancies are present (*i.e.* La$_2$Ce$_2$O$_8$) the disordered fluorite structure is the most stable geometry. However, if O-vacancies are included in the system, then the pyrochlore structure becomes the most stable geometry. So, in contrast to what is generally assumed in literature, La$_2$Ce$_2$O$_7$ is predicted to have a pyrochlore rather than a disordered fluorite geometry.

Total energy calculations have also shown a clear preference of the O-vacancies to be centered in Ce tetrahedra. This might be seen as a driving force in the formation of a pyrochlore geometry during La$_2$Ce$_2$O$_7$ formation. The formation of La$_2$Ce$_2$O$_7$, however, is beyond the scope of this work, and is, as such, a topic for further research.

The third aspect, the XRD spectra, show for both the disordered fluorite and pyrochlore geometry the nine distinct high intensity peaks observed for La$_2$Ce$_2$O$_7$ in experiment. Although the peak positions are in excellent agreement with the experimental positions, only the pyrochlore geometry presents relative peak intensities that are in good agreement with the experimental ones. Furthermore, the pyrochlore geometry also presents the typical pyrochlore reflection peaks, albeit with a lower intensity than expected from other pyrochlores.

Finally, both formation energies and calculated XRD spectra show a highly ordered structure to be preferred over a disordered structure, as model for the La$_2$Ce$_2$O$_7$ system. Of the structures considered in this work, the pyrochlore geometry is clearly favorable over the disordered fluorite geometry.

Part III

Atoms in Molecules

CHAPTER

⑦

Interlude: Atomic models

> *It could be that I've perhaps found out a little bit about the structure*
> *of atoms. You must not tell anyone anything about it...*
>
> –Niels Bohr (1885 - 1965),
> in a letter to his brother (1912)

The concept of atoms is an old and central one in chemistry. It is so intertwined with chemistry itself that it is nearly impossible to think of one without involving the other. Over time, several models describing atoms have come and gone. In this chapter, a short history of atomic models is given and the question of the existence of atoms in molecules is introduced, to provide a reference frame for the concept of atoms in molecules (and solids) of the next chapter. As we will see, the atoms of modern atomic models have evolved to less and less tangible entities, which has important consequences if one wishes to introduce them to the chemistry of molecules and solids.

7.1 The classical atom: From billiard ball to solar system.

7.1.1 An indivisible part of matter.

Already in ancient Greece and India, philosophers speculated on the nature of the world and its constituent components. Some assumed matter to be infinitely divisible, while others assumed the world consisted of atoms and empty voids. In the fifth century BC, Leucippus and his pupil Democritus proposed that there existed indivisible parts of matter which they called atoms (from the Greek $\alpha\tau o\mu o\varsigma$ meaning indivisible). These atoms had a size, shape and mass and other material properties were considered a consequence of the interaction between these atoms (e.g. salt atoms are sharp and pointed because of their taste). At this point it is important to note these atomic concepts were purely philosophical ones.

It was only at the end of the eighteenth and beginning of the nineteenth century, with the early development of (modern) chemistry, that further understanding in the nature of atoms developed. Based on the work of Antoine Lavoisier in 1789 (*principle of mass conservation*[1]) and Joseph Louis Proust in 1799 (*law of definite proportions*[2])

---

[1]The total mass reactants is equal to the total mass of the products.

[2]When a chemical compound is broken down in its constituent components, the component elements will always be present in the exact same mass proportions.
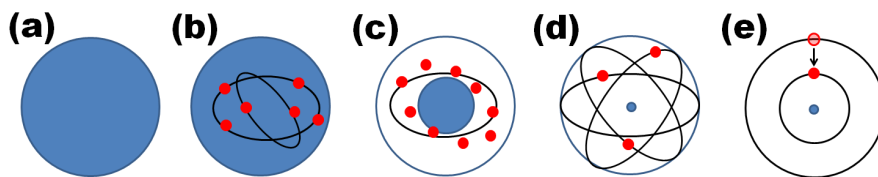
Figure 7.1: *Different atomic models: (a) the Dalton model, showing the atom as a unique single entity, (b) the plum pudding model of Thomson, with electrons on orbits inside a positively charged medium, (c) Saturnian model of Nagaoka, with electrons oscillating around orbits (one orbit shown here), the very small electrons are caught by an attractive force from the heavy nucleus they orbit, (d) Rutherford model with electrons on orbits around a small dens nucleus, (e) the Bohr model, which contains discretely separate orbits on which the electrons move, with transitions releasing or absorbing photons of an energy equal to the difference in energy between the orbits.*

John Dalton developed an atomic theory of matter which could elegantly explain the observations of Lavoisier and Proust. Dalton proposed that a pure chemical element only consisted of one unique type of atoms, which could not be changed or destroyed by chemical means (*cf.* Fig. 7.1a).[3] They could, however, be combined to form compounds. If different compounds could be formed from two elements, then the ratios of the amount of the second element for a fixed amount of the first would relate as small integer values.[4] With this model, published in his own textbook in 1808, Dalton introduced the first scientific atomic model, which allowed one also to deal with molecules and understand/explain simple chemical reactions.[232]

7.1.2 Electrons: where to put them?

With the discovery of the electron by Joseph John Thomson in 1897, the indivisible nature of atoms came to an end. It also led Thomson in 1904 to propose a new atomic model, in which:

> ...the atoms of the elements consist of a number of negatively electrified corpuscules enclosed in a sphere of uniform positive electrification...

> –Taken from Reference [233].

In this model the negative electrons are free to move on orbits or rings in a cloud or medium of positive charge (*cf.* Fig. 7.1b). The rings were stabilized by Gauss's Law

---

[3]Interestingly enough, he mistakenly assumed that pure elements could only be single atoms, giving rise to errors in both chemical formulae (*e.g.* he identified water as HO) and relative atomic weights. These errors were corrected by the work of Avogadro, who as a result correctly identified water as H_2O.

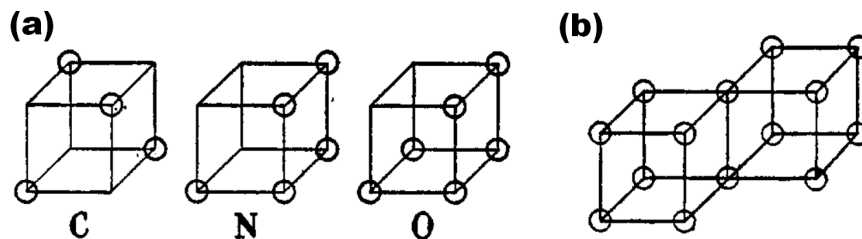[4]This is the law of multiple proportions

Figure 7.2: *In the cubical atomic model proposed by Lewis, electrons resided on the eight edges of a cube. Models for the carbon, nitrogen and oxygen atoms are shown (a) in addition to the representation Lewis used to present a single covalent bond between two atoms (b). Figures are taken from Reference [235].*

and interactions between the electrons themselves. Thomson also tried to make his model account for the observed spectra of pure elements, linking these to the energy differences between the different rings, but he remained unsuccessful in this.

At the same time different atomic models were also presented by Lewis and Nagaoka. Based on the argument that opposite charges are impenetrable, Nagaoka rejected Thomson's model and proposed his own in 1904.[234] In this model, based on an analogy with the stability of the Saturnian rings, all positive charge was located in a (small) very massive nucleus, with electrons revolving around it in rings, comparable to the Saturnian system, under the influence of electrostatic forces (*cf.* Fig. 7.1c). Though the idea of the small heavy nucleus was supported later by the work of Rutherford, the model was soon abandoned since the charged rings proved theoretically to be unstable. Around the same time, Gilbert N. Lewis developed an atomic model consisting of a cubical atom where electrons are positioned at the eight corners of the cube (*cf.* Fig. 7.2). This model, published in 1916, and later expanded by Langmuir, was phenomenologically based and intended to account for valency and explain chemical bonding.[235, 236]

In 1911 Ernest Rutherford concluded, based on the α-scattering experiments on thin foils of gold by Geiger and Marsden, that gold atoms contained a high positive charge concentrated in a very small volume of the atom, which also contained the bulk of its mass.[237, 238] This nucleus was then surrounded by a compensating charge provided by the electrons (*cf.* Fig. 7.1d). For the actual nature of the electrons position or motion he mentions the Saturnian model of Nagaoka. Because Rutherford calculated the core to have a radius more than one thousand times smaller than the actual atom, the analogy to a planetary system became even more striking. And when his student Niels Bohr simplified this view to a system containing only a few planet-like orbiting electrons, in case of light atoms, the model caught the imagination of the general public.

The atomic models at this time suffered one serious problem; they contained rings of electrons (*cf.* Thomson, Nagaoka and Rutherford models). Since classically charged
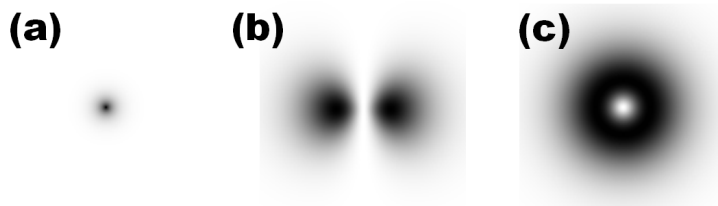
Figure 7.3: *The electron density $\psi(\mathbf{r})\psi^\star(\mathbf{r})$ for different orbitals of the hydrogen atom in the xy-plane. Dark regions indicate high electron density. (a) 1s orbital with a cusp at the nucleus, (b) the $2p_x$ orbital with two lobes symmetrically around the nucleus, (c) the sum of the $2p_x$ and $2p_y$ orbitals, indicating the spherical symmetry of the combined p-orbitals.*

objects undergoing an acceleration lose energy through continuous (electromagnetic) radiation, the electrons should also be losing energy and as a result they should crash into the nucleus. In 1913 Bohr extended and modified the atomic model of Rutherford with the proposition that the angular momentum of the electrons should be quantized to integer values of $\hbar$ (*cf.* Fig. 7.1e).[239, 240] As a result, only certain circular orbits are allowed, which in turn prevents the electron from spiralling into the nucleus. Transition of one orbit to another was now associated with the absorption or emission of a photon with a frequency ν related to the difference in energy between the two orbits. The Bohr model was successful in explaining the experimentally derived Rydberg formula, and gives very accurate results for the hydrogen atom. Although this model has since been superseded by quantum mechanical models based on the Schrödinger equation, it is still one of the most favorite models of representing (and teaching about) atoms. This is probably due to its relative simplicity and didactic benefits.

7.2 The quantum atom: A throw of the dice.

With the advent of (modern) quantum mechanics and its introduction of the particle-wave duality the nature of the atomic model changed drastically. The classical idea of the electron as a particle was replaced by an electron represented as a wave packet allowing for both a particle and a wave nature. As a result of the *Heisenberg uncertainty principle*, Schrödinger, Pauli, Mulliken and others noted that it is impossible to assign an electron an exact position on the orbital it traverses. In response, Max Born suggested to describe the position of an electron in an orbital as a probability distribution based on the wave function of the electron. This probability distribution associated with the electron wave packet would then show how likely it is to find the electron in a given region of space.

In quantum mechanics, an atom, just like any other system, is described using the Schrödinger equation. In the case of atoms, it is possible to analytically solve
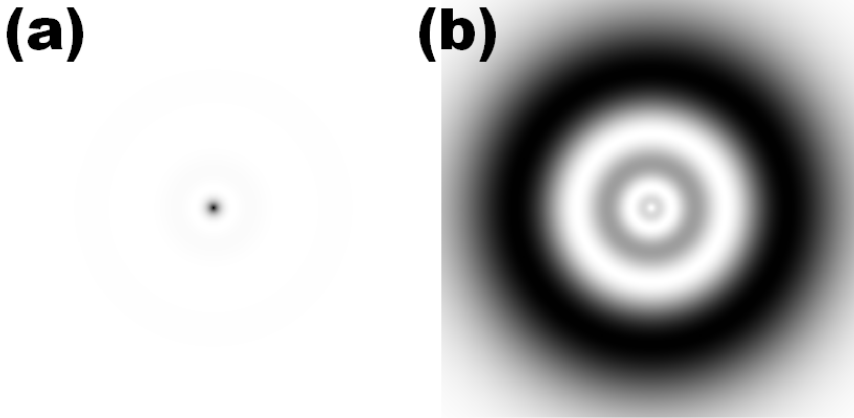
Figure 7.4: *Comparison of the electron density $\psi(\mathbf{r})\psi^\star(\mathbf{r})$ (a) and the radial probability distribution $\mathbf{r}^2\psi(\mathbf{r})\psi^\star(\mathbf{r})$ (b) for the 3s orbital of the hydrogen atom in the xy-plane. Dark regions indicate high electron density/probability.*

the Schrödinger equation only for the hydrogen atom, and hydrogen-like atoms[5]. For multi-electron systems the equation is solved approximately. When solving the Schrödinger equation for the hydrogen atom a set of energy states are obtained that can be linked to the principal quantum number n introduced by Bohr, who used it to indicate the orbits of the electrons in his planetary atomic model. The associated eigenfunctions of the atomic Schrödinger equation are called orbitals, and for multi-electron systems it is found that they are qualitatively similar to those found for the hydrogen atom. Unlike the orbits present in the Bohr model, the orbitals obtained from quantum mechanics are functions spread out over the entire space, which give rise to a probability distribution of where to find an electron (*cf.* Fig. 7.3). With regard to the Hydrogen 1s orbital it is interesting to note that although the electron density is highest at the nucleus, as is shown in Fig. 7.3a, the most likely position to find an electron in that orbital is, however, at a radius of 1 Bohr (= 0.52917721092(17) Å[241]). Because the electron density drops off too quickly, $\mathbf{r}^2\psi(\mathbf{r})\psi^\star(\mathbf{r})$ is also often plotted as a representation of the radial probability distribution, since it enhances for the s-orbitals the radii most probably to find an electron at. Figure 7.4 shows the electron density of the 3s with a clear cusp at the nucleus, but when multiplied with $\mathbf{r}^2$ the different shells become clearly visible with the highest intensity for the radial distance at which it is most probable to find an electron in the 3s orbital. Note also that the cusp at the nucleus has vanished and instead a ring shaped structure appeared.

For the 1s orbital of the hydrogen atom the highest probability of finding the electron is exactly at the Bohr radius, however, as is clear from the images in figures 7.3 and 7.4 there is a non-zero probability of finding the electron elsewhere in the

---

[5]*I.e.* atoms ionized such that only a single electron remains.

universe[6]. This diffuseness of the electron could be considered an argument in favor of density functional based theories, since these present an implementation which is closely related to the probabilistic interpretation of quantum mechanics.

7.3 Atoms in Molecules

Before the introduction of quantum mechanics, solids and molecules were considered to be built from finite and well defined pieces of matter. In the seventeenth and eighteenth century it was common to consider solids to be held together with microscopic hooks and barbs (e.g. Descartes), and a theory assuming the physical existence of such hooks was referred to as '*Cartesian Chemistry*'. This was in line with the classical work of Democritus. Newton, on the other hand, believed that atoms attracted one another through a force which decayed rapidly with the distance to the particle.[243] The two views coexisted for some time (*e.g.* Dalton imagined atoms hooked together to form molecules, while his contemporary Avogadro was convinced molecules were united through some form of attraction), and by the early twentieth century the idea of bonding through valence electrons had taken over. With the introduction of the Lewis cubical atoms and its representation of chemical bonds, Lewis notes that the electrons forming the bond cannot be said to belong to either atom exclusively.[235] This also changes the nature of atoms in molecules; molecules do not longer consist of clearly divisible parts which can be identified with neutral atoms, instead the atoms have become diffuse, sharing their electrons.

The introduction of quantum mechanics strengthens this diffuseness even further due to the diffuseness of the electrons themselves. In addition, all electrons need to be treated as being aware of the presence of the 'other atom(s)'. Despite this awareness, the concept of clearly identifiable atoms in molecules remains central in chemistry, and is founded in the general success of its practical applicability in experiments.[244, 245] Also the success of making atoms visible in experiments through several techniques, leading to stunning images of matter at the atomic scale as is for example shown in Ref. [244], adds to this search for atoms in molecules. As a result, many modern day quantum chemists set out in search for a way to decompose molecules into constituent atoms within the quantum mechanical framework.[173, 174, 246–252] However, from the quantum mechanical framework itself it is clear that one cannot decompose a system of interacting particles into a simple sum of pure (non-interacting) subsystems. Take for example the H_2 molecule, the Schrödinger equation of a single H atom centered at $\mathbf{r_p}$ and an electron at $\mathbf{r_e}$ is given by:[242]

$$\left[-\frac{\hbar}{2m_p}\nabla^2_{\mathbf{r_p}} - \frac{\hbar}{2m_e}\nabla^2_{\mathbf{r_e}} - \frac{e^2}{4\pi\varepsilon_0|\mathbf{r_p} - \mathbf{r_e}|} \right] \Psi_{H_a}(\mathbf{r_p}, \mathbf{r_e}) = E\Psi_{H_a}(\mathbf{r_p}, \mathbf{r_e}), \qquad (7.1)$$

---

[6]The center coordinate of the atomic core being the only exception.[242]

and the Schrödinger equation of the full H_2 is given by:

$$
\begin{aligned}
E\Psi_{H_2}(\mathbf{r_{p_1}}, \mathbf{r_{p_2}}, \mathbf{r_{e_1}}, \mathbf{r_{e_2}}) \quad = \Bigg[\quad & -\frac{\hbar}{2m_p}\nabla^2_{\mathbf{r_{p_1}}} - \frac{\hbar}{2m_e}\nabla^2_{\mathbf{r_{e_1}}} - \frac{e^2}{4\pi\varepsilon_0|\mathbf{r_{p_1}} - \mathbf{r_{e_1}}|} \quad (7.2) \\
& -\frac{\hbar}{2m_p}\nabla^2_{\mathbf{r_{p_2}}} - \frac{\hbar}{2m_e}\nabla^2_{\mathbf{r_{e_2}}} - \frac{e^2}{4\pi\varepsilon_0|\mathbf{r_{p_2}} - \mathbf{r_{e_2}}|} \quad (7.3) \\
& +\frac{e^2}{4\pi\varepsilon_0|\mathbf{r_{p_1}} - \mathbf{r_{p_2}}|} + \frac{e^2}{4\pi\varepsilon_0|\mathbf{r_{e_1}} - \mathbf{r_{e_2}}|} \quad (7.4) \\
& -\frac{e^2}{4\pi\varepsilon_0|\mathbf{r_{p_1}} - \mathbf{r_{e_2}}|} - \frac{e^2}{4\pi\varepsilon_0|\mathbf{r_{p_2}} - \mathbf{r_{e_1}}|} \quad (7.5) \\
\Bigg] \quad & \Psi_{H_2}(\mathbf{r_{p_1}}, \mathbf{r_{p_2}}, \mathbf{r_{e_1}}, \mathbf{r_{e_2}}).
\end{aligned}
$$

This Hamiltonian for the H_2 molecule shows that the Hamiltonian of a combined system is not just the sum of the single atom Hamiltonians (Eq. (7.2) and (7.3)), but there are also terms resulting from the interaction between the different nuclei and the electrons originating from the different atoms (Eq. (7.4)). Furthermore it also contains cross terms introducing the interaction of the electrons with the 'other' nuclei (Eq. (7.5)). Even if one would consider Hamiltonians of non-neutral H ions it would not be possible to construct the H_2 Schrödinger equation from a sum of single atom Schrödinger equations, since the cross terms in Eq. (7.5) would still be missing.

However, from the H_2 Schrödinger equation it is also clear that the sum of single atom Hamiltonians can be seen as a first order approximation, and depending on the relative size of the interaction terms, the approximation will be better or worse, and with it the applicability of a decomposition into 'free atoms'.[7] In case of large multi-electron atoms, the contribution to the Hamiltonian of the cross terms will be limited for the tightly bound core electrons, while larger for the more loosely bound valence electrons, reducing the overall effect.

It is, however, also possible to decompose the molecule in '*another type of atoms*', where the definition of the atom is defined as such that it fulfills certain requirements. These later types of atoms can be quite different from the atoms one is used to in "ball-and-stick" representations of molecules and solids. In such decompositions, an atom should rather be considered as a **tool**, a way of presenting the manifestation of the properties one is interested in. They provide a different view of a system, which can clarify certain behavior and properties. In the end, they may even contribute to answering the question of what an atom in a molecule actually is.

---

[7]In this a free atom should be considered as a single atom alone in the universe.

7.3.1 Different atom in molecule approaches

Over the years different atom in molecule decomposition schemes have been proposed of which a few much used examples are presented below:

Mulliken atoms in molecules (AIM) In this approach the density is decomposed not in real space but in Hilbert-space. For each molecular orbital the contribution to the population of a specific atom is obtained through multiplication of the overlap matrix with the density matrix (of that molecular orbital).[246, 247, 253–255]

Bader QTAIM The Quantum Theory of Atoms In Molecules (QTAIM) proposed by Bader and co-workers decomposes the electron density of the system in real space. In this topological approach the density is split in non-overlapping regions contained within zero-flux surfaces ($\nabla\rho(\mathbf{r}) \cdot \mathbf{n}(\mathbf{r}) = 0 \,\forall \mathbf{r}\epsilon$ atomic surface). Although this approach is widely used and provides good agreement with experimental observation of different properties, there are some issues. The fact that the obtained atoms have sharp edges (comparable to Voronoi[256] or Wigner-Seitz cells[257]) gives them a bit of an unnatural look, though it can be argued that this is just a matter of taste. However, something which I find worrysome is the fact that they appear geometry defined: atoms may appear different in different conformers. Even worse is the fact that the QTAIM approach sometimes produces atoms where non exist (*e.g.* at the center of a circular quantum corral), which is a truly scary aspect for an atoms in molecules approach. Though QTAIM might not provide 'true' atoms, it does provide us with important insights in the nature of solids and molecules, and should therefore certainly not be dismissed.[245, 249, 258, 259]

Hirshfeld approach Like the QTAIM, the Hirshfeld approach is a real space approach, however, in this case the atoms overlap as a consequence of the fact that in quantum mechanics a free atom is spread over the entire space. Because the atoms overlap, the density of the molecule is divided between all atoms in each point of space. This is done in a weighted fashion, using the density of a reference atom at similar distance to obtain the fraction of the contribution to the molecular density. This approach has the advantage that within information theory, the atoms in molecules are minimized with regard to the reference atoms. This latter point also has the unfortunate drawback that the obtained atoms in molecules depend strongly on the starting reference densities.[248, 259, 260]

Hirshfeld-I approach To overcome this problem, Bultinck and co-workers presented an iterative extension to the original Hirshfeld approach. In this approach, the reference density is updated on each iteration until convergence is obtained. As a result, the quality of the approach within information theory is maintained, but the dependence on the reference atoms is removed. In addition it was shown that this approach is basis set independent. In the

following chapter we will discuss the theory behind this approach in more detail.[173, 174, 260, 261]

7.3.2 Are there atoms in molecules and solids?

As may have become clear from the previous sections, this is not a well defined question, for the simple reason that the term "atom" may refer to many different entities, and as such the answer largely depends on the definition of the term atom. From the physical point of view, where an atom can be considered a building block of matter with unique properties I would consider the answer to be yes. However, this with the small addendum that this does not necessarily mean that the *exact identity* of the atom is maintained when it is introduced into a compound, either solid or molecule, and that it also does not need to imply that there still can be considered clear borders between different atoms in a solid or molecule. As such this view combines both chemical/physical intuition and experience, which resulted in what we now know as the periodic table of elements and gave rise to different experimental techniques for visualizing atomic structures, with quantum mechanical knowledge.

However, it does not present a way in which to decompose either solid or molecule into its component atoms, though the idea is attractive. With all this in mind, I think that a tool such as a scanning tunneling microscope (STM) can provide a better feeling for what an atom in a molecule/solid actually is. Depending on the used bias, the image of the system changes, showing individual '*atoms*' at one time, while showing larger structures where the individuality of the atoms is lost at another. It presents the duality of an atom in a molecule; individual at its core and without identity in its bonds.

The atom in a molecule approaches in the following chapter should in this sense only be considered as tools. Though they may result in physically and chemically relevant information and understanding, one should not expect them to represent actual non-interacting subparts of the system, at best only a first approximation to the latter.

CHAPTER

8

Extending Hirshfeld-I to bulk and periodic materials

The discovery of various phenomena has led to a recognition of the fact that the chemical atom is an individual which again is itself made up of several units into a selfcontained whole.

–Johannes Stark (1874 - 1957)

In this work, a method is described to extend the iterative Hirshfeld-I method, generally used for molecules, to periodic systems.[173, 174] The implementation makes use of precalculated pseudo-potential based electron density distributions, and it is shown that high quality results are obtained for both molecules and solids, such as ceria, diamond, and graphite. The use of grids containing (precalculated) electron densities makes the implementation independent of the solid state or quantum chemical code used for studying the system. The extension described here allows for easy calculation of atomic charges and charge transfer in periodic and bulk systems. The conceptual issue of obtaining reference densities for anions is discussed and the delocalization problem for anionic reference densities originating from the use of a plane wave basis set is identified and handled.

8.1 Introduction

One of the most successful concepts in chemistry is that of "atoms in molecules" (AIM). It states that the properties of a molecule can be seen as simple sums of the properties of its constituent atoms. An impressive amount of insights has been obtained from such a viewpoint, although a precise definition of an AIM remains elusive.[245, 258, 262] All AIM methods have the common purpose of trying to improve our understanding of chemical concepts such as molecular similarity and transferability between molecules.[259] Since the concept of AIM is basically about how one should divide the electrons, more specifically electron density distribution (EDD) $\rho(\mathbf{r})$ in the molecule between the different "atoms", this leads to two obvious categories of approaches in which most of the methods used for defining AIM can be divided. The first category of approaches is based on the wave-function/states of the system, and most of the work is performed in the Hilbert space of the basis functions used. One of the most famous examples here is the Mulliken approach.[246, 247] The second category of approaches is based on the division of the EDD as it exists in real-space. In these real-space approaches the molecule is split into atomic basins, that

can overlap such as in the Hirshfeld[248] and derived methods,[173, 174, 250–252] or that are non-overlapping such as in Bader's approach.[249]

The concept of AIM is strongly linked to the concept of transferability. Because both are central in chemistry, and chemists mainly focus on molecules, they are mostly used for molecules.[263, 264] There is, however, no reason why these concepts should not be applicable for periodic systems such as bulk materials. Even more, if these concepts are truly valid, they should hold equally well for solids as for molecules, and should provide additional insight in the chemical properties of defects, such as dopants, interfaces and adsorption of molecules on surfaces.

To this date we are aware of few implementations for periodic systems of the Hirshfeld and Hirshfeld-I approach, but their number is steadily rising. Martín Pendás *et al.*[265] investigated Hirshfeld surfaces as approximations for interatomic surfaces for LiF and CS_2 crystals. The Cut3D plugin of the ABINIT code can be used to calculate Hirshfeld charges,[266–269] and recently Leenaerts *et al.* implemented a "subsystem" based Hirshfeld-I method to study graphane, graphene fluoride and paramagnetic adsorbates on graphene.[270–272] Similarly, Spackman and collaborators presented subsystem-based Hirshfeld surfaces for molecular solids and implemented this in their Crystal-Explorer code.[273–277] In a recent publication Watanabe *et al.*[278] presented Hirshfeld results for metal–organic frameworks using the DDEC-code of Manz and Sholl.[252] The same code was probably also used in the investigation of charge injection in graphene layers by Rogers and Liu.[279] These authors present Hirshfeld-I charges, though they do not mention explicitly how these were obtained. In this DDEC code the function which is minimized is a linear combination of the function minimized in the Hirshfeld-I method, the one minimized in the iterative stockholder approach, and an additional term enforcing the constraint that all electron density is accounted for.[173, 174, 250–252] At the time of writing Verstraelen *et al.* showed that an excellent reproduction of the electrostatic potential (ESP) in silicates is possible using Hirshfeld-I charges.[280]

In this work, we have implemented an extension of the iterative Hirshfeld-I approach to periodic systems,[174] as a module in our HIVE-code.[172] The implementation makes use of grid stored EDDs, which can easily be generated by standard solid state and quantum chemical codes.

In **Sec.** 8.2 a short review of the parameters used in the solid state and quantum chemical codes is given. Afterwards the basic theory behind the Hirshfeld-I method is presented and extended to periodic systems. In addition, the spatial integration grid, pseudo-potentials and stored EDDs are discussed in view of the Hirshfeld-I method for periodic systems. In **Sec.** 8.3 the influence of the different grids on the accuracy is discussed. We also identify a delocalization problem in the radial EDDs which originates from the plane wave approach and periodic boundary conditions (PBC) used in the solid state code. This delocalization problem shows an inherent conceptual problem exists when reference densities need to be generated for anions. We shortly discuss this conceptual issue in **Sec.** 8.3.3 and indicate if and how it is handled in other implementations. We present two effective solutions ourselves, and show how these improve the obtained results. In **Sec.** 8.3.4 the influence of the inclusion of core electrons in the reference densities is presented. As a last point,

the atomic charges in some simple periodic systems are calculated, showing that the algorithm works correctly. Finally, in **Sec.** 8.4 some conclusions are given.

8.2 Methods

8.2.1 Atomic and molecular calculations

Hirshfeld-I calculations require EDDs as input. These can be obtained from electronic structure calculations using standard solid state or quantum chemical codes. In this work we have chosen to perform these calculations within the DFT framework using the projector augmented wave (PAW) approach for the core-valence interaction and the LDA for the exchange-correlation functional as implemented in the VASP code.[137, 138] The kinetic energy cut-off is set at 500 eV and the k-point set is reduced to the Γ-point for molecular and atomic calculations. For the bulk materials sufficiently converged k-point sets were used. To optimize the geometry of the molecules and periodic materials a conjugate gradient algorithm is applied. For molecular calculations only the atom positions are optimized, for bulk materials the cell parameters are optimized simultaneously. All molecules are placed in periodic cells of $20.0 \times 21.0 \times 20.5 \text{Å}^3$, which provide a sufficiently large vacuum region between periodic copies of the molecules, to prevent interaction.

Hirshfeld-I data computed using the approach detailed in the present study, are compared to those obtained using more common molecular calculations of AIM properties. For the set of 168 neutral molecules previously studied by Bultinck *et al.*,[174, 281] geometry optimization and Hirshfeld-I charge calculations are performed at the Local Spin Density Approximation[118, 282] level with the Slater exchange functional[283] and the VWN5 correlation functional[284] as implemented in Gaussian-03.[285] Numerical integrations are carried out using Becke's integration grid with 170 angular points in the Lebedev-Laikov grid.[175, 176] The Hirshfeld-I charges are considered converged if the largest change in charge of any atom is below 0.0005e.

8.2.2 Hirshfeld methods

The basic idea behind the Hirshfeld method,[248] also known as the stockholder method, is that the AIM share the electron density in each point of space. This means that the AIM EDD becomes a weighted partition of the molecular EDD. Formally this can be written as:

$$
\begin{aligned}
\rho_{mol}(\mathbf{r}) &= \sum_A \rho_A^{AIM}(\mathbf{r}) \\
\rho_A^{AIM}(\mathbf{r}) &= w_A^H(\mathbf{r})\rho_{mol}(\mathbf{r}) \qquad \forall \mathbf{r} \\
\text{with } \sum_A w_A^H(\mathbf{r}) &\equiv 1,
\end{aligned}
\tag{8.1}
$$

with $\rho_{mol}(\mathbf{r})$ and $\rho_A^{AIM}(\mathbf{r})$ the EDDs for the molecule and the AIM. All sums are taken over the entire set of AIM, and $w_A^H(\mathbf{r})$ is the Hirshfeld weight function for atom

A. From these equations the Hirshfeld weight can be written as:

$$w_A^H(\mathbf{r}) = \frac{\rho_A^{AIM}(\mathbf{r})}{\sum_B \rho_B^{AIM}(\mathbf{r})}. \tag{8.2}$$

Since the $\rho^{AIM}(\mathbf{r})$ are the EDDs sought, they cannot be used as input. The Hirshfeld method circumvents this problem by using spherically averaged reference state atomic EDDs $\rho_X^\circ(\mathbf{r})$. In the original paper by Hirshfeld the neutral atomic ground state is used as reference state.[248] When summing these isolated atomic EDDs over all AIM, one gets the so-called '*promolecular*' EDD instead of the actual molecular EDD:

$$\rho_{promol}(\mathbf{r}) = \sum_B \rho_B^\circ(\mathbf{r}). \tag{8.3}$$

It is then assumed that the difference between this promolecular EDD and the actual molecular EDD has only little influence on the Hirshfeld weight $w_A^H(\mathbf{r})$. As a result one can write the EDD of an AIM A as:

$$\rho_A^{AIM}(\mathbf{r}) = \frac{\rho_A^\circ(n_A^\circ, \mathbf{r})}{\rho_{promol}(\mathbf{r})} \rho_{mol}(\mathbf{r}), \tag{8.4}$$

where the population of the atom A is given by n_A°. In the original Hirshfeld approach, neutral atoms were used as reference. This, however, has been identified by several authors to be a major weakness of the method as changing the choice of the promolecular atom charges can have a highly significant effect on the resulting AIM[174, 245, 258, 286, 287] From eq.(8.4) it is easy to understand that the resulting $\rho_A^{AIM}(\mathbf{r})$ will tend to be as similar to $\rho_A^\circ(n_A^\circ, \mathbf{r})$ as possible[174, 262, 288], explaining why the Hirshfeld populations strongly depend on the choice of reference atomic EDDs. Fortunately, this problem can be resolved by using the iterative Hirshfeld-I scheme.[173, 174] For each iteration i, the obtained $\rho_A^{AIM}(\mathbf{r})$ are used to calculate the population n_A^i of each atom A. The (spherically symmetric) EDD $\rho_A^i(n_A^i, \mathbf{r})$ of a free atom A with population n_A^i is then used as atomic EDD in $w_A^H(\mathbf{r})$.[1] For each iteration the new promolecular density $\rho_{promol}^i(\mathbf{r})$ is obtained by summing the density distributions $\rho_A^i(n_A^i, \mathbf{r})$ for all atoms of the molecule. This setup is independent of the initial choice of atomic EDDs and the convergence of the iterative scheme is determined by the convergence of the populations of the AIM.[261, 289] Note that the first step in this scheme usually corresponds to the standard Hirshfeld method with $n_X^\circ = Z_X$. At this point it is important to note that the EDDs $\rho_A^{AIM}(\mathbf{r})$ and $\rho_A^i(n_A^i, \mathbf{r})$ will generally be different, despite having the same population. $\rho_A^i(n_A^i, \mathbf{r})$ is constructed as a spherically symmetric EDD, whereas $\rho_A^{AIM}(\mathbf{r})$ is a weighted part of the molecular EDD. The resulting EDD will generally be not spherically symmetric but show protrusions along the directions bonds are formed.

The extension of the Hirshfeld and Hirshfeld-I methods from molecules to bulk

---

[1]For integer value populations n_A^i the atomic EDD is obtained from the calculated ionic (spin-polarized) ground state. In case of fractional populations n_A^i, the EDD is obtained via simple linear interpolation between the EDDs for nearest higher and lower integer value populations.

and other periodic materials is quite trivial from the formal perspective. The main problem is located in the fact that a bulk system is considered to consist of an infinite number of "*atoms in the system*"(AIS). Calculating the atomic electron densities for all AIS can, for a periodic system, be reduced to only the atoms in a single unit cell since all periodic copies should yield the same results.

In addition to this, also the summation limits in Eqs. (8.2), (8.3) and (8.4) change. Where for molecules the sum over B is a finite sum over all AIM, it becomes an infinite sum over all AIS. Because atomic EDDs drop exponentially, the density contribution to the "prosystem" EDD $\rho_{prosys}(\mathbf{r}) = \sum_B^{AIS} \rho_B^{\circ}(n_B^{\circ}, \mathbf{r})$ of atoms at larger distances becomes negligible. This allows us to truncate the infinite sum to include only the atoms within a certain '*sphere of influence*' (SoI), *i.e.* all atoms of which the contribution to the prosystem EDD is not negligible. Within the iterative Hirshfeld-I scheme we then get:

$$w_A^{H,i}(\mathbf{r}) = \frac{\rho_A^{i-1}(n_A^{i-1}, \mathbf{r})}{\sum_B^{SoI} \rho_B^{i-1}(n_B^{i-1}, \mathbf{r})} \quad \forall A \; \epsilon \text{ unit cell} \tag{8.5}$$

where

$$\sum_A^{SoI} w_A^{H,i}(\mathbf{r}) \leq \sum_A^{AIS} w_A^{H,i}(\mathbf{r}) \equiv 1 \qquad \forall \mathbf{r}, \tag{8.6}$$

with i indicating the iteration step, and $\rho_A^i(n_A^i, \mathbf{r})$ the atomic EDD for an atom A with a population n_A^i given by

$$n_A^i = \int w_A^{H,i}(\mathbf{r}) \rho_{system}(\mathbf{r}) \mathrm{d}\mathbf{r}, \tag{8.7}$$

where $\rho_{system}(\mathbf{r})$ is the EDD of the periodic system.

8.2.3 Spatial integration of the population

In chemistry, due to the exponential decay of the electron density of atoms and molecules, and due to the sharp cusps present in EDDs at the atomic nuclei, atom centered grids are widely and successfully used. This makes them ideally suited for integrations such as given in Eq. (8.7). The multicenter integration scheme proposed by Becke splits up the full space integration into a set of overlapping atom centered spherical integrations.[175] To solve the problem of double counting in the overlapping regions a weight $h_A(\mathbf{r})$ is given to each point in space for every atom A in the system, such that

$$\sum_A^{AIS} h_A(\mathbf{r}) \equiv 1 \qquad \forall \mathbf{r}. \tag{8.8}$$

This weight function indicates how much a point 'belongs' to a certain atom A. The weight function can be binary, when the space is split up in Voronoi or Wigner Seitz cells,[256, 257] or smoothly varying, as is the case in the Becke scheme.[175] As
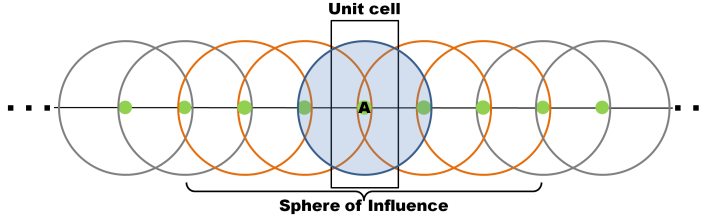
Figure 8.1: *Schematic representation of the integration scheme used for a linear periodic system of atoms (green discs). The black rectangle indicates the unit cell, and the circles indicate the boundaries of the spherical integration regions. The spherical integration regions for the atoms in the* sphere of influence (SoI) *of atom A are shown in orange, those outside are shown in grey. All integrations can be limited to the blue region (or sections thereof) around atom A (see text).*

a result, an integrand $F(\mathbf{r})$ can be decomposed as $F(\mathbf{r}) = \sum_A^{AIS} h_A(\mathbf{r})F_A(\mathbf{r})$ and the full integration becomes

$$I = \int F(\mathbf{r})\mathrm{d}\mathbf{r} = \sum_A^{AIS} \int h_A(\mathbf{r})F_A(\mathbf{r})\mathrm{d}\mathbf{r}, \tag{8.9}$$

where the sum over all AIS is again an infinite sum. However, in numerical implementations for periodic systems, the exponential decay of the atomic EDD allows us to truncate both the infinite sum and integration region of Eq.(8.9), without significant loss of numerical accuracy. The sum can be reduced to contain only the atoms included in the sphere of influence (SoI) of atom A (orange circles in Fig. 8.1), because only these atoms contribute significantly to the density in the integration region around atom A. In addition, the integration region for all atoms in the SoI can be reduced even further, without loss of accuracy, to only the region that overlaps with the spherical integration region of atom A (blue shaded disc in Fig. 8.1).

8.2.4 Grid stored electron densities and frozen core pseudopotentials.

In periodic systems, the use of PBC allows one to reduce the system size dramatically. For bulk materials this even allows simple systems, such as face-centered cubic Cu or Ni, to be represented using single atom unit cells. A useful side effect of such reduced cells is that it is easily possible and relatively cheap to store the EDD $\rho_{system}(\mathbf{r})$ on a three dimensional grid covering the unit cell, and thus fully describing the entire infinite system. The use of such precalculated electron density grids speeds up the Hirshfeld method significantly, since there is no more need to calculate the electron density at any given grid point starting from the wave function of the system. This also makes the implementation independent of the code used to

generate the electron density.[2] The drawback, however, is a slightly reduced accuracy. Since the electron density grid has a finite resolution, interpolation between the stored grid points is needed. This effect is discussed in the following section.

In chemistry, it is usually sufficient to consider only the valence electrons to describe the interactions between atoms. The core electrons are often considered inert as a result, and are kept frozen during calculations, greatly reducing the computational cost for heavy atoms. In the PAW approach an all electron frozen core contribution is used. This has two small but interesting side effects on the calculated radial charge distributions. Firstly, the integrated charge equals the number of valence electrons only, since the core electrons are not explicitly treated. Secondly, the resulting radial profile is not necessarily monotonically decreasing, showing a minimum or even negative values at the core of the atom (*e.g.* Fig. 8.4). The origin of this behavior lies in the practical implementation of the PAW pseudo-potentials.[137, 138] By using the same pseudo-potentials for generating the atomic EDDs and the EDD of the system under study, however, no errors are introduced since both systems contain the same frozen core contribution. Furthermore, it is known that for inorganic compounds, such as oxides, the oxygen atoms artificially absorb core electron density of (transition) metals. For this reason recent other Hirshfeld-I work in solids focused on valence densities only.[280]

Because the EDDs used in our implementation of the Hirshfeld-I method for periodic systems are valence only, and as a result the core electrons are not accounted for during the integration of the AIM densities, we implicitly add the core electrons exclusively to their respective atoms. On the one hand, this is fully in line with an atomic model where only the valence electrons are assumed to be involved in chemical interactions, such as bond formation. On the other hand, this can also be derived from the Hirshfeld weights defined in Eq. (8.2). Consider the atomic EDD as the sum of the core and the valence densities, then Eq. (8.2) can be written as:

$$w_{A,cv}^{H}(\mathbf{r}) = \frac{\rho_{A,core}^{AIM}(\mathbf{r}) + \rho_{A,val}^{AIM}(\mathbf{r})}{\sum_{B}\left(\rho_{B,core}^{AIM}(\mathbf{r}) + \rho_{B,val}^{AIM}(\mathbf{r})\right)}. \tag{8.10}$$

For these atomic densities it is reasonable to assume that for a given atom A the core electrons are contained within a certain core region $\mathbf{r}_{A,core}$. For any $\mathbf{r} > \mathbf{r}_{A,core}$ this means $\rho_{A,core}^{AIM}(\mathbf{r})$ is practically zero, and for $\mathbf{r} < \mathbf{r}_{A,core}$ it is reasonable to assume $\rho_{A,core}^{AIM}(\mathbf{r}) \gg \rho_{A,val}^{AIM}(\mathbf{r}) > \rho_{B,val}^{AIM}(\mathbf{r})$. As a result, Eq. (8.10) can in both regions be

---

[2]In theory, one might even use electron density data determined from X-ray crystallography. In that case however, there would be the problem of the choice of the atomic reference densities. One would have to use all electron atomic radial densities, which in itself is not really an issue. The choice of the functional, however, would be a bit of a wild card. Actual tests will have to be performed to investigate how significantly this choice influences the obtained results.

reduced. If $\mathbf{r} < \mathbf{r}_{A,core}$:

$$
\begin{aligned}
w_{A,cv}^H(\mathbf{r}) &= \frac{\rho_{A,core}^{AIM}(\mathbf{r}) + \rho_{A,val}^{AIM}(\mathbf{r})}{\rho_{A,core}^{AIM}(\mathbf{r}) + \sum_B \rho_{B,val}^{AIM}(\mathbf{r})} \\
&\cong \frac{\rho_{A,core}^{AIM}(\mathbf{r})}{\rho_{A,core}^{AIM}(\mathbf{r})} = 1 \quad ,
\end{aligned}
\tag{8.11}
$$

showing that within the core region the entire density is fully claimed by the respective atom. Outside the core region for $\mathbf{r} > \mathbf{r}_{A,core}$ one finds:

$$
w_{A,cv}^H(\mathbf{r}) = \frac{\rho_{A,val}^{AIM}(\mathbf{r})}{\sum_B \rho_{B,val}^{AIM}(\mathbf{r})} \quad ,
\tag{8.12}
$$

which is the valence only version of the Hirshfeld weight as it was defined in Eq. 8.2. In **Sec.** 8.3.4, we will test the validity of this assumption by comparing results of valence only EDDs with those of all electron EDDs.

8.3 Results and Discussion

It is clear that there is a growing interest in codes that can provide atomic populations, however, only few true bulk systems have been investigated using a purely atom based Hirshfeld-I method (*cf.* **Sec.** 8.1).[252, 265–280] For this reason most numerical tests in this work are performed on molecules, though we will investigate the behavior of periodic systems at the end of this section. As a first test system we have chosen the CO molecule. Its small size makes it easily suitable for quick test calculations, and its heteronuclear structure should result in a non-zero charge transfer, at least at equilibrium distance.

Before proceeding, the different grids used in our current setup of the Hirshfeld-I scheme for periodic systems are introduced. In this setup there are two 'types' of EDDs: that of the system and that of the free atoms/ions, which are indicated in the following as the subscripts '*sys*' and '*atom*', respectively. In this, 'system' refers to the object of which we want to obtain the atomic charges, and can thus refer to bulk materials, wires, molecules or even single ions. The free atoms/ions on the other hand refer to the single atoms which are used for the generation of the reference radial EDD ρ_X^i of Eq.(8.5). For both types there are two kinds of 3D grids involved:

1. Linear grids: Instead of using the analytical expression for the underlying wave function, we use the EDDs stored by VASP on a finite numerical grid. These grids span a single unit cell and use uniformly spaced grid points in direct coordinates.[3] (*cf.* **Sec.** 8.3.1) In the remainder, the following notation is used:

   - V_{atom} : The linear grid for the reference atom density distributions as obtained from the atomic calculations.

---

[3]In our setup we use the CHGCAR-file produced by VASP as input. Due to it's simple format this means that comparably formatted input can easily be generated for different solid state codes, making our setup independent of the used solid state/quantum chemical code

Table 8.1: *Differences in the Hirshfeld-I populations shown in Fig. 8.2. The presented change in population is the difference in population going from V_{sys}/V_{atom} grids with I grid points per Å, to grids with J grid points per Å. The respective grid changes are indicated as Δ_J^I.*
Top table: Differences along the curves shown in Fig. 8.2.
Bottom table: Differences between the curves shown in Fig. 8.2.

V_{sys}	V_{atom} (grid points/Å)		
	10	20	30
Δ_{20}^{10}	0.00738	0.00743	0.00744
Δ_{30}^{20}	0.00126	0.00128	0.00128
Δ_{40}^{30}	0.00049	0.00048	0.00049
V_{sys} (grid points/Å)	V_{atom}		
	Δ_{20}^{10}	Δ_{30}^{20}	
10	-0.00617	-0.00112	
20	-0.00612	-0.00111	
30	-0.00610	-0.00111	
40	-0.00611	-0.00110	

- V_{sys} : The linear grid for the (poly)atomic system under study

2. Spherical grids: These are atom centered grids which are not limited to a single unit cell. The spherical grids decompose into a radial and a shell grid. In our current setup, a logarithmic grid is used as radial grid, such that closer to the core the grid is sufficiently dense to describe this region accurately. The number of radial points was chosen to equal the numbers suggested by Becke.[175] At each point in this radial grid, a shell is located on which grid points are distributed according to a Lebedev-Laikov grid.[176] (*cf.* **Sec.** 8.3.2) The total number of grid points S equals the sum over all atoms of the number of radial points (R_A) used for that atom times the number of points on each shell (σ): $S = \sum_A R_A \cdot \sigma$. In the remainder only σ is varied to study the stability of the integrations. Two three-dimensional spherical grids are distinguished:

   - S_{atom} : Total spherical grid used to generate the reference spherically averaged radial density distribution for the atoms.

   - S_{sys} : The multi-center spherical grid for the system under study.

Note that the results of the Hirshfeld-I AIM analysis depend directly on S_{sys} but also indirectly on S_{atom} as this determines the quality of the isolated atomic EDDs.
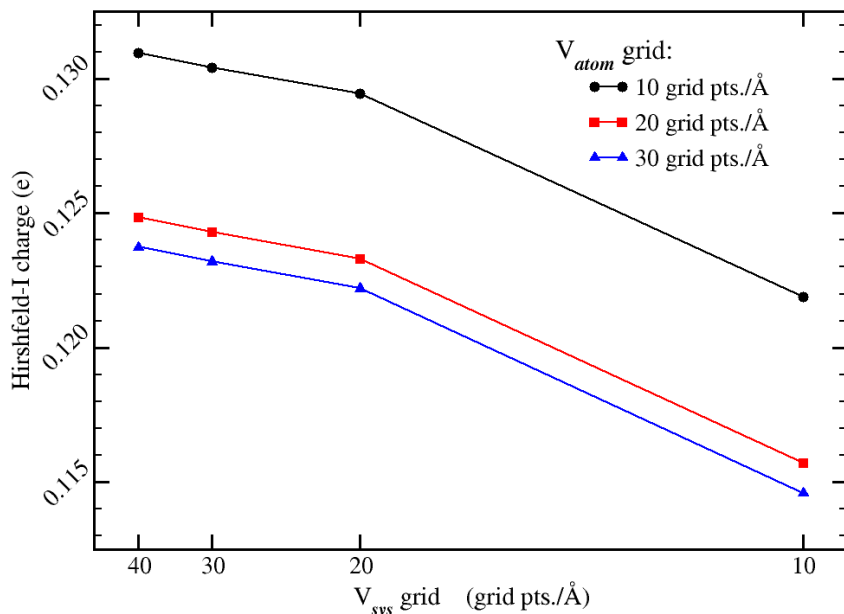
Figure 8.2: *The Hirshfeld-I charge for the C atom in a CO molecule as function of the V_{sys} grid resolution. The different curves show the results for the use of different resolutions in the V_{atom} grids, used for generating the atomic radial densities. In all molecular calculations we used spherical integration grids of 1202 grid points per shell.*

8.3.1 Electron density grids V_{sys} and V_{atom}

As was mentioned in the previous section, the use of precalculated grid-based EDDs introduces small inaccuracies due to the need for interpolation between the existing grid points. The charge of the C atom in a CO molecule as a function of the grid spacing used in the V_{sys} grid is shown in Fig. 8.2. The different curves are for different grid spacings used in the V_{atom} grids, from which the atomic radial EDD $\rho_C^i(n_C^i, \mathbf{r})$ and $\rho_O^i(n_O^i, \mathbf{r})$ are generated. It clearly shows the influence of both grids to be independent, since all curves have the same shape. Looking in detail at the exact numbers reveals that for both grids the same accuracy is obtained (*cf.* Table 8.1). This means that the same change in population of the C atom in CO is observed when either the V_{atom} or the V_{sys} grid is changed in an identical way; *i.e.* the change in the population (in absolute value) of the C atom is comparable when going from the black to the red curve and when going from a point at 10 grid points per Å to a point at 20 grid points per Å on the same curve in Fig. 8.2. Figure 8.2 and Table 8.1 also show that quite a dense mesh is needed to obtain very accurate results. Though

this is not a big problem for periodic systems with small unit cells, it could become problematic for molecules which require big unit cells to accommodate the vacuum required to prevent interaction between the periodic copies. The same is true for high accuracy V_{atom} grids, which are required for generating high accuracy atomic radial densities. Fortunately, these must only be calculated once, and the resulting high resolution radial densities can then be stored in a small size library containing only **r** dependent densities. In **Sec.** 8.3.3 the atomic radial EDDs are discussed in more detail.

8.3.2   Spherical integration grids S_{sys} and S_{atom}

Because the populations and charges in the Hirshfeld(-I) approach are obtained by integration of the EDD of the system, attention needs to be paid to the integration grid used. The current implementation uses a multi-centered grid, as was noted in **Sec.** 8.2.3. In this setup we used Lebedev-Laikov grids on the spherical shells of the integration grids.[176] Figure 8.3a shows the influence of the number of grid points per spherical shell on the accuracy; note the log-log scale used. In general, a denser grid results in a more accurate value for the population. However, different atoms in the same system, and the same calculation can show different convergence, as is shown by the curves of the C and O atoms of a CO molecule. To have the population of the system atoms converged to within 0.001 electron a few hundred grid points per shell are required. For a molecular calculation the multi-center grid, S_{sys}, only requires a few tens of thousands of grid points, as is seen in Fig. 8.3b. However, a Hirshfeld-I calculation for a bulk material such as diamond, which also has only two atoms in its unit cell, requires a multi-center grid S_{sys} with several tens of millions of grid points. This difference by a factor thousand originates from the fact that the SoI for the diamond unit cell contains a few thousand atoms, which all contribute to the total number of grid points that need to be evaluated. This makes it very important to reduce the SoI as much as possible in size without significant loss of accuracy.

8.3.3   Atomic radial EDDs

The atomic EDDs are calculated in a periodic cell under PBC, and stored on 3D electron density grids V_{atom} (*cf.* **Sec.** 8.3.1). The atomic radial EDDs are obtained from these through spherical averaging of the density distributions. Spherical averaging is done using the S_{atom} grid, with spherical shells containing Lebedev-Laikov grids of 5810 grid points.[176] The resulting distributions for different C ions are shown in Fig. 8.4a. The populations obtained by spherical integration over these distributions shows that the correct populations are obtained for the neutral and the positively charged ions. In contrast, the negatively charged ions show a population which is too small. Moreover, the curves in Fig. 8.4a increase again for longer ranges. At first glance, one might attribute this behavior entirely to the overlapping tails of periodic copies in neighboring cells. However, a rough extrapolation of the decreasing part of the curve (multiplied with the number of neighboring cells) shows a much
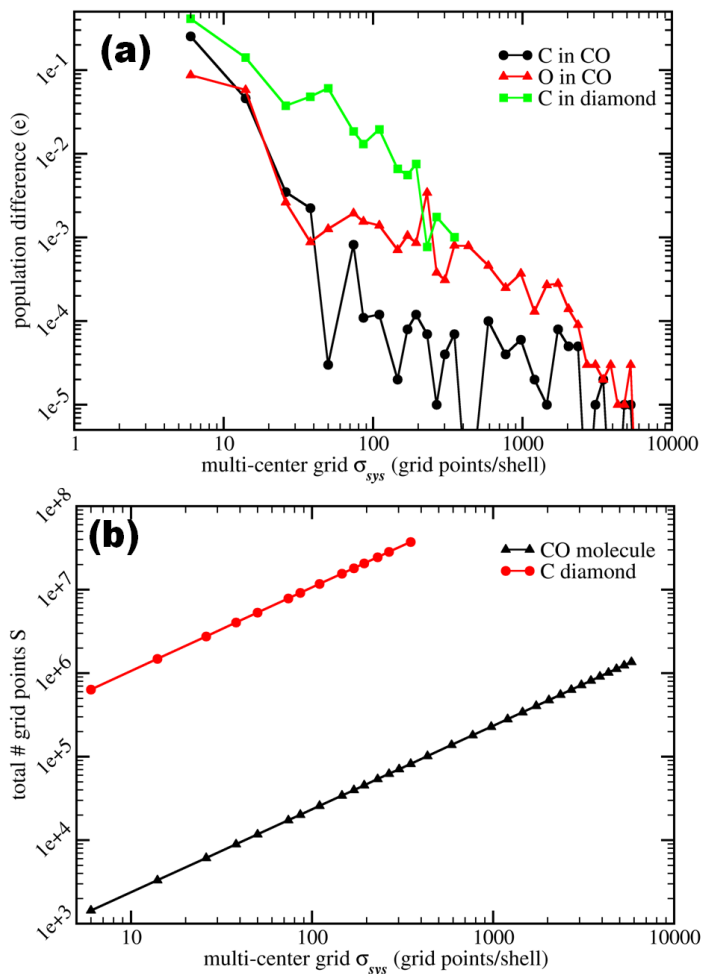
Figure 8.3: *(a) Convergence behavior of the population/charge as function of the number of grid points per spherical integration shell. For the C(black line) and O(red line) atom of the CO molecule the value shown is the absolute value of the difference between the calculated population and the calculated population using the most dense grid. In case of the C atom in the diamond system (green line) the charge should be zero, so the absolute value of the calculated charge is presented. (b) The total number of grid points as function of the number of Lebedev-Laikov grid points per spherical shell.[176] The large number of grid points for the diamond system, is due to its large SoI (see text).*
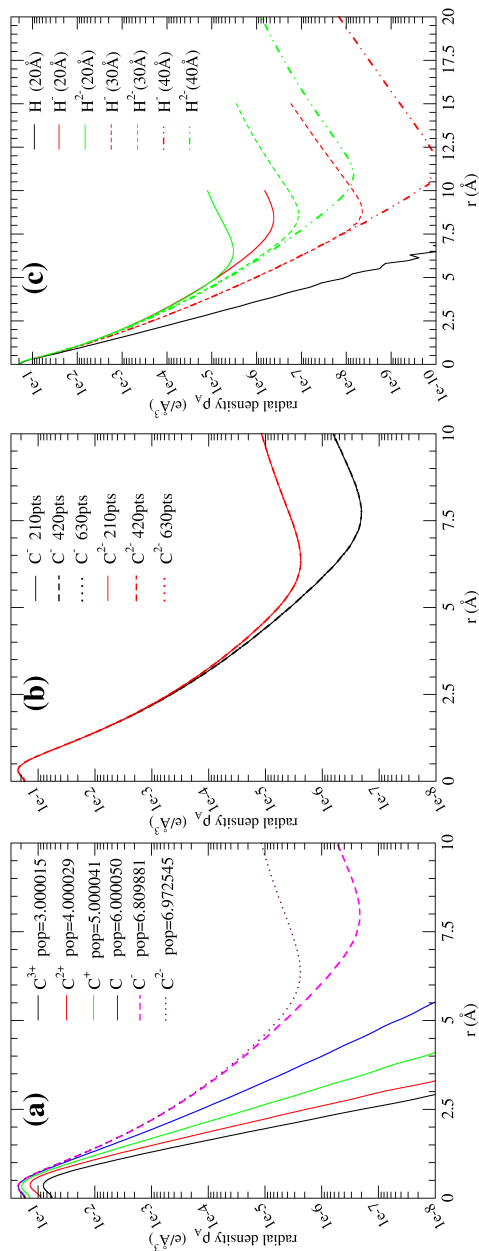
Figure 8.4: *Atomic radial electron densities $\rho_A(r)$ calculated from grid stored atomic charge distributions. (a) Radial electron densities for different carbon ions obtained from charge distributions in a cubic periodic unit cell of $20.5 \times 20.5 \times 20.5$ Å^3. The populations (pop) given of each ion are calculated by spherical integration of this radial distribution. (b) Radial charge distributions for two negative carbon ions obtained from the same size periodic unit cell as (a), but with different grid spacings: 210, 420, and 630 grid points per 20.5Å. (c) Radial EDDs for different hydrogen ions. For the H^- and H^{2-} ions the results for different unit cell sizes are compared: $20 \times 20 \times 20\text{Å}^3$, $30 \times 30 \times 30$ Å^3, and $40 \times 40 \times 40$ Å^3.*
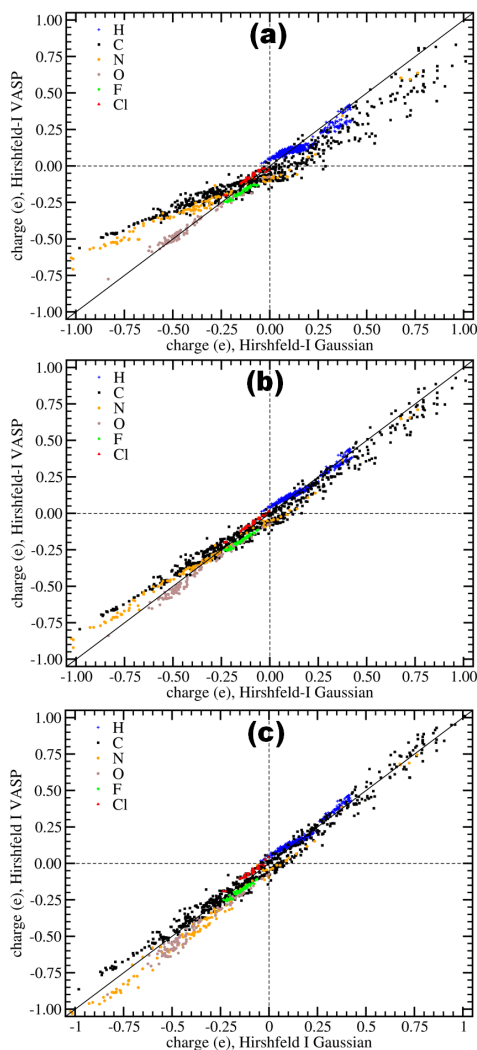
Figure 8.5: *Correlation plots of the charges obtained using the periodic Hirshfeld-I implementation and the standard all electron molecular implementation: (a) using the atomic radial density distributions of set R2 with the corrected tails, (b) using the R3 set with the corrected tails and normalized distributions assuming correct shape functions, and (c) using the R4 set with corrected tails and anion distributions normalized assuming piecewise linear interpolation of fractional densities (see text). In each case the* VASP *optimized geometry was used for the* VASP *based Hirshfeld-I calculations, while Gaussian optimized geometries were used for the reference calculations.*

lower electron density at a distance of 10 Å than is currently the case. The actual origin of the increase lies in the fact that the plane wave approach used for the atom calculations can only bind a limited amount of extra electrons to a given atom. This amount varies from atom to atom. As a result, it tries to place the excess electrons as far from the atom as possible. Due to strong delocalization inherent to plane waves these electrons are spread out over the vacuum between the atoms, with the highest electron density at the center of the unit cell; *i.e.* as far from the atoms as possible.

It is interesting to note that this artifact is purely due to the use of plane waves, which try to smear out the unbound electrons over the entire (empty) space. If one uses a (finite) Gaussian basis set instead, the additional electrons are 'bound' by definition through the basis set used, even if these electrons should not be bound to the atom anymore. In addition there looms also a conceptual dilemma: should one use such 'artifacts' as reference states or should one avoid them and restrict oneself only to reference systems that can exist. For example, take the O^{2-} anion. In the gas phase, the second electron is unbound by over 8 eV and one may suggest to use the O^- electron density instead. However, the computational repercussion of this would be that the Hirshfeld-I method would become unstable for systems where a higher charge is found than is available as ground state free anion. This behavior and conceptual dilemma is not unique to Hirshfeld-I. Other approaches using external reference atomic densities suffer it too, since it is inherent to the generation of external atomic reference densities (*e.g.* DDEC-code,[252] although this is not investigated by those authors). Some other approaches, like the iterative stockholder approach (ISA) of Lillestolen and Wheatley, appear to sidestep this dilemma by generating reference atomic densities as part of the iterative process.[250, 251] The drawback, in comparison to Hirshfeld-I, of such an approach is that the transferability of the reference atoms is lost. Also, the physical meaning of the reference atom in ISA becomes unclear. On the other hand, the ISA approach shows that the reference atomic densities are to be considered first and foremost 'tools'. This should alleviate the pressure on our conceptual conscience a little. Returning to the atomic reference densities used in Hirshfeld-I, it is possible to define them as the density of free ions in the gas phase. This definition is then softened such that also *useful* densities can be obtained beyond the range of ground state ions in the gas phase. This can be done in several ways: using meta-stable anion densities, binding the additional electrons through the basis set (Gaussian approach), or keeping the shape-function of the first anion and scaling it in an appropriate way such that the required number of electrons is found on integration. These last two methods correspond to the approaches presented at the beginning of this section.

From the modeling point of view one might prefer this latter type of pragmatism over the former, since we are interested in the EDD of the electrons for 'free ions', irrespective of their bound or unbound nature. Later in this section we will show how this delocalization problem can be solved in a simple way.

Fig. 8.4b shows that this artifact is independent of the resolution used for the V_{atom} grid, as the different curves nicely overlap. Fig. 8.4c shows the influence of the periodic cell size on this artefact. In case of the presented hydrogen ions, it shows that using a cubic periodic cell with a side of 20Å, the curves for H^- and H^{2-}

coincide in the short range region. Moreover, they don't show the expected exponential decay, and increase sharply at longer range. Using a larger unit cell appears to solve these problems: firstly, the radial distributions for the two anions become distinguishable, and show the expected exponential decay. Secondly, the point where the excess electrons start to interfere noticeably is pushed back to a larger distance. At this point it is interesting to note that for the DDEC-code this problem is not mentioned, although the references densities in the c1 method appear to be obtained in the same fashion as presented here.[252] Furthermore, from Fig. 8.4 it is clear that large unit cells are required for calculating correct radial reference densities for anions. For both C and H anions it is shown that a significant charge density is still present at a distance of 7–10Å from the nucleus making unit cells of $20 \times 20 \times 20$ Å^3 necessary to prevent additional overlap errors.

This type of behavior is seen for all atom types investigated, positive up to neutral ions give the expected radial distributions, while the negative ions seem hampered by the fact that only a fraction of the additional electrons can be attached to the atom. Fluorine and chlorine are in this respect exceptional since for these atoms also the F$^-$ and Cl$^-$ ions give good distributions and populations. This could be considered a result of the high electron affinity of these elements.

We find that for most negatively charged ions the populations are too small.[4] As a result, the calculated Hirshfeld weight $w_A^H(\mathbf{r})$ for a negatively charged AIM A is underestimated. The easiest way to compensate for this discrepancy is by scaling these specific distributions such that the correct population is found after integration. This way the shape function of the curve is maintained,[120, 290] but the resulting weights $w_A^H(\mathbf{r})$ increase. Another possible approach is based on the assumption that the fractional density is piecewise linear between integer charges.[174, 291, 292] This gives rise to an alternative way of normalizing the anion radial densities to present the correct integer charges. To investigate the effects of such a normalization and the erroneous tails shown in Fig. 8.4, we compare the results of four types of atomic radial density distributions. To that end, the reference set of molecules previously used in Hirshfeld-I studies by Bultinck *et al.*[174, 281] is used. This set consists of 168 neutral molecules containing only H, C, N, O, F, and Cl.

The first set of atomic radial EDDs, called R1, contains the density distributions as shown in 8.4a, where the radial distribution is obtained from a periodic cell of $20 \times 20 \times 20$ Å^3.

For the second set, which is referred to as R2, we have combined these results with the results from a periodic cell of $40 \times 40 \times 40$ Å^3 but with a lower grid resolution. In this case, the central part of the radial distribution is taken from the $20 \times 20 \times 20$ Å^3 unit cell with the high resolution grid and connected to the tail part obtained from the $40 \times 40 \times 40$ Å^3 unit cell. As a result, the high accuracy for the center part of the distribution is maintained, and the tail is corrected through the removal of the delocalized electron contribution. Note that for these distributions, the curves are limited to a distance of 10 Å from the core, i.e. the same maximum radius as is

---

[4]Note that for the DDEC-code no such corrections are mentioned for the similar c1 method. The effect of using such under-populated reference anions is shown by comparison of Fig. 8.5a to Fig. 8.5b or c.

available from the $20 \times 20 \times 20$ Å^3 periodic cells. Because the excess tail electrons are not included anymore, the spherically integrated populations of the negative ions are slightly smaller than they are for the R1 set.

For the third set, R3, the same procedure as for R2 is used, but this time the curves are normalized for the negative ions such that the correct population is given on spherical integration of these radial EDDs while retaining the original shape function.

The fourth set, R4, is obtained using the same procedure as for R2, fixing the tail part, and like R3 the resulting curves are then normalized for the anions. In this case, however, the starting assumption for this last step is that the fractional density is given by:

$$\rho(n + x, \mathbf{r}) = (1 - x)\rho(n, \mathbf{r}) + x\rho(n + 1, \mathbf{r}) \quad n \ \in \ \mathbb{N}, \ x \ \in \ [0..1], \qquad (8.13)$$

where $n+x$ gives the fractional population. In the present situation, $\rho(n, \mathbf{r})$ represents the density distribution of the neutral atom, and $\rho(n + x, \mathbf{r})$ the obtained density distribution for the anion. Note that for the $\rho(n + x, \mathbf{r})$ distribution the spurious tail has already been fixed at this point, resulting in the expected exponentially decreasing tail. Rewriting Eq. 8.14 gives:

$$\rho(n + 1, \mathbf{r}) = \frac{\rho(n + x, \mathbf{r}) - (1 - x)\rho(n, \mathbf{r})}{x} \quad n \ \in \ \mathbb{N}, \ x \ \in \ ]0..1]. \qquad (8.14)$$

The resulting $\rho(n + 1, \mathbf{r})$ yields the full anion charge of $n + 1$ upon spherical integration.

To test the accuracy of the results obtained in our periodic implementation using these four different atomic radial density distribution sets, we compare the results for a large benchmark set of molecules with those obtained by a Hirshfeld-I implementation based on a molecular program (*cf.* **Sec.** 8.2.1).

First, two sets of calculations are performed to check the influence of the geometry on the results. The first set used the optimized geometries obtained from Gaussian calculations, and the second set used optimized geometries obtained through VASP calculations. For both sets the R1 atomic radial distributions are used. Table 8.2 shows that the resulting correlations are nearly identical, despite the small differences in geometries for the two sets. Although the correlation coefficients r can be considered reasonable, the spread on the C and N data points is quite large. Furthermore, the slope of the linear fit of the C and N data is much too big. In both cases the intercepts are acceptably small.

Looking at the effect of fixing the tail of the atomic distributions, through the use of the R2 set of atomic radial density distributions, we see a slight increase in the slope for the C and N data, but in general the obtained values for the correlation, intercept and slope remain comparable to the previous sets of calculations. For the results obtained with the R2 radial distributions, Table 8.2 also shows the standard deviation of the difference between our calculated results and those of the reference data. The values of these standard deviations are similar for the first two sets, which are therefore not shown. Table 8.2 shows the deviation for the C and N data sets to
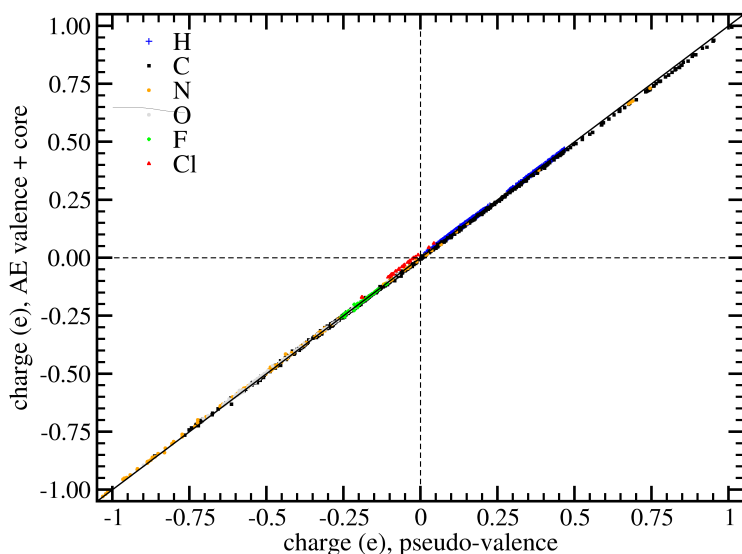
Figure 8.6: *Comparison of Hirshfeld-I charges for a set of* 168 *molecules using pseudo valence densities (method R4) and all electron (AE) valence+core densities.*

be one order of magnitude larger than for the other elements. It is unclear to the authors why specifically these two elements show such a bad behavior. Looking at the underestimation of the atomic population for the monovalent anions we find an error of roughly 0.5e for H and N, and 0.3e for C and O. On the other hand for F and Cl an underestimation of 0.1 and 0.0e, respectively, is found. The only aspect in which C and N differ from the other elements is that both can show large positive *and* negative charges.

The correlation results of the R3 atomic radial density distributions show a clear improvement over the previous results. For each data set the slope is closer to unity, though the intercepts remain as before. Especially the C and N results show a large improvement. Their standard deviation gets halved which is clearly visible in the correlation plots in Fig. 8.5a and b. This immediately shows that the simple scaling used for fixing the underestimated population due to the delocalization problem does not introduce large artifacts. In contrast, it actually suggests that the shape function of the radial EDD of the negatively charged ions contains roughly the same information as the Gaussian all electron EDD.

The results obtained with the R4 set show even better results. The correlation plot in Fig. 8.5c shows improved slopes for the C and N data. The slopes presented in Table 8.2 are closer to unity for nearly all elements, while small values for the intercepts are retained. The correlation and the standard deviation, however, have stayed roughly the same in comparison to the results of the R3 set. This shows that the R4 set can be used as a good approximation for the gaussian all electron EDDs.

Table 8.2: *The fitting and correlation results for the different sets of radial EDDs used in Hirshfeld-I calculations for a set of* 168 *molecules. The molecular geometries are either optimized with Gaussian or VASP. The radial distributions R1 are the default distributions obtained from VASP atomic density distributions. The radial distributions R2 contain a fix for the tail of the distribution, and the radial distributions R3 contain a fix for the tail of the distributions and in addition the resulting distributions are normalized to give the correct number of electrons (see text). The radial distributions R4 contain the same tail fix as R2 and R3, but the normalization makes use of the assumption that fractional densities show a piecewise linear behavior (see text). a and b are the slope and the intercept of the linear fit. r is the correlation with Gaussian molecular results, and σ gives the standard deviation.*

| | Gaussian geometry | | | VASP geometry | | | | | | |
| | R1 | | | R1 | | | R2 | | | |
	a	b	r	a	b	r	a	b	r	σ
H	1.187	−0.014	0.940	1.208	−0.019	0.944	1.185	−0.008	0.933	0.026
C	1.353	0.020	0.966	1.344	0.026	0.970	1.439	0.020	0.963	0.181
N	1.454	0.026	0.978	1.455	0.018	0.979	1.483	0.025	0.975	0.154
O	1.131	0.066	0.992	1.123	0.057	0.991	1.152	0.064	0.992	0.031
F	1.110	0.064	0.982	1.150	0.072	0.977	1.197	0.070	0.981	0.011
Cl	1.117	−0.009	0.979	1.124	−0.018	0.980	1.110	−0.013	0.966	0.015

| | VASP geometry | | | | | | | |
| | R3 | | | | R4 | | | |
	a	b	r	σ	a	b	r	σ
H	1.109	−0.021	0.979	0.016	0.997	−0.016	0.980	0.014
C	1.131	0.014	0.989	0.086	1.027	0.003	0.991	0.057
N	1.161	0.033	0.995	0.072	0.967	0.052	0.995	0.031
O	1.025	0.048	0.993	0.019	0.947	0.042	0.984	0.027
F	1.162	0.071	0.987	0.009	1.131	0.064	0.974	0.013
Cl	1.072	−0.018	0.993	0.007	1.024	−0.032	0.979	0.011

8.3.4   Inclusion of core electrons

From Eqs. (8.10)–(8.12) it was deduced that the atomic core density can be exclusively added to the atom it originates from. Furthermore, it was show that only the valence electrons are shared between different atoms, giving rise to the obtained atomic charges, in line with chemical intuition. To test the validity of this deduction, we have calculated the atomic charges for the set of benchmark molecules using the total all electron densities, and compared the results to those obtained with the R4 reference densities. Reference all electron core and valence densities are obtained in a similar way as before, and are summed to provide full all electron reference den-
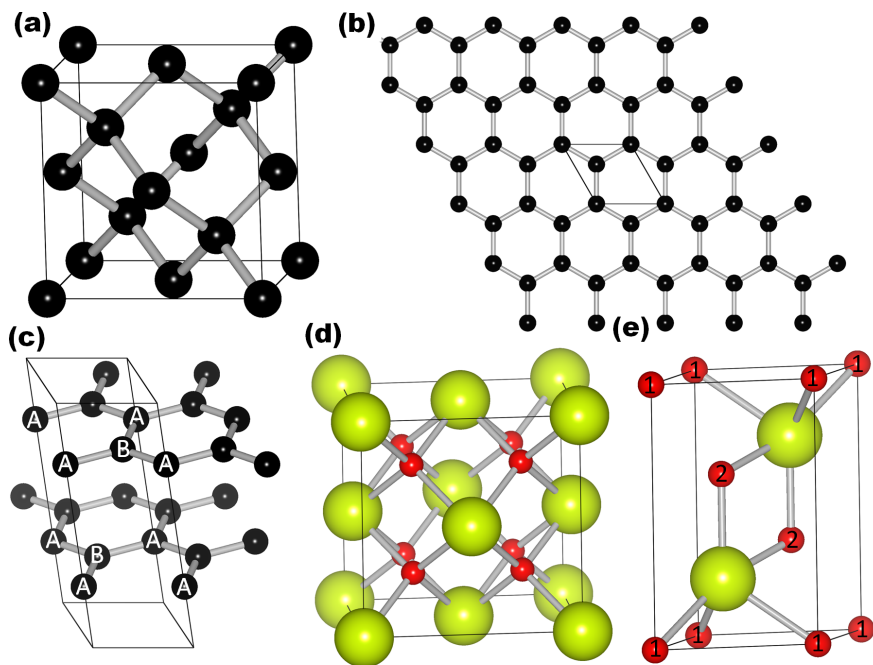
Figure 8.7: *Ball-and-stick representations of (a) the cubic diamond super cell, (b) the graphene sheet (unit cell indicated with black parallelogram), (c) graphite (unit cell indicated) in black, (d) the cubic CeO_2 super cell, and (e) the Ce_2O_3 unit cell. The black, red and yellow spheres indicate the positions of the carbon, oxygen and cerium atoms, respectively. The inequivalent C atoms in the graphite structure are indicated as A and B. The B atoms are always located at the center of the hexagons of the neighboring sheets. The inequivalent O positions in Ce_2O_3 are indicated as 1 and 2.*
The ball-and-stick representations are generated using the VESTA *visualization tool.[33]*

sities.[5] The same is done for the system EDDs, *i.e.* all electron core and valence densities are added to result in full all electron EDDs. As can be seen in Fig. 8.6, the obtained Hirshfeld-I charges for the valence calculations of the previous section, show excellent agreement with the full all electron results. The differences in the obtained atomic charges are generally below 0.01 e, and always smaller than the differences due to the use of a too coarse V_{sys} grids. This clearly shows the assumption based on Eqs. (8.10)–(8.12) is a valid one to make.

---

[5]VASP allows for the generation of all electron core (AECCAR0) and valence (AECCAR2) densities.

8.3.5 Periodic systems

In this final section some actual periodic systems are considered. The choice of the example systems is such that they can be used to verify that the obtained results are reasonable. As such these systems are in essence quite trivial. If they were not, then any results presented would be meaningless numbers, unless reference values are available in literature, of which there are at the time of writing very few. One might be tempted to use indirect ways of trying to verify the results (e.g. ESP fitting), but this generally complicates matters and obfuscates the validity of the results. In addition, small simple systems also keep the obtained results clear. For these reasons we have chosen the systems presented below. Their structures are presented in Fig. 8.7: the systems of choice are diamond, graphene, graphite, CeO_2, and Ce_2O_3. The diamond and graphene systems, have the property that all C atoms are equivalent, which should result in zero charges on all atoms. Graphite is quite similar to graphene, however, two inequivalent C positions are present (*cf.* Fig. 8.7c). The ceria systems on the other hand are chosen for the presence of Ce atoms with different valency; tetravalent Ce in CeO_2 and trivalent Ce in Ce_2O_3. Note that for both systems the same Ce pseudo-potential is used. Furthermore, in CeO_2, the O ions are all equivalent, while in Ce_2O_3 the Ce ions are equivalent but the O ions are not, only two of them are equivalent. Furthermore, for Ce_2O_3 we consider both the ferromagnetic (FM) and anti-ferromagnetic (AF) configurations, allowing us to check how strongly different spin-configurations influence the results in this system.

For all these systems we use the radial atomic EDDs of the R3 set, with the S_{atom} spherical integration grids containing 5810 grid points per shell. Table 8.3 shows the k-point sets used for the periodic systems, the number of atoms per unit cell and the number of atoms included in the SoI. The grid point separation for the V_{sys} grid for each of these systems was set to ≤ 0.01 Å. The Hirshfeld(-I) populations are calculated using spherical integration grids S_{sys} with 1202 Lebedev-Laikov grid points per shell.

The large number of atoms in the SoI with regard to the small unit cell sizes might make one wonder if this method can efficiently be used for larger (more interesting) systems. Due to the very nature of the SoI it are the small unit cells which have the highest cost per system cell atom. As the system cell grows, the relative weight of the SoI decreases and as a result it becomes relatively cheap to handle large supercells. This is clearly demonstrated in Fig. 8.8 where the scaling of the CPU time and the SoI is presented for a set of diamond system cells of varying size. The smallest cell is the unit cell containing 2 atoms, while the largest cell is a super cell of 128 atoms. Because our implementation does not make use of symmetry, a system containing 100 equivalent atoms is treated the same way as one containing 100 inequivalent atoms. This allows us to use the diamond system to test the scaling of the implementation. In addition, since all supercells present 'the same system', an equal number of Hirshfeld iteration are performed for all supercells to obtain convergence, making them ideally suited to check the scaling behavior. As can be seen in Fig. 8.8, going from the unit cell to the largest super cell the SoI roughly doubles, while the system cell has become 64× larger. On the other hand, the CPU time required for the Hirshfeld-I
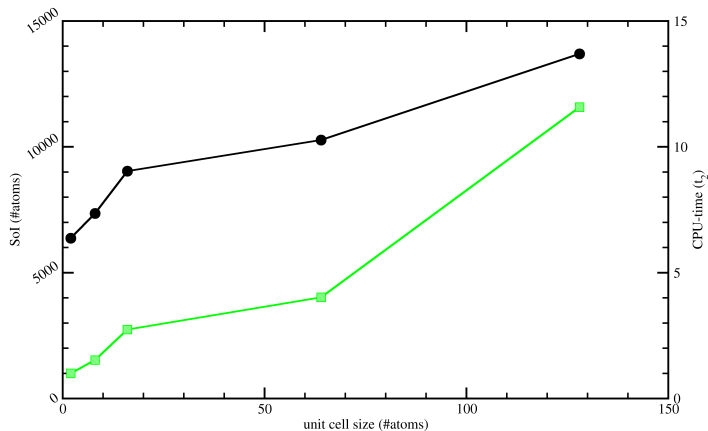
Figure 8.8: *Scaling behavior of the implemented Hirshfeld-I method. Black discs show the SoI in function of the system cell size (left axis), while the green squares show the required CPU time normalized with regard to the unit cell calculation (right axis).*

Table 8.3: *k-point sets and the number of atoms in the unit cell and SoI for the periodic systems under investigation. In addition, also the total number of grid points used for the spherical integration grid are given.*

	k-point set	atoms per unit cell	atoms in the SoI	grid points ($\times 10^6$)
diamond	$21\times21\times21$	2	6374	128
graphene	$21\times21\times\ 1$	2	1276	22
graphite	$21\times21\times11$	4	4618	104
CeO_2	$8\times\ 8\times\ 8$	3	3063	69
Ce_2O_3 FM	$10\times10\times\ 5$	5	3009	77
Ce_2O_3 AF	$10\times10\times\ 5$	5	3025	78

calculation is only increased roughly tenfold, again showing the beneficial trend for larger systems. From this it may be clear that this method is well suited for large systems, and we expect it could easily handle systems containing a few thousand atoms in the system cell. (Although this might not be the case for the solid state or quantum chemistry code used to provide the required EDDs.)

However, to investigate the obtained results we opted for small systems. The resulting Hirshfeld and Hirshfeld-I charges for the inequivalent atoms are shown in

Table 8.4: *Hirshfeld and Hirshfeld-I charges calculated using LDA generated EDDs. The geometries of the periodic systems are shown in Fig. 8.7 where the labels for the inequivalent atoms are given.*

		Hirshfeld (e)	Hirshfeld-I (e)
diamond	C	-0.00007	-0.00007
graphene	C	0.00000	0.00000
graphite	C_A	0.00113	0.00705
	C_B	-0.00115	-0.00707
CeO_2	Ce	0.59463	2.79393
	O	-0.30091	-1.40056
Ce_2O_3 FM	Ce	0.49081	2.32119
	O_1	-0.31318	-1.61119
	O_2	-0.33576	-1.51663
Ce_2O_3 AF	Ce	0.48575	2.32755
	O_1	-0.30825	-1.63062
	O_2	-0.33317	-1.51378

Table 8.4. It clearly shows the Hirshfeld values are closer to zero (i.e. the charge at which the atoms are initialized) than the Hirshfeld-I ones. This is the expected behavior and its origin was discussed earlier by Ayers[262] and Bultinck *et al.*[174] The diamond and graphene charges are (nearly) zero as one would expect based on symmetry arguments. This shows there are no significant artifacts which introduce spurious charges due to the PBC. The results for graphite are somewhat remarkable. Table 8.4 shows there is a small charge transfer going from the A to the B sites. This could be understood as a consequence of the very weak bonding between the A sites in different sheets. For each C atom, three electrons are placed in hybridized sp^2 orbitals, where the fourth electron delocalizes in distributed π bonds. For the A site C atoms, the contribution to the AIS charge of these π bond electrons is shared between the A sites of neighboring sheets. Since the C atom at the B site has no direct neighbor on the neighboring sheet the contribution goes entirely to this atom, resulting in the slightly negatively charged C atom. Charge neutrality results in a slightly positively charged C atom at the A site. Similar behavior was observed by Baranov and Kohout[293] using the Bader approach. These authors, however, find a larger and opposite charge transfer, resulting in a charge of $+0.08e$ and $-0.08e$ on the C_A and C_B atoms respectively. This difference could originate from the different methods used.

The ceria compounds show the behavior expected with regard to equivalent / inequivalent atoms. The Hirshfeld-I values presented in Table 8.4 are comparable with Bader charges presented in literature. Castleton *et al.* found for CeO_2 Bader

charges of +2.3e and −1.15e for Ce and O, respectively.[101] The Mulliken atomic charges for Ce in Ce_2O_3 presented in literature appear strongly dependent on the functional used, varying from +1.29e for PBE up to +2.157e for Hartree-Fock.[108, 294] The lack of Hirshfeld-I values in the literature makes it difficult to make a true qualitative assessment of our obtained results. However, our results appear to show an overall qualitative agreement with the results obtained from other AIM methods. Table 8.4 also shows there is a clear difference between the tri-and tetra-valent Ce ions, also the different configurations for the O ions show distinctly different charges. Looking at the relative atomic charges of the Ce and O atoms in CeO_2 and Ce_2O_3 we find the same relative order as was found by Hay *et al.*[108] and a difference in atomic charge for the Ce ions of comparable size. The different charges for the tri-and tetra-valent Ce ions might tempt one to consider these charges as indicators of the oxidation state if not the actual oxidation state of the atoms involved. As a result one could then assume that the same charge in a different configuration would be the result of the same oxidation state (*cf.* concept of transferability). Looking at the charges of the O atoms in both CeO_2 and Ce_2O_3 shows this is clearly not the case, since all O atoms formally have the same oxidation state, while the calculated Hirshfeld-I charges vary 0.2 electron. The Hirshfeld charges on the other hand show a much smaller variation of only 0.03 electron. At this point, it is important to stress that atomic charges do not, as opposed to what is often assumed, directly reveal the oxidation state, nor the valence of an atom. A Hirshfeld(-I) analysis, just like a Bader analysis, can only reveal atomic domains. The actual valence of an atom can be derived from the localization indices, which correspond in the simplest form to integrating twice the exchange-correlation density over the same atomic domain.[295, 296] Delocalization indices are obtained from double integration of the exchange correlation density over two different atomic domains.[297] Such matrices have been less thoroughly explored in solid state calculations.[293]

Another interesting point to note is that different spin-configurations have little to no influence on the obtained charges. This is seen when comparing the FM and AF configurations of Ce_2O_3. This means that for generating the required system EDDs for Ce_2O_3 a non-spin-polarized calculation suffices for the study of the system. Note, however, that the single atom calculations used to generate the reference radial densities are spin-polarized.

8.4   Conclusion

We have presented an implementation of the Hirshfeld-I method specifically aimed at periodic systems, such as wires, surfaces, and bulk materials. Instead of calculating the electron densities at each point in space on the fly using the precalculated wave function of the system, we interpolate the electron density from a precalculated EDD on a dense spatial grid, speeding up the calculation of the density significantly. The use of such grids is possible because PBC allow for the use of a relatively small grid to describe the entire system accurately.

Unlike total energy calculations, the number of atoms involved can not be fully

reduced to only those in the unit cell. Although, the populations only need to be calculated for the atoms in the unit cell, the Hirshfeld-I calculations require a large '*sphere of influence*' containing a few thousand of atoms. By selecting only the grid points which contribute significantly to the calculations, the computational cost of the used multi-center integration grids can be substantially reduced.

We have shown that the uniform grids used to store both the atom and the system EDDs have an equal influence on the accuracy of the final Hirshfeld-I calculated populations, leading to the suggestion of building the library of atomic radial EDDs using as dense as possible grids. In addition, we have shown that both different atomic types and different chemical environments give rise to a different convergence behavior as function of the spherical integration grid.

The problems observed for the atomic radial EDDs of negatively charged ions are solved in a simple way, and we show that the introduced scaling of the distributions significantly improves the obtained results for the Hirshfeld-I charges. The resulting values for a benchmark set of 168 neutral molecules show very good agreement with the values obtained by a previous implementation of the Hirshfeld-I method aimed solely at molecular systems.

In the final section we have investigated some periodic systems to show the validity of our implementation. For each of these systems the expected behavior of the charges is observed. Because of their simplicity these systems are ideal test cases for Hirshfeld-I implementations for periodic systems.

Part IV

Conclusions

CHAPTER

9

Conclusions & Outlook

We must not forget that when radium was discovered no one knew that it would prove useful in hospitals. The work was one of pure science. And this is a proof that scientific work must not be considered from the point of view of the direct usefulness of it. It must be done for itself, for the beauty of science, and then there is always the chance that a scientific discovery may become like the radium a benefit for humanity.

–Marie Skłodowska-Curie (1867 - 1934),
Lecture at Vassar College, May 14, 1921

9.1 CeO$_2$: a tunable buffer layer and much more

Doping provides a straightforward way of tuning the properties of CeO$_2$ to specific values for specific applications. This makes the ideal dopant for one application ill-suited for another. Although the work presented here originated in the quest for better buffer layers for coated superconductor architectures, it is clear that this theoretical work can also be of great interest for other applications. As such we have refrained from focussing solely on buffer layers, and tried to focus more on the properties themselves.

A recurring aspect of the study of doped systems is the uncertainty of the atomic scale structure. Although the atomic scale crystal structure of CeO$_2$ is well known, the same is not true for doped and mixed systems. A striking example here is the ground state[1] crystal structure of La$_2$Ce$_2$O$_7$. Although this compound has been produced since the early 1900's, the actual ground state crystal structure remains a point of debate to this date. The two proposed structures are derived from the CeO$_2$ fluorite structure, where the *pyrochlore* structure features a strictly organized distribution of the cations over the cation-sublattice and the vacancies over the oxygen sublattice, the *defective fluorite* structure is characterized by random distribution of cations and vacancies of the respective sublattices. Both structures are supported by XRD and neutron diffraction measurements either observing or not observing the unique pyrochlore reflections. By studying different distributions of the cations and vacancies for stoichiometric La$_2$Ce$_2$O$_7$, we conclude that the pyrochlore structure is

---

[1]As usual this refers to the absolute physical ground state at zero temperature and pressure, not to be confused with the chemical standard state at room temperature and 1 atmosphere.

more stable than the defective fluorite structure. This conclusion is based on several different aspects:

- Heat of formation ΔH_f: shows that the formation of a pyrochlore structure is more favorable than the formation of a defective fluorite structure.

- Oxygen vacancy formation energy: there is a clear trend indicating a preference for a pure Ce surrounding and a penalty for a pure La surrounding. This trend also provides a driving force towards ordered structures.

- Simulated XRD spectra show better agreement with experiment for the pyrochlore structure than the disordered fluorite structure. In addition, the very low intensity ($< 1\%$ of the peak intensity) of the "typical pyrochlore reflections" may explain why they are often not observed in experiments.

In addition, this work also showed that for $La_2Ce_2O_8$, *i.e.* $La_2Ce_2O_7$ without the oxygen vacancies or under oxidizing atmosphere, the preference is reversed, making the disordered fluorite type structure more stable than the pyrochlore or any of the other ordered structures studied. This is an important aspect to bear in mind when comparing to experimental results.

In contrast to the case of $La_2Ce_2O_7$, where two competing crystal structures are proposed, for most doped CeO_2 systems the situation is worse. There the atomic scale structure is generally unknown; sometimes it is not even clear if the dopant is present in the bulk of the material or only at the surface. For catalysts and buffer layers alike, improved macroscopic properties[2] can be observed, although no actual bulk doping is involved. This uncertainty complicates theoretical work, and directs one to use prototype structures, which make some (reasonable) idealizations and assumptions, such as:

- Homogeneous distribution of dopants. (Unless one is specifically studying the possible clustering of dopants.)

- Periodicity of the doped system. (This is inherent for *ab-initio* DFT calculations.)

- Conservation of symmetry. (In a general study, one is not so much interested in the influence of a specific atomic species as in the influence of a specific property such as atomic size.)

Even with these idealizations the number of possible structures to investigate remains large. To reduce the complexity further we started from a set of dopants which have no need for charge compensating vacancies: the group IV elements. For doped systems without vacancies, retaining a cubic symmetry, we derived the empirical Vegard law. From this it is then possible to calculate the atomic crystal radius, which we showed to be in good agreement with the values presented by Shannon. This

---

[2]This may refer to anything above atomic scale: *e.g.* catalytic activity, oxygen storage capacity, reduction of (micro-) crack formation, lowered roughness, *etc.*

shows that Shannon crystal radii should be used when trying to empirically determine relations between a system property and the atomic size, instead of the much used ionic radius. In addition, since Shannon crystal radii are provided in function of the atomic valence and coordination, this also provides an alternative and quick method of estimating the dopant coordination and valence in a compound based on the measured lattice parameter.

The defect formation energy on the other hand shows a clear split between the group IVa and IVb elements, with the former shown to be unfavorable dopants, and the latter favorable ones. In addition, the oscillation in the correlation between the defect formation energy and atomic size, is shown to relate to the presence of a gap state below or above the unoccupied Ce $4f$ band. Another interesting observation is the fact that formation energies seem to show only little dependence on the dopant concentration, allowing the use of small unit cells (with high dopant concentrations) to have a rough estimate of the stability of the doped system.

Also with regard to the calculated bulk modulus and thermal expansion coefficient, the group IVa and group IVb dopants show a different behavior. Whereas the group IVa dopants give rise to a decrease in the bulk modulus and increase in the thermal expansion coefficient, the opposite is found for the group IVb dopants. This opposite behavior for the bulk modulus and thermal expansion coefficient appears to be a general trend, which is also observed for aliovalent dopants with and without the inclusion of charge compensating vacancies.

Studying aliovalent dopants with and without the presence of charge compensating vacancies shows generally the same trends as are observed for the group IV dopants. The inverse trends for the bulk moduli and thermal expansion coefficients remain and calculated atomic radii show good agreement with Shannon crystal radii. From the latter, however, we note that aliovalent dopants have a coordination of less than 8, being indicative for a preference to positions near vacancy sites.

The inclusion of charge compensating vacancies is shown to have some important effects on doped systems:

- Stabilization of the doped system, as long as no over-compensation is present. However, relative to the formation of oxygen vacancies in non-doped systems, the formation of oxygen vacancies is still favorable in over-compensated Gd doped CeO$_2$.

- Increase of the lattice parameter relative to the system without vacancies, compensating (partially) dopant induced lattice contraction.

- Strong reduction of the bulk modulus, allowing for bulk modulus matching at low dopant concentrations.

From these general conclusions it is possible to draw some conclusions focussing on doped CeO$_2$ in buffer layer architectures for coated superconductors. For this system, we are interested in knowing which dopants at which concentrations would

give rise to a match with $La_2Zr_2O_7$ with regard to the lattice parameter, the bulk modulus and thermal expansion coefficient:

- From fitting Vegard's law to the calculated lattice parameters at different concentrations we show that lattice matching with $La_2Zr_2O_7$ is possible for dopant concentrations of about 5% for all group IV elements but Pb. Similar values are also found for Co, Cu, Mg, Nb, V, and Zn.

- The introduction of charge compensating vacancies reduces the lattice contraction, effectively slightly increasing the required dopant concentrations for lattice parameter matching by a few %.

- The defect formation energies, show Sm, Hf, Zr, Gd, La, Ti, and Nb as most favorable candidates for bulk doping,

- while Ge, Zn, Co, Cu, and C are shown to be the least favorable candidates.

- Since both the bulk modulus and thermal expansion coefficient of $La_2Zr_2O_7$ are lower than that of CeO_2 and there is an observed inverse trend between these two properties, we need to conclude that it is only possible to optimize one of these properties in CeO_2.

- Only the introduction of oxygen vacancies modifies the bulk modulus sufficiently for bulk modulus matching with $La_2Zr_2O_7$ to be possible, restricting the real of dopants of interest to aliovalent dopants

9.2 Outlook: theory and experiments, two sides of one coin.

Comparison of theoretical and experimental results is always a difficult endeavor. This is due to the large difference in starting knowledge and assumptions, which often tend to be orthogonal. Where small concentrations of dopants are often easier in experiments due to the presence of a solubility limit, they require large unit cells making computational work more expensive. For the latter high concentrations are preferred, since this means smaller unit cells and fewer possible combinations.

An important aspect for being able to compare theoretical and experimental results, is to make sure that the same system is studied by both. Although this may sound trivial, it is most probably the most frequent reason why experiments and theoretical work appear to contradict one another. The difference in the systems generally originates in experiments, for the simple reason that unlike a for theoretical structures, the exact stoichiometry and atomic structure are unknown. Even ignoring inaccuracies on the stoichiometry, a compound like $La_2Ce_2O_7$ can be constructed in a huge number of different ways, and different synthesis methods will give rise to different actual structures. As a result, different experimental groups will present different findings for formally the same material.

Our study of the $La_2Ce_2O_7$ structure presented in **chapter** 6,[150] recently gave

rise to the publication of experimental work by Reynolds *et al.*[298] These authors present a La$_2$Ce$_2$O$_7$ system which based on their measurements appears as a disordered fluorite structure in contrast to our conclusion in favor of the pyrochlore structure. As a result they make the following remark:

> This is in conflict with recent DFT calculations of Vanpoucke *et al.*, and it is important to consider the origin of this difference, which may reflect assumptions in the theoretical calculation and experimental limitations.

> – Taken from Reference [298].

It is clear that the question of the structure of La$_2$Ce$_2$O$_7$ is far from over, and additional theoretical work should provide new insight in the matter. Simulation of neutron diffraction spectra for different configurations of La$_2$Ce$_2$O$_7$ could reveal if the 'assumed pyrochlore reflections' could be observed experimentally. (Note that from our calculations it followed that the intensity of the '*most prominent*' pyrochlore reflections would be smaller than the size of the experimental data points used in the XRD graphs by Reynolds *et al.* This shows the assumption that such reflections should be observed probably does not hold.) Simulations for lower concentration La content in CeO$_2$ may provide insights in the interaction between La, Ce and the oxygen vacancies. Several authors infer the experimental presence of a phase transition at La content above 40%. In conclusion, collaboration between theoretical and experimental scientists will help to identify implicit assumptions made by either group. In the end this will lead to a better understanding of the system under study, and may after almost a century of uncertainty provide a definitive and complete answer on the structure of La$_2$Ce$_2$O$_7$.

9.3 Outlook on doped CeO$_2$

If one thing is clear from this thesis, then it is the fact that much more general work is needed on this topic. To better understand the behavior and trends observed, an in-depth study of the electronic structure of these materials is required. From the work presented on group IV elements it is clear that valence only is insufficient to parameterize several properties, and also electrons in states near the Fermi need to be included. The intrinsic interplay with the Ce $4f$ electrons was beyond the scope of this work, but will provide a deeper understanding of the trends presented for stability and mechanical properties.

Also the interplay between dopants and oxygen vacancies requires further study. It is clear that different dopants interact differently, but there are also indications that dopant and vacancy concentrations play an important role in this interaction. Such studies would also contribute to a better understanding of for example the pyrochlore/fluorite transition.

Knowing the relative stability of different dopants, and as a consequence the preference for segregation to the surface of the doped system, makes it now also interesting

to investigate the influence such dopants have at the interface between layers. In buffer layer architectures this will provide clues why dopants which are clearly unfavorable as bulk dopants (*e.g.* Cu) still result in improved experimental properties (lower roughness, less crack formation). For other 'unstable' systems (such as Co doped CeO_2) understanding the mechanism which stabilizes it may be very informative from thee fundamental theoretical point of view, or present a new class of materials to experiment with, or just plainly show which experimental assumptions are wrong.

9.4   Chemistry in solid state physics

The fields of quantum chemistry and solid state physics have a lot in common: both use the same underlying theory (quantum theory) and study the physical world at the atomic scale. Their main difference is located in the systems under consideration and the employed concepts. Whereas the (solid state) physicist uses states to investigate solids, the (quantum) chemist uses orbitals to investigate molecules. Although some might argue that chemistry is '*just*' applied physics, philosophers of science have argued that chemical concepts cannot be reduced to physics. Scerri and McIntyre summarize this as follows:

> [Conceptual reduction] is not even possible in principle due to the very nature of the concepts themselves. That is, the concepts of composition, bonding, and molecular structure cannot be expressed except at the chemical level.

> – Taken from Reference [299].

As a result, if one wants to make use of chemical concepts in (solid state) physics, then these need to be introduced from chemistry, and interpreted using a chemical context. In the second part of this thesis we introduced such a chemical concept into solid state calculations: "*Atoms in Molecules*".

Although it is clear from a quantum mechanical point of view that a compound system can not be decomposed into non-interacting free sub-systems[3], one is free to define a sub-system division scheme based on physical or chemical properties.

In the Hirshfeld-I scheme, the electron density is divided between atoms in a stockholder fashion. In case of a solid, we show that the general theoretical derivation remains the same as for molecules, although some approximations need to be made to allow for the calculations to remain computationally feasible. Our method also makes use of the pseudo-valence density only when dividing the electron density between the atoms. The good agreement with atomic charges obtained based on all electron densities indicates that the method is quite robust. Moreover it also shows that core electrons remain true to their name, and as such are not (or barely)

---

[3]Note that even in a mean field approach the particles interact, albeit through an averaged potential due to 'the other' particles.

shared between atoms. The presented method has, however, one major drawback, it is computationally quite expensive (though the cost rises very slowly for increasing system size). This is due to the fact that it was built as an interface to a molecular code combined with the need to evaluate a large number of atoms as a result of the periodic boundary conditions. In future work, this will be remedied through the use of different grid schemes. Also the contribution of core electrons and the difference between all electron and pseudo valences requires a more careful study.

Because interactions between particles prevent the clean decomposition of a system into subsystems, it is expected that the atom based and subsystem based implementations of the Hirshfeld-I division schemes will yield different results. A comparative study between the two should lead to new insights and possibly a superior atoms in molecules partitioning scheme.

The growing interest from the solid state physics community in the chemical concept of atoms in molecules, raises the question if there exist other chemical concepts which could be of interest to the solid state community. Since chemistry is as much present in solids as it is in molecules the answer should most certainly be positive. Where atoms-in-a-molecule partitioning schemes can provide quantitative ways to investigate charge transfer and aggregation near interfaces and defects, reactivity indices such as the Fukui functions will improve the understanding of interactions between surfaces and molecules, and in extension the growth of new layers on a substrate surface.[120, 300, 301]

The larger part of the theoretical framework for these concepts is already present in the chemical community. The only thing that remains to be done is their implementation and application to solids. It is expected that the inherently different nature of solids and molecules will give rise to some practical complications during such implementations, but these should be manageable. More importantly, the application of chemical concepts to solids may reveal peculiarities which do not exist in molecules and induce conceptual refinement of some of the chemical concepts.

Part V

Appendices

$\bigodot$ A

Bulk modulus and thermal expansion coefficients

A.1 Bulk modulus

The isothermal bulk modulus (BM) is a measure for the resistance of a material to uniform compression. It is given as

$$B = -V\frac{\partial P}{\partial V}, \tag{A.1}$$

where V is the volume of the system, and P is the pressure. Since ab-initio DFT calculations are performed at 'zero' pressure, a different method is required to obtain a value for B.

Doing a set of DFT calculations for the same material but at slightly different equilibrium volumes provides a set of $E(V)$ data. Fitting these data to an equation of state (EQS) can then be used to provide a value for B. There exist several different equations of state which contain B as one of its parameters. Two examples are the Murnaghan EQS and its extension the Birch-Murnaghan EQS.[143, 144] The Murnaghan EQS is given by:

$$E(V) = E_0 + \frac{B_0 V}{B_0'} \left(\frac{\left(\frac{V_0}{V}\right)^{B_0'}}{B_0' - 1} + 1 \right) - \frac{B_0 V_0}{B_0' - 1}, \tag{A.2}$$

where the subscript 0 indicates the property at $P = 0$ and $B' = \left(\frac{\partial B}{\partial P}\right)_T$. Since $B = B_0 + B'P$, $B = B_0$ at zero pressure. In addition, B' is assumed constant, such that $B' = B_0'$. The third order isothermal Birch-Murnaghan equation of state is given by:

$$E(V) = E_0 + \frac{9 B_0 V 0}{16} \left(\left(\left(\frac{V_0}{V}\right)^{\frac{2}{3}} - 1 \right)^3 B_0' + \left(\left(\frac{V_0}{V}\right)^{\frac{2}{3}} - 1 \right)^2 \left(6 - 4\left(\frac{V_0}{V}\right)^{\frac{2}{3}} \right) \right). \tag{A.3}$$

Although the results obtained using both EQS are comparable, we have only used the latter for calculating the bulk modulus. Also in the algorithm calculating the

thermal expansion coefficients only the Birch-Murnaghan EQS is used for fitting purposes.

A.2   Thermal expansion coefficients

Most materials tend to expand with increasing temperature. This is due to the increased thermal vibration leading to an increase in the average interatomic distance. The amount of expansion as function of the temperature is called the thermal expansion coefficient (TEC). The volumetric (β) and linear (α) TECs are given by

$$\beta(T) \quad = \quad \frac{1}{V}\left(\frac{\partial V}{\partial T}\right)_p \tag{A.4}$$

$$\alpha(T) \quad = \quad \frac{1}{L}\left(\frac{\partial L}{\partial T}\right)_p, \tag{A.5}$$

with V and L the volume and linear dimension respectively. For cubic isotropic materials the two are related as:

$$\beta(T) \quad \approx \quad 3\alpha(T). \tag{A.6}$$

As is shown in Eq. (A.4), the volumetric (α) is calculated by taking the partial temperature derivative at constant pressure. The required pressure and temperature dependent equilibrium volumes are obtained by minimizing the thermal non-equilibrium Gibbs function with respect to the volume at any pair of values p and T:

$$G^{\star}(V; p, T) = E_{lat} + p \cdot V + F_{vib}(T, V), \tag{A.7}$$

with E_{lat} the system total energy obtained from DFT calculations and F_{vib}, the vibrational Helmholtz free energy. Since *ab-initio* DFT calculations are at zero pressure and temperature, the second term in Eq. (A.7) vanishes.

The vibrational Helmholtz free energy can be obtained within the harmonic approximation, following Maradudin, we start from :[169]

$$F_{vib} = 3nk_B T \int_0^{\omega_L} \ln\left[2\sinh\left(\frac{\hbar\omega}{2k_B T}\right)\right] g(\omega)\mathrm{d}\omega, \tag{A.8}$$

with n the total number of atoms in the system, ω_L the maximum vibrational (angular) frequency and the phonon DOS $g(\omega)$ for which $\int_0^{\omega_L} g(\omega)\mathrm{d}\omega = 1$. The phonon DOS $g(\omega)$ can be obtained either from (computationally expensive) phonon calculations, or derived within the quasi-harmonic Debye approximation. Within this approximation $\omega_L = \omega_D$, the Debye frequency.

For a crystal containing n atoms, the limit to the total number of independent modes is $3n$. These modes are divided into two types leading to n longitudinal and

$2n$ transversal modes. The number of frequencies for the two modes in an interval $[\nu, \nu + \mathrm{d}\nu]$ is given by:

$$g_t(\nu)\mathrm{d}\nu = \frac{8\pi V}{v_t^3}\nu^2 \mathrm{d}\nu \quad \& \quad g_l(\nu)\mathrm{d}\nu = \frac{4\pi V}{v_l^3}\nu^2 \mathrm{d}\nu, \tag{A.9}$$

with v_t and v_l the transversal en longitudinal speeds of sound of the material. Combined this gives

$$\begin{aligned} g(\nu)\mathrm{d}\nu &= (g_t(\nu) + g_l(\nu))\mathrm{d}\nu \tag{A.10} \\ &= 4\pi V\left(\frac{1}{v_l^3} + \frac{2}{v_t^3}\right)\nu^2 \mathrm{d}\nu \tag{A.11} \\ \Rightarrow g(\omega)\mathrm{d}\omega &= \frac{V}{2\pi^2}\left(\frac{1}{v_l^3} + \frac{2}{v_t^3}\right)\omega^2 \mathrm{d}\omega, \tag{A.12} \end{aligned}$$

since $\omega = 2\pi\nu$. Because the total number of independent modes is limited to $3n$ in a solid, a limit is imposed on the maximum vibrational frequency. As a result, the Debye frequency ω_D is found via:[302]

$$\begin{aligned} 3n &= \int_0^{\omega_D} g(\omega)\mathrm{d}\omega \tag{A.13} \\ \Rightarrow \omega_D &= \sqrt[3]{\frac{18\pi^2 n}{V}\left(\frac{1}{v_l^3} + \frac{2}{v_t^3}\right)^{-1}} \tag{A.14} \end{aligned}$$

Taking the norm of $g(\omega)$ through division by $3n$, to satisfy the requirement $\int_0^{\omega_L} g(\omega)\mathrm{d}\omega = 1$, the Helmholtz vibrational energy can now be calculated as:

$$\begin{aligned} F_{vib} &= 3nk_BT\int_0^{\omega_D} \ln\left[2\sinh\left(\frac{\hbar\omega}{2k_BT}\right)\right]\frac{g(\omega)}{3n}\mathrm{d}\omega \tag{A.15} \\ &= k_BT\frac{V}{2\pi^2}\left(\frac{1}{v_l^3} + \frac{2}{v_t^3}\right)\int_0^{\omega_D} \ln\left[2\sinh\left(\frac{\hbar\omega}{2k_BT}\right)\right]\omega^2 \mathrm{d}\omega. \tag{A.16} \end{aligned}$$

Using $A = k_BT\frac{V}{2\pi^2}\left(\frac{1}{v_l^3} + \frac{2}{v_t^3}\right)$ and $\ln(2\sinh\left(\frac{x}{2}\right)) = \frac{x}{2} + \ln(1 - e^{-x})$, and introducing the Debye temperature $\Theta_D = \frac{\hbar\omega_D}{k_B}$ this leads to:

$$F_{vib} = \frac{9}{8}nk_BT\left(\frac{\Theta_D}{T}\right) + A\int_0^{\omega_D} \ln\left(1 - e^{-\frac{\hbar\omega}{k_BT}}\right)\omega^2 \mathrm{d}\omega. \tag{A.17}$$

Solving the integral one finally ends up with:

$$F_{vib} = nk_BT\left[\frac{9}{8}\left(\frac{\Theta_D}{T}\right) + 3\ln\left(1 - e^{-\frac{\Theta_D}{T}}\right) - \frac{3}{\left(\frac{\Theta_D}{T}\right)^3}\int_0^{\frac{\Theta_D}{T}} \frac{u^3}{e^u - 1}\mathrm{d}u\right], \tag{A.18}$$

where the last integral is the third order Debye function.

The only thing that remains to be done is to obtain an explicit form for the Debye
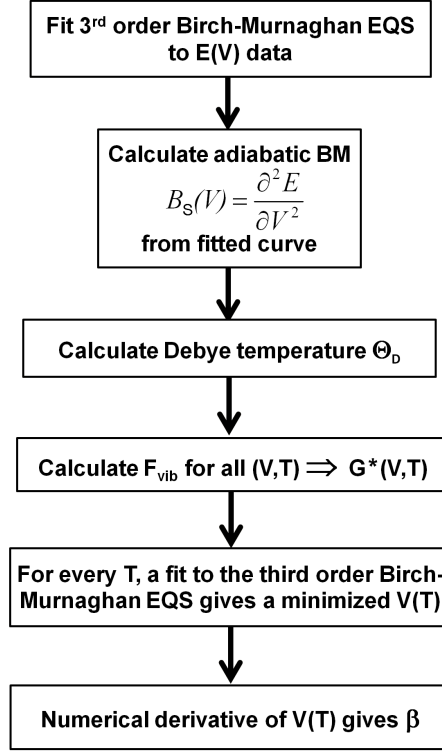
Figure A.1: *Schematic representation of the algorithm used to calculate the* TEC.

temperature Θ_D without velocities. From Eq. (A.14) and the relation $\omega = 2\pi\nu$, the Debye temperature can be written as:

$$\Theta_D(V) \quad = \quad \frac{h\nu_D}{k_B} \tag{A.19}$$

$$= \quad \frac{h}{k_B}\left(\frac{3n}{4\pi V}\right)^{\frac{1}{3}}\left[\frac{1}{3}\left(\frac{1}{v_l^3} + \frac{2}{v_t^3}\right)\right]^{\frac{-1}{3}} \tag{A.20}$$

In this, v_l and v_t can be related to the stress coefficients of the solid:

$$v_l \quad = \quad \sqrt{\frac{B_S + \frac{4}{3}G}{\varrho}} = \sqrt{\frac{E(1-\nu)}{\varrho(1+\nu)(1-2\nu)}}$$

$$v_t \quad = \quad \sqrt{\frac{G}{\varrho}}, \tag{A.21}$$
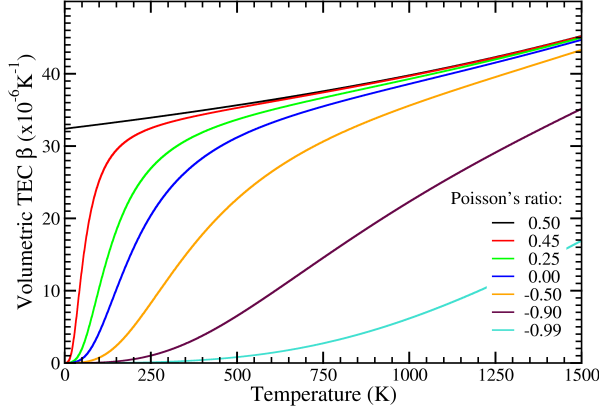
Figure A.2: *The volumetric* TEC *β for CeO$_2$ for different values of Poisson's ratio ν.*

with the shear modulus G, the adiabatic bulk modulus B_S, the Young modulus E, and $\nu \in [-1 \dots 0.5]$ Poisson's ratio. ϱ is the material density, given as $\frac{M}{V}$. The adiabatic bulk modulus is found as the second volume derivative of the internal energy E_{int} at constant entropy $B_S = V \left(\frac{\partial^2 E_{int}}{\partial V^2} \right)_S$. Assuming the material under study is a homogeneous isotropic linear elastic material, then it is possible to write the above relations using only Poisson's ratio and the adiabatic bulk modulus using the following conversion relations:

$$G = \frac{3B_S(1 - 2\nu)}{2(1 + \nu)} \qquad \& \qquad E = 3B_S(1 - 2\nu). \qquad (A.22)$$

Combining Eq. (A.21) and (A.22), and substituting them in Eq. (A.20), the Debye temperature can now be written as:

$$\Theta_D(V) = \frac{\hbar}{k_B} \left(18\pi^2 n \sqrt{3V} \right)^{\frac{1}{3}} f(\nu) \sqrt{\frac{B}{M}} \qquad (A.23)$$

with

$$f(\nu) = \left\{ 3 \left[\left(\frac{1 + \nu}{1 - \nu} \right)^{\frac{3}{2}} + 2 \left(\frac{2(1 + \nu)}{1 - 2\nu} \right)^{\frac{3}{2}} \right]^{-1} \right\}^{\frac{1}{3}}. \qquad (A.24)$$

Using the results obtained in the above derivations, it is now possible to numerically calculate the linear TEC requiring only a set of *ab-initio* calculated $E(V)$ data, the number and mass of the atoms in the used supercell, and a value for Poisson's ratio. Figure A.1 gives a schematic of how this is done in the HIVE program.[172] Figure A.2 shows the influence of using different values for Poisson's ratio. For all calculations presented in this thesis, a value of 0.25 was used (Cauchy solid).

B

High Performance Computing

The complexity for minimum component cost has increased at a rate of roughly a factor of two per year...Certainly over the short term this rate is expected to continue, if not to increase. Over the longer term, the rate of increase is a bit more uncertain, although there is no reason to believe it will not remain nearly constant for at least 10 years

– Gordon E. Moore
(Moore's Law 1965)

B.1 Stevin super computer facilities

In 1965, Gordon Moore observed that the number of components per integrated circuits, produced at the lowest cost, doubled every two years.[303][1] This, primarily economic, law still remains valid almost half a century later. However, the first signs of its limitations start to become apparent. Until a few years ago, the main source of increasing computational capacity of a computer was a result of further miniaturization and increasing clock speed. With features well in the nanoscale regime (currently produced chips have features of a size of $\sim$ 30nm) quantum effects will start to play a role complicating architectures in further miniaturizations, while physical size limits (features smaller than an single atom are not possible) present a hard limit to this miniaturization in the foreseeable future. Furthermore the increased complexity of modern computer architectures leads to additional problems:

The more functional units are crammed into a CPU, the higher the probability that the "average" code will not be able to use them, because the number of independent instructions in a sequential instruction stream is limited. Moreover, a steady increase in clock frequencies is required to keep single-core performance on par with Moore's Law. However, a faster clock boosts power dissipation, making idling transistors even more useless.

– Taken from Reference [304].

---

[1] Actually, this is the version of 10 years later; in 1965 Moore predicted, based on 5 data points, a doubling every single year.

Figure B.1: *One of the* STEVIN *supercomputers. (Image obtained from www.ugent.be)*

As a result, manufacturers nowadays opt to place more cores on a chip to provide the computational boost required to follow Moore's Law, giving rise to dual-, quad- and hexa-core machines.

Despite the resulting constant increase in computing power for personal machines, the computational scientist often requires (much) more resources. Because the Schrödinger many body equations can only be solved numerically, and the time required to do so grows quickly with increasing size of the problem, modern day solid state physicists and quantum chemists rely on supercomputers for this task.

A supercomputer is in essence nothing more than a large set of computers connected trough a network.[2] However, unlike a normal desktop or laptop, there is no need for graphics or sound cards.[3] One is only interested in the raw computing power, located in the CPU.[4] Stripping everything else away, one ends up with a machine containing just large sets of multi-core CPUs connected to one another. As such, a supercomputer is no more than a set of racks containing modules with multiple CPUs, as is shown in Fig. B.1

At Ghent university, the high performance computing (HPC) center has currently five such machines as part of the STEVIN supercomputer facilities. Table B.1 shows the total number of nodes and cores for each machine and the amount of RAM memory available on a single node. Different machines have a slightly different setup making them interesting for different applications.

---

[2]In the case of a Beowulf cluster this is taken quite literally.

[3]There is one big exception. Since a graphics card can be considered a massively parallel 'machine', some people have started to develop methods to make use of graphics cards for scientific computing. These are so-called GPU supercomputers.

[4]The terminology CPU, core and node can be quite confusing. Especially since core and CPU are sometimes used to refer to cores.

Table B.1: *The different machines of the Ghent supercomputer* STEVIN, *and the amount of* CPU *hours used for this dissertation.* CPU *hours refers to how long it would take a single core to do the same computations. (Note that there are* 8760 *hours in a* 365 *day year.)*

name	nodes	cores	RAM/node (GB)	used resources (CPU hours)
gengar	192	1536	16	760960
gastly	54	432	12	156365
haunter	167	1336	12	117083
dugtrio	4	192	384	96709
gulpin	34	1088	64	483700

B.2   Resources used

Over the last two and a half years, I have made extensive use of these machines, allowing me to do the simulations for the work presented in this dissertation. A total of over 1.6 million CPU hours[5] have been used (roughly 186 years), showing that supercomputing facilities are indispensable for this type of work. It also puts in perspective the idea that simulations are faster than experiments. This is only the case due to the ability of doing much of the work in parallel. Table B.1 shows the resources used, split over the different machines.

---

[5]In this context, CPU is used to refer to a single core.

<div align="center">

APPENDIX

C

</div>

<div align="right">

Unit conversions

</div>

1 Mbar	=	1	$\times 10^6$	bar
	=	1	$\times 10^{11}$	Pa
	=	1	$\times 10^{-2}$	GPa
	=	9.87	$\times 10^5$	atm

1	=	1	$\times 10^{-1}$	nm
	=	1	$\times 10^{-10}$	m
	=	1.88972612464		a_0

1 eV	=	1.602176565(35)	$\times 10^{-19}$	J
	=	96.4853365(21)		kJ/mol
	=	23.0609		kcal/mol
	=	0.03674932379(81)		Hartree
	=	0.073498647554		Ry

1 J	=	6.24150934(14)	$\times 10^{18}$	eV
1 kJ/mol	=	0.010364269		eV
1 kcal/mol	=	0.043363442		eV
1 Hartree	=	27.21138505(60)		eV
1 Ry	=	13.60569253(30)		eV

LIST OF TABLES

List of Figures

List of Abbreviations

AE	all-electron
AF	anti-ferromagnetic
AIM	atoms in molecules
AIS	atoms in the system
B3LYP	Becke, three-parameter, Lee, Yang, and Parr (functional)
BC	before Christ
BCS	Bardeen, Cooper, and Schrieffer
BM	bulk modulus
CA	Ceperley–Alder
CPU	central processing unit
CSC	coated superconductors
CSM	core-state model
DFT	density functional theory
DFT+U	DFT with on-site Coulomb corrections (Hubbard U)
DOS	density of states
EDD	electron density distribution
EQS	equation of state
ESP	electrostatic potential
fcc	face-centered cubic
FFT	fast Fourier transforms
FM	ferromagnetic
GGA	generalised gradient approximation (functional)
GPU	graphical processing unit
HF	Hartree–Fock
HIVE	Humble Interface for VASP data Extraction
HK	Hogenberg and Kohn
HKS	Hohenberg–Kohn–Sham
HPC	high performance computing
HSE	Heyd, Scuseria, and Ernzerhof (functional)
HTS	high temperature superconductors
IBM	International Business Machines corporation
ICSD	Inorganic Crystal Structure Database
ISA	iterative stockholder approach
LDA	local density approximation (functional)
LDOS	local density of states
LHC	Large Hadron Collider
LZO	$La_2Zr_2O_7$
MAGLEV	Magnetic Levitation train
MOD	metal-organic deposition
MRI	Magnetic Resonance Imaging scanner

NCPP	norm-conserving pseudo-potentials
NMR	Nuclear Magnetic Resonance scanner
NN	nearest neighbor
NNN	next nearest neighbor
NV	used to indicate a system with "No oxygen Vacancies"
OSC	oxygen storage capacity
PAW	projector augmented waves
PBC	periodic boundary conditions
PBE	Perdew, Burke and Ernzerhof (functional)
PBE0	Hybrid version of the PBE functional.
PP	pseudo-potentials
QM	quantum mechanics
QTAIM	quantum theory of atoms in molecules
RABiTS	Rolling Assisted Biaxially Textured Substrates
RAM	random access memory
SCF	self consistent field procedure
SMES	superconducting magnetic energy storage
SoI	sphere of influence
SQS	Special Quasi-random Structure
SQUID	superconducting quantum interference device
STM	scanning tunneling microscope
TBC	thermal barrier coatings
TEC	thermal expansion coefficient
TEM	transmission electron microscope
TWC	three-way catalysts
USPP	ultra-soft pseudo-potentials
VASP	Vienna Ab-initio Simulation Package
VBM	valence-band model
VESTA	Visualization for Electronic and STructural Analysis (program)
VWN	Vosko, Wilk, and Nusair correlation functional
XAFS	X-ray adsorption fine structure
XRD	X-ray diffraction
YBCO	$YBa_2Cu_3O_{7-\delta}$

List of Symbols and Constants

●

Symbols regarding units or chemical elements are not listed.

Symbol	Description	(Value)	Units
a_0, b_0, c_0	lattice parameters		Å
Δa_0	lattice expansion/contraction		Å or %
α	linear thermal expansion coefficient		K^{-1}
a_{RT}	lattice parameter at room temperature		Å
a_x	lattice parameter for compound x		Å
B_0	bulk modulus at zero pressure		Mbar
β	volumetric thermal expansion coefficient		K^{-1}
$d_{\mathrm{vac-vac}}$	Inter-vacancy distance, calculated as the distance between the centers of mass of the cation-tetrahedra surrounding the oxygen vacancy		Å
e	elementary charge	$1.602176487(40) \times 10^{-19}$	C
E_f	defect formation energy		eV
ε_0	electric constant	$8.8541878 \times 10^{-12}$	$C^2 \ J^{-1} \ m^{-1}$
ε_i	single particle energy		eV
E_{red}	reduction energy		eV
E_{vac}	(oxygen) vacancy formation energy		eV

Symbol	Description	(Value)	Units
E^{xc}	exchange and correlation energy functional		
$\hat{H}$	Hamiltonian		
$\hbar$	Planck constant$/(2\pi)$	$1.054571596(82) \times 10^{-34}$	J s
$\mathbf{H}_c$	critical magnetic field		T
ΔH_f	heat of formation		eV
$\mathbf{J}_c$	critical current density		$A\ m^{-2}$
k_B	Boltzmann constant	$1.3806488(13) \times 10^{-23}$	J K^{-1}
λ_L	London penetration depth		Å
m	particle mass		kg
m_e	electron mass	$9.10938188(72) \times 10^{-31}$	kg
μ_B	Bohr magneton $(\mu_B = \frac{e\hbar}{2m_e})$	$927.400968(20) \times 10^{-26}$	J T^{-1}
N_A	Avogadro's number	$6.02214179(30) \times 10^{23}$	mol^{-1}
n_A°, n_A^i	population of atom A at the initial (i^{th}) iteration		
ν	frequency		s^{-1}
n_x	concentration of dopant x in CeO_2		%
ω	angular frequency $(\omega = 2\pi\nu)$		s^{-1}
π	ratio of the circumference to the diameter of a circle in Euclidean space	$3.14159265\ldots$	

Symbol	Description	(Value)	Units
Ψ	system wave function		
ψ	single particle wave function		
$\mathbf{r}$	position vector		Å
R^2	correlation coefficient		
ρ	electron density		e Å^{-3}
R_{sh}^8	experimental Shannon crystal radius of en element in an 8 coordinated environment		Å
RT	room temperature. This is not a scientific term, and may refer to temperatures in the range of $20 - 25°$C. For numerical convenience, often 300K is used. As such, it should not be confused with standard temperature (273.15K) or standard ambient temperature (298.15K).		
R_x	atomic crystal radius for element x		Å
$\mathbf{T}_c$	critical temperature		K
V_{ext}	external potential		
V^H	Hartree potential		
V^x	exchange potential within the Hartree–Fock approximation		
w_A^H	Hirshfeld weight function for atom A		

Bibliography

[1] M. K. Hubbert, "The world's evolving energy system," *Am. J. Phys.*, vol. 49, no. 11, pp. 1007–1029, 1981.

[2] P. B. Weisz, "Basic Choices and Constraints on Long-Term Energy Supplies.," *Physics Today*, vol. 57, no. 7, pp. 47–52, 2004.

[3] P. V. Kamat, "Meeting the Clean Energy Demand: Nanostructure Architectures for Solar Energy Conversion," *J. Phys. Chem. C*, vol. 111, no. 7, pp. 2834–2860, 2007.

[4] D. Clery, "Imagining a City Where (Electrical) Resistance Is Futile," *Science*, vol. 319, no. 5864, p. 753, 2008.

[5] "Superconductivity: Present and Future Applications." http://www.ccas-web.org/, 2009.

[6] J. E. C. Williams, "Superconducting Magnets for MRI," *IEEE T. Nucl. Sci.*, vol. 31, no. 4, pp. 994–1005, 1984.

[7] B. D. Josephson, "The discovery of tunnelling supercurrents," *Rev. Mod. Phys.*, vol. 46, pp. 251–254, 1974.

[8] S. Hasuo, "Towards the Josephson computer," *Physics World*, vol. May, pp. 37–40, 1990.

[9] S. Hasuo, "Toward the Realization of a Josephson Computer," *Science*, vol. 255, no. 5042, pp. 301–305, 1992.

[10] A. L. Robinson, "IBM Drops Superconducting Computer Project," *Science*, vol. 222, no. 4623, pp. 492–494, 1983.

[11] H. Hayakawa, "Josephson computer technology.," *Physics Today*, vol. 39, no. 3, p. 46, 1986.

[12] S. Ortoli and J. Klein, *De uitzonderlijke geschiedenis van de supergeleiding.* Amsterdam: Van Gennep, 1990.

[13] C. W. F. Everitt, D. B. DeBra, B. W. Parkinson, J. P. Turneaure, J. W. Conklin, M. I. Heifetz, G. M. Keiser, A. S. Silbergleit, T. Holmes, J. Kolodziejczak, M. Al-Meshari, J. C. Mester, B. Muhlfelder, V. G. Solomonik, K. Stahl, P. W. Worden, W. Bencze, S. Buchman, B. Clarke, A. Al-Jadaan, H. Al-Jibreen, J. Li, J. A. Lipa, J. M. Lockhart, B. Al-Suwaidan, M. Taber, and S. Wang, "Gravity Probe B: Final Results of a Space Experiment to Test General Relativity," *Phys. Rev. Lett.*, vol. 106, p. 221101, 2011.

[14] P. N. Barnes, M. D. Sumption, and G. L. Rhoads, "Review of high power density superconducting generators: Present state and prospects for incorporating YBCO windings," *Cryogenics*, vol. 45, no. 10–11, pp. 670–686, 2005.

[15] H. Kamerlingh Onnes, "Liquefaction of helium," *Proceedings Koninklijke Akademie van Wetenschappen te Amsterdam*, pp. 168–185, 1908.

[16] J. de Nobel and P. Lindenfeld, "The discovery of superconductivity.," *Physics Today*, vol. 49, no. 9, pp. 40–42, 1996.

[17] H. Kamerlingh Onnes, "The resistance of pure mercury at helium temperatures. Further experiments with liquid helium. IV," *Proceedings Koninklijke Akademie van Wetenschappen te Amsterdam*, vol. 13, pp. 1274–1276, 1911.

[18] H. Kamerlingh Onnes, "Further experiments with liquid helium. H. On the galvanic resistance of pure metals etc. VII. The potential difference necessary for an electrical current through below $4°.19$ K," in *Proceedings Koninklijke Akademie van Wetenschappen te Amsterdam*, vol. 16, pp. 113–124, 1913.

[19] "Nobel prize organisation." http://www.nobelprize.org/.

[20] W. Meissner and R. Ochsenfeld, "Ein neuer Effekt bei Eintritt der Supraleitfähigkeit," *Naturwissenschaften*, vol. 21, pp. 787–788, 1933.

[21] J. Bardeen, L. N. Cooper, and J. R. Schrieffer, "Microscopic theory of superconductivity," *Phys. Rev.*, vol. 106, pp. 162–164, 1957.

[22] J. Bardeen, L. N. Cooper, and J. R. Schrieffer, "Theory of superconductivity," *Phys. Rev.*, vol. 108, pp. 1175–1204, 1957.

[23] J. E. Hirsch, "BCS theory of superconductivity: it is time to question its validity," *Phys. Scr.*, vol. 80, no. 3, p. 035702, 2009.

[24] A. J. Leggett, "What DO we know about high T_c?," *Nature Physics*, vol. 2, pp. 134–136, 2006.

[25] J. G. Bednorz and K. A. Müller, "Possible high T_c superconductivity in the Ba-La-Cu-O system," *Z. Phys. B*, vol. 64, pp. 189–193, 1986.

[26] M. K. Wu, J. R. Ashburn, C. J. Torng, P. H. Hor, R. L. Meng, L. Gao, Z. J. Huang, Y. Q. Wang, and C. W. Chu, "Superconductivity at 93 K in a new mixed-phase Y-Ba-Cu-O compound system at ambient pressure," *Phys. Rev. Lett.*, vol. 58, pp. 908–910, 1987.

[27] P. Dai, B. Chakoumakos, G. Sun, K. Wong, Y. Xin, and D. Lu, "Synthesis and neutron powder diffraction study of the superconductor $HgBa_2Ca_2Cu_3O_{8+\delta}$ by Tl substitution," *Phys. C*, vol. 243, no. 3–4, pp. 201–206, 1995.

[28] Y. Kamihara, T. Watanabe, M. Hirano, and H. Hosono, "Iron-Based Layered Superconductor $La[O_{1-x}F_x]FeAs$ (x = 0.05–0.12) with $T_c = 26$ K," *JACS*, vol. 130, no. 11, pp. 3296–3297, 2008.

[29] Z.-A. Ren, G.-C. Che, X.-L. Dong, J. Yang, W. Lu, W. Yi, X.-L. Shen, Z.-C. Li, L.-L. Sun, F. Zhou, and Z.-X. Zhao, "Superconductivity and phase diagram in iron-based arsenic-oxides ReFeAsO$_{1-\delta}$ (Re = rare-earth metal) without fluorine doping," *EPL (Europhysics Letters)*, vol. 83, no. 1, p. 17002, 2008.

[30] M. R. Norman, "High-temperature superconductivity in the iron pnictides," *Physics*, vol. 1, p. 21, 2008.

[31] D. C. Johnston, "The puzzle of high temperature superconductivity in layered iron pnictides and chalcogenides," *Adv. Phys.*, vol. 59, no. 6, pp. 803–1061, 2010.

[32] X. F. Sun, X. F. Rui, F. Wang, L. Zhang, and H. Zhang, "Influence of structural changes induced by co-doping in YBCO on superconductivity," *J. Phys.: Cond. Matter*, vol. 16, no. 12, pp. 2065–2070, 2004.

[33] K. Momma and F. Izumi, "VESTA: a three-dimensional visualization system for electronic and structural analysis," *J. Appl. Cryst.*, vol. 41, no. Part 3, pp. 653–658, 2008.

[34] B. Schoofs, V. Cloet, P. Vermeir, J. Schaubroeck, S. Hoste, and I. Van Driessche, "A water-based sol-gel technique for chemical solution deposition of (RE) Ba$_2$Cu$_3$O$_{7-y}$ (RE = Nd and Y) superconducting thin films," *Supercond. Sci. Technol.*, vol. 19, no. 11, pp. 1178–1184, 2006.

[35] T. Holesinger, L. Civale, B. Maiorov, D. Feldmann, J. Coulter, D. Miller, V. Maroni, Z. Chen, D. Larbalestier, R. Feenstra, X. Li, Y. Huang, T. Kodenkandath, W. Zhang, M. Rupich, and A. Malozemoff, "Progress in Nano-engineered Microstructures for Tunable High-Current, High-Temperature Superconducting Wires," *Adv. Mater.*, vol. 20, no. 3, pp. 391–407, 2008.

[36] W. Zhang, M. Rupich, U. Schoop, D. Verebelyi, C. Thieme, X. Li, T. Kodenkandath, Y. Huang, E. Siegal, D. Buczek, W. Carter, N. Nguyen, J. Schreiber, M. Prasova, J. Lynch, D. Tucker, and S. Fleshler, "Progress in AMSC scale-up of second generation HTS wire," *Phys. C*, vol. 463–465, no. 0, pp. 505–509, 2007. Proceedings of the 19th International Symposium on Superconductivity (ISS 2006).

[37] K. S. Cheung and S. Yip, "Brittle-Ductile Transition in Intrinsic Fracture Behavior of Crystals," *Phys. Rev. Lett.*, vol. 65, pp. 2804–2807, 1990.

[38] B. Glowacki, M. Vickers, and E. Maher, "A smart look at grain boundaries," *Materials World*, vol. 6, no. 11, pp. 683–686, 1998.

[39] J. Durrell and N. Rutter, "Importance of low-angle grain boundaries in YBa$_2$Cu$_3$O$_{7-\delta}$ coated conductors," *Supercond. Sci. Technol.*, vol. 22, no. 1, p. 013001, 2009.

[40] X. Obradors, T. Puig, A. Pomar, F. Sandiumenge, N. Mestres, M. Coll, A. Cavallaro, N. Romà, J. Gázquez, J. C. González, O. C. no, J. Gutierrez, A. Palau, K. Zalamova, S. Morlens, A. Hassini, M. Gibert, S. Ricart, J. M. Moretó, S. P. nol, D. Isfort, and J. Bock, "Progress towards all-chemical superconducting YBa$_2$Cu$_3$O$_7$-coated conductors," *Supercond. Sci. Technol.*, vol. 19, no. 3, p. S13, 2006.

[41] K. Knoth, B. Schlobach, R. Hühne, L. Schultz, and B. Holzapfel, "La$_2$Zr$_2$O$_7$ and Ce-ŨGd-ŨO buffer layers for YBCO coated conductors using chemical solution deposition," *Physica C*, vol. 426-431, Part 2, pp. 979–984, 2005.

[42] S. Oh, J. Yoo, K. Lee, J. Kim, and D. Youm, "Comparative study on the crack formations in the CeO$_2$ buffer layers for YBCO films on textured Ni tapes and Pt tapes," *Physica C*, vol. 308, no. 1-2, pp. 91 – 98, 1998.

[43] M. Paranthaman, A. Goyal, F. List, E. Specht, D. Lee, P. Martin, Q. He, D. Christen, D. Norton, J. Budai, and D. Kroeger, "Growth of biaxially textured buffer layers on rolled-Ni substrates by electron beam evaporation," *Physica C*, vol. 275, no. 3-4, pp. 266 – 272, 1997.

[44] M. Mogensen, N. M. Sammes, and G. A. Tompsett, "Physical, chemical and electrochemical properties of pure and doped ceria," *Solid State Ionics*, vol. 129, no. 1–4, pp. 63–94, 2000.

[45] N. Van de Velde, D. Van de Vyver, O. Brunkahl, S. Hoste, E. Bruneel, and I. Van Driessche, "CeO$_2$ Buffer Layers for HTSC by an Aqueous Sol-Gel Method - Chemistry and Microstructure," *Eur. J. Inor. Chem.*, no. 2, pp. 233–241, 2010.

[46] L. Kundakovic and M. Flytzani-Stephanopoulos, "Cu- and Ag-Modified Cerium Oxide Catalysts for Methane Oxidation," *J. Catal.*, vol. 179, no. 1, pp. 203 – 221, 1998.

[47] A. Trovarelli, "Catalytic properties of ceria and CeO$_2$-containing materials," *Catal. Rev.-Sci. Eng.*, vol. 38, no. 4, pp. 439–520, 1996.

[48] H. Yao and Y. Yu Yao, "Ceria in automotive exhaust catalysts: I. Oxygen storage," *J. Catal.*, vol. 86, no. 2, pp. 254–265, 1984.

[49] B. Steele, "Appraisal of Ce$_{1-y}$Gd$_y$O$_{2-y/2}$ electrolytes for IT-SOFC operation at 500°C," *Solid State Ionics*, vol. 129, no. 1-Ũ4, pp. 95–110, 2000.

[50] Q. Fu, H. Saltsburg, and M. Flytzani-Stephanopoulos, "Active nonmetallic au and pt species on ceria-based water-gas shift catalysts," *Science*, vol. 301, no. 5635, pp. 935–938, 2003.

[51] Z. Shao and S. M. Haile, "A high-performance cathode for the next generation of solid-oxide fuel cells," *Nature*, vol. 431, pp. 170–173, 2004.

[52] D. C. Koskenmaki, K. A. Gschneidner, and Jr., "Chapter 4 cerium," in *Metals* (J. Karl A. Gschneidner and L. Eyring, eds.), vol. 1 of *Handbook on the Physics and Chemistry of Rare Earths*, pp. 337 – 377, Elsevier, 1978.

[53] F. A. Kröger and H. J. Vink, *Solid State Physics*, vol. 3. 7 ed., 1956. p. 273–301.

[54] J. Kašpar, P. Fornasiero, and M. Graziani, "Use of CeO_2-based oxides in the three-way catalysis," *Catal. Today*, vol. 50, no. 2, pp. 285–298, 1999.

[55] Y. She, Q. Zheng, L. Li, Y. Zhan, C. Chen, Y. Zheng, and X. Lin, "Rare earth oxide modified CuO/CeO2 catalysts for the waterŰgas shift reaction," *Int. J. Hydrogen Energy*, vol. 34, no. 21, pp. 8929–8936, 2009.

[56] M. Manzoli, G. Avgouropoulos, T. Tabakova, J. Papavasiliou, T. Ioannides, and F. Boccuzzi, "Preferential CO oxidation in H_2-rich gas mixtures over Au/doped ceria catalysts," *Catal. Today*, vol. 138, no. 3-4, pp. 239 – 243, 2008.

[57] X. Q. Cao, R. Vassen, W. Fischer, F. Tietz, W. Jungen, and D. Stover, "Lanthanum-cerium oxide as a thermal barrier-coating material for high-temperature applications," *Adv. Mater.*, vol. 15, no. 17, pp. 1438–1442, 2003.

[58] X. Q. Cao, R. Vassen, and D. Stoever, "Ceramic materials for thermal barrier coatings," *J. Eur. Ceram. Soc.*, vol. 24, no. 1, pp. 1–10, 2004.

[59] W. Ma, S. Gong, H. Xu, and X. Cao, "On improving the phase stability and thermal expansion coefficients of lanthanum cerium oxide solid solutions," *Scripta Mater.*, vol. 54, no. 8, pp. 1505–1508, 2006.

[60] X. Cao, "Application of rare earths in thermal barrier coating materials," *J. Mater. Sci. Technol.*, vol. 23, no. 1, pp. 15–35, 2007.

[61] G. Penneman, I. Van Driessche, E. Bruneel, and S. Hoste, "Deposition of CeO_2 buffer layers and $YBa_2Cu_3O_{7-\delta}$ superconducting layers using an aqueous sol-gel method," in *Euro Ceramics VIII, Pts 1-3* (Mandal, H and Ovecoglu, L, ed.), vol. 264–268 of *Key Engineering Materials*, pp. 501–504, Turkish Ceram Soc; European Ceram Soc, 2004. 8th Conference of the European-Ceramic-Society, Istanbul, Turkey, jun 29-jul 03, 2003.

[62] D. Mullins, P. Radulovic, and S. Overbury, "Ordered cerium oxide thin films grown on Ru(0001) and Ni(111)," *Surf. Sci.*, vol. 429, no. 1–3, pp. 186–198, 1999.

[63] H. C. Aspinall, J. Bacsa, A. C. Jones, J. S. Wrench, K. Black, P. R. Chalker, P. J. King, P. Marshall, M. Werner, H. O. Davies, and R. Odedra, "Ce(IV) Complexes with Donor-Functionalized Alkoxide Ligands: Improved Precursors for Chemical Vapor Deposition of CeO_2," *Inorg. Chem.*, vol. 50, no. 22, pp. 11644–11652, 2011.

[64] P. Plonczak, M. Joost, J. Hjelm, M. Søgaard, M. Lundberg, and P. V. Hendriksen, "A high performance ceria based interdiffusion barrier layer prepared by spin-coating," *J. Power Sources*, vol. 196, no. 3, pp. 1156–1162, 2011.

[65] M. Henderson, C. Perkins, M. Engelhard, S. Thevuthasan, and C. Peden, "Redox properties of water on the oxidized and reduced surfaces of $CeO_2(111)$," *Surf. Sci.*, vol. 526, no. 1–2, pp. 1–18, 2003.

[66] M. Anwar, S. Kumar, N. Arshi, F. Ahmed, Y. Seo, C. Lee, and B. H. Koo, "Structural and optical study of samarium doped cerium oxide thin films prepared by electron beam evaporation," *J. Alloys Compd.*, vol. 509, no. 13, pp. 4525–4529, 2011.

[67] V. Narayanan, P. Lommens, K. De Buysser, D. E. P. Vanpoucke, R. Huehne, L. Molina, G. Van Tendeloo, P. Van Der Voort, and I. Van Driessche, "Aqueous CSD approach for the growth of novel, lattice-tuned $La_xCe_{1-x}O_\delta$ epitaxial layers," *J. Mater. Chem.*, vol. 22, pp. 8476–8483, 2012.

[68] Y. Takahashi, Y. Aoki, T. Hasegawa, T. Maeda, T. Honjo, Y. Yamada, and Y. Shiohara, "Preparation of YBCO coated conductor on metallic tapes using an MOD process," *Physica C*, vol. 412-414, Part 2, pp. 905–909, 2004.

[69] Y. Hamlaoui, F. Pedraza, and L. Tifouti, "Investigation of electrodeposited cerium oxide based films on carbon steel and of the induced formation of carbonated green rusts," *Corros. Sci.*, vol. 50, no. 8, pp. 2182–2188, 2008.

[70] P. Bera, K. R. Priolkar, P. R. Sarode, M. S. Hegde, S. Emura, R. Kumashiro, and N. P. Lalla, "Structural Investigation of Combustion Synthesized Cu/CeO_2 Catalysts by EXAFS and Other Physical Techniques: Formation of a $Ce_{1-x}Cu_xO_{2-\delta}$ Solid Solution," *Chem. Mater.*, vol. 14, no. 8, pp. 3591–3601, 2002.

[71] B. Li, X. Wei, and W. Pan, "Electrical properties of Mg-doped $Gd_{0.1}Ce_{0.9}O_{1.95}$ under different sintering conditions," *J. Power Sources*, vol. 183, no. 2, pp. 498–505, 2008.

[72] S. Rossignol, F. Gerard, and D. Duprez, "Effect of the preparation method on the properties of zirconia-ceria materials," *J. Mater. Chem.*, vol. 9, pp. 1615–1620, 1999.

[73] J. R. McBride, K. C. Hass, B. D. Poindexter, and W. H. Weber, "Raman and X-ray studies of $Ce_{1-x}RE_xO_{2-y}$, where RE=La, Pr, Nd, Eu, Gd, and Tb," *J. Appl. Phys.*, vol. 76, no. 4, pp. 2435–2441, 1994.

[74] S. Rossignol, F. Gerard, D. Mesnard, C. Kappenstein, and D. Duprez, "Structural changes of Ce-Pr-O oxides in hydrogen: a study by in situ X-ray diffraction and Raman spectroscopy," *J. Mater. Chem.*, vol. 13, pp. 3017–3020, 2003.

[75] R. de Biasi and M. Grillo, "Evidence for clustering in Cu^{2+}-doped CeO_2," *J. Alloys Compd.*, vol. 462, no. 1–2, pp. 15–18, 2008.

[76] R. de Biasi and M. Grillo, "Electron spin resonance of diluted solid solutions of Gd_2O_3 in CeO_2," *J. Sol. State Chem.*, vol. 178, no. 6, pp. 1973–1977, 2005.

[77] H. L. Tuller and A. S. Nowick, "Doped ceria as a solid oxide electrolyte," *J. Electrochem. Soc.*, vol. 122, no. 2, pp. 255–259, 1975.

[78] C. de Leitenburg, A. Trovarelli, F. Zamar, S. Maschio, G. Dolcetti, and J. Llorca, "A novel and simple route to catalysts with a high oxygen storage capacity - the direct room-temperature synthesis of Ceo_2-ZrO_2 solid solutions," *J. Chem. Soc.-Chem. Commun.*, pp. 2181–2182, Nov 7 1995.

[79] D. Fagg, J. Frade, V. Kharton, and I. Marozau, "The defect chemistry of $Ce(Pr, Zr)O_{2-\delta}$," *J. Sol. State Chem.*, vol. 179, no. 5, pp. 1469–1477, 2006.

[80] B. Li, X. Wei, and W. Pan, "Improved electrical conductivity of $Ce_{0.9}Gd_{0.1}O_{1.95}$ and $Ce_{0.9}Sm_{0.1}O_{1.95}$ by co-doping," *Int. J. Hydrogen Energy*, vol. 35, no. 7, pp. 3018 – 3022, 2010.

[81] A. Ainirad, M. K. Motlagh, and A. Maghsoudipoor, "A systematic study on the synthesis of Ca, Gd codoped cerium oxide by combustion method," *J. Alloys Compd.*, vol. 509, no. 5, pp. 1505–1510, 2011.

[82] T. Miki, T. Ogawa, M. Haneda, N. Kakuta, A. Ueno, S. Tateishi, S. Matsuura, and M. Sato, "Enhanced Oxygen Storage Capacity of Cerium Oxides in CeO_2/La_2O_3/Al_2O_3 Containing Precious Metals," *J. Phys. Chem.*, vol. 94, no. 16, pp. 6464–6467, 1990.

[83] D. A. Andersson, S. I. Simak, N. V. Skorodumova, I. A. Abrikosov, and B. Johansson, "Theoretical study of CeO_2 doped with tetravalent ions," *Phys. Rev. B*, vol. 76, p. 174119, 2007.

[84] D. A. Andersson, S. I. Simak, N. V. Skorodumova, I. A. Abrikosov, and B. Johansson, "Redox properties of CeO_2–MO_2 (M = Ti, Zr, Hf, or Th) solid solutions from first principles calculations," *Appl. Phys. Lett.*, vol. 90, no. 3, p. 031909, 2007.

[85] V. Butler, C. Catlow, B. Fender, and J. Harding, "Dopant ion radius and ionic conductivity in cerium dioxide," *Solid State Ionics*, vol. 8, no. 2, pp. 109–113, 1983.

[86] C. Catlow, "Static lattice simulation of structure and transport in superionic conductors," *Solid State Ionics*, vol. 8, no. 2, pp. 89–107, 1983.

[87] D.-J. Kim, "Lattice Parameters, Ionic Conductivities, and Solubility Limits in Fluorite-Structure MO_2 Oxide [M = Hf^{4+}, Zr^{4+}, Ce^{4+}, Th^{4+}, U^{4+}] Solid Solutions," *J. Am. Ceram. Soc.*, vol. 72, no. 8, pp. 1415–1421, 1989.

[88] D. A. Andersson, S. I. Simak, N. V. Skorodumova, I. A. Abrikosov, and B. Johansson, "Optimization of ionic conductivity in doped ceria," *PNAS*, vol. 103, no. 10, pp. 3518–3521, 2006.

[89] X. Wei, W. Pan, L. Cheng, and B. Li, "Atomistic calculation of association energy in doped ceria," *Solid State Ionics*, vol. 180, no. 1, pp. 13–17, 2009.

[90] Y. Jiang, J. B. Adams, and M. van Schilfgaarde, "Density-functional calculation of CeO_2 surfaces and prediction of effects of oxygen partial pressure and temperature on stabilities," *J. Chem. Phys.*, vol. 123, no. 6, p. 064701, 2005.

[91] Z. Yang, G. Luo, Z. Lu, and K. Hermansson, "Oxygen vacancy formation energy in Pd-doped ceria: A DFT+U study," *J. Chem. Phys.*, vol. 127, no. 7, p. 074704, 2007.

[92] Z. Yang, Y. Wei, Z. Fu, Z. Lu, and K. Hermansson, "Facilitated vacancy formation at Zr-doped ceria(111) surfaces," *Surf. Sci.*, vol. 602, no. 6, pp. 1199–1206, 2008.

[93] A. D. Mayernick and M. J. Janik, "Methane Activation and Oxygen Vacancy Formation over CeO_2 and Zr, Pd Substituted CeO_2 Surfaces," *J. Phys. Chem. C*, vol. 112, no. 38, pp. 14955–14964, 2008.

[94] A. D. Mayernick and M. J. Janik, "Ab initio thermodynamic evaluation of Pd atom interaction with CeO_2 surfaces," *J. Chem. Phys.*, vol. 131, no. 8, p. 084701, 2009.

[95] F. Ye, T. Mori, D. R. Ou, and A. N. Cormack, "Dopant type dependency of domain development in rare-earth-doped ceria: An explanation by computer simulation of defect clusters," *Solid State Ionics*, vol. 180, no. 20–22, pp. 1127 – 1132, 2009.

[96] F. Esch, S. Fabris, L. Zhou, T. Montini, C. Africh, P. Fornasiero, G. Comelli, and R. Rosei, "Electron Localization Determines Defect Formation on Ceria Substrates," *Science*, vol. 309, no. 5735, pp. 752–755, 2005.

[97] C. Zhang, A. Michaelides, D. A. King, and S. J. Jenkins, "Oxygen vacancy clusters on ceria: Decisive role of cerium f electrons," *Phys. Rev. B*, vol. 79, no. 7, p. 075433, 2009.

[98] N. V. Skorodumova, R. Ahuja, S. I. Simak, I. A. Abrikosov, B. Johansson, and B. I. Lundqvist, "Electronic, bonding, and optical properties of CeO_2 and Ce_2O_3 from first principles," *Phys. Rev. B*, vol. 64, no. 11, p. 115108, 2001.

[99] J. Hubbard, "Electron Correlations in Narrow Energy Bands," *Proc. R. Soc. London, Ser. A*, vol. 276, no. 1365, pp. 238–257, 1963.

[100] H. Tasaki, "The hubbard model - an introduction and selected rigorous results," *J. Phys.: Condens. Matter*, vol. 10, no. 20, p. 4353, 1998.

[101] C. W. M. Castleton, J. Kullgren, and K. Hermansson, "Tuning LDA + U for electron localization and structure at oxygen vacancies in ceria," *J. Chem. Phys.*, vol. 127, no. 24, p. 244704, 2007.

[102] S. Fabris, S. de Gironcoli, S. Baroni, G. Vicario, and G. Balducci, "Taming multiple valency with density functionals: A case study of defective ceria," *Phys. Rev. B*, vol. 71, no. 4, p. 041102, 2005.

[103] G. Kresse, P. Blaha, J. L. F. Da Silva, and M. V. Ganduglia-Pirovano, "Comment on "taming multiple valency with density functionals: A case study of defective ceria","" *Phys. Rev. B*, vol. 72, no. 23, p. 237101, 2005.

[104] S. Fabris, S. de Gironcoli, S. Baroni, G. Vicario, and G. Balducci, "Reply to "comment on 'taming multiple valency with density functionals: A case study of defective ceria' "," *Phys. Rev. B*, vol. 72, no. 23, p. 237102, 2005.

[105] D. A. Andersson, S. I. Simak, B. Johansson, I. A. Abrikosov, and N. V. Skorodumova, "Modeling of CeO_2 , Ce_2O_3 , and CeO_{2-x} in the LDA+U formalism," *Phys. Rev. B*, vol. 75, no. 3, p. 035109, 2007.

[106] J. L. F. Da Silva, M. V. Ganduglia-Pirovano, J. Sauer, V. Bayer, and G. Kresse, "Hybrid functionals applied to rare-earth oxides: The example of ceria," *Phys. Rev. B*, vol. 75, no. 4, p. 045121, 2007.

[107] C. Loschen, J. Carrasco, K. M. Neyman, and F. Illas, "First-principles LDA+U and GGA+U study of cerium oxides: Dependence on the effective U parameter," *Phys. Rev. B*, vol. 75, no. 3, p. 035115, 2007.

[108] P. J. Hay, R. L. Martin, J. Uddin, and G. E. Scuseria, "Theoretical study of CeO_2 and Ce_2O_3 using a screened hybrid density functional," *J. Chem. Phys.*, vol. 125, no. 3, p. 034712, 2006.

[109] J. Heyd, G. E. Scuseria, and M. Ernzerhof, "Hybrid functionals based on a screened Coulomb potential," *J. Chem. Phys.*, vol. 118, no. 18, pp. 8207–8215, 2003.

[110] J. L. F. Da Silva, "Stability of the Ce_2O_3 phases: A DFT+U investigation," *Phys. Rev. B*, vol. 76, no. 19, p. 193108, 2007.

[111] J. Kullgren, C. W. M. Castleton, C. Muller, D. M. Ramo, and K. Hermansson, "B3LYP calculations of cerium oxides," *J. Chem. Phys.*, vol. 132, no. 5, p. 054110, 2010.

[112] T. Désaunay, A. Ringuedé, M. Cassir, F. Labat, and C. Adamo, "Modeling basic components of solid oxide fuel cells using density functional theory: Bulk and surface properties of CeO_2," *Surf. Sci.*, vol. 606, no. 3–4, pp. 305–311, 2012.

[113] A. D. Becke, "Density-functional thermochemistry. III. The role of exact exchange," *J. Chem. Phys.*, vol. 98, no. 7, pp. 5648–5652, 1993.

[114] E. Schrödinger, "An Undulatory Theory of the Mechanics of Atoms and Molecules," *Phys. Rev.*, vol. 28, no. 6, pp. 1049–1070, 1926.

[115] M. Born and J. R. Oppenheimer, "Zur Quantentheorie der Molekeln," *Ann. Physik*, vol. 84, p. 457, 1927.

[116] J. C. Slater, "The Theory of Complex Spectra," *Phys. Rev.*, vol. 34, no. 10, pp. 1293–1322, 1929.

[117] P. Geerlings, F. De Proft, and W. Langenaeker, "Conceptual Density Functional Theory," *Chem. Rev.*, vol. 103, no. 5, pp. 1793–1874, 2003.

[118] P. Hohenberg and W. Kohn, "Inhomogeneous electron gas," *Phys. Rev.*, vol. 136, pp. B864–B871, Nov 1964.

[119] P. A. M. Dirac, "Note on Exchange Phenomena in the Thomas Atom.," *Proc. Cambridge Phil. Roy. Soc.*, vol. 26, pp. 376–385, 1930.

[120] R. G. Parr and W. Yang, *Density-Functional Theory of Atoms and Molecules*, vol. 16 of *International series of monographs on chemistry*. Oxford: Oxford Science Publications, 1989.

[121] J. P. Perdew and A. Zunger, "Self-interaction correction to density-functional approximations for many-electron systems," *Phys. Rev. B*, vol. 23, no. 10, pp. 5048–5079, 1981.

[122] D. M. Ceperley and B. J. Alder, "Ground state of the electron gas by a stochastic method," *Phys. Rev. Lett.*, vol. 45, no. 7, pp. 566–569, 1980.

[123] J. P. Perdew, K. Burke, and M. Ernzerhof, "Generalized Gradient Approximation Made Simple," *Phys. Rev. Lett.*, vol. 77, no. 18, pp. 3865–3868, 1996.

[124] A. Alkauskas, P. Broqvist, and A. Pasquarello, "Defect levels through hybrid density functionals: Insights and applications," *Phys. Status Sol. B*, vol. 248, no. 4, pp. 775–789, 2011.

[125] A. Avogadro, "Essai d'une manière de déterminer les masses relatives des molécules élémentaires des corps, et les proportions selon lesquelles elles entrent dans ces combinaisons," *Journal de Physique*, vol. 73, pp. 58–76, 1811.

[126] N. W. Ashcroft and N. D. Mermin, *Solid State Physics*. Harcourt College Publishers, 1976. College Edition.

[127] H. Hellmann, *Einfuhrung in die Quantumchemie*. Leipzig: Franz Deutsche, 1937.

[128] R. P. Feynman, "Forces in Molecules," *Phys. Rev.*, vol. 56, no. 4, pp. 340–343, 1939.

[129] P. Pulay, "Ab initio calculation of force constants and equilibrium geometries in polyatomic molecules I. Theory," *Mol. Phys.*, vol. 17, no. 2, pp. 197–204, 1969.

[130] E. Fermi, "Sopra lo spostamento per pressione delle righe elevate delle serie spettrali.," *Nuovo Cimento*, vol. 11, no. 3, pp. 157–166, 1934.

[131] D. R. Hamann, M. Schlüter, and C. Chiang, "Norm-Conserving Pseudopotentials," *Phys. Rev. Lett.*, vol. 43, no. 20, pp. 1494–1497, 1979.

[132] G. P. Kerker, "Non-singular atomic pseudopotentials for solid state applications.," *J. Phys. C: Sol. State Phys.*, vol. 13, no. 9, pp. L189–L194, 1980.

[133] D. Vanderbilt, "Optimally smooth norm-conserving pseudopotentials," *Phys. Rev. B*, vol. 32, no. 12, pp. 8412–8415, 1985.

[134] P. E. Blöchl, "Generalized separable potentials for electronic-structure calculations," *Phys. Rev. B*, vol. 41, no. 8, pp. 5414–5416, 1990.

[135] N. Troullier and J. L. Martins, "Efficient pseudopotentials for plane-wave calculations," *Phys. Rev. B*, vol. 43, no. 3, pp. 1993–2006, 1991.

[136] D. Vanderbilt, "Soft self-consistent pseudopotentials in a generalized eigenvalue formalism," *Phys. Rev. B*, vol. 41, no. 11, pp. 7892–7895, 1990.

[137] P. E. Blöchl, "Projector augmented-wave method," *Phys. Rev. B*, vol. 50, no. 24, pp. 17953–17979, 1994.

[138] G. Kresse and D. Joubert, "From ultrasoft pseudopotentials to the projector augmented-wave method," *Phys. Rev. B*, vol. 59, no. 3, pp. 1758–1775, 1999.

[139] S. J. Duclos, Y. K. Vohra, A. L. Ruoff, A. Jayaraman, and G. P. Espinosa, "High-pressure X-ray diffraction study of CeO_2 to 70 GPa and pressure-induced phase transformation from the fluorite structure," *Phys. Rev. B*, vol. 38, pp. 7755–7758, 1988.

[140] A. Nakajima, A. Yoshihara, and M. Ishigame, "Defect-induced Raman spectra in doped CeO_2," *Phys. Rev. B*, vol. 50, pp. 13297–13307, 1994. Bulk modulus calculated from elastic constants.

[141] L. Gerward, J. S. Olsen, L. Petit, G. Vaitheeswaran, V. Kanchana, and A. Svane, "Bulk modulus of CeO_2 and PrO_2–an experimental and theoretical study," *J. Alloys Compd.*, vol. 400, no. 1–2, pp. 56–61, 2005.

[142] J. J. Plata, A. M. Márquez, and J. F. Sanz, "Communication: Improving the density functional theory +U description of CeO_2 by including the contribution of the O $2p$ electrons," *J. Chem. Phys.*, vol. 136, no. 4, p. 041101, 2012.

[143] F. Birch, "Finite Elastic Strain of Cubic Crystals," *Phys. Rev.*, vol. 71, pp. 809–824, 1947.

[144] F. D. Murnaghan, "The Compressibility of Media under Extreme Pressures," *Proc. Natl. Acad. Sci. USA*, vol. 30, no. 9, pp. 244–247, 1944.

[145] L. Wang, T. Maxisch, and G. Ceder, "Oxidation energies of transition metal oxides within the GGA+U framework," *Phys. Rev. B*, vol. 73, p. 195107, 2006.

[146] E. Wuilloud, B. Delley, W. D. Schneider, and Y. Baer, "Spectroscopic Evidence for Localized and Extended f-Symmetry States in CeO_2," *Phys. Rev. Lett.*, vol. 53, pp. 202–205, 1984.

[147] A. Prokofiev, A. Shelykh, and B. Melekh, "Periodicity in the band gap variation of Ln_2X_3 (X=O, S, Se) in the lanthanide series," *J. Alloys Compd.*, vol. 242, no. 1–2, pp. 41–44, 1996.

[148] F. Marabelli and P. Wachter, "Covalent insulator CeO_2: Optical reflectivity measurements," *Phys. Rev. B*, vol. 36, no. 2, pp. 1238–1243, 1987.

[149] A. Pfau and K. Schierbaum, "The electronic structure of stoichiometric and reduced CeO_2 surfaces: an XPS, UPS and HREELS study," *Surf. Sci.*, vol. 321, no. 1–2, pp. 71–80, 1994.

[150] D. E. P. Vanpoucke, P. Bultinck, S. Cottenier, V. Van Speybroeck, and I. Van Driessche, "Density functional theory study of $La_2Ce_2O_7$: Disordered fluorite versus pyrochlore structure," *Phys. Rev. B*, vol. 84, p. 054110, 2011.

[151] T. Kudo and H. Obayashi, "Oxygen Ion Conduction of the Fluorite-Type $Ce_{1-x}Ln_xO_{2-x/2}$ (Ln = Lanthanoid Element)," *J. Electrochem. Soc.*, vol. 122, no. 1, pp. 142–147, 1975.

[152] L. Kundakovic and M. Flytzani-Stephanopoulos, "Reduction characteristics of copper oxide in cerium and zirconium oxide systems," *Appl. Catal. A*, vol. 171, no. 1, pp. 13–29, 1998.

[153] H. Yamamura, H. Nishino, K. Kakinuma, and K. Nomura, "Crystal phase and electrical conductivity in the pyrochlore-type composition systems, $Ln_2Ce_2O_7$ (Ln = La, Nd, Sm, Eu, Gd, Y and Yb)," *J. Ceram. Soc. Jpn*, vol. 111, no. 12, pp. 902–906, 2003.

[154] X. Wang, J. A. Rodriguez, J. C. Hanson, D. Gamarra, A. Martínez-Arias, and M. Fernández-García, "Unusual Physical and Chemical Properties of Cu in $Ce_{1-x}Cu_xO_2$ Oxides," *J. Phys. Chem. B*, vol. 109, no. 42, pp. 19595–19603, 2005.

[155] A. Tiwari, V. M. Bhosle, S. Ramachandran, N. Sudhakar, J. Narayan, S. Budak, and A. Gupta, "Ferromagnetism in Co doped CeO_2: Observation of a giant magnetic moment with a high Curie temperature," *Appl. Phys. Lett.*, vol. 88, no. 14, p. 142511, 2006.

[156] A. Nakamura, N. Masaki, H. Otobe, Y. Hinatsu, J. Wang, and M. Takeda, "Defect-fluorite oxides $M_{1-y}Ln_yO_{2-y/2}$(Ln = lanthanide; M = Hf, Zr, Ce, U, Th): Structure, property, and applications," *Pure Appl. Chem.*, vol. 79, pp. 1691–1729, 2007.

[157] Y. Q. Song, H. W. Zhang, Q. Y. Wen, H. Zhu, and J. Q. Xiao, "Co doping effect on the magnetic properties of CeO_2 films on Si(111) substrates," *J. Appl. Phys.*, vol. 102, no. 4, p. 043912, 2007.

[158] B. Vodungbo, Y. Zheng, F. Vidal, D. Demaille, V. H. Etgens, and D. H. Mosca, "Room temperature ferromagnetism of Co doped $CeO_{2-\delta}$ diluted magnetic oxide: Effect of oxygen and anisotropy," *Appl. Phys. Lett.*, vol. 90, no. 6, p. 062510, 2007.

[159] R. K. Singhal, P. Kumari, S. Kumar, S. N. Dolia, Y. T. Xing, M. Alzamora, U. P. Deshpande, T. Shripathi, and E. Saitovitch, "Room temperature ferromagnetism in pure and Co- and Fe-doped CeO_2 dilute magnetic oxide: effect of oxygen vacancies and cation valence," *J. Phys. D: Appl. Phys.*, vol. 44, no. 16, p. 165002, 2011.

[160] B. M. Reddy, A. Khan, P. Lakshmanan, M. Aouine, S. Loridant, and J.-C. Volta, "Structural Characterization of Nanosized CeO_2-SiO_2, CeO_2-TiO_2, and CeO_2-ZrO_2 Catalysts by XRD, Raman, and HREM Techniques," *J. Phys. Chem. B*, vol. 109, no. 8, pp. 3355–3363, 2005.

[161] B. Reddy and A. Khan, "Nanosized CeO_2ŨSiO_2, CeO_2ŨTiO_2, and CeO_2ŨZrO_2 Mixed Oxides: Influence of Supporting Oxide on Thermal Stability and Oxygen Storage Properties of Ceria," *Catal. Surv. Asia*, vol. 9, pp. 155–171, 2005.

[162] E. Rocchini, A. Trovarelli, J. Llorca, G. W. Graham, W. H. Weber, M. Maciejewski, and A. Baiker, "Relationships between Structural/Morphological Modifications and Oxygen Storage–Redox Behavior of Silica-Doped Ceria," *J. Catal.*, vol. 194, no. 2, pp. 461–478, 2000.

[163] E. Rocchini, M. Vicario, J. Llorca, C. de Leitenburg, G. Dolcetti, and A. Trovarelli, "Reduction and Oxygen Storage Behavior of Noble Metals Supported on Silica-Doped Ceria," *J. Catal.*, vol. 211, no. 2, pp. 407–421, 2002.

[164] R. Lin, M.-F. Luo, Y.-J. Zhong, Z.-L. Yan, G.-Y. Liu, and W.-P. Liu, "Comparative study of $CuO/Ce_{0.7}Sn_{0.3}O_2$, CuO/CeO_2 and CuO/SnO_2 catalysts for low-temperature CO oxidation," *Appl. Catal., A*, vol. 255, no. 2, pp. 331–336, 2003.

[165] G. Kresse and J. Hafner, "Ab initio molecular dynamics for liquid metals," *Phys. Rev. B*, vol. 47, no. 1, pp. 558–561, 1993.

[166] G. Kresse and J. Furthmüller, "Efficient iterative schemes for ab initio total-energy calculations using a plane-wave basis set," *Phys. Rev. B*, vol. 54, no. 16, pp. 11169–11186, 1996.

[167] S. L. Dudarev, G. A. Botton, S. Y. Savrasov, C. J. Humphreys, and A. P. Sutton, "Electron-energy-loss spectra and the structural stability of nickel oxide: An LSDA+U study," *Phys. Rev. B*, vol. 57, pp. 1505–1509, 1998.

[168] H. J. Monkhorst and J. D. Pack, "Special points for brillouin-zone integrations," *Phys. Rev. B*, vol. 13, pp. 5188–5192, Jun. 1976.

[169] A. A. Maradudin, E. W. Montroll, G. H. Weiss, and I. P. Ipatova, *Theory of lattice dynamics in the harmonic approximation*. New York: Academic press, 2 ed., 1971.

[170] M. A. Blanco, A. M. Pendas, E. Francisco, J. M. Recio, and R. Franco, "Thermodynamical properties of solids from microscopic theory: Applications to MgF_2 and Al_2O_3," *Theochem-J. Mol. Struct.*, vol. 368, pp. 245–255, 1996.

[171] E. Francisco, M. A. Blanco, and G. Sanjurjo, "Atomistic simulation of SrF_2 polymorphs," *Phys. Rev. B*, vol. 63, p. 094107, 2001.

[172] D. E. P. Vanpoucke, "HIVE v2.1." http://users.ugent.be/~devpouck/hive_refman/index.html, 2011.

[173] P. Bultinck, "Critical analysis of the local aromaticity concept in polyaromatic hydrocarbons," *Farad. Discuss.*, vol. 135, pp. 347–365, 2007. General Meeting on Chemical Concepts from Quantum Mechanics, Univ Manchester, Manchester, England, Sep. 04-06, 2006.

[174] P. Bultinck, C. Van Alsenoy, P. W. Ayers, and R. Carbó-Dorca, "Critical analysis and extension of the Hirshfeld atoms in molecules," *J. Chem. Phys.*, vol. 126, no. 14, p. 144111, 2007.

[175] A. D. Becke, "A multicenter numerical integration scheme for polyatomic molecules," *J. Chem. Phys.*, vol. 88, no. 4, pp. 2547–2553, 1988.

[176] V. I. Lebedev and D. Laikov, "Quadrature formula for the sphere of 131-th algebraic order of accuracy," *Doklady Mathematics*, vol. 59, no. 3, pp. 477–481, 1999.

[177] A. R. Denton and N. W. Ashcroft, "Vegard's law," *Phys. Rev. A*, vol. 43, pp. 3161–3164, Mar 1991.

[178] E. Clementi and D. L. Raimondi, "Atomic Screening Constants From SCF Functions," *J. Chem. Phys.*, vol. 38, no. 11, p. 2686, 1963.

[179] J. Slater, "Atomic Radii in Crystals," *J. Chem. Phys.*, vol. 41, no. 10, p. 3199, 1964.

[180] J. D. Van Horn, "Electronic Table of Shannon Ionic Radii," 2001. downloaded 08/13/2010.

[181] R. D. Shannon, "Revised effective ionic radii and systematic studies of inter-atomic distances in halides and chalcogenides," *Acta Cryst.*, vol. A32, no. 5, pp. 751–767, 1976.

[182] M. Panhans and R. Blumenthal, "A thermodynamic and electrical conductivity study of nonstoichiometric cerium dioxide," *Solid State Ionics*, vol. 60, no. 4, pp. 279–298, 1993.

[183] C. Kittel, *Introduction to Solid State Physics.* New York: John Wiley and Sons, Inc., 7 ed., 1996.

[184] Y. Tsuru, Y. Shinzato, Y. Saito, M. Shimazu, M. Shiono, and M. Morinaga, "Estimation of linear thermal expansion coefficient from cohesive energy obtained by ab-initio calculation of metals and ceramics," *J. Ceram. Soc. Jpn.*, vol. 118, no. 1375, pp. 241–245, 2010.

[185] V. Shapovalov and H. Metiu, "Catalysis by doped oxides: CO oxidation by $Au_xCe_{1-x}O_2$," *J. Catal.*, vol. 245, no. 1, pp. 205–214, 2007.

[186] I. Van Driessche, G. Penneman, C. De Meyer, I. Stambolova, E. Bruneel, and S. Hoste, "The influence of sol gel precursors and substrate type in the spin coating of CeO_2 thin films.," in *Euro Ceramics VII, PT 1-3*, vol. 206-2 of *Key Engineering Materials*, (Brandrain 6, CH-8707 Zurich-Uetikon, Switzerland), pp. 479–482, Trans Tech Publications Ltd, 2002.

[187] Y. Q. Song, H. W. Zhang, Q. H. Yang, Y. L. Liu, Y. X. Li, L. R. Shah, H. Zhu, and J. Q. Xiao, "Electronic structure and magnetic properties of Co-doped CeO_2 : based on first principle calculation," *J. Phys.: Condens. Matter*, vol. 21, no. 12, p. 125504, 2009.

[188] Z. Lu, Z. Yang, B. He, C. Castleton, and K. Hermansson, "Cu-doped ceria: Oxygen vacancy formation made easy," *Chem. Phys. Lett.*, vol. 510, no. 1–3, pp. 60–66, 2011.

[189] L. Minervini, R. W. Grimes, and K. E. Sickafus, "Disorder in pyrochlore oxides," *J. Am. Ceram. Soc.*, vol. 83, pp. 1873–1878, 2000.

[190] D. E. Vanpoucke, S. Cottenier, V. V. Speybroeck, P. Bultinck, and I. V. Driessche, "Tuning of CeO_2 buffer layers for coated superconductors through doping," *Appl. Surf. Sci.*, no. 4, pp. –, 2012.

[191] D. E. P. Vanpoucke, P. Bultinck, S. Cottenier, V. Van Speybroeck, and I. Van Driessche, "Tetravalent doping of CeO_2: The impact of valence electron character on group IV dopant influence.," pp. –, 2012. to be submitted.

[192] X. Wang, J. A. Rodriguez, J. C. Hanson, D. Gamarra, A. Martínez-Arias, and M. Fernández-García, "In Situ Studies of the Active Sites for the Water Gas Shift Reaction over Cu-CeO_2 Catalysts: Complex Interaction between Metallic Copper and Oxygen Vacancies of Ceria," *J. Phys. Chem. B*, vol. 110, no. 1, pp. 428–434, 2006.

[193] F. Brisse and O. Knop, "Pyrochlores. II. An investigation of $La_2Ce_2O_7$ by neutron diffraction," *Can. J. Chem.*, vol. 45, pp. 609–614, 1967.

[194] K. M. Ryan, J. P. McGrath, R. A. Farrell, W. M. O'Neill, C. J. Barnes, and M. A. Morris, "Measurements of the lattice constant of ceria when doped with lanthana and praseodymia - the possibility of local defect ordering and the observation of extensive phase separation," *J. Phys. Condens. Matter*, vol. 15, no. 2, pp. L49–L58, 2003.

[195] J. S. Bae, W. K. Choo, and C. H. Lee, "The crystal structure of ionic conductor $La_xCe_{1-x}O_{2-x/2}$," *J. Eur. Ceram. Soc.*, vol. 24, no. 6, pp. 1291–1294, 2004.

[196] V. Fernandes, J. J. Klein, N. Mattoso, D. H. Mosca, E. Silveira, E. Ribeiro, W. H. Schreiner, J. Varalda, and A. J. A. de Oliveira, "Room temperature ferromagnetism in Co-doped CeO_2 films on Si(001)," *Phys. Rev. B*, vol. 75, p. 121304, 2007.

[197] Q.-Y. Wen, H.-W. Zhang, Y.-Q. Song, Q.-H. Yang, H. Zhu, and J. Q. Xiao, "Room-temperature ferromagnetism in pure and Co doped CeO_2 powders," *J. Phys.: Condens. Matter*, vol. 19, no. 24, p. 246205, 2007.

[198] J. Sacanell, M. A. Paulin, V. Ferrari, G. Garbarino, and A. G. Leyva, "Reversible switching of room temperature ferromagnetism in CeO_2-Co nanoparticles," *Appl. Phys. Lett.*, vol. 100, no. 17, p. 172405, 2012.

[199] D. Xu, X. Liu, S. Xu, D. Yan, L. Pei, C. Zhu, D. Wang, and W. Su, "Fabrication and performance of $Ce_{0.85}Sm_{0.15}O_{1.925}$–$Fe_2O_3$ electrolytes in IT-SOFCs," *Solid State Ionics*, vol. 192, no. 1, pp. 510–514, 2011.

[200] H.-C. Yao, X.-L. Zhao, X. Chen, J.-C. Wang, Q.-Q. Ge, J.-S. Wang, and Z.-J. Li, "Processing and characterization of CoO and Sm_2O_3 codoped ceria solid solution electrolyte," *J. Power Sources*, vol. 205, pp. 180–187, 2012.

[201] F. Deganello and A. Martorana, "Phase Analysis and Oxygen Storage Capacity of Ceria-Lanthana-Based TWC Promoters Prepared by Sol-Gel Routes," *J. Solid State Chem.*, vol. 163, no. 2, pp. 527–533, 2002.

[202] F. Deganello, A. Longo, and A. Martorana, "EXAFS study of ceria-lanthana-based TWC promoters prepared by sol-gel routes," *J. Solid State Chem.*, vol. 175, no. 2, pp. 289 – 298, 2003.

[203] B. C. Morris, W. R. Flavell, W. C. Mackrodt, and M. A. Morris, "Lattice parameter changes in the mixed-oxide system $Ce_{1-x}La_xO_{2-x/2}$: a combined experimental and theoretical study," *J. Mater. Chem.*, vol. 3, pp. 1007–1013, 1993.

[204] V. Bellière, G. Joorst, O. Stephan, F. M. F. de Groot, and B. M. Weckhuysen, "Phase segregation in cerium–lanthanum solid solutions," *J. Phys. Chem. B*, vol. 110, pp. 9984–9990, 2006.

[205] B. Cordero, V. Gomez, A. E. Platero-Prats, M. Reves, J. Echeverria, E. Cremades, F. Barragan, and S. Alvarez, "Covalent radii revisited," *Dalton Transactions*, no. 21, pp. 2832–2838, 2008.

[206] A. Ismail, J. Hooper, J. B. Giorgi, and T. K. Woo, "A DFT+U study of defect association and oxygen migration in samarium-doped ceria," *Phys. Chem. Chem. Phys.*, vol. 13, pp. 6116–6124, 2011.

[207] G. Murgida, V. Vildosola, V. Ferrari, and A. Llois, "Charge localization in Co-doped ceria with oxygen vacancies," *Solid State Communications*, vol. 152, no. 5, pp. 368–371, 2012.

[208] N. Van de Velde, T. Bruggeman, L. Stove, G. Pollefeyt, O. Brunkahl, and I. Van Driessche, "Influence of Morphology and Texture of CeO_2 on $YBa_2Cu_3O_7$ (YBCO) Growth and $BaCeO_3$ Formation in Solution-Derived Synthesis," *Eur. J. Inor. Chem.*, vol. 2012, no. 8, pp. 1186–1194, 2012.

[209] H. Yamamura, H. Nishino, and K. Kakinuma, "Conductivity for $Eu_2Zr_2O_7$ and $La_2Ce_2O_7$ with pyrochlore-type composition," *J. Ceram. Soc. Jpn*, vol. 112, no. 1310, pp. 553–558, 2004.

[210] E. Zintl and U. Croatto, " Fluoritgitter mit leeren Anionenplätzen," *Z. Anorg. Allg. Chem.*, vol. 242, pp. 79–86, 1939.

[211] M. Reddy, Benjaram, L. Katta, and G. Thrimurthulu, "Novel Nanocrystalline $Ce_{1-x}La_xO_{2-\delta}$ $(x = 0.2)$ Solid Solutions: Structural Characteristics and Catalytic Performance," *Chem. Mater.*, vol. 22, no. 2, pp. 467–475, 2010.

[212] S. Liang, E. Broitman, Y. Wang, A. Cao, and G. Veser, "Highly stable, mesoporous mixed lanthanumŨcerium oxides with tailored structure and reducibility," *J. Mater. Sci.*, vol. 46, pp. 2928–2937, 2011.

[213] I. Van Driessche, G. Penneman, E. Bruneel, and S. Hoste, "Nonvacuumbased deposition techniques for superconducting ceramic coatings," *Pure Appl. Chem.*, vol. 74, no. 11, pp. 2101–2109, 2002.

[214] I. Van Driessche, G. Penneman, J. S. Abell, E. Bruneel, and S. Hoste, "Chemical approach to the deposition of textured ceo2 buffer layers based on sol gel dip coating," *Thermec'2003, parts 1–5*, vol. 426-4, pp. 3517–3522, 2003.

[215] D. Chambonnet, D. Keller, and C. Belouet, "Control of the 2d/3d transition of the growth mechanism in the ybco/ce1-xlaxo2-x/2/srtio3 system," *Physica C*, vol. 302, no. 2-3, pp. 198 – 206, 1998.

[216] W. M. O'Neill and M. A. Morris, "The defect chemistry of lanthana-ceria mixed oxides by MASNMR," *Chem. Phys. Lett.*, vol. 305, no. 5-6, pp. 389 – 394, 1999.

[217] G. Bergerhoff and I. D. Brown in *Crystallographic Databases* (F. H. Allen, G. Bergerhoff, and R. Sievers, eds.), vol. 77, Chester: International Union of Crystallography, 1987.

[218] A. Belsky, M. Hellenbrandt, V. L. Karen, and Luksch *Acta Cryst. B*, vol. 58, pp. 364–Ű369, 2002.

[219] F. W. Bezerra Lopes, C. P. de Souza, A. M. Vieira de Morais, J.-P. Dallas, and J.-R. Gavarri, "Determination of $RE_2Ce_2O_7$ pyrochlore phases from monazite-allanite ores," *Hydrometallurgy*, vol. 97, no. 3–4, pp. 167–172, 2009.

[220] C. Jiang, C. R. Stanek, K. E. Sickafus, and B. P. Uberuaga, "First-principles prediction of disordering tendencies in pyrochlore oxides," *Phys. Rev. B*, vol. 79, no. 10, p. 104203, 2009.

[221] N. J. Ramer and A. M. Rappe, "Virtual-crystal approximation that works: Locating a compositional phase boundary in $Pb(Zr_{1-x}Ti_x)O_3$," *Phys. Rev. B*, vol. 62, no. 2, pp. R743–R746, 2000.

[222] D. Lerch, O. Wieckhorst, G. L. W. Hart, R. W. Forcade, and S. Mueller, "UNCLE: a code for constructing cluster expansions for arbitrary lattices with minimal user-input," *Modell. Simul. Mater. Sci. Eng.*, vol. 17, no. 5, 2009.

[223] J. Sanchez, F. Ducastelle, and D. Gratias, "Generalized cluster description of multicomponent systems," *Physica A*, vol. 128, no. 1–2, pp. 334–350, 1984.

[224] A. Zunger, S.-H. Wei, L. G. Ferreira, and J. E. Bernard, "Special quasirandom structures," *Phys. Rev. Lett.*, vol. 65, no. 3, pp. 353–356, 1990.

[225] S.-H. Wei, L. G. Ferreira, J. E. Bernard, and A. Zunger, "Electronic properties of random alloys: Special quasirandom structures," *Phys. Rev. B*, vol. 42, no. 15, pp. 9622–9649, 1990.

[226] A. V. Ruban, S. I. Simak, S. Shallcross, and H. L. Skriver, "Local lattice relaxations in random metallic alloys: Effective tetrahedron model and supercell approach," *Phys. Rev. B*, vol. 67, no. 21, p. 214302, 2003.

[227] A. Svane, "Electronic structure of cerium in the self-interaction-corrected local-spin-density approximation," *Phys. Rev. B*, vol. 53, no. 8, pp. 4275–4286, 1996.

[228] M. Nolan, S. Grigoleit, D. C. Sayle, S. C. Parker, and G. W. Watson, "Density functional theory studies of the structure and electronic structure of pure and defective low index surfaces of ceria," *Surf. Sci.*, vol. 576, no. 1-3, pp. 217 – 229, 2005.

[229] I. Yeriskin and M. Nolan, "Doping of ceria surfaces with lanthanum: a DFT+U study," *J. Phys.: Condens. Matter*, vol. 22, no. 13, p. 135004, 2010.

[230] J.-P. Crocombette and A. Chartier, "Molecular dynamics studies of radiation induced phase transitions in $La_2Zr_2O_7$ pyrochlore," *Nucl. Instrum. Methods Phys. Res., Sect. B*, vol. 255, no. 1, pp. 158–165, 2007.

[231] H. Yamamura, H. Nishino, K. Kakinuma, and K. Nomura, "Relationship between oxide-ion conductivity and ordering of oxide ion in the $(Y_{1-x}La_x)_2(Ce_{1-x}Zr_x)_2O_7$ system with pyrochlore-type composition," *Solid State Ionics*, vol. 178, no. 3-4, pp. 233 – 238, 2007.

[232] J. Dalton, *A New System of Chemical Philosophy, Part 1.* 1808.

[233] J. Thomson, "XXIV. On the structure of the atom: an investigation of the stability and periods of oscillation of a number of corpuscles arranged at equal intervals around the circumference of a circle; with application of the results to the theory of atomic structure," *Philosophical Magazine Series 6*, vol. 7, no. 39, pp. 237–265, 1904.

[234] H. Nagaoka, "Kinetics of a System of Particles illustrating the Line and the Band Spectrum and the Phenomena of Radioactivity," *Philosophical Magazine Series 6*, vol. 7, pp. 445–455, 1904.

[235] G. N. Lewis, "The atom and the molecule.," *JACS*, vol. 38, no. 4, pp. 762–785, 1916.

[236] I. Langmuir, "The Arrangement of Electrons in Atoms and Molecules.," *JACS*, vol. 41, no. 6, pp. 868–934, 1919.

[237] H. Geiger and E. Marsden, "On a Diffuse Reflection of the α-Particles," *Proceedings of the Royal Society of London. Series A*, vol. 82, no. 557, pp. 495–500, 1909.

[238] E. Rutherford, "The Scattering of α and β Particles by Matter and the Structure of the Atom," *Philosophical Magazine Series 6*, vol. 21, pp. 669–688, 1911.

[239] N. Bohr, "I. On the constitution of atoms and molecules," *Philosophical Magazine Series 6*, vol. 26, no. 151, pp. 1–25, 1913.

[240] N. Bohr, "XXXVII. On the constitution of atoms and molecules," *Philosophical Magazine Series 6*, vol. 26, no. 153, pp. 476–502, 1913.

[241] P. J. Mohr, B. N. Taylor, and D. B. Newell, "CODATA Recommended Values of the Fundamental Physical Constants: 2010," *ArXiv e-prints*, 2012.

[242] B. H. Bransden and C. J. Joachain, *Quantum Mechanics.* Essex: Pearson Education, 2 ed., 2000.

[243] I. Newton, *Opticks: or a Treatise of the Reflections, Refractions, Inflections and Colours of Light. Also Two treatises of the species and magnitude of Curvilinear Figures.* 1704. pg. 389.

[244] T. T. Tsong, "Fifty years of seeing atoms.," *Physics Today*, vol. 59, no. 3, pp. 31–37, 2006.

[245] C. Matta and R. Bader, "An experimentalist's reply to "What is an atom in a molecule?"," *J. Phys. Chem. A*, vol. 110, no. 19, pp. 6365–6371, 2006.

[246] R. S. Mulliken, "Electronic Structures of Molecules XI. Electroaffinity, Molecular Orbitals and Dipole Moments," *J. Chem. Phys.*, vol. 3, no. 9, pp. 573–585, 1935.

[247] R. S. Mulliken, "Electronic Population Analysis on LCAO-MO Molecular Wave Functions. I," *J. Chem. Phys.*, vol. 23, no. 10, pp. 1833–1840, 1955.

[248] F. L. Hirshfeld, "Bonded-atom fragments for describing molecular charge densities," *Theor. Chim. Acta*, vol. 44, pp. 129–138, 1977.

[249] R. F. Bader, "A Quantum Theory of Molecular Structure and Its Applications," *Chem. Rev.*, vol. 91, no. 5, pp. 893–928, 1991.

[250] T. C. Lillestolen and R. J. Wheatley, "Redefining the atom: atomic charge densities produced by an iterative stockholder approach," *Chem. Comm.*, no. 45, pp. 5909–5911, 2008.

[251] T. C. Lillestolen and R. J. Wheatley, "Atomic charge densities generated using an iterative stockholder procedure," *J. Chem. Phys.*, vol. 131, no. 14, 2009.

[252] T. A. Manz and D. S. Sholl, "Chemically Meaningful Atomic Charges That Reproduce the Electrostatic Potential in Periodic and Nonperiodic Materials," *J. Chem. Theory Comp.*, vol. 6, no. 8, pp. 2455–2468, 2010.

[253] R. S. Mulliken, "Electronic Population Analysis on LCAO-MO Molecular Wave Functions. II. Overlap Populations, Bond Orders, and Covalent Bond Energies," *J. Chem. Phys.*, vol. 23, no. 10, pp. 1841–1846, 1955.

[254] R. S. Mulliken, "Electronic Population Analysis on LCAO-MO Molecular Wave Functions. III. Effects of Hybridization on Overlap and Gross AO Populations," *J. Chem. Phys.*, vol. 23, no. 12, pp. 2338–2342, 1955.

[255] R. S. Mulliken, "Electronic Population Analysis on LCAO-MO Molecular Wave Functions. IV. Bonding and Antibonding in LCAO and Valence-Bond Theories," *J. Chem. Phys.*, vol. 23, no. 12, pp. 2343–2346, 1955.

[256] G. Voronoï, "Nouvelles applications des paramètres continus à la theorie des formes quadratiques," *Journal für die Reine und Angewandte Mathematik*, vol. 133, pp. 97–178, 1907.

[257] E. Wigner and F. Seitz, "On the Constitution of Metallic Sodium," *Phys. Rev.*, vol. 43, pp. 804–810, 1933.

[258] R. Bader and C. Matta, "Atomic charges are measurable quantum expectation values: A rebuttal of criticisms of QTAIM charges," *J. Phys. Chem. A*, vol. 108, no. 40, pp. 8385–8394, 2004.

[259] R. G. Parr, P. W. Ayers, and R. F. Nalewajski, "What Is an Atom in a Molecule?," *J. Phys. Chem. A*, vol. 109, no. 17, pp. 3957–3959, 2005.

[260] S. Saha, R. K. Roy, and P. W. Ayers, "Are the Hirshfeld and Mulliken population analysis schemes consistent with chemical intuition?," *International Journal of Quantum Chemistry*, vol. 109, no. 9, pp. 1790–1806, 2009.

[261] P. Bultinck, P. W. Ayers, S. Fias, K. Tiels, and C. Van Alsenoy, "Uniqueness and basis set dependence of iterative Hirshfeld charges," *Chem. Phys. Lett.*, vol. 444, pp. 205–208, Aug 17 2007.

[262] P. W. Ayers, "Atoms in molecules, an axiomatic approach. I. Maximum transferability.," *J. Chem. Phys.*, vol. 113, no. 24, pp. 10886–10898, 2000.

[263] E. Francisco, A. M. Pendás, A. Costales, and M. García-Revilla, "Electron number distribution functions with iterative Hirshfeld atoms," *Comp. Theor. Chem.*, vol. 975, no. 1-3, pp. 2–8, 2011.

[264] E. Francisco, A. Pendás, and M. Blanco, "Generalized electron number distribution functions: real space versus orbital space descriptions," *Theor. Chem. Acc.*, vol. 128, pp. 433–444, 2011.

[265] A. M. Pendás, V. Luaña, L. Pueyo, E. Francisco, and P. Mori-Sánchez, "Hirshfeld surfaces as approximations to interatomic surfaces.," *J. Chem. Phys.*, vol. 117, no. 3, p. 1017, 2002.

[266] X. Gonze, B. Amadon, P.-M. Anglade, J.-M. Beuken, F. Bottin, P. Boulanger, F. Bruneval, D. Caliste, R. Caracas, M. Côté, T. Deutsch, L. Genovese, P. Ghosez, M. Giantomassi, S. Goedecker, D. Hamann, P. Hermet, F. Jollet, G. Jomard, S. Leroux, M. Mancini, S. Mazevet, M. Oliveira, G. Onida, Y. Pouillon, T. Rangel, G.-M. Rignanese, D. Sangalli, R. Shaltaf, M. Torrent, M. Verstraete, G. Zerah, and J. Zwanziger, "ABINIT: First-principles approach to material and nanosystem properties," *Comp. Phys. Comm.*, vol. 180, no. 12, pp. 2582 – 2615, 2009.

[267] M. D. Smith, S. M. Blau, K. B. Chang, M. Zeller, J. Schrier, and A. J. Norquist, "Beyond Charge Density Matching: The Role of $C-H\cdots O$ Interactions in the Formation of Templated Vanadium Tellurites," *Cryst. Growth Des.*, vol. 11, no. 9, pp. 4213–4219, 2011.

[268] E. C. Glor, S. M. Blau, J. Yeon, M. Zeller, P. S. Halasyamani, J. Schrier, and A. J. Norquist, "[R-$C_7H_{16}N_2$][$V_2Te_2O_{10}$] and [S-$C_7H_{16}N_2$][$V_2Te_2O_{10}$]; new polar templated vanadium tellurite enantiomers," *J. Solid State Chem.*, vol. 184, no. 6, pp. 1445–1450, 2011.

[269] J. Schrier, "Fluorinated and Nanoporous Graphene Materials As Sorbents for Gas Separations," *ACS Applied Materials & Interfaces*, vol. 3, no. 11, pp. 4451–4458, 2011.

[270] O. Leenaerts, H. Peelaers, A. D. Hernández-Nieves, B. Partoens, and F. M. Peeters, "First-principles investigation of graphene fluoride and graphane," *Phys. Rev. B*, vol. 82, p. 195436, 2010.

[271] O. Leenaerts, B. Partoens, and F. M. Peeters, "Paramagnetic adsorbates on graphene: A charge transfer analysis," *Appl. Phys. Lett.*, vol. 92, no. 24, p. 243125, 2008.

[272] O. Leenaerts, B. Partoens, and F. M. Peeters, "Water on graphene: Hydrophobicity and dipole moment using density functional theory," *Phys. Rev. B*, vol. 79, p. 235440, 2009.

[273] M. A. Spackman and D. Jayatilaka, "Hirshfeld surface analysis," *Cryst. Eng. Comm.*, vol. 11, pp. 19–32, 2009.

[274] M. A. Spackman and P. G. Byrom, "A novel definition of a molecule in a crystal," *Chem. Phys. Lett.*, vol. 267, no. 3Ũ4, pp. 215–220, 1997.

[275] J. J. McKinnon, A. S. Mitchell, and M. A. Spackman, "Hirshfeld Surfaces: A New Tool for Visualising and Exploring Molecular Crystals," *Chem.-Eur. J.*, vol. 4, no. 11, pp. 2136–2141, 1998.

[276] J. J. McKinnon, M. A. Spackman, and A. S. Mitchell, "Novel tools for visualizing and exploring intermolecular interactions in molecular crystals," *Acta Crystallogr., Sect. B*, vol. 60, no. 6, pp. 627–668, 2004.

[277] S. K. Wolff, D. J. Grimwood, J. J. McKinnon, D. Jayatilaka, and M. A. Spackman, "Crystal explorer 2.1," 2007. University of Western Australia, Perth.

[278] T. Watanabe, T. A. Manz, and D. S. Sholl, "Accurate Treatment of Electrostatics during Molecular Adsorption in Nanoporous Crystals without Assigning Point Charges to Framework Atoms," *J. Phys. Chem. C*, vol. 115, no. 11, pp. 4824–4836, 2011.

[279] G. W. Rogers and J. Z. Liu, "Graphene Actuators: Quantum-Mechanical and Electrostatic Double-Layer Effects," *J. Am. Chem. Soc.*, vol. 133, no. 28, pp. 10858–10863, 2011.

[280] T. Verstraelen, S. V. Sukhomlinov, V. Van Speybroeck, M. Waroquier, and K. S. Smirnov, "Computation of Charge Distribution and Electrostatic Potential in Silicates with the Use of Chemical Potential Equalization Models," *J. Phys. Chem. C*, vol. 116, no. 1, pp. 490–504, 2012.

[281] S. Van Damme, P. Bultinck, and S. Fias, "Electrostatic Potentials from Self-Consistent Hirshfeld Atomic Charges," *J. Chem. Theory Comput.*, vol. 5, no. 2, pp. 334–340, 2009.

[282] W. Kohn and L. J. Sham, "Self-consistent equations including exchange and correlation effects," *Phys. Rev.*, vol. 140, pp. A1133–A1138, Nov 1965.

[283] J. C. Slater, *The Self-Consistent Field for Molecular and Solids*, vol. 4 of *Quantum Theory of Molecular and Solids*. New York: McGraw-Hill, 1974.

[284] S. H. Vosko, L. Wilk, and M. Nusair, "Accurate spin-dependent electron liquid correlation energies for local spin density calculations: a critical analysis," *Can. J. Phys.*, vol. 58, no. 8, pp. 1200–1211, 1980.

[285] M. J. Frisch, G. W. Trucks, H. B. Schlegel, G. E. Scuseria, M. A. Robb, J. R. Cheeseman, J. A. Montgomery, Jr., T. Vreven, K. N. Kudin, J. C. Burant, J. M. Millam, S. S. Iyengar, J. Tomasi, V. Barone, B. Mennucci, M. Cossi, G. Scalmani, N. Rega, G. A. Petersson, H. Nakatsuji, M. Hada, M. Ehara, K. Toyota, R. Fukuda, J. Hasegawa, M. Ishida, T. Nakajima, Y. Honda, O. Kitao, H. Nakai, M. Klene, X. Li, J. E. Knox, H. P. Hratchian, J. B. Cross, V. Bakken, C. Adamo, J. Jaramillo, R. Gomperts, R. E. Stratmann, O. Yazyev, A. J. Austin, R. Cammi, C. Pomelli, J. W. Ochterski, P. Y. Ayala, K. Morokuma, G. A. Voth, P. Salvador, J. J. Dannenberg, V. G. Zakrzewski, S. Dapprich, A. D. Daniels, M. C. Strain, O. Farkas, D. K. Malick, A. D. Rabuck, K. Raghavachari, J. B. Foresman, J. V. Ortiz, Q. Cui, A. G. Baboul, S. Clifford, J. Cioslowski, B. B. Stefanov, G. Liu, A. Liashenko, P. Piskorz, I. Komaromi, R. L. Martin, D. J. Fox, T. Keith, M. A. Al-Laham, C. Y. Peng, A. Nanayakkara, M. Challacombe, P. M. W. Gill, B. Johnson, W. Chen, M. W. Wong, C. Gonzalez, and J. A. Pople, "Gaussian 03, Revision E.01." Gaussian, Inc., Wallingford, CT, 2004.

[286] E. R. Davidson and S. Chakravorty, "A test of the Hirshfeld definition of atomic charges and moments," *Theor. Chim. Acta*, vol. 83, no. 5–6, pp. 319–330, 1992.

[287] E. Francisco, A. M. Pendás, M. A. Blanco, and A. Costales, "Comparison of direct and flow integration based charge density population analyses," *J. Phys. Chem. A*, vol. 111, no. 48, pp. 12146–12151, 2007.

[288] P. W. Ayers, R. C. Morrison, and R. K. Roy, "Variational principles for describing chemical reactions: Condensed reactivity indices.," *J. Chem. Phys.*, vol. 116, no. 20, p. 8731, 2002.

[289] D. Ghillemijn, P. Bultinck, D. Van Neck, and P. W. Ayers, "A Self-Consistent Hirshfeld Method for the Atom in the Molecule Based on Minimization of Information Loss," *J. Comput. Chem.*, vol. 32, no. 8, pp. 1561–1567, 2011.

[290] R. G. Parr and L. J. Bartolotti, "Some remarks on the density functional theory of few-electron systems," *J. Phys. Chem.*, vol. 87, no. 15, pp. 2810–2815, 1983.

[291] J. P. Perdew, R. G. Parr, M. Levy, and J. L. Balduz, "Density-Functional Theory for Fractional Particle Number: Derivative Discontinuities of the Energy," *Phys. Rev. Lett.*, vol. 49, pp. 1691–1694, 1982.

[292] W. Yang, Y. Zhang, and P. W. Ayers, "Degenerate Ground States and a Fractional Number of Electrons in Density and Reduced Density Matrix Functional Theory," *Phys. Rev. Lett.*, vol. 84, pp. 5172–5175, 2000.

[293] A. I. Baranov and M. Kohout, "Electron localization and delocalization indices for solids," *J. Comput. Chem.*, vol. 32, no. 10, pp. 2064–2076, 2011.

[294] J. Yang and M. Dolg, "Valence basis sets for lanthanide 4f-in-core pseudopotentials adapted for crystal orbital ab initio calculations," *Theor. Chem. Acc.*, vol. 113, pp. 212–224, May 2005.

[295] R. F. W. Bader and M. E. Stephens, "Spatial localization of the electronic pair and number distributions in molecules," *J. Am. Chem. Soc.*, vol. 97, no. 26, pp. 7391–7399, 1975.

[296] R. Ponec and D. L. Cooper, "Anatomy of bond formation. bond length dependence of the extent of electron sharing in chemical bonds from the analysis of domain-averaged fermi holes," *Faraday Discuss.*, vol. 135, pp. 31–42, 2007.

[297] P. Bultinck, D. L. Cooper, and R. Ponec, "Influence of atoms-in-molecules methods on shared-electron distribution indices and domain averaged Fermi holes," *J. Phys. Chem. A*, vol. 114, no. 33, pp. 8754–8763, 2010.

[298] E. Reynolds, P. E. R. Blanchard, Q. Zhou, B. J. Kennedy, Z. Zhang, and L.-Y. Jang, "Structural and spectroscopic studies of $La_2Ce_2O_7$: Disordered fluorite versus pyrochlore structure," *Phys. Rev. B*, vol. 85, p. 132101, 2012.

[299] E. R. Scerri and L. McIntyre, "The Case for the Philosophy of Chemistry," *Synthese*, vol. 111, pp. 213–232, 1997.

[300] M. Galvan, A. Dal Pino, J. Wang, and J. D. Joannopoulos, "Local softness, scanning tunneling microscopy, and surface reactivity," *J. Phys. Chem.*, vol. 97, no. 4, pp. 783–785, 1993.

[301] P. W. Ayers, W. Yang, and L. J. Bartolotti, *Chemical reactivity theory : a density functional view*. Boca Raton : CRC Press/Taylor & Francis, 2009. Fukui Function, Chapter 18 of.

[302] M. Alonso and E. J. Finn, *Quantum and Statistical Physics*, vol. 3 of *Fundamental University Physics*. Reading, Massachusetts: Addison-Wesley, 1969.

[303] G. E. Moore, "Cramming more components onto integrated circuits," *Electronics*, vol. 38, p. 8, 1965.

[304] G. Hager and W. Gerhard, *Introduction to High Performance Computing for Scientists and Engineers*. Computational Science Series, 6000 Broken Sound Parkway NW, Suite 300, Boca Raton, FL 33487-2742: CRC Press, 2011.

Acknowledgements

●

Doing a PhD is a once-in-a-lifetime experience. The same goes for a second PhD. You meet new people and encounter new worldviews. At this place I would like to thank the new, but also the old people, who crossed my path and made life interesting and enjoyable during these last three years.

First and foremost I would like to thank my promoters Prof. Dr. Isabel Van Driessche and Prof. Dr. Patrick Bultinck. Isabel, thank you for the trust you put in me as theoretician of the SCRiPTS group, and for the careful reading of my manuscripts. Your point of view as an experimentalist has been very beneficial to this work, and has always been appreciated. In addition, the organization of group dinners and barbecues added much color to the life at S3.
Patrick, over the last three years, you have taught me that quantum physics and quantum chemistry can be very much the same, while at the same time being almost totally different. This makes it "interesting" to translate concepts, such as *atoms in molecules*, from one field to the other. Something I hope we will be able to continue doing in the coming years. However, the most important thing I learned from you is the fact that even as a group leader you can keep doing your own research, which is what science is all about.

I also wish to thank Prof. Dr. Stefaan Cottenier and Prof. Dr. Ir. Veronique Van Speybroeck for their active representation of the third partner in this collaborative project, and for being members of the jury. A special thanks to Stefaan for his always extensive and very detailed examination of my manuscripts. Your comments are always constructive and helpful, surely contributing to their overall quality.

Being a member of two groups puts one in a special position, especially if these groups are quite different from one another and one's own background. I would like to thank the SCRiPTS group for adopting this theoretician in their midst. Thank you for the pleasant atmosphere during lunch, but also at the group events. I will always look back fondly on the SCRiPTS team building experience; thank you Glenn, Katrien, Kenny, Marcos, Melis, Nigel, Pieter, Ruben, and Tom. Klaartje, Petra, and Vyshnavy, I enjoyed our collaboration on lanthanum cerate very much, and the discussions on this and other topics have been very elucidating, to say the least. Nigel, the man with the golden paint ball gun, and an experimental skill and focus to match: it was always nice to see how your measurements and my calculations could show such nice qualitative agreement, I really enjoyed our discussions and wish you the best for the future.
Likewise, I would like to thank the GQCG for adopting this physicist in their midst, for making me feel welcome and providing a stimulating and nice atmosphere, for both serious and random discussions here at S3 and on conferences. I would also like to thank our foreign group members and visitors for bringing more color to the

GQCG. Thank you Andrés, Dieter, Ewoud, Guillaume, Hellen, Jelle, Mustafa, Santeri, Slavko, Sofie, Stijn, and Vijay.

A computationally intensive work like this one would have been impossible without access to HPC facilities, and the people keeping it running. Tom Kuppens, Stijn De Weirdt and Kenneth Hoste, thank you for all your help, and the patience you had with me and my questions. Your relentless efforts in keeping everything running smoothly and helping out with all my questions, despite being understaffed and overbooked, is more than appreciated.

On a similar note, I would like to thank Pierre and Claudine for keeping the administration at S3 running smoothly, and your help with working out the university paperwork. Pierre, the life you bring to the lunch time breaks makes you irreplaceable.

De laatste, en zeker niet de minste die ik hier zou willen bedanken zijn m'n familie en vriendin. Mama, papa, jullie hebben me geleerd dat alles mogelijk is, en dat je je hart moet volgen waar het je leidt. Liefste zusje, wat kan ik zeggen, dit boek is natuurlijk ook een klein beetje opgedragen aan m'n toekomstig petekindje.

Lieve Sylvia, twee maal samen doctoreren, twee maal elkaars steun en toeverlaat zijn. Je bent de zon en de hoop in mijn leven, mijn dans- en levenspartner. Je bent mijn Lorelai Gilmore en mijn Olivia Dunham. Zonder jouw liefde zou alles een stuk moeilijker gaan, daarom wil ik je vandaag bedanken voor jouw steun en liefde.

Weldra zijn we samen mama en papa, en daarom wens ik dit boek aan jou en onze kleine spruit op te dragen.

Gent, oktober 2012
Danny Vanpoucke

LIST OF PUBLICATIONS AND PRESENTATIONS

━━━━━━━━━━ ⬤ ━━━━━━━━━━

Publications relevant to this thesis

[1] *Aliovalent Doping of CeO$_2$: DFT study of Valence and Vacancy effects*
Danny E. P. Vanpoucke, Patrick Bultinck, Stefaan Cottenier, Veronique Van Speybroeck, and Isabel Van Driessche
in preparation (2012).
(**Chapter 5**)

[2] *Tetravalent Doping of CeO$_2$: The impact of valence electron character on group IV dopant influence*
Danny E. P. Vanpoucke, Patrick Bultinck, Stefaan Cottenier, Veronique Van Speybroeck, and Isabel Van Driessche
in preparation (2012).
(**Chapter 4**)

[3] *Extending Hirshfeld-I to bulk and periodic materials*
D. E. P. Vanpoucke, P. Bultinck, and I. Van Driessche
submitted to Journal of Computational Chemistry (2012).
(**Chapter 8**)

[4] *Tuning of CeO$_2$ buffer layers for coated superconductors through doping*
D. E. P. Vanpoucke, S. Cottenier, V. Van Speybroeck, P. Bultinck, and I. Van Driessche
Applied Surface Science, in press, corrected proof,
doi:10.1016/j.apsusc.2012.01.032 (2012).
(**Chapter 4**)

[5] *Aqueous CSD approach for the growth of novel, lattice-tuned La$_x$Ce$_{1-x}$O$_\delta$ epitaxial layers*
Vyshnavi Narayanan, Petra Lommens, Klaartje De Buysser, Danny E.P. Vanpoucke, Ruben Huehne, Leopoldo Molina, Gustaaf Van Tendeloo , Pascal Van Der Voort, Isabel Van Driessche
Journal of Materials Chemistry 22, 8476 (2012).

[6] *Density functional theory study of La$_2$Ce$_2$O$_7$: Disordered fluorite versus pyrochlore structure*
D. E. P. Vanpoucke, P. Bultinck, S. Cottenier, V. Van Speybroeck, and I. Van Driessche
Physical Review **B 84**, 054110 (2011).
(**Chapter 6**)

Other publications

[1] *Models and simulations in material science: two cases without error bars*
Sylvia Wenmackers and Danny E. P. Vanpoucke
Statistica Neerlandica, doi:10.1111/j.1467-9574.2011.00519.x (2012).

[2] *Probability of inconsistencies in theory revision; A multi-agent model for updating logically interconnected beliefs under bounded confidence*
S. Wenmackers, D. E. P. Vanpoucke, and I. Douven
The European Physical Journal B 85, doi:10.1140/e2011-20617-8 (2012).

[3] *[Feature Article] Pt Nanowires on Ge(001): Sheep in Wolf's Clothing?*
Danny E. P. Vanpoucke
Belgian Physical Society Magazine 3, 11-16 (2011).

[4] *CO adsorption on Pt induced Ge nanowires*
D. E. P. Vanpoucke and G. Brocks
Physical Review **B 81**, 235434 (2010).

[5] *Pt-induced nanowires on Ge(001): A density functional theory study*
D. E. P. Vanpoucke and G. Brocks
Physical Review **B 81**, 085410 (2010).

[6] *Density functional theory study of Pt-induced Ge(001) reconstructions*
D. E. P. Vanpoucke and G. Brocks
Physical Review **B 81**, 035333 (2010).

[7] *The formation of self-assembled nanowire arrays on Ge(001): a DFT study of platinum induced nanowire arrays* in *Computational Nanoscience – How to Exploit Synergy between Predictive Simulations and Experiment.*
D. E. P. Vanpoucke and G. Brocks
(Materials Research Society Symposium Proceedings **Volume 1177E**, Warrendale, PA, 2009),1177-Z03-09 (2009).

[8] *Ab Initio study of Pt Induced Nanowires on Ge(001)*
D. E. P. Vanpoucke
Ph.D. Thesis University of Twente, The Netherlands, ISBN: 978-90-365-2873-3 (2009).

[9] *Formation of Pt-induced Ge atomic nanowires on Pt/Ge(001): A density functional theory study*
D. E. P. Vanpoucke and G. Brocks
Physical Review **B 77**, 241308(R) (2008).

Presentations relevant to this thesis

Oral presentations

[1] *Atomic charges in solids: Calculating Hirshfeld-I charges for overlapping atoms from the electron density distribution*
ICAMM 2012 & VASP workshop, Nantes, France, June 11–16th, 2012.

[2] *Tuning of CeO$_2$ buffer layers for coated superconductors through metal doping*
E-MRS 2011 Fall Meeting, Warsaw, Poland, September 19–23rd, 2011.

[3] *DFT study of La$_2$Ce$_2$O$_7$: a Question of Order*
2011 meeting of the Belgian Ceramic Society, Mons, Belgium, February 7th, 2011.

Poster presentations

[1] *Chemistry in Solids; Extending the Hirshfeld-I method.*
Quantum Chemistry in Belgium, tenth edition, Etterbeek, Belgium, February 10th, 2012

[2] *Tuning of CeO$_2$ buffer layers through doping*
Seventh International Conference on Inorganic Materials, Biarritz, France, September 12–14th, 2010

Other Presentations

Oral presentations

[1] *Pt nanowires on Ge(001): Sheep in Wolf's Clothing?*
(First prize at the '2011 Young Speaker Contestt')
Belgian Physical Society General Scientific Meeting 2011, Namur, Belgium, May 25th, 2011.

[2] *The formation of self-assembled nanowire arrays on Ge(001): a DFT study of platinum induced nanowires*
MRS Spring meeting, San Fransisco, USA, April 13–17th, 2009.

[3] *DFT Study of Pt Induced Nanowires*
DPG Spring meeting, Dresden, Germany, March 22–27th, 2009.

[4] *Nanowires on the Germanium-Platinum(001)-surface*
CW-study group Spectroscopy and Theory, Luntheren, The Netherlands, January 28–29th, 2008

Poster presentations

[1] *CO Adsorption on Pt induced Nanowires*
Mesa$^+$-day, Enschede, The Netherlands, September 21th, 2009

[2] *Road To Nanotechnology*
Science as Art competition at the MRS Spring meeting, San Fransisco, USA, April 13–17th, 2009.

[3] *Formation of Pt Induced Nanowires on Ge(001): a DFT study*
CW-study group Spectroscopy and Theory, Luntheren, The Netherlands, January 26–27th, 2009

[4] *The Germanium-Platinum(001) surface as a template for nanowires*
ICTP 14th international workshop on computational physics and material science: Total energy and force methods, Trieste, Italy, January 8–10th, 2009

[5] *The Germanium-Platinum(001) surface as a template for nanowires*
CECAM Workshop: Structural, electronic and transport properties of quantum wires, Lyon, France, June 9–12th, 2008

[6] *The Germanium-Platinum(001) surface as a template for nanowires*
FOM Physics@Veldhoven, Veldhoven, the Netherlands, January 22–23th, 2008

[7] *Depositing Pt on Ge(001): Where do the Pt Atoms Go?*
Mesa^{+}-day, Enschede, The Netherlands, September 11th, 2007

[8] *Depositing Pt on Ge(001): Where do the Pt Atoms Go?*
CW-study group Spectroscopy and Theory, Luntheren, The Netherlands, January 29–30th, 2007

[9] *Depositing Pt on Ge(001): Where do the Pt Atoms Go?*
FOM Physics@Veldhoven, Veldhoven, the Netherlands, January 23-24th, 2007

[10] *Surface and Interface calculations: GaAs/Ge, LaAlO$_3$/SrTiO$_3$ and Pt on Ge(001)*
NIC winterschool 2006: Computational Nanoscience: Do It Yourself!, Forschungszentrum Jülich, Germany, February 14–22th, 2006

High temperature ceramic superconductors can be grown in layered structures on metallic wires to provide the mechanical flexibility required for industrial applications. To prevent the metal atoms of diffusing into the superconductor – destroying its superconductivity – buffer layers are grown between the metal substrate and the superconductor. Recently, cerium oxide has been used as such a buffer layer. However, the layer thickness of these buffer layers is limited by the formation of cracks during deposition. This behaviour has been linked to internal stress due to lattice mismatch and different thermal expansion coefficients of the substrate and the buffer layer. A simple way to reduce these mismatches is through metal doping.

In this work, we study the influence of dopants on the properties of cerium oxide through the use of *ab initio* calculations. Trends in the stability, lattice parameter, bulk modulus and thermal expansion coefficient of cerium oxide doped with different dopants are investigated. In addition, the influence of charge compensating oxygen vacancies is studied, and their role in the stability of heavily La-doped cerium oxide ($La_2Ce_2O_7$) is presented.

The use of dopants with different valences also leads to a modification of the charge distribution around the dopant sites. A way to have a more quantitative estimate of the charge transfer induced by dopants is via the introduction of the chemical concept of 'atoms in a molecule' into solids. This can be considered a first step in the direction of answering the experimental question: What is the charge of a given atom in a certain compound? In this work we present an implementation of this Hirshfeld method for solids, and calculate the atomic charges in doped cerium oxides.